



HAL
open science

Meso-scale FE and morphological modeling of heterogeneous media : applications to cementitious materials ”

Emmanuel Roubin

► **To cite this version:**

Emmanuel Roubin. Meso-scale FE and morphological modeling of heterogeneous media : applications to cementitious materials ”. Other. École normale supérieure de Cachan - ENS Cachan, 2013. English. NNT : 2013DENS0038 . tel-00957377

HAL Id: tel-00957377

<https://theses.hal.science/tel-00957377>

Submitted on 10 Mar 2014

HAL is a multi-disciplinary open access archive for the deposit and dissemination of scientific research documents, whether they are published or not. The documents may come from teaching and research institutions in France or abroad, or from public or private research centers.

L'archive ouverte pluridisciplinaire **HAL**, est destinée au dépôt et à la diffusion de documents scientifiques de niveau recherche, publiés ou non, émanant des établissements d'enseignement et de recherche français ou étrangers, des laboratoires publics ou privés.



ENSC-2013-n° 467



**THÈSE DE DOCTORAT
DE L'ÉCOLE NORMALE SUPÉRIEURE DE CACHAN**

Présentée par

Emmanuel Roubin

pour obtenir le grade de

DOCTEUR DE L'ÉCOLE NORMALE SUPÉRIEURE DE CACHAN

Domaine

MÉCANIQUE - GÉNIE MÉCANIQUE - GÉNIE CIVIL

Sujet de la thèse

**Modélisation EF et morphologique de milieux
hétérogènes à l'échelle mésoscopique : applications aux
matériaux à matrice cimentaire**

Soutenue à Cachan le 10 octobre 2013 devant le jury composé de :

Pr. Nicolas BURLION	LML, Polytech' Lille	<i>Président du jury</i>
Pr. Jean-Michel TORRENTI	IFSTTAR	<i>Rapporteur</i>
Pr. Djimedo KONDO	IJLRDA, UPMC	<i>Rapporteur</i>
Pr. Javier OLIVER	UPC Barcelona	<i>Examineur</i>
Dr. Nathan BENKEMOUN	GeM, UNAM	<i>Examineur</i>
Pr. Jean-Baptiste COLLIAT	LML, Univ. Lille 1	<i>Directeur de thèse</i>

LMT-Cachan

ENS Cachan / CNRS / UPMC / PRES UniverSud Paris
61 avenue du Président Wilson, F-94235 Cachan cedex, France

Avants-propos

Ce document, rédigé en anglais, constitue la synthèse de mes travaux de recherches effectués au sein du secteur Génie Civil et Environnement du LMT-Cachan durant les trois années de mon doctorat — de octobre 2010 à octobre 2013.

RÉSUMÉ : Le travail effectué tend à représenter le comportement quasi-fragile des matériaux hétérogènes (matériaux à matrice cimentaire). Le principe suivi s'inscrit dans le cadre des approches multi-échelles séquencées où la description des matériaux est faite à une échelle fine (mésoscopique) et l'information est transférée à une échelle plus grande (macroscopique). Les résultats montrent que la prise en compte explicite des hétérogénéités offre des perspectives intéressantes vis-à-vis de l'identification, la compréhension ainsi que la modélisation des comportements macroscopiques. En pratique : à partir d'une description simple de chaque phase ainsi que du comportement des interfaces, un effet structurel est observé, menant à des comportements macroscopiques compliqués. Le travail est donc axé autour de deux problématiques principales. D'un coté, la représentation morphologique des hétérogénéités est produite en utilisant la théorie des excursions de champs aléatoires corrélés, produisant des inclusions de forme aléatoires dont les caractéristiques géométriques et topologiques sont analytiquement contrôlées. D'un autre coté, dans un cadre Elément Fini, un double enrichissement cinématique permet de prendre en compte les hétérogénéités ainsi que le phénomène de dégradation local (microfissuration). En couplant ces deux aspects, le méso-modèle montre des réponses macroscopiques émergentes possédant d'intéressantes propriétés typiques des matériaux à matrice cimentaires telles que : asymétrie de la réponse en traction et en compression, profils de fissurations réalistes ou encore dépendance du comportement vis-à-vis de l'historique du chargement.

ABSTRACT: The present thesis is part of an approach that attempts to represent the quasi-brittle behavior of heterogeneous materials such as cementitious ones. The guideline followed fits in a sequenced multi-scale framework for which descriptions of the material are selected at a thin scale (mesoscopic or microscopic) and information is transferred to a larger scale (macroscopic). It shows how the explicit representation of heterogeneities offers interesting prospects on identification, understanding and modeling of macroscopic behaviors. In practice, from a simple description of each phases and interfaces behavior, a structural effect that leads to more complex macroscopic behavior is observed. This work is therefore focusing on two main axes. On the one hand, the morphological representation of the heterogeneities is handle using the excursion sets theory. Randomly shaped inclusions, which geometrical and topological characteristics are analytically controlled, are produced by applying a threshold on realizations of correlated Random Fields. On the other hand, the FE implementation of both heterogeneity and local degradation behavior (micro-cracking) are dealt with by a double kinematics enhancement (weak and strong discontinuity) using the Embedded Finite Element Method. Finally, combining both axes of the problematic, the resulting model is tested by modeling cementitious materials at the meso-scale under uniaxial loadings mainly. It reveals an emergent macroscopic response that exhibits several features such as asymmetry of the tension-compression stress-strain relationship, cracks' patterns or historical-dependency, which are typical of concrete-like materials.

Remerciements

Mes remerciements vont en premier lieu à MM. les Professeurs Djimedo Kondo et Jean-Michel Torrenti pour avoir accepté la tâche de rapporteurs de mes travaux de thèse synthétisés dans ce document. *Agradezco asimismo al Profesor Javier Oliver haber querido formar parte del tribunal en la presentación de mi tesis.* Ma reconnaissance va également au Professeur Nicolas Burlion pour avoir bien voulu prendre part à mon jury de soutenance en tant que président.

Je tiens à remercier très chaleureusement mon directeur de thèse, le Professeur Jean-Baptiste Colliat, pour m'avoir encadré, formé et guidé depuis mon stage de master 2. Ton encadrement fut très précieux et enrichissant. Mon envie de continuer dans le monde de la recherche n'est bien évidemment pas décorrélée de la vision que tu en as et que tu m'as transmise au cours de ces trois années. J'espère sincèrement que le futur nous réserve de nombreuses collaborations. Je remercie aussi Nathan Benkemoun pour m'avoir initié à sa thématique de recherche et aidé à y contribuer. Merci à vous deux finalement pour votre aide précieuse lors de la rédaction de ce document.

Enfin, je tiens particulièrement à féliciter mes relect(eur|rice)s, Laura, Pascale, Brigitte et Bill, pour l'effort d'abstraction qu'(il|elle)s ont fourni afin de déceler les coquilles de ce mémoire. Merci.

Aux aminches, aux villes et aux autres... à ceux et celles avec qui j'ai vécu durant ces trois années.

Zouzou, Nico, la villa et le Stendhal, ma soeur, le Zabar et les binouzes. Le XX^{ième}, son pont, ses poivrots et ses troquets. Renaud et Mano Solo. Sans qui, sans quoi, Paname ne serait pas Paname pour moi.

Marseille, sa lumière, ses rues, ses calanques et ses collines. Ainsi que Laura, IAM, Izzo, Pagnol et Espérandieu, qui en sont les meilleurs guides. Et à la Provence de façon générale, je lève mon verre. Un jour je reviendrai.

Et en vrac, à Steely Dan, Antoine Doinel, Laura de Corinne, Vincent, Bill Deraime, Boutix, Gainsbourg, Leonard Cohen, mes parents, au petit âne gris, à Prince, Patate, Carole, Édith, Camille, Lille, Marie-Christine et Nathalie, au LMT, son bar et ses habitants, à Arnaud et aux gars du CDC, au DGC et son équipe, Pascale, Caro, Xavier, Farid, Avelyne, Adrien, Alexandre, Maxime, à Marcel Carné, Prévert et Baptiste, au jaune, à la Sainte, la vraie, au Var, à l'action Christine, Henri Poitiers, Loul, au gars qui rentre rentre dans un café, aux pâtes à l'huile, à Théo et Louissette, à Momo, David, l'auvergnat de Kabylie et leurs tournées, au Cercle rouge et aux blind tests, à Ernst Lubitsch, Frizou, Michel Audiard, Warren Ellis, Benjamin, Fred, aux Trappier-Benhamou and affiliated, au Queyras, à la neige et au calcaire, au café et aux cafés, à Earth Wind & Fire, Massilia Sound System, la petite ceinture, Edmond Rostand, Ayman, David, Michael Jackson, Black Dynamite, à l'Estaque et aux Goudes, à Morgane, Leos Carax, Agent Cooper, aux Maraîchers, aux Monty Python, à la Vieille Charité, au train et au trajet Braunschweig-Marseille, au Clos, à Assassin's Creed, au Petit Longchamp, aux clopes... Et à bien d'autres.

À tout ce petit monde, *le bécot et à bientôt.*

Manu

ÉCOLE NORMALE SUPÉRIEURE DE CACHAN

ENSC-2013-N°467

PH.D. THESIS

**Meso-scale FE and morphological
modeling of heterogeneous media**

—

Applications to cementitious materials

Author:

Emmanuel ROUBIN

Supervisor:

Pr. Jean-Baptiste COLLIAT

Version: November 1, 2013

This one is to my grandfather Théo

Table Of Contents

Introduction	1
1 Morphological modeling: a generalized method based on excursion sets	5
1 Introduction	6
2 Review on correlated Random Fields	9
2.1 Basic definitions	9
2.2 Gaussian and Gaussian related distribution	10
2.3 Covariance functions	11
2.4 Numerical implementation	16
3 Excursion set theory	19
3.1 General principle	19
3.2 Measures of excursion set	21
3.3 Expectation formula	28
4 Application to cementitious materials at different scales	32
4.1 Meso-scale modeling of concrete	33
4.2 Micro-scale modeling of cement paste	44
5 Analytical model for size effect of brittle material	50
5.1 Correlation lengths as scale parameters	51
5.2 One-dimensional case	52
5.3 Validation, results and comments	53
6 Continuous percolation on finite size domains	54
6.1 Accounting for side effects	55
6.2 Representative Volume Element for percolation	57
7 Concluding remarks	59
2 Unified numerical implementation of quasi-brittle behavior for heterogeneous material through the Embedded Finite Element Method	61
1 Introduction	62
2 Kinematics of strain and displacement discontinuity	65
2.1 Jump in the strain field	67
2.2 Jump in the displacement field	68
2.3 Strong discontinuity analysis	70
3 Variational formulation	71
3.1 Three-field variational formulation	71
3.2 Assumed strain and double enhancement	73
3.3 Finite Element interpolation	76
4 Discrete model at the discontinuity	78
4.1 Localization	79

4.2	Traction-separation law	80
5	Resolution methodology	81
5.1	Integration and linearization with constant strain elements	82
5.2	Solving the system	84
5.3	Application to spatial truss and spatial frame	86
5.4	Application to volume Finite Elements	97
6	Concluding remarks	103
3	Applications to cementitious materials modeling	105
1	Introduction	106
2	One-dimensional macroscopic loading paths	108
2.1	Analysis of the asymmetric macroscopic response for traction and compression loading paths	108
2.2	Transversal strain	118
2.3	Dissipated energy	120
2.4	Induced anisotropy	122
2.5	Uniaxial cyclic compression loading	124
3	Representative Volume Element for elastic and failure properties	129
3.1	Experimental protocol	130
3.2	Young moduli analysis	131
3.3	Tensile and compressive strength	133
3.4	Comments	135
4	Application to the Delayed Ettringite Formation	136
4.1	Numerical simulation	137
4.2	Homogeneous mortar expansion	138
4.3	Residual Young modulus	139
5	Concluding remarks	140
	Conclusions and perspectives	143
A	Gaussian Minkowski Functionals	145
1	Volume of the unit ball	145
2	Probabilist Hermite polynomials	145
3	Gaussian volumes of spherical set in \mathbb{R}^k	146
B	Correlated Random Fields	149
1	Orthogonal decomposition of correlated random fields	149
2	Finite Element discretization of the Fredholm problem	150
3	The turning band method	151
	Bibliography	155

Introduction

The homogeneity of a heterogeneous material is a concept of statistical nature that cannot be isolated from the observation scale to which it is considered. This logical statement takes on a particular significance for understanding and modeling concrete-like materials. The inherent stationary and ergodic¹ nature of material heterogeneities results in large enough specimens — in regards to their heterogeneity sizes — that exhibit expected values of a given property with a very low variability [Matheron, 1966]. Thus, statistical Representative Volume Elements (RVE) are defined, in which macroscopic characteristics of the material can be considered [Hill, 1963]. It is as a result of these statistical bases that a multi-phase material is considered homogeneous.

Phenomenological — or macroscopic — models [Ollivier et al., 2012] are built on this principle, defining the material behavior upon homogenized — or effective — mechanical properties. Considering degradation mechanisms or evolution processes of concrete or any cementitious material, their intricate nature leads to macroscopic governing laws increasingly more specific and difficult to identify. It is in view of this growing complexity that the question of observation scales becomes relevant. Since it clearly appears that most of these macroscopic behaviors (creep, shrinkage, cracking, *etc*) take their origin at smaller scales (mesoscopic, microscopic, *etc*), accurate identification and modeling of local degradation phenomena seem to be a key step of research towards predictive and robust representations of macroscopic behaviors onto RVE. On the one hand, from a theoretical point of view, that leads to micromechanics-based models including anisotropic damage and plasticity [Zhu et al., 2008]. On the other hand, numerically speaking, those issues can be addressed within a sequenced multi-scale framework [Zaitsev, 1985], both selecting local mechanisms and transferring information from small to large scales.

The very essence of multi-scale strategy is to consider the macroscopic behavior modeling as a non-linear complex adaptive system [Ahmed et al., 2005]. Somehow, “unpredictable emergent” responses are produced by local basic evolution rules depending on each phase of the material. The definition of this local level — or scale — is therefore made upon the explicit geometry of the material heterogeneities. Henceforth, simulating such systems exhibits the underlying structural effect that morphological modeling provides. Finally, by their physically meaningful aspects, these procedures can be seen as virtual testing [Heimbs, 2009]. The structural random aspect of heterogeneity representation strongly links this virtual testing framework with Monte Carlo experiments [Caflisch, 1998].

Regarding concrete-like materials, the two local levels usually defined are the meso-scale and the micro-scale, giving millimeter and micrometer-sized heterogeneity details,

¹Convergence property of random functions granting null variability over infinite volume.

respectively. Naturally, by going deeper into the scale precision, the morphology of concern changes. On the one hand, at the meso-scale, concrete may be represented by a two-phase material in which aggregates are included within a coarse mortar matrix. On the other hand, at the micro-scale, the latter mortar representation is detailed by smaller heterogeneities of different natures such as sand particles or large pores. Furthermore, depending on the problematic of concern, it can become relevant to represent additional phases. The geometrical and topological characteristics change from one scale to another, together with the resulting structural effect, gaining physical meaning along with the scale precision.

If the meso-scale is considered, this numerical strategy is referred to as meso-models [Zaitsev and Wittmann, 1981]. They are built upon local behaviors of the present phases and an explicit representation of the meso-structure. Their goals are to compute the macroscopic behavior of representative disordered meso-structures such as effective elastic moduli and stress field distribution. This type of numerical calculation provides an efficient alternative to homogenization theories which mainly take into account volume fractions without dealing with the exact phase arrangement. In addition, several non-linear features can be implemented at the meso-scale, giving the possibility of observing the up-scaling process of local degradation to the global behavior. The strength of these models is to be built on a physical structural effect. Therefore, the degradation modeling of the meso-scale can be kept simple and still produce complex macroscopic mechanisms. The predominant focus of this document is on this particular aspect and, even if cementitious materials exhibit numerous phenomena at the micro- — or even nano- — scale, attention is mainly drawn to the intermediate meso-scale.

In view of the significant impact of thin scale² heterogeneities with regards with to macroscopic response, a particular effort is dedicated to morphological representation. Thus, the development of a model based on spatially correlated random functions is proposed in **Chapter 1**. It is shown how the stationary ergodic property coupled with the spatial structure of correlated Random Fields can efficiently address the problematic when submitted to a threshold process³ [Adler, 2008]. Recent results from this mathematical field give accurate ways to analytically control the resulting morphology, both geometrically and topologically speaking. Solutions to adapt the initial framework to cementitious material problematics are given, responding to several common issues such as reaching high fraction volumes, representing grain size distributions, modeling additional phases and making them evolve over time. Finally, the fact that side effects are taken into the model gives relevant information on finite size problems [Worsley, 1996]. This important

²The classical geographer definition of scales is based on the ratio of the distance on a map to the corresponding distance on the ground. Hence, maps are often described as large scale if they show small areas with details. For example, a map of Marseille is of smaller scale than a map of ‘Les Goudes’, one of its fisherman villages. However, the physicist community defines scale sizes in regards to the details they can depict. Hence, thin scales refer to meso, micro or nano-scales and large scales to macro-scales.

³Excursion set theory.

feature is used in the context of RVE determination for percolation and one-dimensional size effect modeling, both being dealt with analytically.

The numerical implementation of the framework is presented in **Chapter 2**. Based on the non-adapted mesh methods, it is shown how a kinematics enhancement — strain discontinuity — is an efficient solution to address the main issues of heterogeneous material modeling and its integration within a Finite Element context [Ortiz et al., 1987, Sukumar et al., 2001]. In addition, a second kinematics enhancement — displacement discontinuity — models the local degradations by a meso-cracking representation [Simo et al., 1993]. The advantages of the latter method compared to the more conventional approaches usually retained for macroscopic phenomenological models are pointed out. Moreover, this chapter is the opportunity to present how, by using Finite Elements with embedded discontinuities [Simo and Rifai, 1990], these two problematics can be integrated within a unified framework in which the local aspect of meso-scale behavior is strongly present. The different choices that lead to the solution proposed are mostly made accordingly to a simple meso-scale modeling spirit. However, attention is focused on geometrical information, such as crack orientation, in order to improve the structural effect significance. Finally, details of several discretizations using trusses, frames or volume meshes are given, showing how the Finite Element kinematics impact on the macroscopic response.

Morphological modeling based on correlated Random Fields and Finite Element with embedded discontinuities are implemented into a meso-model whose performances are shown in **Chapter 3** through several typical applications related to cementitious materials. First, specimens are loaded following uniaxial monotonic and cyclic paths in both tension and compression. It is the opportunity to show that the meso-model exhibits several common features of complex system highly representative of macroscopic failure mechanisms. Among the most significant, the next three are worth noticing:

Emergent phenomena (illustration in FIG. (1))

The resulting behavior is more complex than the simple local implementation and features such as tension-compression asymmetrical responses or complex cracks' patterns due to the structural effect can only be analyzed at the macroscopic scale.

Cascading failures

A single local failure — micro-cracking — can lead to severe consequences at the macroscopic scale, representing the brittle nature of crack initiation.

Memory

The structural effect leads to non-symmetrical failure mechanism during loading-unloading tests or non-proportional loading. This feature naturally represents the cementitious material historically-dependent property and thus leads to mechanical behaviors that are highly anisotropic.

Then, Monte Carlo experiments are made to define RVE for elastic modulus as well as non-linear features (strengths). Then, multi-physics examples related to concrete durability are addressed revealing the impact of damaged states on material properties.

Finally, concluding remarks and comments are made on the general framework. Perspectives are investigated in order to: on the one hand improve the model and on the other hand propose other applications corresponding to its performances.

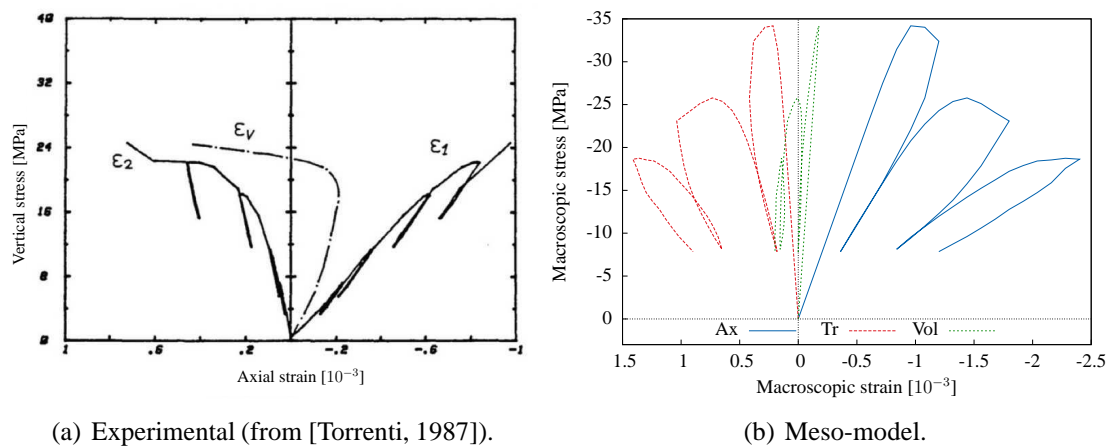


Figure 1: Illustration of an emergent phenomena: macroscopic responses on cyclic compression loading: stress versus axial, transversal and volumetric strain.

Chapter 1

Morphological modeling: a generalized method based on excursion sets

Contents

1	Introduction	6
2	Review on correlated Random Fields	9
2.1	Basic definitions	9
2.2	Gaussian and Gaussian related distribution	10
2.3	Covariance functions	11
2.4	Numerical implementation	16
3	Excursion set theory	19
3.1	General principle	19
3.2	Measures of excursion set	21
3.3	Expectation formula	28
4	Application to cementitious materials at different scales	32
4.1	Meso-scale modeling of concrete	33
4.2	Micro-scale modeling of cement paste	44
5	Analytical model for size effect of brittle material	50
5.1	Correlation lengths as scale parameters	51
5.2	One-dimensional case	52
5.3	Validation, results and comments	53
6	Continuous percolation on finite size domains	54
6.1	Accounting for side effects	55
6.2	Representative Volume Element for percolation	57
7	Concluding remarks	59

1 Introduction

At the macroscopic scale, probabilistic aspects of material heterogeneities are embedded in choices and identifications of predictive models. Based on thinner observation scales, multi-scale frameworks highlight the underlying variability aspect of the random aspect of heterogeneities. Henceforth, in addition to any mechanical model, a morphological one has to be developed to describe phase arrangements, with regard to the observation scale.

In this chapter, a generalized framework for morphological modeling based on the excursion set theory of correlated Random Fields is proposed. The term “generalized” has to be seen here as the ability of the model to represent, with the same theoretical basis, several kinds of morphology (*e.g.* matrix-inclusion, porous media, *etc*) that may turn out to be a handy tool when cementitious materials are considered for different observation scales.

The most common representation of heterogeneities is often performed using objects with simple geometrical definitions such as spheres [Bezrukov et al., 2002] or ellipsoids [Bezrukov and Stoyan, 2006]. For example, considering cementitious materials at the meso-scale, they can be represented by a two-phase matrix-inclusion medium using non-overlapping spheres [Torquato, 2002]. Introduced in [Matérn, 1960] and generalized for a random distribution of independent sphere radii in [Stoyan and Stoyan, 1994], the numerical implementation of these models is based on a Gibbs point process. In a volume V , the number of points follows a Poisson distribution of parameter λV , in which λ is the mean number of spheres per unit volume. Then, depending on the radii (that can follow a grain size distribution [Wriggers and Moftah, 2006]), each sphere is placed in order to avoid overlapping. These methods, often referred to as “take-and-place methods”, can be found in the literature with different optimization procedures and geometrical shapes [Wittmann et al., 1985, Bažant et al., 1990, Schlangen and Van Mier, 1992, Wang et al., 1999].

Although the formulation of these models is rather simple, their numerical implementations raise several issues, especially considering high volume fractions. Even if experience has shown that for equal spheres a maximal volume fractions of 64% can be obtained, reaching this value corresponds to unreasonable computation time if no improvement is made on the basic algorithm. In [Stoyan, 2002], Dietrich Stoyan describes methods to address these issues. Among them, for their natural and physically meaningful spirit, two algorithms based on simple Newtonian principles are worth noticing. These principles are *gravitation* and *repulsion-force*.

Sedimentation

First, improvement — in terms of computation time — can be obtained by performing a sedimentation algorithm [Jodrey and Tory, 1979]. The idea of this method is to drop each sphere one by one onto an initial layer of spheres. Each sphere falls — following “gravitation” — until it reaches a pre-existing sphere and then rolls

to a stable position (three contact points). According to Stoyan, this algorithm produces packings of 58 % volume fractions with identical spheres. Computation time may be improved but, due to the lack of a densification process, the density obtained is lower than before. Furthermore, due to gravitational forces a resulting weak anisotropy in the vertical direction is observed. Variations of this algorithm can be found in [Jodrey and Tory, 1985, Barker and Grimson, 1989].

Collective rearrangement

Packings with higher volume fractions can be obtained using the so called collective rearrangement (or force biased or Stillinger's) algorithms [Mościński et al., 1989, Bargiel and Mościński, 1991]. The principle is to start with an initial configuration of a fixed number of (possibly) overlapping spheres. Then, intersections are dealt with by moving them following a "repulsion-force" law and shrinking them. New positions and sizes of the spheres are computed at each step of the algorithm until a complete non-overlapping configuration — which is the convergence criterion — is found. In [Bargiel and Tory, 2001], it allows the authors to produce more than 70 % volume fraction packings.

Improving both time computation and resulting volume fraction, the latter family of algorithms has been retained in the ongoing Ph.D. thesis of Alexis Vallade. Following [Bezrukov et al., 2002], implementation (without the shrinking mechanism) adapted to a distribution of radii has been made and results can be seen in FIG. (1.1(a)) on a converged configuration. For high volume fractions, it can occur that no non-overlapping configuration is found. A remarkable example of this non converged case is depicted in FIG. (1.1(b)), in which the unique spheres tend to form an optimized crystalline pattern.

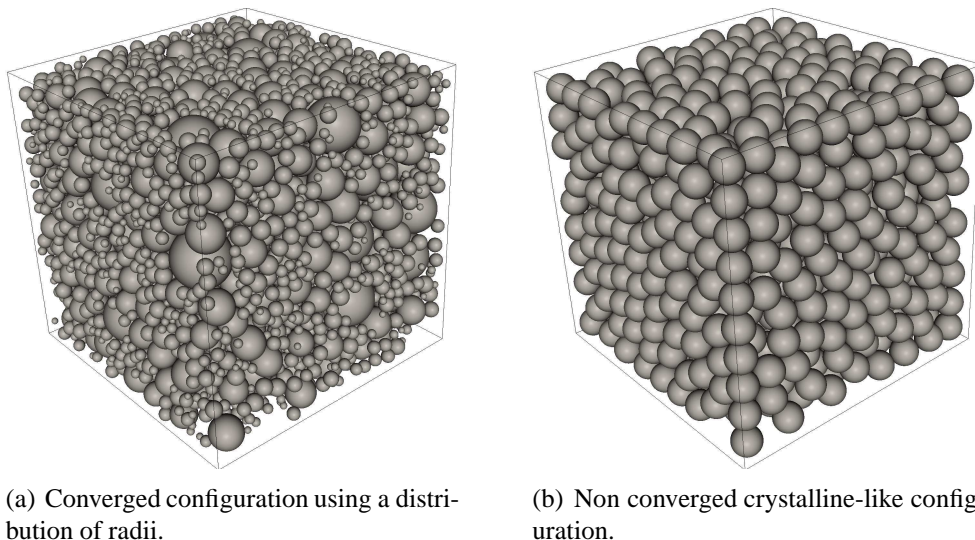


Figure 1.1: Sphere packing using the collective rearrangement algorithm.

Even though algorithms can help solve the intrinsic issue of reaching high volume

fractions of these methods, the amount of information necessary to describe these morphologies can become important when a large number of inclusions is considered. Indeed, it is linear to the number N of objects: $4N$ for spheres and $7N$ for ellipsoids. Furthermore, the perfect aspect of simple objects such as spheres is hardly representative of concrete aggregates. Integration of complex shapes in the latter frameworks is unknown to the author but seems rather difficult to generalize. Finally, representing other kind of morphology, *e.g.* porous media, will require another set of methodologies.

These reasons led the author to turn to morphological models with a more important underlying random aspect such as excursion sets.

An excursion set is the thresholding process resulting set of a random function defined over a finite space. For example, if $g(\mathbf{x}) : M \subset \mathbb{R}^3 \rightarrow \mathbb{R}$ is a realization of a random function (see FIG. (1.2(a)), then for a given threshold (hereafter called level set) κ , the excursion set $E_s \subset \mathbb{R}^3$ (see FIG. (1.2(b))) can be defined by the part of M where g is greater than κ :

$$E_s = \{\mathbf{x} \in M \mid g(\mathbf{x}) > \kappa\}.$$

A more general definition is given in this chapter.

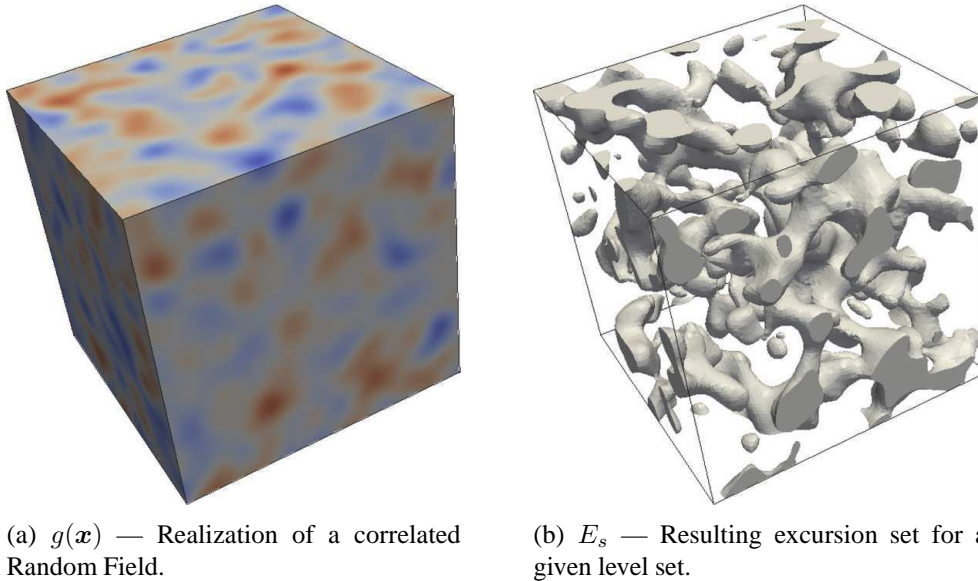


Figure 1.2: Illustration of the excursion set principle.

Excursion sets as depicted in FIG. (1.2) can have very different aspects depending on the level set and the random function characteristics. Henceforth, it seems relevant to use them in the context of correlated Random Fields since their intrinsic spatial structure — through covariance functions — leads to complex shapes and flexible structures that can be statistically controlled both geometrically and topologically speaking. Indeed, as mentioned in [Serra, 1982] and [Roberts and Garboczi, 1999] for cementitious materials, the strength of this theory is in its representation of morphologies by global descriptors

(volume, number of components, *etc*) that are defined statistically and not for a given realization. Furthermore they can possess the suitable stationary, ergodic [Matheron, 1966] and isotropic [Bažant et al., 1990] properties for material heterogeneity modeling. In addition, the model presented here is based on a formula [Adler, 2008] that links together expectations of geometrical and topological characteristics of the excursion set and Random Field characteristics, granting a powerful predictive aspect to the model.

This chapter attempts to present in detail this theory along with several adaptations for cementitious materials. For that matter, the first section covers both theoretical and numerical basis of correlated Random Fields. Then, mathematical tools to characterize excursion sets along with the main results of [Adler, 2008] is presented. Based on recommendations made in the latter publication, an helpful extension of the basic result is proposed through a rather general formula. In the next section, several applications related cementitious materials observed at the meso- and the micro-scale are proposed. It is the occasion to show the generalized aspect of the model by representing different kinds of morphologies. Finally, the last two sections use the fact that side effects are taken into account in the expectation formulae in order to construct analytical models for both size effect and percolation in finite clusters.

2 Review on correlated Random Fields

The use of correlated Random Fields brings a major improvement to morphological modeling. Indeed, in addition to the usual characteristics of Random Variables such as mean or variance, the *correlated* aspect leads to a spatial structure for the fields, which can statistically be controlled through the definition of a covariance function. This section briefly summarizes the different ingredients of these mathematical tools.

2.1 Basic definitions

A Random Variable represents a phenomenon possessing an unpredictable output. However, with *repetition*, it can possess a regular nature. The theory of probability brings a mathematical framework to model those processes. It is based on three mathematical components that forms the so-called *probability space*. The first one, noted Ω , is the universe. It is a set of all the possible results of a given random variable. A subset of the universe is called an *event*. Basically, it can be defined as a property that can be called true or false once the random experiment is made. The main idea of this theory, brought by Kolmogorov, is to consider the set of all the events \mathcal{F} . For stability reasons over logical operations (not developed here) \mathcal{F} has a structure of σ -algebra of the universe. Now, let ω be a result of a random experiment. The strength of the probability theory lies on the quantification of ω to be in an event $F \in \mathcal{F}$ without manipulating ω itself. In order to do these quantifications, a probability function P is defined, measuring the chance for an event F to occur. It can be seen as a measure of \mathcal{F} . The triplet (Ω, \mathcal{F}, P) defines the probability space. Now, let $X : \Omega \rightarrow E$ be a measurable function defined over the

probability space (Ω, \mathcal{F}, P) which takes its value in a measurable space (E, \mathcal{A}) (in which \mathcal{A} is a σ -algebra of E). As it is often the case, the result ω will be omitted in the notation. Hence, for $A \in \mathcal{A}$, the event $X^{-1}(A) = \{\omega \in \Omega, X(\omega) \in A\} \in \mathcal{F}$ will be noted simply $\{X \in A\}$. In this framework, focus is made on the particular case $E = \mathbb{R}$. Then X is called *Random Variable* (hereafter RV) though still a function. A density probability function $f_X : \mathbb{R} \rightarrow \mathbb{R}_+$ can be defined so that:

$$P\{X \in A\} = \int_A f_X(x) dx \quad \forall A \subset \mathbb{R}. \quad (1.1)$$

This function defines the *distribution* of a RV, *i.e.* the chance for this variable to get a given value. The first two moments of a distribution are known as the *expected value* $\mathbb{E}\{X\}$ and the *variance* $\mathbb{V}\{X\}$, that can be seen as the mean of a sample whose size grows to infinity and how far its values can be spread out from this mean, respectively.

Based on the definition of RV, a *Random Field* (hereafter RF) can be defined by adding to this function a space parameter. If g is such a field then it can be defined over both the probability space and an Euclidean space $M \in \mathbb{R}^N$:

$$g : \Omega \times \mathbb{R}^N \rightarrow \mathbb{R}. \quad (1.2)$$

As a RV $X(\omega)$ is noted X , a RF $g(\omega, \mathbf{x})$ is noted $g(\mathbf{x})$. For a given \mathbf{x} , a field can be seen as a RV — defined by a given distribution called *marginal distribution*. Herein it is assumed that the marginal distribution is the same for all $\mathbf{x} \in M$. Therefore, a global distribution is used in order to statistically defines the RF.

2.2 Gaussian and Gaussian related distribution

It has been seen that the statistical distribution of a RV (or a RF) is made through its density probability function. Because of its smooth properties, the most popular is the normal distribution (also referred as the Gaussian distribution). It is defined by the well known bell shaped density probability function:

$$f_X(x) = \frac{1}{\sigma\sqrt{2\pi}} e^{-(x-\mu)^2/2\sigma^2} \quad \forall x \in \mathbb{R}, \quad (1.3)$$

in which the two parameters μ and σ correspond to the mean and the standard deviation of the distribution, respectively. If X follow this distribution (noted $X \sim \mathcal{N}(\mu, \sigma^2)$), then the variable simulates values in \mathbb{R} and its first two moments are $\mathbb{E}\{X\} = \mu$ and $\mathbb{V}\{X\} = \sigma^2$.

Considering the underlying properties of Gaussian laws, the presented framework is based on those distributions (especially the centered ones, when $\mu = 0$). However, the theory still applies in a more general case, using a wider range of distributions known as *Gaussian related*. It is named after the fact that their underlying RVs automatically derive

from Gaussian ones. In other words, if X_r follows a Gaussian related distribution, it can be decomposed as follows:

$$X_r : \Omega \xrightarrow{\mathbf{X}} \mathbb{R}^k \xrightarrow{S} \mathbb{R}, \quad (1.4)$$

in which \mathbf{X} is a size k vector of independent Gaussian RV and S a given application. For example, by taking $k = 1$ and $S = \exp$, the *log-normal* distribution can be retrieved (commonly used in order to yield positive values). Another example that shall be used in the following is the χ^2 distribution of k degrees of freedom (noted χ_k^2). In this case a random vector of k independent Gaussian RVs can be transformed by $S(\mathbf{X}) = \|\mathbf{X}\|_2$, giving the requisite Gaussian related RV. Herein, this principle can be transposed to RFs the same way since they are defined by a single marginal distribution. If g_r is such a field, it can therefore be defined by:

$$g_r : \Omega \times \mathbb{R}^N \xrightarrow{\mathbf{g}} \mathbb{R}^k \xrightarrow{S} \mathbb{R}, \quad (1.5)$$

in which $\mathbf{g} = \{g_i\}, i = [1..k]$ is a vector valued Gaussian RF (*i.e.* all g_i are independent).

2.3 Covariance functions

2.3.1 Generalities

As previously mentioned, a RF is defined over a parameter space $M \subset \mathbb{R}^N$. The covariance function brings to the field a *spatial structure*. It means that for any couple $(\mathbf{x}, \mathbf{y}) \in M^2$, $g(\mathbf{x})$ and $g(\mathbf{y})$ are *not* two independent variables. They are said to be *correlated*. The measure of this correlation is made through the covariance function \mathcal{C} and can be defined for a zero mean distribution by:

$$\mathcal{C}(\mathbf{x}, \mathbf{y}) = \mathbb{E}\{g(\mathbf{x})g(\mathbf{y})\}. \quad (1.6)$$

From this equation both limit cases (not or perfectly correlated) can be interpreted. On one side, let g be a not correlated RF (corresponding to a white noise). It means that $g(\mathbf{x})$ and $g(\mathbf{y})$ are independent, leading to $\mathcal{C}(\mathbf{x}, \mathbf{y}) = \mathbb{E}\{g(\mathbf{x})\}\mathbb{E}\{g(\mathbf{y})\} = 0$ ($\forall \mathbf{x} \neq \mathbf{y}$). Now, on the opposite side, if g is perfectly correlated, it has a constant field over M , *i.e.* it is a random variable. Hence, still for a zero mean distribution, the covariance function is also constant and takes the value of the distribution's variance: $\mathcal{C}(\mathbf{x}, \mathbf{y}) = \mathbb{E}\{g^2\} = \sigma^2$. In between these cases, the covariance function defines the way g is structured, introducing a spatial parameter (noted L_c) defining how much the field is correlated.

Simplification: Herein, only *stationary* and *isotropic* covariance functions are considered. Those properties of invariance to translation and rigid motion allow $\mathcal{C}(\mathbf{x}, \mathbf{y})$ to be expressed in terms of a single variable $h = \|\mathbf{x} - \mathbf{y}\|$. Since the RF distributions are also invariant to translation, the RF is said to be *strictly stationary*. In order to simplify the notations, only strictly stationary RFs are now considered. However, it has to be kept in mind that the framework can be extended.

The principle of mean square differentiability of correlated RFs and its link with the covariance function is now presented. It helps understanding some spectral properties of

the covariance function and their links with the RF smoothness. Following [Adler, 1981, Adler and Taylor, 2007], mean-squared (MS) derivative of a Gaussian RF g is defined in the i^{th} direction (of unit vector \mathbf{e}_i) by:

$$\frac{\partial g(\mathbf{x})}{\partial x_i} = \lim_{\delta x \rightarrow 0} \frac{g(\mathbf{x} + \delta x \mathbf{e}_i) - g(\mathbf{x})}{\delta x}. \quad (1.7)$$

If g is defined by its covariance function $\mathcal{C}(\mathbf{x})$ then its derivatives $\partial g(\mathbf{x})/\partial x_i$ are defined by $\partial^2 \mathcal{C}(h)/\partial h^2$ (hereafter noted $\mathcal{C}^{(2)}(h)$). This principle can be applied to a higher order of derivatives. Thus, the k^{th} derivative of a RF has a covariance function corresponding to the $2k^{\text{th}}$ derivative of \mathcal{C} . If the latter exists and is finite in zero then the k^{th} derivative of g exists too and is said mean square differentiable. Existence, or not, of these k^{th} derivatives defines the RF regularity. Hence, the smoothness of a RF is strongly linked with the existence of $2k^{\text{th}}$ derivatives of its underlying covariance function at zero.

2.3.2 Characteristic length-scale and Gaussian model of covariance functions

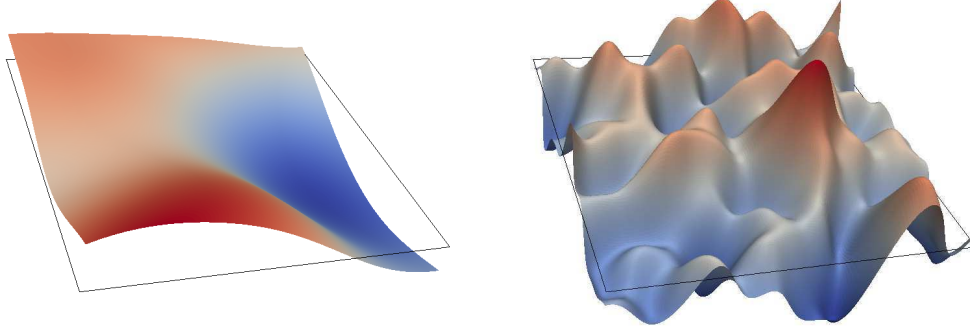
The Gaussian model (or squared exponential) is one of the most commonly used models for covariance function. It is defined by only two parameters; one that characterizes the distribution variance σ^2 and another, called *correlation length* L_c , that assigns a certain characteristic length-scale L_c . It is defined by:

$$\mathcal{C}(h) = \sigma^2 \exp\left(-\frac{h^2}{L_c^2}\right), \quad (1.8)$$

Since for all k , $\mathcal{C}^{(2k)}(0)$ exists and is finite, this covariance function grants to any Gaussian field infinite differentiability. This property leads to strongly smooth RFs. Notice that for $h \neq 0$, $L_c \rightarrow 0$ leads to a zero valued covariance function (corresponding to decorrelated RFs) and $L_c \rightarrow \infty$ leads to $\mathcal{C}(h) = \sigma^2$ (corresponding to constant RF of variance σ^2). In between these cases, FIG. (1.3) illustrates the role of the correlation length on the RF spatial structure, showing two realizations of the same distribution with both large and small L_c . About the size of the square and one-tenth of it, respectively. It can already be remarked that this length-scale parameter plays a key role regarding morphological modeling since it governs the morphology length-scale. Taking $h = 0$ shows that the variance can be defined as the correlation of $g(\mathbf{x})$ with itself. It depicts the fact that a Gaussian correlated RF of zero mean is completely defined by its covariance function.

Another way of understanding the role of the correlation length is through the number of up-crossings of a level set $\mathcal{N}(\kappa)$ for a one-dimensional RF. It can be found in [Adler et al., 2010] that the expected number of up-crossings $\mathcal{N}(\kappa)$ of the level set κ can be determined for a stationary zero mean correlated Gaussian RFs yielded over a segment of size a . Actually its value only depends on the underlying covariance function and its second derivative for $h = 0$. It is given by:

$$\mathbb{E}\{\mathcal{N}(\kappa)\} = \frac{a}{2\pi} \sqrt{-\frac{\mathcal{C}^{(2)}(0)}{\mathcal{C}(0)}} \exp\left(-\frac{\kappa^2}{2\mathcal{C}(0)}\right). \quad (1.9)$$



(a) Large correlation length (the domain size).

(b) Small correlation length (one-tenth of the domain size).

Figure 1.3: Impact of the correlation length on two Gaussian RF realizations.

Applied to the Gaussian covariance function, the expected value of the number of up-crossings can easily compute:

$$\mathbb{E}\{\mathcal{N}(\kappa)\} = \frac{a}{\sqrt{2\pi}L_c} \exp\left(-\frac{\kappa^2}{2\sigma^2}\right), \quad (1.10)$$

and it can be noted that it decreases hyperbolically as the correlation length increases, illustrating the length-scale role of L_c . In addition to its depicting nature, EQ. (1.9) is actually a fundamental base of the excursion set theory presented below.

It is worth noting that the full knowledge of the covariance function is not necessary to predict characteristics such as the number of up-crossings of level sets. In fact, it is also the case for other characteristics such as the volume, the surface or the Euler characteristic of complex morphologies in higher space dimensions. It is the aim of the next section to present an alternative way of defining covariance function through its spectral representation. It presents useful tools for the following theory such as spectral moments.

2.3.3 Spectral representation and Matérn class of covariance functions

A stationary Gaussian RF is still considered. The statement of Bochner's theorem defines a spectral representation of the covariance function as the RF is represented by a Fourier transform of a positive finite measure. If the measure has a density $\hat{f}(\lambda)$ then \hat{f} is called the *spectral density* corresponding to \mathcal{C} . If \hat{f} exists, then the covariance function and the spectral density are Fourier duals of each other [Chatfield, 2004]. The covariance

function can therefore be expressed as follows:

$$\mathcal{C}(h) = \int_{\mathbb{R}} \exp(i\lambda h) f(\lambda) d\lambda. \quad (1.11)$$

For simplification, only covariance functions with finite variance are considered. Hence, since $\mathcal{C}(0) = \sigma^2 = \int f(\lambda) d\lambda$, the spectrum is assumed to be integrable. As the probability function, the spectral moment can be represented by its moments. They are called *spectral moments* and, provided they exist, they are given by:

$$\lambda_{2k} = \int_{\mathbb{R}} \lambda^{2k} f(\lambda) d\lambda = (-1)^k \mathcal{C}^{(2k)}(0) = \mathbb{V} \left\{ \frac{\partial^k g(\mathbf{x})}{\partial x_i^k} \right\}. \quad (1.12)$$

Henceforth existence of spectral moments of a RF is directly linked with its MS differentiability. It can be seen that all spectral moments are defined for the Gaussian correlation model. For that matter, this modeling of infinite smoothness can be considered unrealistic and therefore not adapted to simulate physical problems [Stein, 1999].

Hence, a more general class of covariance functions called *Matérn class* is now considered. It is called class since the introduction of a new parameter $\nu > 0$ provides an additional flexibility to the covariance model, leading to RFs with rather different properties. Especially regarding its differentiability, *i.e.* its smoothness. It is defined by:

$$\mathcal{C}_\nu(h) = \frac{\sigma^2}{\Gamma(\nu)2^{1-\nu}} \left(\frac{\sqrt{2\nu}h}{L_c} \right)^\nu K_\nu \left(\frac{\sqrt{2\nu}h}{L_c} \right), \quad (1.13)$$

in which K_ν is the modified Bessel function of the second kind and L_c , a positive parameter that still works as a length-scale. It appears that a RF fitted by these covariance functions is k -time MS differentiable if and only if $\nu > k$. In these cases, k finite spectral moments are defined. For multiples of $1/2$, a rather simple expression of \mathcal{C}_ν can be yielded (more details can be found in [Rasmussen and Williams, 2006] for the general formulae). In order to illustrate the point, attention is drawn to $\nu = 1/2, 3/2$ and when ν tend toward infinity. As a matter of fact the first and the latter are the exponential and the squared exponential function, respectively. Their analytical expressions and the number of finite moments defined are as follows:

Analytical expression of the function	Spectral moments	
$\mathcal{C}_{1/2} = \sigma^2 \exp\left(-\frac{h}{L_c}\right)$	λ_0	(1.14)
$\mathcal{C}_{3/2} = \sigma^2 \left(1 + \sqrt{3}\frac{h}{L_c}\right) \exp\left(-\sqrt{3}\frac{h}{L_c}\right)$	λ_0, λ_2	
$\mathcal{C}_\infty = \sigma^2 \exp\left(-\frac{h^2}{L_c^2}\right)$	$\lambda_0, \lambda_2, \dots$	

With EQ. (1.12) the number of spectral moments defined by these three examples can be checked. FIG. (1.4) represents them in terms of h . Naturally, all the initial values are the

first spectral moment $\lambda_0 = \sigma^2$. The key difference relies on their derivatives. The non-definiteness of λ_2 , directly linked with the non smooth aspect of the covariance function in 0 for $\nu = 1/2$, can clearly be seen on the graph¹.

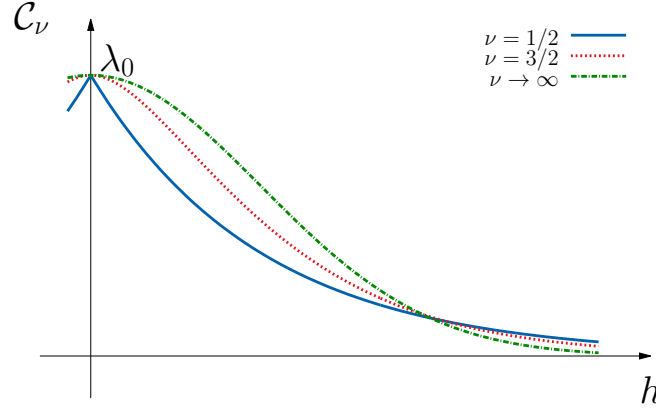


Figure 1.4: Matérn class covariance functions for $\nu = 1/2, 3/2, \infty$.

The reason why the Matérn class results in an important improvement is that the additional parameter ν completely changes the spectral property of the RF. In opposition, even if the γ -exponential covariance function, defined by $\mathcal{C}_\gamma = \sigma^2(-(h/L_c)^\gamma)$ for $0 < \gamma \leq 2$, also has another parameter, the modification of spectrum that γ induces is far less interesting, bringing no real flexibility [Stein, 1999]. Indeed, it is only when $\gamma = 2$ that the underlying RF is MS differentiable. FIG. (1.5) shows three realizations of two-dimensional RFs with Matérn class covariance functions. Those realizations have been yielded using Martin Schlather RANDOMFIELDS package [Schlather, 2012] of the R environment [Team, 2012]. The impact of RF MS differentiability can be visualized. Indeed, its surface aspect seems smoother as the number of the defined finite spectral moments increases. Finally, the Matérn class function brings two parameters. The correlation length L_c , that sets a scale factor to the RF, and ν , that sets a thinner geometrical property that can be interpreted as its roughness.

It can also be interpreted by the previous equation dealing with up-crossings of a level set. First, regarding EQ. (1.9), notice that it can be expressed only in terms of the two spectral moments λ_0 and λ_2 :

$$\mathbb{E}\{\mathcal{N}(\kappa)\} = \frac{a}{2\pi} \sqrt{\frac{\lambda_2}{\lambda_0}} \exp\left(-\frac{\kappa^2}{2\lambda_0}\right), \quad (1.15)$$

and since $\lambda_0 = \sigma^2$ is assumed to be finite, attention is drawn on λ_2 . Then, when applying this equation to Matérn class covariance function, the fact that for $\nu = 1/2$, the second

¹Even though it has no physical meaning, covariance functions are symbolically drawn for $h < 0$ only in order to represent their symmetrical aspect which leads to non differentiability of $\mathcal{C}_{1/2}$ in zero.

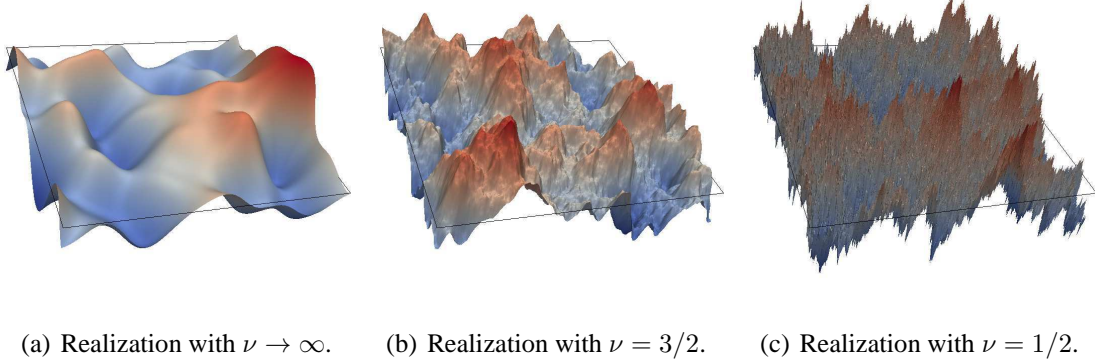


Figure 1.5: Impact of spectrum on the RF shape using Matérn class covariance function.

spectral moment is not defined can be interpreted to an infinite number of up-crossing of level set. On the other hand, for $\nu = 3/2$ and $\nu \rightarrow \infty$, λ_2 is $3\sigma^2/L_c^2$ and $2\sigma^2/L_c^2$, respectively. The higher value of the moment for the first case represents the logical higher number of up-crossing level set due to the RF roughness.

2.4 Numerical implementation

As the whole framework lies on realizations of Gaussian correlated RF, efforts have to be made in their numerical implementation. Two methods used in order to generate these fields are described here. The first one is known as the Karhunen-loève expansion [Loève, 1978] and the second as the turning band method [Matheron, 1973].

2.4.1 Realizations of correlated Random Fields

Let $g(\mathbf{x}, \omega)$ be a Gaussian RF defined over a bounded region of a parameter space ($M \subset \mathbb{R}^N$) which takes value in \mathbb{R} . It is assumed that g has mean zero, variance σ^2 , is isotropic and stationary with a covariance function $\mathcal{C}(\mathbf{x}, \mathbf{y}) = \mathcal{C}(\|\mathbf{x} - \mathbf{y}\|)$ equipped with a correlation length L_c .

The orthogonal decomposition of Gaussian correlated RF theory stipulates that, if \mathcal{C} is smooth enough, g can be written:

$$g(\mathbf{x}, \omega) = \sum_{n=1}^{\infty} \varphi_n(\mathbf{x}) \xi_n(\omega), \quad (1.16)$$

in which it clearly can be seen that the spatial variables \mathbf{x} , and the stochastic ones ω , are separated in two functions. $\{\varphi_n\}$ is a set of functions defined over M . They carry spatial and statistical information of the covariance function. Whereas $\{\xi_n\}$ are zero mean, unit variance Gaussian *independent* RVs. They do not carry any specific information neither

on the distribution probability (except the Gaussian aspect) nor on the correlation. Because they are independent, they are easy to compute and do not cost much numerical resources. A simple random number generator is needed. It is only from this set of RVs that one realization distinguishes itself from another. Explanations on this decomposition is given in APP. B in which $\{\varphi_n\}$ is defined as a spatial base and $\{\xi_n\}$ a stochastic one.

The Karhunen-Loève expansion proposes to construct the spatial functions $\{\varphi_n\}$ as solutions of the Fredholm problem EQ. (1.17), for simple compact in \mathbb{R}^N . Let M be an N -cube and $\mathcal{C} : L^2(M) \rightarrow L^2(M)$ an application defined by $(\mathcal{C}\psi)(\mathbf{x}) = \int_M \mathcal{C}(\mathbf{x}, \mathbf{y})\psi(\mathbf{y})d\mathbf{y}$. The Fredholm problem can then be written:

$$\int_M \mathcal{C}(\mathbf{x}, \mathbf{y})\psi(\mathbf{y})d\mathbf{y} = \lambda\psi(\mathbf{x}). \quad (1.17)$$

The resolution of this problem gives a natural decomposition of \mathcal{C} in terms of the resulting eigenvalues $\{\lambda_n\}$ and their corresponding eigenvectors $\{\psi_n\}$. It can be proved that the Mercer theorem gives the following decomposition [Zaanen, 1953, Riesz and Szőkefalvi-Nagy, 1955]:

$$\mathcal{C}(\mathbf{x}, \mathbf{y}) = \sum_{i=1}^{\infty} \lambda_n \psi_n(\mathbf{x})\psi_n(\mathbf{y}). \quad (1.18)$$

Finally in [Adler and Taylor, 2007], the authors show that $\varphi_n \leftarrow \{\sqrt{\lambda_n}\psi_n\}$ is a suitable base for the orthogonal decomposition leading to the Karhunen-Loève expansion of a correlated RF.

Karhunen-Loève expansion of correlated RFs

$$g(\mathbf{x}, \omega) = \sum_{n=1}^{\infty} \sqrt{\lambda_n} \xi_n(\omega) \psi_n(\mathbf{x}), \quad (1.19)$$

where λ_n (resp. ψ_n) are the eigenvalues (resp. eigenvectors) of the Fredholm problem EQ. (1.17) and $\xi_n \sim \mathcal{N}(0, \sigma^2)$ are a set of independent RVs.

In terms of numerical implementation, EQ. (1.21) is very useful. Indeed, for a given RF, the spatial functions $\{\sqrt{\lambda_n}\psi_n(\mathbf{x})\}$ have to be computed only once, by solving the Fredholm problem. Then, in order to yield a realization of this field, only a sequence of independent RVs is to be computed. It enables the possibility of generating a huge amount of realizations of the same field in a reasonable time.

Prior to that, a discretization of the continuum Fredholm problem is needed. APP. B describes it within a Finite Element context, leading to the following generalized eigenvalue problem:

$$\mathbf{M}\mathbf{C}\mathbf{M}\boldsymbol{\psi} = \lambda\mathbf{M}\boldsymbol{\psi}, \quad (1.20)$$

in which \mathbf{M} is the Gramm matrix, \mathbf{C} the covariance matrix, $\boldsymbol{\psi}$ the nodal values of the eigenvectors and λ the eigenvalues (further details in APP. B). The Gramm matrix is

equivalent to a unit mass matrix, only containing information on the mesh geometry, whereas the covariance matrix contains the nodal values of the covariance function. For Gaussian covariance, this matrix is theoretically full, leading to a huge demand in memory resources.

As already mentioned, one of the great advantages of the Karhunen-Loève decomposition is that the eigvalue problem has to be solved only one time for a given correlated RF, giving the spatial structure by the mean of spectrum $\{\lambda_n\}$ and modes $\{\psi_n\}$. Once stored, a realization is computed only by changing the stochastic space base $\{\xi_n\}$ (not time consuming since all the variables are independent). Theoretically, a Gaussian RF is retrieved when the infinite sum EQ. (1.21) is yielded (*i.e.* the whole spectrum is used). For the numerical implementation, the most important modes only (regarding the spectrum) are calculated. Hence a truncation is made, giving an approximation of the correlated RF:

$$g(\mathbf{x}, \omega) \approx \sum_{n=1}^m \sqrt{\lambda_n} \xi_n(\omega) \psi_n(\mathbf{x}), \quad (1.21)$$

in which m is the number of modes that are kept. The importance of a mode is estimated through its eigenvalue (compared to the maximum one). Since the whole spectrum cannot be numerically evaluated, the greatest values of $\{\lambda_n\}$ are calculated with an iterative solver based on Lanczos algorithm [Cullum and Willoughby, 2002]. Handful implementation is made in the EIGS function of MATLABTM. The following graphs show the role of the correlation length on the spectral content of correlated RFs. Herein, two-dimensional Gaussian fields of standard distribution ($\mathcal{N}(0, 1)$) are yielded over a unit square for three different correlation lengths; $L_c = 1/100, 1/50$ and $1/20$. FIG. (1.6(a)) represents it with the eigenvalue of each mode and FIG. (1.6(b)) with spectra $\hat{f}(\lambda)$. In order to compare them on the same graph, they are normalized, $\int \hat{f} d\lambda = 1$ and represented in terms of normalized eigenvalues $\{\lambda_n/\lambda_{\max}\}$ for each field.

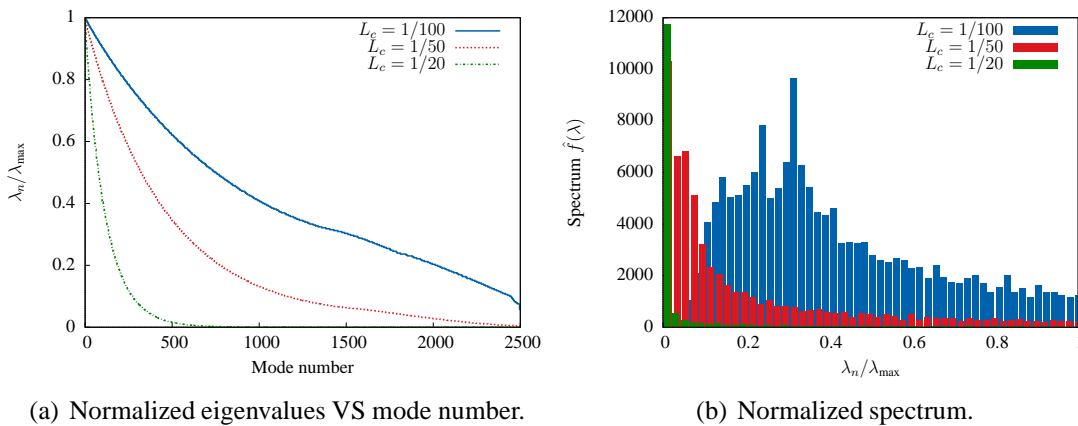


Figure 1.6: Spectral content of correlated RFs for three correlation lengths.

The spectrum can be interpreted as the amount of spatial information needed. It clearly can be seen that a small number of modes is needed for a RF with a large correlation

length. By comparison, a small one will entail more modes that correspond to more complicated spatial shapes (as it is represented in FIG. (1.7)).

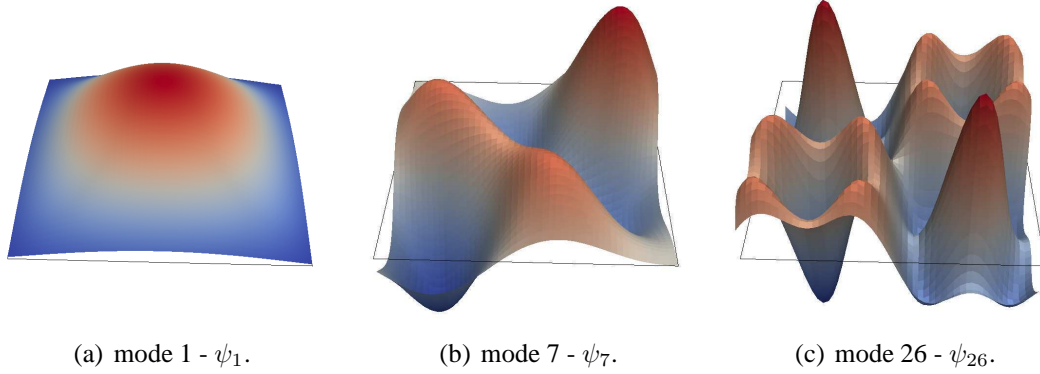


Figure 1.7: Mode number 1, 7 and 26 for a two-dimensional RF.

Experience can help evaluate m prior to calculations mainly taking into account the correlation length. Hence, less correlated RF are more time consuming than strongly correlated ones. A criterium (for example $\lambda_m = \lambda_{\max}/100$) can be set, eliminating modes from the sum EQ. (1.21), even after the spectrum computation.

Even though it has been seen that the number of modes needed can be reduced, the eigenvalue problem still involves a full squared matrix. When dealing with multi-dimensional RFs of large size, memory storage and calculation time can quickly become an issue. The turning band method [Matheron, 1973] considerably helps increasing the RF size. The idea is to yield several one-dimensional correlated RFs (bands). The direction vectors — corresponding to each band — are uniformly distributed over the unit sphere and the contribution of each field is added to the resulting three-dimensional RF (details are given APP. B). In [Glimm and Sharp, 1991], a link is made between each covariance functions (one and three-dimensional), giving complete control of the spatial correlation of the resulting field to be obtained. Improvements made using this method are summarized TAB. (1.1).

Method	Discretization	<i>CPU</i> time
Direct	$\approx 10^3$ nodes	\approx one week
Turning band	$\approx 10^6$ nodes	< one hour

Table 1.1: Rough estimation of Direct and Turning Band method performances.

The numerical implementation of correlated Gaussian RF has been presented in this section. As it has been seen above, in order to yield Gaussian related distributions, a simple transformation S is to be applied to the Gaussian field.

3 Excursion set theory

3.1 General principle

An excursion set is defined as the resulting subset of correlated RF thresholding. This operation transforms a continuous field to a binary one, creating randomly shaped morphologies. If $g : M \subset \mathbb{R}^N \rightarrow \mathbb{R}$ is a RF defined over parameter space M (bounded region of \mathbb{R}^N), a subset of its codomain $H_s \subset \mathbb{R}$ can be defined in order to set the thresholding rules. Herein, excursion sets, noted E_s , are defined as the set of points where the RF value is in H_s , hereafter called *hitting set*. Thus yielding to:

$$E_s \triangleq \{\mathbf{x} \in M \mid g(\mathbf{x}) \in H_s\}. \quad (1.22)$$

The hitting set will often be taken as the open set $H_s = [\kappa, \infty[$, κ working as a level set for the RF. Each point where the RF value is above κ defines the excursion. Contours of the morphology, ∂E_s , are the isovalues κ of g :

$$\partial E_s(\kappa) \triangleq \{\mathbf{x} \in M \mid g(\mathbf{x}) = \kappa\}, \quad (1.23)$$

and EQ. (1.22) can simply be written:

$$E_s(\kappa) \triangleq \{\mathbf{x} \in M \mid g(\mathbf{x}) \geq \kappa\}. \quad (1.24)$$

This principle is depicted in FIG. (1.8) in the one-dimensional case and examples of three-dimensional excursions are given in FIG. (1.9) for two different level sets. In the pre-

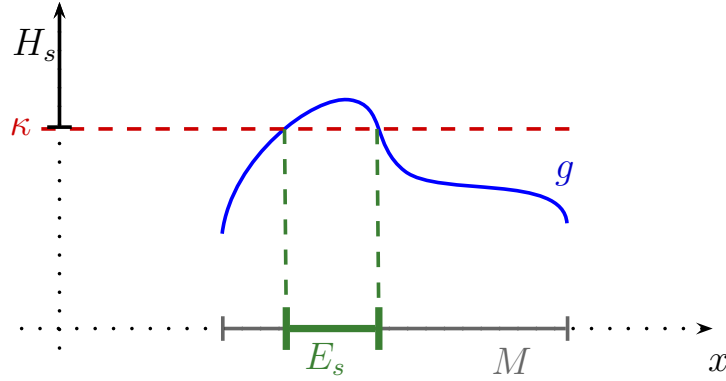


Figure 1.8: Excursion set of correlated RF in one-dimension.

sented framework, the RF is defined over a three-dimensional space ($M \subset \mathbb{R}^3$), creating three-dimensional excursion sets. The two excursions of FIG. (1.9) are made from the same realization of a RF with two different level sets. Level set value has clearly an important impact on the resulting morphology. For low values of κ , a major part of the field still hits H_s , leading to high volume fraction excursion set mainly made of cavities and handles. This sponge-like topology (FIG. (1.9(a))) can be a suitable representation

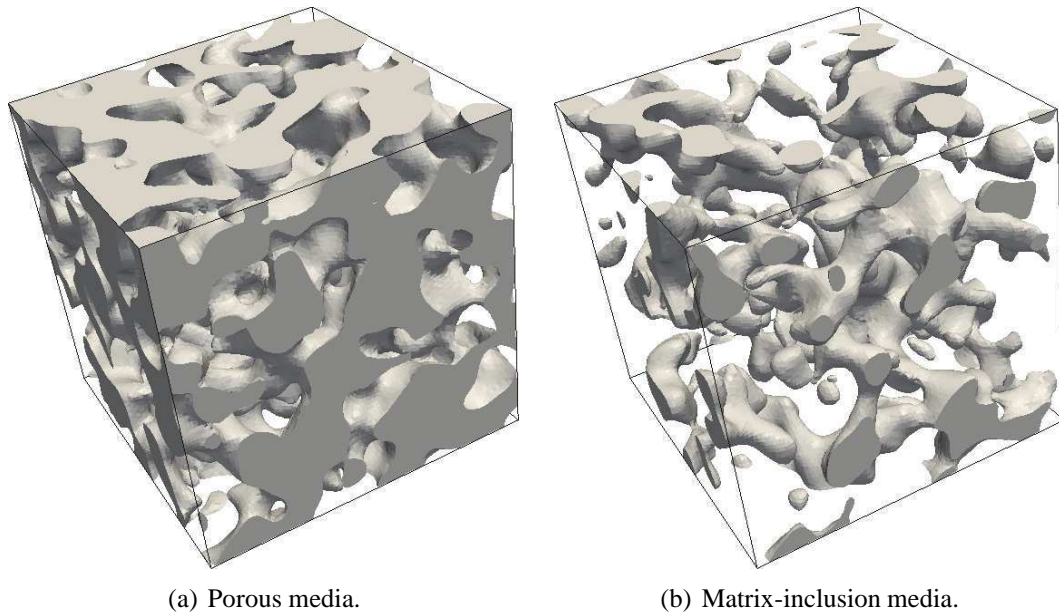


Figure 1.9: Two excursion sets of the same realization with different level sets.

of porous media (see 4.2.1 in this chapter). By comparison, high values of κ lead to meatball-like topology (FIG. (1.9(b))) where just several connected components remain. These excursions, despite their very low volume fraction, could represent disconnected media such as aggregates within a matrix. This last point raises the main issue of excursion set modeling. In this chapter, solutions are proposed in order to yield high volume fraction morphologies with disconnected topologies.

As the level set value has an impact on the kind of morphology obtained, both probability distribution of the RF and its covariance function have a major influence as well. Among them, the correlation length L_c , fixing the length-scale of the excursion set, has a key role. Playing with all these parameters gives a wild range of morphologies. But, in order to manipulate these “objects”, tools that quantify them mathematically speaking are needed.

In the next section functionals that measure both geometrical and topological quantities are defined. They provide global descriptors for excursion sets, giving a mathematical basis for the main results presented in this chapter.

3.2 Measures of excursion set

3.2.1 General aspect

In order to specify a morphology both *geometrical* and *topological* properties have to be considered. It has been proved that in a N -dimensional space, $N + 1$ descriptors are enough to fully describe it. A large family of *functionals* aims to quantify those

properties, differentiating themselves by scale factors. Among them, due to their intrinsic properties, the *Lipschitz-Killing curvatures* [Federer, 1959], hereafter referred as LKCs, are used here. Hence, a manifold is characterized with a set of LKCs \mathcal{L}_j , $j = [0..N]$ that can be interpreted as a j^{th} measure of the subset. Herein, the three-dimensional Euclidean space \mathbb{R}^3 being of concern, four LKCs are defined, measuring volumes, areas, integral of mean curvatures and Euler characteristics, respectively.

In order to help the understanding of each LKC, a quick overview of measure characterization in \mathbb{R}^3 is proposed. A recall of the four symmetrical functions of three variables is first proposed SYS. (1.25). It can be remarked already that, if x is taken to be of unit [u], then e_j is homogeneous to $[u^j]$. These polynomial functions can be used in order to properly define a measure.

$$e_0(\mathbf{x}) = 1, \quad (1.25a)$$

$$e_1(\mathbf{x}) = x_1 + x_2 + x_3, \quad (1.25b)$$

$$e_2(\mathbf{x}) = x_1x_2 + x_1x_3 + x_2x_3 \text{ and} \quad (1.25c)$$

$$e_3(\mathbf{x}) = x_1x_2x_3. \quad (1.25d)$$

Now, let μ be a measure of \mathbb{R}^3 . A unique measure can be defined if it respects the four following axioms. Attention has to be drawn to the last one.

Axiom 1: $\mu(\emptyset) = 0$

Axiom 2: If A and B are two measurable sets: $\mu(A \cup B) = \mu(A) + \mu(B) - \mu(A \cap B)$

Axiom 3: The measure of A is independent of its position

Axiom 4: Still an infinite number of measures can be determined. This last axiom selects one of them, using one of the functions defined in SYS. (1.25). Hence, the referential measure of a parallelepiped $P = \prod_{i=1}^3 [0, a_i]$ can be taken as one's choice:

$$\mu(P) = \begin{cases} \mu_0(P) = e_0(a_1, a_2, a_3) = 1 \\ \mu_1(P) = e_1(a_1, a_2, a_3) = a_1 + a_2 + a_3 \\ \mu_2(P) = e_2(a_1, a_2, a_3) = a_1a_2 + a_1a_3 + a_2a_3 \\ \mu_3(P) = e_3(a_1, a_2, a_3) = a_1a_2a_3 \end{cases} \quad (1.26)$$

Each measure can here be interpreted by; Euler characteristic ($j = 0$), average caliper diameter ($j = 1$), half surface area ($j = 2$) or volume ($j = 3$).

Since the Euler characteristic brings an important aspect to the framework a brief reminder of its properties is now proposed.

3.2.2 Euler characteristic

Introduction to the Euler characteristic is often made with the so-called *Polyhedra Formula*. Among its countless contributions, Euler found out that alternative the sum of the number of vertices (V), edges (E) and faces (F) of a convex polyhedra is constant, no matter how it is constructed: $V - E + F = 2$. Now, P polyhedra at least glued together by one common face are considered. It occurs that, for a wild bunch of configurations, $V - E + F - P = 1$. This rather more general formula holds until the union of polyhedra form a hole in the resulting structure, leading to $V - E + F - P = 0$. Two holes inevitably lead to $V - E + F - P = -1$ no matter how many polyhedra are used and how they are constructed. Each hole reduces the alternative sum by 1. It is from this consideration that the topology field is born, creating a new descriptor for a solid subdivided in polyhedra, invariant under its geometrical properties. Named after its instigator, the Euler characteristic χ is defined for a solid subdivided into polyhedra as follows:

$$\chi = V - E + F - P. \quad (1.27)$$

The contribution of Carl Friedrich Gauss to (classical) differential geometry has led to several useful concepts (*Disquisitiones generales circa superficies curva*, 1827), and among them, the Gaussian curvature. At a point on a surface, it can be defined as the product of the minimum and the maximum curvatures $K = k_{\min}k_{\max}$. Things become interesting when focus is made on global values (integrated over the surface) of this curvatures. Known as one of the most elegant theorems of differential geometry, the *Gauss-Bonnet* theorem links this global geometrical value to the *genus*, a topological invariant (remains unchanged under homeomorphisms of the surface). If a compact surface (that closes on itself) in \mathbb{R}^3 is considered, its genus g is the number of its holes. It turns out that the integrated value of the Gaussian curvature follows the simple relationship

$$\int_{\partial M} K dS = 2\pi\chi(\partial M), \quad (1.28)$$

in which ∂M is the compact surface and $\chi = 2 - 2g$. The beauty of this theorem is that the local geometrical property such as Gauss curvature, when integrated over the surface becomes topological invariants. It appends that χ is none other that the Euler characteristic of the surface. It is also a topological invariant. For example, for a sphere of radius r , the Gaussian curvature will be at each point $1/r^2$, leading to an Euler characteristic of 2. For a torus, the genus is $g = 1$, leading to a zero Euler characteristic. It means that the positive part of the Gaussian curvature and the negative one cancel each other out when integrated over all the surface. Any of the two examples results in χ not depending on any radius, showing the invariant aspect of topological properties. The Euler characteristic can now be tackled from the manifold (and not his surface) point of view. ‘‘Holes’’ in the surface are now seen as ‘‘handles’’ of the manifold. It turns out that the Euler characteristic can be computed as an alternative sum of the number of j -dimensional topological features. In three dimensions it gives:

$$\chi(M) = \#\{\text{connected component}\} - \#\{\text{handles}\} + \#\{\text{holes}\}. \quad (1.29)$$

An interesting example is if M is a set of disconnected components with neither hole nor handles, its Euler characteristic is the number of its components, making it a useful particle counter. This property is used later.

The Euler characteristic has been introduced by the polyhedra formula. It can characterize a more complex body if subdivided into polyhedra glued together EQ. (1.27). Then for a body of smooth surface it is presented by the mean of surface Gaussian curvatures in \mathbb{R}^3 linking topological invariant to geometrical properties once considered in a global fashion EQ. (1.28). Finally it can be seen as a counter of j -dimensional objects, counting alternatively in positive and negative EQ. (1.29). Actually the latter definition and the polyhedra formula are closely linked together. Indeed, it can be proved that, if a set with a smooth boundary is covered by a lattice fine enough, the Euler characteristic of the set (EQ. (1.29)) equals the Euler characteristic of the lattice (EQ. (1.27)). This is a useful property used in this study in order to validate the numerical implementation.

3.2.3 Lipschitz-Killing curvatures

The aim of the brief reminder on measure is to introduce the notion of j^{th} -dimensional measure. As specified above, in \mathbb{R}^3 , four LKCs are defined, noted \mathcal{L}_j , $j = [0..3]$, each one corresponding to a different measure. TAB. (1.2) summarizes all the measures and each corresponding LKC. Their values for a cube of size a as well as their meaning are also given.

Measure	Corresponding LKC	Value for a cube	Meaning
μ_0	\mathcal{L}_0	1	Euler characteristic
μ_1	\mathcal{L}_1	$3a$	Twice the caliper diameter
μ_2	\mathcal{L}_2	$3a^2$	Half the surface area
μ_3	\mathcal{L}_3	a^3	Volume
μ_j	\mathcal{L}_j	$\binom{3}{j} a^j$	j^{th} -measure

Table 1.2: Meaning of each four LKC for a cube in \mathbb{R}^3 .

Another way of defining LKCs (proposed in [Adler, 2008]) through the *Steiner's formula* is now proposed. It also introduces useful notions for the next section such as *tubes*. A *tube* $\mathcal{K}(A, \rho)$ is the volume enlargement of a convex $A \subset \mathbb{R}^N$ of diameter $\rho \geq 0$. It can be defined as follows:

$$\mathcal{K}(A, \rho) = \left\{ \mathbf{x} \in \mathbb{R}^N \mid \min_{\mathbf{y} \in A} (\|\mathbf{x} - \mathbf{y}\|) \leq \rho \right\}. \quad (1.30)$$

Interest in Steiner's formula EQ. (1.31) resides in calculating the volume \mathcal{V}_N of these enlarged sets in \mathbb{R}^N by adding contribution of each $N + 1$ LKCs of A . It can already be

noticed that an exact result is retrieved with a simple *finite* summation. The volume of a unit ball in dimension j is used and noted ω_j (further details in APP. A).

$$\mathcal{V}_N(\mathcal{K}(A, \rho)) = \sum_{j=0}^N \omega_{N-j} \rho^{N-j} \mathcal{L}_j(A). \quad (1.31)$$

The reader is invited to check, by the mean of usual calculations and by using EQ. (1.31), that this volume applied to a cube in \mathbb{R}^3 of size a ($C = \prod_{i=1}^3 [0, a]$) is:

$$\mathcal{V}_3(\mathcal{K}(C, \rho)) = a^3 + 6a^2\rho + 12a\rho^2 + \frac{4}{3}\pi\rho^3, \quad (1.32)$$

and therefore, that each term can be identified, giving the meaning of j^{th} measure of each LKCs. Notice that it exists as a formula for much more general sets (not necessary useful in the presented framework), usually called *tubes formulae* [Weyl, 1939].

LKCs and their physical meanings in the Euclidean space \mathbb{R}^3 have been presented. They were quickly said to be *intrinsic*, thus giving the property of invariance to the computed volumes through the measure chosen in the Euclidean space. Used as a measure of the probability space, another set of *non-intrinsic* functionals referred to as *Minkowski functionals* are now presented.

3.2.4 Gaussian Minkowski functionals

Minkowski functionals are closely linked to LKCs and can be defined as follows for a subset $A \subset \mathbb{R}^N$:

$$\mathcal{M}_{N-j}(A) = (N-j)! \omega_{N-j} \mathcal{L}_j(A). \quad (1.33)$$

More popular than LKCs, Minkowski functionals are used in many fields in order to characterize morphologies. Especially in the astrophysics community (see the pioneer work of [Mecke et al., 1994] in which *Steiner's formula* is presented with these functionals) leading to huge amount of literature on the topic [Mecke and Wagner, 1991, Winitzki and Kosowsky, 1997, Kerscher et al., 2001].

In contrast to LKCs, the Minkowski functionals are not intrinsic. Therefore, they depend on the used measure. This can be seen as a foretaste of how calculating geometrical properties of excursion sets is linked to the probability of a Gaussian RV to be in the so-called hitting set. Hence, the measure of a Gaussian distribution is of concern here. Let γ_k be such a measure in the Euclidean space \mathbb{R}^k . If $\mathbf{X} = \{X_i\}$ is a standard Gaussian vector of size k in which $X_i \sim \mathcal{N}(0, \sigma^2)$, $i = [1..k]$ are independent and $A \subset \mathbb{R}^k$:

$$\gamma_k(A) = P\{\mathbf{X} \in A\} = \frac{1}{\sigma^k (2\pi)^{k/2}} \int_A e^{-\|\mathbf{x}\|^2/2\sigma^2} d\mathbf{x}. \quad (1.34)$$

Associated to this measure, the functionals are now called *Gaussian Minkowski functionals* (hereafter GMFs). In a k -dimensional space, also $k+1$ GMFs are defined, noted

$\mathcal{M}_j^{\gamma_k}$, $j = [0..N]$. The main results of [Taylor, 2006] is to yield a Taylor expansion of tube probability content EQ. (1.35) for small enough ρ . It can be seen as an extension of the Steiner-Weyls formula EQ. (1.31), in which γ_k represents the volume in the sense of Gaussian measure (Gaussian volume).

Taylor expansion of tube Gaussian volume

$$\gamma_k(\mathcal{K}(A, \rho)) = \sum_{j=0}^{\infty} \frac{\rho^j}{j!} \mathcal{M}_j^{\gamma_k}(A). \quad (1.35)$$

By taking $\rho = 0$, it can be concluded that the first Gaussian Minkowski functional is the Gaussian volume of A itself, $\mathcal{M}_0^{\gamma_k}(A) = \gamma_k(A)$. Other GMFs can be identified in specific cases. The content of the next section deals with A where it is specified to fall in the excursion set framework presented in the previous sections.

3.2.5 Application to Gaussian distribution

Even though the presented formulae work for more general cases, it suffices in our case to take $k = 1$, corresponding to single value RF $g : \mathbb{R}^3 \rightarrow \mathbb{R}$. GMFs, by their non intrinsic aspect, are Gaussian measures. In order to fit in the excursion set framework, it is only natural to take interest in measuring the hitting set, $A = H_s = [\kappa, \infty[$. It leads to several simplifications. First, the Gaussian volume of the hitting set is the complementary cumulative density function (or tail distribution, noted Ψ) of the underlying standard distribution:

$$\gamma_1([\kappa, \infty[) = P\{X \geq \kappa\} = \frac{1}{\sigma\sqrt{2\pi}} \int_{\kappa}^{\infty} e^{-x^2/2\sigma^2} dx = \Psi(\kappa), \quad (1.36)$$

furthermore, the tube of $[\kappa, \infty[$ can easily be defined and its tail probability linked to the tail distribution as follows:

$$\mathcal{K}([\kappa, \infty[, \rho) = [\kappa - \rho, \infty[\text{ and } \gamma_1([\kappa - \rho, \infty[) = \Psi(\kappa - \rho). \quad (1.37)$$

Each GMFs of EQ. (1.35) can be identified by the unique standard Taylor expansion of $\Psi(\kappa - \rho)$ for small ρ , leading to:

GMFs for Gaussian distribution

$$\text{For } j = 0, \mathcal{M}_0^{\gamma_1}([\kappa, \infty[) = \Psi(\kappa), \quad (1.38a)$$

$$\text{for } j \geq 1, \mathcal{M}_j^{\gamma_1}([\kappa, \infty[) = (-1)^j \frac{d^j \Psi(\kappa)}{d\kappa^j} = \frac{e^{-\kappa^2/2\sigma^2}}{\sigma^j \sqrt{2\pi}} H_{j-1}(\kappa/\sigma), \quad (1.38b)$$

where $H_j, j \geq 0$ are the j^{th} probabilist Hermite polynomials (see APP. A for details).

In this section, it has been seen how are computed the Gaussian Minkowski functionals for Gaussian distribution. The next section shows how it can be extended to Gaussian related ones and how it can easily fall down to the latter method.

3.2.6 Application to the Gaussian related χ -square distribution

It has previously been stated (EQ. (1.5)) that Gaussian related RFs can be defined by a transformation (noted S) of a Gaussian RF. It occurs that because these fields are a product of an underlying Gaussian distribution, the principle of Gaussian measurement stated just above can be applied. In order to retrieve the previous formulation, the transformation S can be taken into account for the hitting. Hence GMFs can still be used even if they are defined for a Gaussian measure.

This principle can be explained by the following statements. First, let g_r be a Gaussian related RF defined by \mathbf{g} , a vector valued Gaussian RF of size k and S , a transformation from \mathbb{R}^k to \mathbb{R} . The Gaussian related RF is then given by $g_r = S(\mathbf{g})$. Now, if H_s is the hitting set defined for g_r , then attention has to be focused on the probability measure of g_r to be in this hitting set. Starting from that point and using the decomposition of Gaussian related RF, the following equations can easily be yielded [Adler, 2008]:

$$\begin{aligned} P \{g_r \in H_s\} &= P \{S(\mathbf{g}) \in H_s\} \\ &= P \{\mathbf{g} \in S^{-1}(H_s)\} \\ &= \gamma_k(S^{-1}(H_s)). \end{aligned} \quad (1.39)$$

It shows that the Gaussian related measure can fall down to the simple Gaussian measure γ_k . Hence, the Gaussian Minkowski functionals can be used the same way as shown above, but on a modified hitting set $S^{-1}(H_s)$. However, since S is defined over \mathbb{R}^k , the development of EQ. (1.34) for $k \in \mathbb{N}$ is needed. Application for the specific case of χ_k^2 case is now presented.

For a χ_k^2 distribution, the function S of a Gaussian related RF is the norm function:

$$S(\mathbf{g}) = \|\mathbf{g}\|_2 \rightarrow g_r = \sum_{i=1}^k g_i^2. \quad (1.40)$$

The first step is to construct the transformed hitting set $S^{-1}(H_s)$ corresponding to the Gaussian measure. If $H_s = [\kappa, \infty[$ is the hitting set considered for the Gaussian related RF then:

$$S^{-1}(H_s) = S^{-1}([\kappa, \infty[) = \mathbb{R}^k \setminus \mathcal{B}_{\mathbb{R}^k}(0, \sqrt{\kappa}), \quad (1.41)$$

with \mathcal{B} the centered ball in \mathbb{R}^k of radius $\sqrt{\kappa}$. The next step is to yield the Gaussian volume of this hitting set with EQ. (1.34). Using spherical coordinates, the k -dimensional integration falls down to one dimension (the development is made in APP. A):

$$\gamma_k(S^{-1}([\kappa, \infty[)) = \frac{1}{\sigma^k (2\pi)^{k/2} \Gamma(k/2)} \int_{r=\sqrt{\kappa}}^{\infty} r^{k-1} e^{-r^2/2\sigma^2} dr. \quad (1.42)$$

The resolution is now the same as for Gaussian RFs. A standard Taylor expansion of $\gamma_k(\mathcal{K}(S^{-1}([\kappa, \infty]), \rho))$ is made and each Gaussian Minkowski functional is identified with EQ. (1.35). In order to get back to the initial definition of the hitting set H_s , using κ , a variable substitution $t \leftarrow r^2/2\sigma^2$ leads to the following definition of the Gaussian Minkowski functionals applied to a χ_k^2 distribution:

GMFs applied to χ_k^2 distribution

$$\text{For } j = 0, \mathcal{M}_0^{\gamma_k}(S^{-1}([\kappa, \infty])) = \bar{\Gamma}(k/2, \kappa/2\sigma^2). \quad (1.43a)$$

$$\text{For } j \geq 1, \mathcal{M}_j^{\gamma_k}(S^{-1}([\kappa, \infty])) = (-1)^j \frac{d^j}{d\kappa^j} \bar{\Gamma}(k/2, \kappa/2\sigma^2), \quad (1.43b)$$

where

$$\bar{\Gamma}(k, x) = \int_{t=x}^{\infty} t^{k-1} e^{-t} dt / \Gamma(k)$$

is the regularized upper incomplete gamma function.

It is worth understanding that those Minkowski functionals are still based on Gaussian measure. In order to fit the χ_k^2 distribution, only the initial hitting set is modified by S^{-1} .

In this section, two classes of functionals that characterize a morphology have been presented. First, the *Lipschitz-Killing curvatures*, considering intrinsic properties (not dependent on the measure used), are used in order to characterize the excursion set morphology. Furthermore, it has been seen that *Minkowski* ones can compute Gaussian volumes (using Gaussian measure, γ_k). It is through those functionals that statistical information of the random distribution used is gathered. Analytical definition has been given for hitting set $[\kappa, \infty[\subset \mathbb{R}$ for both Gaussian and χ_k^2 distribution.

The next section presents the main result of this chapter: a formulae that links the excursion set morphological characteristics (LKC) to statistical information of the RF and the hitting set used.

3.3 Expectation formula

The result presented in this section is of fundamental importance in this chapter. It is the basis of the work of [Taylor, 2001, Taylor and Adler, 2003, Taylor, 2006]. It links the statistical information of the distribution used, the hitting set (via the GMFs) and the spatial structure of the correlated RF (via its covariance function second spectral moment) to the geometrical and topological characteristics of the excursion set (via LKC). Since excursion sets are the results of a level set of RFs *realizations*, naturally, the LKC has to be seen in terms of expected values. Basically, this chapter defines the F function of the following equation:

$$\mathbb{E}\{\mathcal{L}_j(E_s)\} = F(H_s, \mathcal{C}, S), \quad (1.44)$$

in which \mathcal{L}_j are the j^{th} Lipschitz-Killing curvatures, E_s , the excursion set, H_s , the hitting set, \mathcal{C} the covariance function of the correlated RF (containing information on the distribution, σ^2 and the spatial structure $L_c \dots$) and S the function defining Gaussian related distributions.

3.3.1 A first taste of the formula

It has been seen that the first Gaussian Minkowski functionals are measures of the probabilistic space. Furthermore, the first functional has been identified as the Gaussian measure itself γ_k , enabling the computations of Gaussian volumes. As recalled just above, this measure only provides information on the distribution, not on the spatial structure of correlated RFs. Nonetheless, the computation of the expectation of the last LKC of an excursion set (volume) can be done while only knowing this.

If \mathbf{g} is a stationary correlated Gaussian RF, at any point $\mathbf{x} \in M$, it can be seen as a RV with the same given marginal distribution. Hence, the probability of this point to be part of the excursion set (*i.e.* that $\mathbf{g}(\mathbf{x}) \in H_s$) is equal to the Gaussian measure of the hitting set, thus yielding to:

$$\forall \mathbf{x} \in M, P\{\mathbf{g}(\mathbf{x}) \in H_s\} = \gamma_k(H_s) = \mathcal{M}_0^{\gamma_k}(H_s). \quad (1.45)$$

The first GMF can be seen as a local descriptor of the excursion set volume. Notice that it does not depend on \mathbf{x} , making it easier to integrate over M . This property can be used in order to calculate the volume of the corresponding excursion set. Since the marginal distribution is constant over M it can be yielded by simply multiplying the probability of each point to be in H_s by the volume of M ($\mathcal{L}_N(M)$). It leads, for the more general case of Gaussian related RF, to:

$$\mathbb{E}\{\mathcal{L}_N(E_s(g_r, M, H_s))\} = \mathcal{L}_N(M) \mathcal{M}_0^{\gamma_k}(S^{-1}(H_s)). \quad (1.46)$$

This equation only applies in the case of volume computation. No structural information of the correlated RF (for example its correlation length) is needed since $P\{\mathbf{g}(\mathbf{x}) \in H_s\}$ is constant over M . Unfortunately, this simplistic vision cannot be extended to more complex measures such as the other LKCs. The following section presents the general results of [Adler, 2008].

3.3.2 General formula

Let g_r be a Gaussian related correlated RF defined as in EQ. (1.5). Since Gaussian RFs are Gaussian related ($S = \text{id}$), the following result is rather general. Let λ_2 be the second spectral moment of the underlying Gaussian RF and $H_s \in \mathbb{R}$ the hitting set. If E_s is the resulting excursion set, expectation of the LKCs can be computed as follows [Adler, 2008]:

Expectation Formula

$$\mathbb{E}\{\mathcal{L}_j(E_s(g_r, M, H_s))\} = \sum_{i=0}^{N-j} \binom{i+j}{i} \frac{\omega_{i+j}}{\omega_i \omega_j} \left(\frac{\lambda_2}{2\pi}\right)^{i/2} \mathcal{L}_{i+j}(M) \mathcal{M}_i^{\gamma_k}(S^{-1}(H_s)). \quad (1.47)$$

It can be sensed that this relationship between, on the one hand hitting set and probabilist characteristics of the correlated RF, and, on the other hand, the measure of the resulting excursion set, is strongly non linear. Hence, the end of this section focuses on developing it in a special case and analyzing the curves. Verifications of this theory on actual excursion sets are also presented and commented on.

Prior to that, it can be quickly checked that, in the one-dimensional case presented above, the Euler characteristic can be linked to the number of up-crossing levels defined EQ. (1.15):

$$\mathbb{E}\{\mathcal{L}_0\} = \mathcal{M}_0^{\gamma_k} + \mathbb{E}\{\mathcal{N}\}. \quad (1.48)$$

3.3.3 Physical interpretation

In this section, EQ. (1.47) is developed for $g : C \subset \mathbb{R}^3 \rightarrow \mathbb{R}$ a correlated Gaussian RF of zero mean and σ^2 variance. Its covariance function is taken to be Gaussian with correlation length L_c , making the second spectral moment $\lambda_2 = 2\sigma^2/L_c^2$. g is defined over a three-dimensional cube C of size $a \times a \times a$. LKCs of this set are summarized in TAB. (1.2) The hitting set is the open subset of \mathbb{R} , $H_s = [\kappa, \infty[$ as above. Hence Minkowski functionals can be yielded as in EQ. (1.38). LKCs of the resulting excursion set in these conditions can now be explicitly developed, in terms of κ :

Expected LKCs for Gaussian distribution

$$\mathbb{E}\{\mathcal{L}_0(E_s(\kappa))\} = \left[\frac{1}{\sqrt{2\pi^2}} \frac{a^3}{L_c^3} \left(\frac{\kappa^2}{\sigma^2} - 1 \right) + \frac{3}{\sqrt{2\pi^{3/2}}} \frac{a^2}{L_c^2} \frac{\kappa}{\sigma} + \frac{3}{\sqrt{2\pi}} \frac{a}{L_c} \right] e^{-\kappa^2/2\sigma^2} + \Psi(\kappa/\sigma) \quad (1.49a)$$

$$\mathbb{E}\{\mathcal{L}_1(E_s(\kappa))\} = \left[\frac{\sqrt{2}}{\pi^{3/2}} \frac{a^3}{L_c^2} \frac{\kappa}{\sigma} + \frac{3}{2^{3/2}} \frac{a^2}{L_c} \right] e^{-\kappa^2/2\sigma^2} + 3a\Psi(\kappa/\sigma) \quad (1.49b)$$

$$\mathbb{E}\{\mathcal{L}_2(E_s(\kappa))\} = \frac{\sqrt{2}}{\pi} \frac{a^3}{L_c} e^{-\kappa^2/2\sigma^2} + 3a^2\Psi(\kappa/\sigma) \quad (1.49c)$$

$$\mathbb{E}\{\mathcal{L}_3(E_s(\kappa))\} = a^3\Psi(\kappa/\sigma) \quad (1.49d)$$

where Ψ is the complementary cumulative density function (tail distribution) of a Gaussian distribution.

FIG. (1.10) represents the volume and the Euler characteristic of excursion sets of g for a large range of level sets.

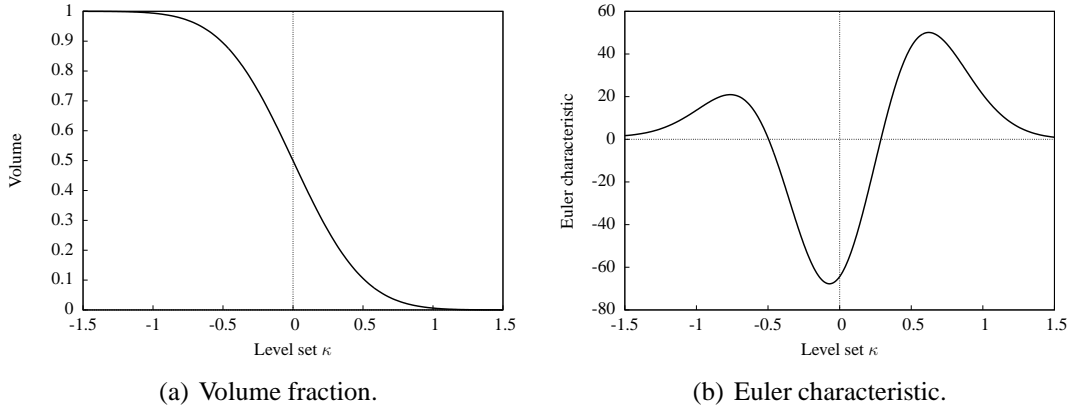


Figure 1.10: Two Gaussian excursion set LKCs.

It has been seen that the volume is proportional to the tail probability of the underlying RF. Its constant decreasing shape clearly reflects the level set effect on the excursion and its link with Gaussian measure γ_1 . In other words, the volume of the excursion is the Gaussian volume. Hence it is rather intuitive that its value is the tail distribution. Even if more peculiar, the Euler characteristic curve shape also easily reflects the effect of the level on excursion set topology. For values of κ lower than the lowest value of g , the Euler characteristic is that of the full cube C ($\mathcal{L}_0 = 1$). By increasing it, several holes appear, counting in positive for the Euler characteristic ($\mathcal{L}_0 > 1$). Then, the expansion of the holes starts to form handles which lead to a sponge-like topology ($\mathcal{L}_0 < 0$). By increasing κ even more, handles disappear forming a meatball-like topology of connected components ($\mathcal{L}_0 > 0$). Finally, the Euler characteristic decreases to $\mathcal{L}_0 = 0$ when no more connected components remain.

The theoretical framework of correlated RF excursion sets has been presented in this section. First, mathematical functionals known as the *Lipschitz-Killing curvatures* that characterize the manifold have been defined. Then a formula that links the probabilistic properties of the underlying RF and the hitting set with those characteristics has been given. It predicts and controls, statistically speaking, the excursion set properties. In three dimensions, four measures are defined. Herein, focus is only made on the volume and the Euler characteristic, giving both geometrical and topological descriptors. The next section aims to validate the numerical implementation by comparing experimental measures of actual excursion set realizations and theoretical values.

3.3.4 Validation of the numerical implementation

Excursion sets are represented by a discretized binary field defined by 1 if in the excursion and 0 if elsewhere. In order to validate the numerical implementation, morphological characteristics of actual excursion sets are compared to theoretical results.

Gaussian correlated RFs of zero means, standard deviation $\sigma = 5$ and Gaussian co-

variance of correlation length $L_c = 10$ are yielded in a three-dimensional cube of size $a = 100$. Attention is focused on the volume fraction $V_f = \mathcal{L}_3/a^3$ and on the Euler characteristic $\chi = \mathcal{L}_0$. It is recalled that the latter is calculated with the polyhedra formula EQ. (1.27). Results are plotted in FIG. (1.11) where mean values of both volume fraction and Euler characteristic are represented in terms of level set values κ from -25 to 25 (corresponding to the whole range of RF values). In order to collate relevant statistical information, calculations are made over 100 realizations. Analysis is made using the mean square error for V_f and χ over all level sets for each realization (results are given in TAB. (1.3)).

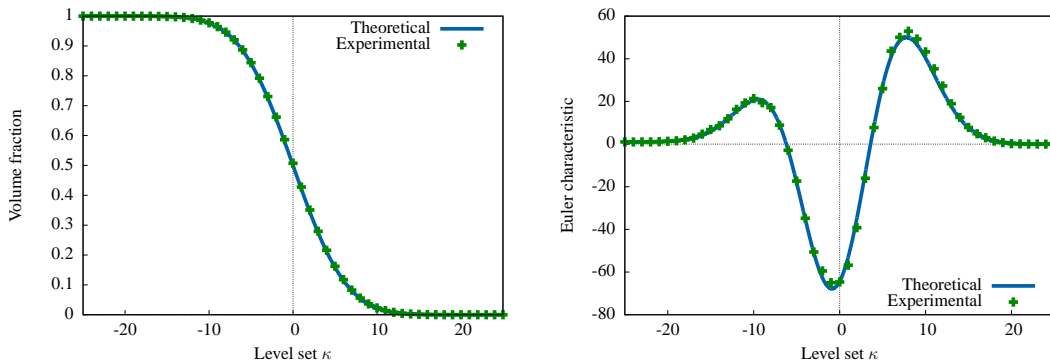


Figure 1.11: Validation of the numerical implementation.

It is recalled that the theoretical equations only give information regarding the first statistical moment. From this point of view, validation of the numerical implementation can be done by a simple look at the curves. Indeed experimental mean values fit quite well with the theoretical curves. It is quantified by the mean value of the error function as well.

Characteristic	Mean μ	Variance σ^2	Coefficient of variation σ/μ
Error on V_f	0.006	10^{-5}	0.6
Error on χ	3.3	0.5	0.2

Table 1.3: Statistical analysis of the error of excursion set characteristics.

The statistical analysis on several realizations also provides rather interesting information on the second moment. Herein, the very low variance of the error (and the coefficient of variation) insures that the characteristics of the excursions are not too spread around the expected values. In other words: it is insured that the morphological characteristics of *one* realization will be close to these targeted. Hence, the random aspect that the excursion set brings to any morphological model is only about the spatial repartition of the shapes, not about their characteristics, a key and necessary property.

4 Application to cementitious materials at different scales

In the two previous sections a morphological model using correlated RF excursion sets has been introduced emphasizing both theoretical and numerical aspects. Attention is now drawn to applying it in order to model heterogeneities of concrete-like material. Two scales are considered leading to two different kinds of morphology, and so two different kinds of problematics. The section is organized as follows. The first part deals with meso-scale representation that is of the order of the millimeter [mm]. Hence, the morphology of interest is made of aggregates melt within a mortar matrix. Topologically speaking, a set of disconnected components needs to be modeled. Added to the non uniform length characteristic of aggregates, this part is an opportunity to raise two main issues: *reaching high volume fractions with a disconnected topology* and *representing a grain size distribution*. The second part presents two applications for which concrete is looked at the (thinner) microscopic scale, which is less than the micrometer [μm]. At this scale and for obvious numerical reasons, smaller volumes are considered and only a cement paste without any aggregates may be represented. However, it is now seen as a heterogeneous porous media. The main change is that this sponge-like topology grants a better flexibility to the morphological model. In this part, a first application on cement paste will be an occasion to represent porous space with very high specific surface. Then, a second application which aims to model early age cement paste hydration will explore two other representative aspects of the excursion set handiness: a multiple — here three — phases representation and an analytical procedure to render evolution through time of those phases.

Notice that, with regard to those tangible applications, only morphological aspect is of concern.

4.1 Meso-scale modeling of concrete

In this section, details on the morphological modeling of concrete-like material heterogeneities are given. A scale range has to be determined in order to define which kind of geometrical information is needed to be represented. Herein, focus is placed on the first scale below the macroscopic one referred as the meso-scale. The length range taken into consideration goes from above the millimeter to hundreds of millimeters. At this scale, concrete-like material can be represented by two phases (each of them assumed to be homogeneous): the aggregates and the mortar. Hence a specific topology is considered in which disconnected inclusions are embedded within a mortar matrix. Several features of these morphologies, *e.g.* high volume fractions or grain size repartition, have to be tackled with attention, especially within the excursion set framework. Both aspects are now treated.

4.1.1 Reaching high volume fraction with disconnected topology

In order to understand the problematic of this section, it is recalled that several characteristics have to be taken into account when a morphology is considered (actually four in a three-dimensional space as seen above). Herein, only two of them are assumed to be relevant. The first characteristic is the volume fraction Φ and the second is the Euler characteristic χ . While the first grants a geometrical measure, the latter is used as an indicator of the topological rendering. The two others (one and two-dimensional measures) are let free. Due to the length range considered here, volume fractions higher than 30% are targeted. These values can easily be reached if no topological restraint is set. Actually, by choosing the right level set, EQ. (1.49d) shows that any fraction can be computed from 0% to 100% (corresponding to $\kappa \rightarrow \infty$ and $\kappa \rightarrow -\infty$ for a Gaussian distribution, respectively FIG. (1.10(a))). It becomes more complicated whether a second restraint appears, in our case, the topology. As it has just been said, a disconnected morphology of inclusions within a matrix is wanted. It naturally corresponds to high values of the level set and therefore to low volume fractions. By considering the physical meaning of Euler characteristic (see EQ. (1.29)), this topology is quantified by positive values of χ due to components and not to holes. In FIG. (1.10(b)), it is located after the second zero, around the second local maximum. It can be checked in FIG. (1.10(a)) that indeed, these level sets lead to low volume fractions. The quantity of interest is taken to be this second zero. This point is discussed with more details in the last section of this chapter but for now, it can be admitted that it corresponds to the percolation of the excursion set. In other words, by taking κ decreasingly from infinity, it is when χ is first null that a path among the excursion is made between two faces. If κ_{p+} is this level set, it is assumed that all values greater than it are acceptable for the modeling.

Before proceeding further, a handful length-scale ratio (α) of an excursion set is defined EQ. (1.50) by the ratio between the correlation length L_c and the domain size a .

$$\alpha = \frac{L_c}{a}. \quad (1.50)$$

The graph in FIG. (1.12) draws expected values of χ in terms of κ for several ratios α (Euler characteristics are normalized $\mathbb{E}\{\chi\}/\max(\mathbb{E}\{\chi\})$ in order to represent them on the same graph). As mentioned above, attention is focused on κ_{p+} , corresponding to $\chi = 0$ for $\kappa > 0$. Notice that, κ_{p+} decreases along with the ratio α until a certain value where it is not defined anymore. An analysis of this feature is now proposed.

First, notice can be made that the equation of the Euler characteristic EQ. (1.49a) is made of order three polynomial in $a/L_c (= 1/\alpha)$ (with no constant term) multiplied by an exponential to which the tail function is added. For very small α , only the first term of the polynomial can be retained, thus leading to a very simple expression of the Euler characteristic EQ. (1.51). Actually, this equation was discovered by Robert Adler in 1976 during his Ph.D. thesis. The other terms have been introduced by the late Keith J. Worsley

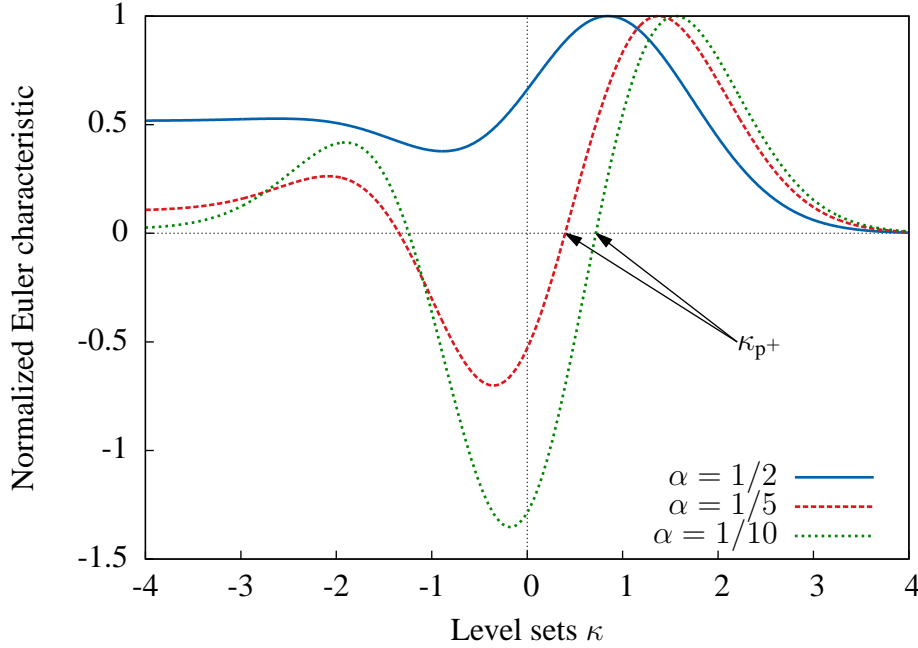


Figure 1.12: Expected values of the Euler characteristics in terms of level sets for Gaussian excursion sets of unit variance and several ratios α .

[Worsley, 1996] and may be seen as *boundary corrections* or *boundary effects*.

$$\mathbb{E}\{\chi\} \approx \frac{1}{\sqrt{2\pi^2}} \frac{a^3}{L_c^3} \left(\frac{\kappa^2}{\sigma^2} - 1 \right) e^{-\kappa^2/2\sigma^2}. \quad (1.51)$$

Hence, a null value of the Euler characteristic necessarily leads to $\kappa_{p+} = \sigma$. The corresponding volume fraction is then $\Phi = \Psi(1) \approx 16\%$. This case gives an accurate result for suitable topologies, although it is a lower bound. The graph in FIG. (1.13) draws the higher volume fractions, $\Phi(\kappa_{p+})$ (plain curve) in terms of the ratio α . The horizontal dashed line corresponds to the latter asymptotic value. It can be seen that by reducing the cube size, this volume fraction increases until a limit around $\alpha \approx 0.3$ depicted by the vertical dashed line (for a unit correlation length, it corresponds to a cube of size $a \approx 3.4$). Beyond this value, the expected Euler characteristic is always positive (see FIG. (1.12) for $\alpha = 1/2$). It can be understood by considering the other extreme case, for which an excursion set is considered in a very small cube. Simplification of EQ. (1.49a) tells that the Euler characteristic equals the tail probability and then, also equals the volume fraction. It can be interpreted as follows: if $\alpha \gg 1$ then the RF tends to be constant in space. Hence, an excursion is whether the cube itself or nothing. On an actual realization, $\chi(\kappa)$ would be a step function, getting from 1 to 0 discontinuously. It is the statistical expected value aspect that grants the smooth shape of $\mathbb{E}\{\chi(\kappa)\}$. Anyway, no further topological information can be withdrawn from these cases.

Even if the volume fraction between the two extreme cases seems to be high enough on the graph, experiences have shown that, considering a higher ratio than $\alpha \approx 0.15$

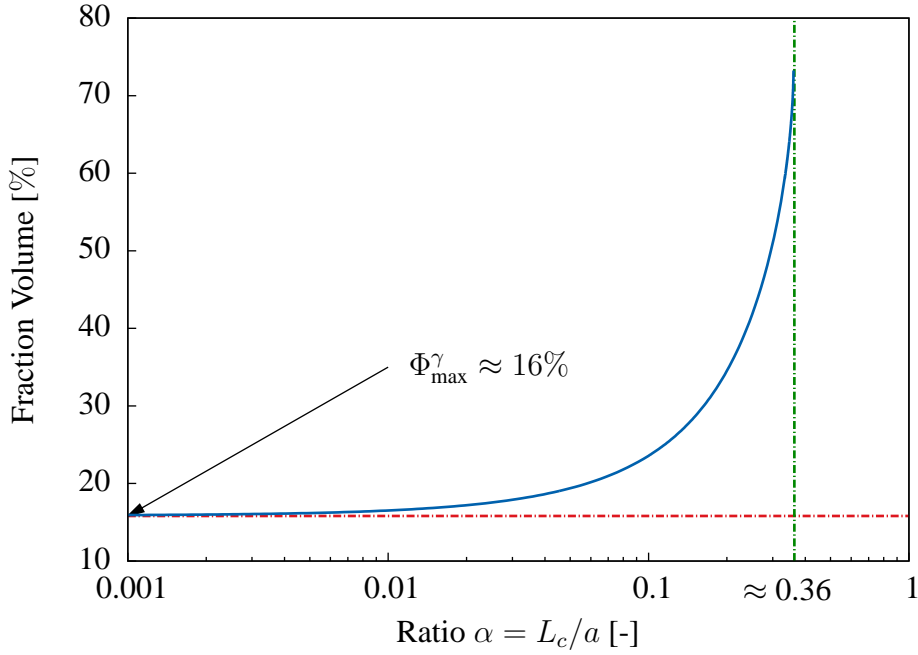


Figure 1.13: Higher volume fractions for disconnected topology.

leads to connected topologies even for level sets slightly higher than κ_{p+} . The side effects are too strong in these length-scales and the statistical meaning of expected percolation does not stand anymore. Discussion on that matter is made on the last section of this chapter where these considerations leads to the determination of a Representative Volume Element for percolation. On the other hand, it is important to be able to represent volume fractions regardless any heterogeneity sizes. It is for those reasons that the maximal volume fraction is assumed to be the asymptotic value for infinite domains. Hence, for Gaussian distribution:

$$\Phi_{\max}^{\gamma} = 16\%. \quad (1.52)$$

In order to increase this value, a solution using χ_k^2 distribution is now proposed.

First a χ^2 distribution with one degree of freedom ($k = 1$) is considered. If g is a Gaussian RF then $g_r = S(g) = g^2$ follows the χ_1^2 distribution. As seen during the presentation of excursion set theory, dealing with excursion sets of Gaussian related distribution falls down to a simple hitting set transformation S^{-1} . Herein, if the hitting set of interest is $H_s = [\kappa \infty[$ for χ_1^2 , it becomes $S^{-1}(H_s) =]-\infty - \sqrt{\kappa}] \cup [\sqrt{\kappa} \infty[$ in the Gaussian point of view (notice that now $\kappa > 0$ since g_r takes its value in \mathbb{R}_+). Basically, due to the symmetrical aspect of Gaussian distributions, the excursion set volume has doubled. This feature is represented with two-dimensional excursions in FIG. (1.14) where both Gaussian and corresponding χ_1^2 excursion are represented.

It is then only natural to stipulate that the maximum volume fraction has doubled too

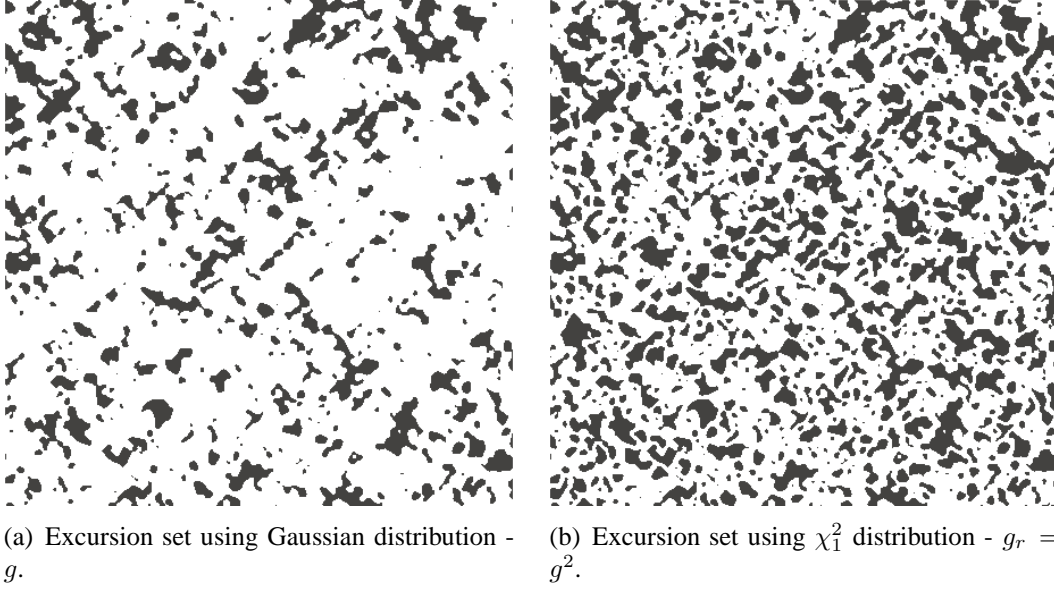


Figure 1.14: Comparison between Gaussian and χ_1^2 excursion sets using the same underlying RF.

(it can easily be shown the same manner as for Gaussian distribution). Hence:

$$\Phi_{\max}^{\chi_1^2} = 32\%. \quad (1.53)$$

However, the behavior of excursion when $\kappa \rightarrow 0$ has to be tackled with caution. A topological discontinuity occurs at zero, corresponding to the transition between $S^{-1}(H_s) = \mathbb{R}^*$ and $S^{-1}(H_s) = \mathbb{R}$. In the first case, two completely disconnected parts of the excursion can be identified; the one from the lower part of $S^{-1}(H_s)$, $]-\infty - \sqrt{\kappa}]$ and the one from the upper part $[\sqrt{\kappa} \infty[$. Those two phases are connected together only when $\kappa = 0$, leading to a jump from a very low value of the Euler characteristic ($\chi < 0$) to a unit value ($\chi = 1$). It is proved that a regular behavior is obtained by increasing the number of degrees of freedom ($k \geq 5$), thus avoiding this discontinuity. Herein, it is not the concern since κ is taken greater than κ_{p+} (*i.e.* far from this discontinuity).

By analyzing the maximum volume fraction with several numbers of degrees of freedom of the χ_k^2 distribution, it can be directly seen that the best case remains for $k = 1$. FIG. (1.15) shows for a very low length ratio ($\alpha = 0.001$): on the left, three curves representing the Euler characteristic with $k = 1, 2$ and 5 and their respective κ_{p+} and on the right, the corresponding volume fractions $\Phi(\kappa_{p+})$ for $1 \leq k \leq 25$, showing its decreasing shape. For infinite number of degrees of freedom, it naturally tends to the Gaussian limit of 16% (due to central limit theorem). Finally, a χ_1^2 distribution is retained in order to model a disconnected topology. The precaution consisting in taking a level set slightly higher than κ_{p+} is taken in order to insure the desired topology. Determining all parameters of the morphological model can be decomposed in the following steps:

Step 1: Determination of the ratio κ/σ

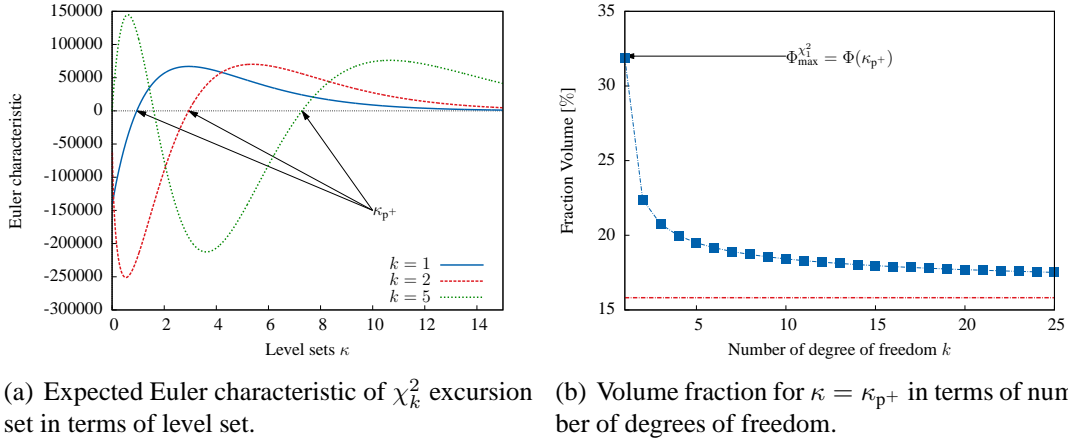


Figure 1.15: Maximum volume fraction in the χ_k^2 case for a ratio $\alpha = 0.001$.

Thanks to the previous analysis, the maximum volume computable for a suitable disconnected topology is known. For example let consider a targeted volume fraction of 20%. As depicted in FIG. (1.16(a)), EQ. (1.49d) gives the value of κ/σ . If a unit variance distribution is considered, then $\kappa_{20\%}$ is explicitly known. Notice that this step is independent of any length scale.

Now, in order to move on topological considerations, a length-scale has to be fixed. Depending on the problematic, EQ. (1.49a) can be used as described in step 2a or step 2b. It is recalled that for these disconnected topologies, the Euler characteristic represents the number of components.

Step 2a: Determination of the correlation length L_c

If no length-scale is imposed, a number of inclusions can be targeted. Since κ is determined during step 1, a simple inversion of EQ. (1.49a) for a given size a leads to a value of L_c . Note that choosing the volume fraction and the number of components leads to a single component size.

Step 2b: Determination of the number of inclusions

If a length-scale is imposed by the problem; for example inclusions of size 1 in a cube of size 1000, as shown in FIG. (1.16(b)), EQ. (1.49a) gives the expected number of inclusions $\chi \approx 44873$.

Unfortunately, this theoretical case is hardly computable since the ratio $\alpha = 0.001$ implies a generation of heavily discretized correlated RFs. However, using the numerical framework presented above yields three-dimensional realizations of $200 \times 200 \times 200$ points in a reasonable time (less than an hour). It can accurately represent a length ratio of $\alpha = 0.01$. Examples in a cube of size $a = 100$ with $L_c = 1$ and 10 are shown in FIG. (1.17).

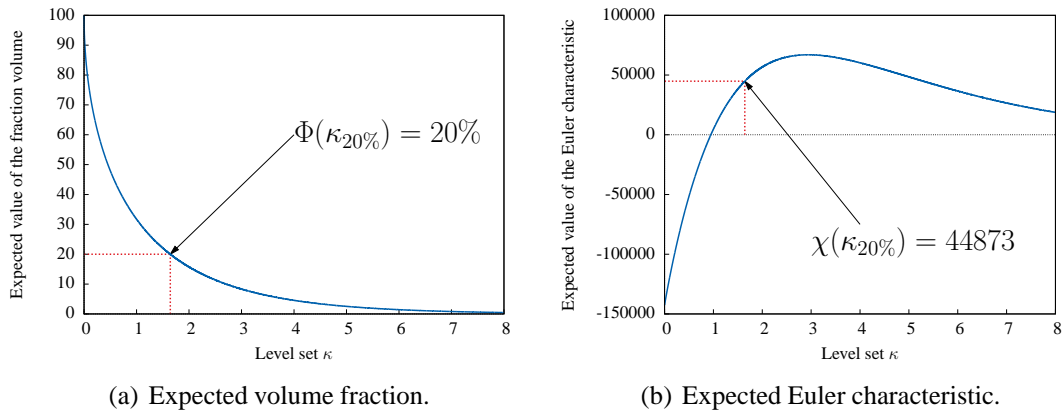


Figure 1.16: Expected LKCs for χ_1^2 excursion set of unit variance and $\alpha = 0.001$. A volume fraction of 20% is targeted giving a corresponding Euler characteristic of 44873.

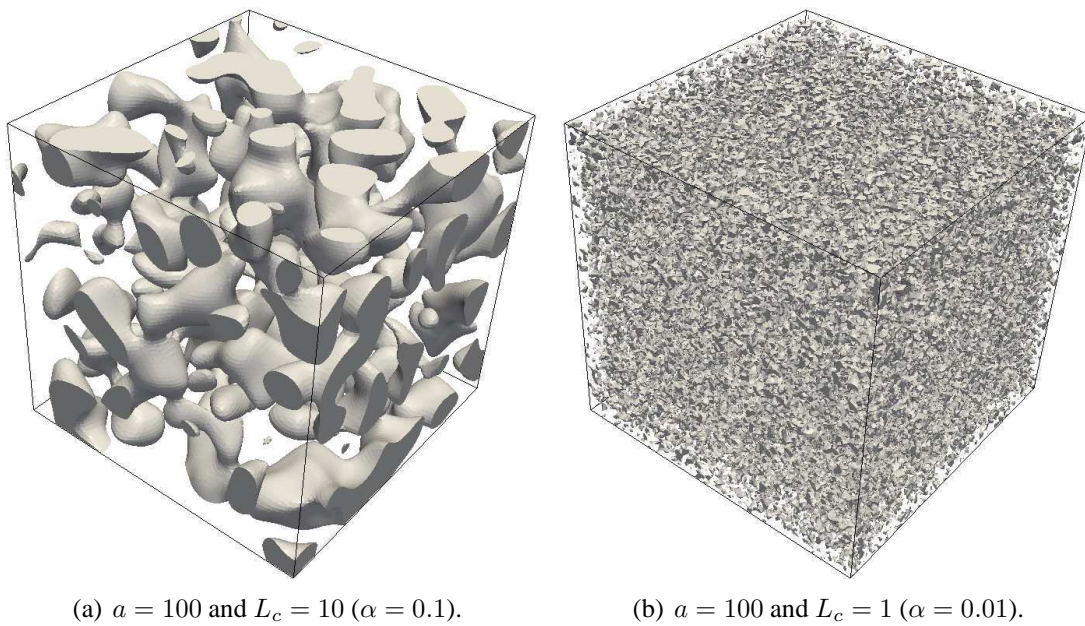


Figure 1.17: Disconnected excursions with 20% volume fraction using a χ_1^2 distribution with two correlation lengths.

In this section it has been described how to double the maximum volume fraction of disconnected morphologies using a χ^2 distribution of one degree of freedom instead of a Gaussian one. A criterion independent from the length ratio α based on percolation of the excursion is used. With a certain margin to insure a suitable topology, it has been seen that 20% of volume fraction can easily be modeled. The following section gives directions on an additional method that combines several excursion sets with different correlation lengths in order to, on the one hand, still increase the volume fraction and, on

the other hand, represent a size distribution for heterogeneities.

4.1.2 Modeling of the grain size distribution

Up to this point, only one characteristic length was considered for excursion sets. However, morphological modeling of aggregates has to be represented by heterogeneities that follow a given grain size distribution. Henceforth, the challenge is to yield a single excursion with different characteristic lengths and still to be able to control its geometrical and topological properties. The idea is to consider a set of K independent excursions $\{E_s^k\}$, $k = [1..K]$ with their own characteristics. Among them, the most important characteristic is of course the correlation length L_c^k . And finally, the union of every excursions defines a new excursion which possesses multiple characteristic lengths. These excursions are referred as:

$$E_s^\cup = \bigcup_{k=1}^K E_s^k. \quad (1.54)$$

Along with several hypothesis, the principle of measure of union of sets is used in order to estimate the different LKCs of the resulting excursion.

To begin with, a simple two-dimensional example is considered. Let E_s^1 et E_s^2 be two excursions of respective LKCs and correlation lengths $\{\mathcal{L}_n^1\}$, L_c^1 and $\{\mathcal{L}_n^2\}$, L_c^2 . It is assumed that $L_c^1 > L_c^2$. FIG. (1.18(a)) represents the two excursions defined on the same domain, E_s^1 being in light grey and E_s^2 in dark grey while FIG. (1.18(b)) represents the union of both, *i.e.* E_s^\cup .

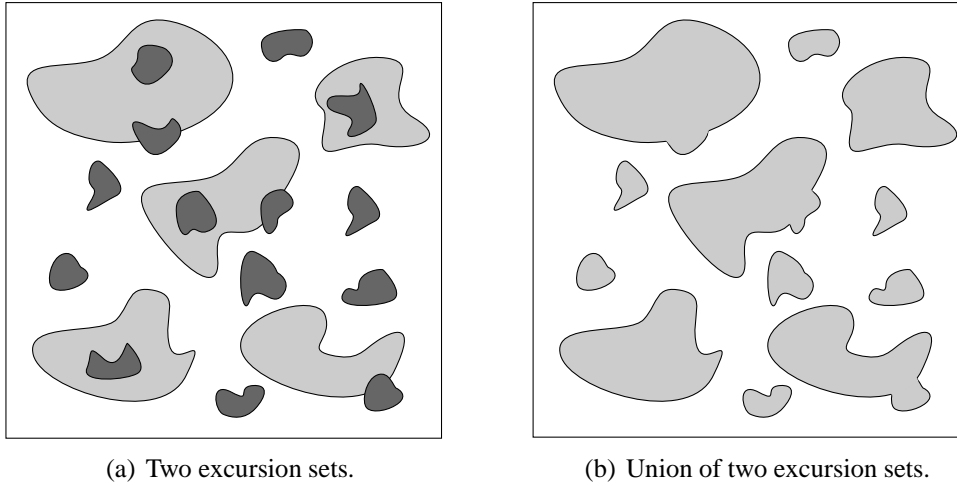


Figure 1.18: Illustration of the use of several excursions — two here.

In a more general case, attention is drawn to the calculation of each LKC \mathcal{L}_n , $n = [0..N]$ of E_s^\cup in a N -dimensional space. Following the axiomatic that defines any measure, it can be yielded by:

$$\mathcal{L}_n(E_s^\cup) = \mathcal{L}_n(E_s^1 \cup E_s^2) = \mathcal{L}_n(E_s^1) + \mathcal{L}_n(E_s^2) - \mathcal{L}_n(E_s^1 \cap E_s^2). \quad (1.55)$$

Under hypothesis of sufficient ergodicity for the underlying RFs and statistically representative volumes (low length ratio α for both excursions) the assumption that the k^{th} measure of the intersection is approximated by the actual measure of the lower correlation length excursion pondered by the specific value of the last LKC of the higher one (the specific surface area in two dimensions or the fraction volume in three dimensions) can be made. It leads to a completely predictable approximation of each measure of the union:

$$\mathcal{L}_n(E_s^\cup) = \mathcal{L}_n(E_s^1 \cup E_s^2) \approx \mathcal{L}_n(E_s^1) + \mathcal{L}_n(E_s^2) (1 - \Phi_N(E_s^1)), \quad (1.56)$$

$\Phi_N(E_s^1) = \mathcal{L}_N(E_s^1)/\mathcal{L}_N(M)$ being the specific value.

Under the same assumptions, the generalization of this principle to the union of more than two excursions is rather straightforward. If K excursions are considered with different *sorted* correlation lengths ($L_c^1 > \dots > L_c^k > \dots > L_c^K$), using a recursion process on EQ. (1.55), the LKCs can be computed:

$$\mathcal{L}_n(E_s^\cup) \approx \mathcal{L}_n(E_s^1) + \sum_{k=2}^K \mathcal{L}_n(E_s^k) \left(1 - \bigcup_{l=1}^{k-1} \Phi_N(E_s^l) \right), \quad (1.57)$$

in which, thanks to the Poincaré formula and the approximation made in EQ. (1.56), the union of Φ_N can be computed as follows:

$$\bigcup_{k=1}^K \Phi_N(E_s^k) \approx \sum_{k=1}^K \left((-1)^{k-1} \sum_{1 \leq i_1 < i_2 < \dots < i_k \leq K} \Phi_N(E_s^{i_1}) \Phi_N(E_s^{i_2}) \dots \Phi_N(E_s^{i_k}) \right). \quad (1.58)$$

Finally, since measures of each excursion set E_s^k are predictable, expected values of the LKCs, $\mathbb{E}\{\mathcal{L}_i(E_s^\cup)\}$ can now be computed. It is recalled that EQ. (1.57) is an approximation. Hence, comparison with experimental results is recommended. Three excursions using χ_1^2 distribution and characteristic lengths $L_c = 10, 5$ and 2 are defined in a three-dimensional cube of size $a = 100$. Both Euler characteristic $\chi = \mathcal{L}_0$ and volume fraction $\Phi = \mathcal{L}_3/a^3$ of the resulting excursion are compared to the analytical approximation EQ. (1.57). Results are drawn in FIG. (1.19), notice that, even if not mandatory, for the sake of handful representation, the excursion set is the resulting union of excursion sets thresholded with the same level set.

It can be seen directly that the approximation for the volume fraction is rather good. On the other hand, the theoretical Euler characteristic is always overestimated for low level sets. It can be explained by a too coarse discretization regarding the sponge-like aspect of morphologies and by the discontinuous aspect of χ_1^2 excursion sets near 0 (numerically hard to catch). Anyway, regarding disconnected topology, the maximum number of particles is well estimated, as for the decreasing part of the curve. Another important feature that unions enable is that the computable volume fractions are much higher than while using a single excursion. Notice that on the presented example that, for κ_{p+} , the volume fraction is around 50%. As a precaution, the level set is taken so that $\kappa \gg \kappa_{p+}$, leading to excursion sets of 40% volume fraction and disconnected topology.

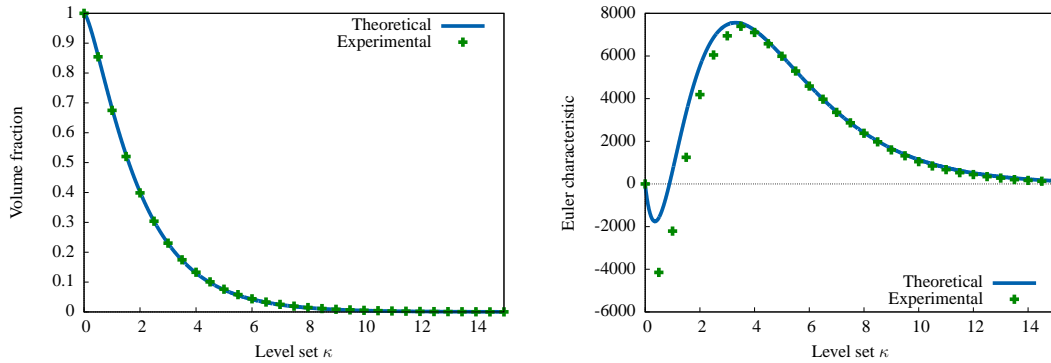


Figure 1.19: Comparison between experimental and theoretical characteristics of excursion sets union.

At this stage, it is wise to base any morphological modeling using union of RF on the volume fraction and consider the topological aspect more as an indicator than a reliable value. Finally, higher values of the level set than those estimated are recommended in order to model disconnected topologies.

Now that the use of several lengths has been presented, the matter of their choice in order to model realistic morphologies is of concern. Among the multiple classifications of grain size ranges, TAB. (1.4) refers to that of [Wentworth, 1922]. The morphological

Name	Size range (diameter D)	[unit]
Boulder	$D > 256$	[mm]
Cobble	$64 < D < 256$	[mm]
Very coarse gravel	$32 < D < 64$	[mm]
Coarse gravel	$16 < D < 32$	[mm]
Medium gravel	$8 < D < 16$	[mm]
Fine gravel	$4 < D < 8$	[mm]
Very fine gravel	$2 < D < 4$	[mm]
Very coarse sand	$1 < D < 2$	[mm]
Coarse sand	$0.5 < D < 1$	[mm]
Medium sand	$0.25 < D < 0.5$	[mm]
Fine sand	$125 < D < 250$	[μm]
Very fine sand	$62.5 < D < 125$	[μm]
Silt	$4 < D < 62.5$	[μm]
Clay	$D < 4$	[μm]

Table 1.4: Simplified classification of granular materials following [Wentworth, 1922].

modeling of a set of *only one class* particles can be made by using an excursion set with a *single* correlation length chosen in the range $D_{\min} < L_c < D_{\max}$. For example, fine

gravels can be modeled by taking $L_c = 6 \text{ mm}$. It is assumed that, due to the random aspect of the framework, a distribution of disconnected particles which sizes are spread around the correlation length produces an acceptable representation. It can be extended to several classes using unions of excursion sets in which each excursions of the union represents a single class. In order to follow a given distribution of sizes (granulometry), the volume fraction of each excursion has to be determined.

In mathematical morphology, the field related to grain size distributions is also referred as *granulometry*. It has been introduced by Georges Matheron [Matheron, 1975] and defines the size distribution of a set of particles (or aggregates) G through a series of sieving. Each sieve has a hole size s and can be represented by a mathematical operator Ψ_s that returns the subset of all particles of G smaller than s . This operator has the three following properties:

Anti-extensivity

This first property depicts the fact that if a particle $G_i \in G$ is larger s then, it does not pass through the sieve Ψ_s . Hence, the result of a sieving is contained in the original set of particles. It can be the set itself if all particles are smaller than s . This property is written:

$$\Psi_s(G) \subseteq G. \quad (1.59)$$

Increasingness

This second property reflects a regular aspect of the physical meaning of sieving. If a subset H of set of particles G is sieved by Ψ_s , then the result is a subset of the sieving of G . Thus leads to:

$$H \subseteq G \Rightarrow \Psi_s(H) \subseteq \Psi_s(G). \quad (1.60)$$

Stability

Finally, this last axiom considers two sieves of size s_1 and s_2 . Whatever the order, a passing through both sieves is equivalent to a single passing through the thinner. It can be expressed by:

$$\Psi_{s_1} \Psi_{s_2}(G) = \Psi_{s_2} \Psi_{s_1}(G) = \Psi_{\min(s_1, s_2)}(G). \quad (1.61)$$

Notice that it can easily be generalized to more than two sieves.

The physical meaning of this mathematical tool reflects the sieve analysis used to measure grain size distributions of actual concrete-like materials. If a measure $\mu(G)$ defines the mass of G then the cumulative distribution of particles can be represented by the ratio $\mu(\Psi_s(G))/\mu(G)$ in terms of s . Under the hypothesis of identical density, it can also be interpreted as a volume fraction.

In order to fit in the numerically computable range, only medium, fine and very fine gravels are considered here in a cube of size $a = 100 \text{ mm}$ for a total volume fraction of $\Phi = 40\%$. It is assumed that the granulometry gives the following values:

$$\begin{aligned} \text{For medium gravels: } \mu(\Psi_{16}(G)) &= \mu(G). \\ \text{For fine gravels: } \mu(\Psi_8(G)) &= 0.75 \mu(G). \\ \text{For very fine gravels: } \mu(\Psi_4(G)) &= 0.25 \mu(G). \end{aligned} \quad (1.62)$$

For this granulometry, the parameters of each excursion set can now be set. Volume fractions are $\Phi^{\{1,2,3\}} = \{0.25\Phi, 0.5\Phi, 0.25\Phi\}$, respectively, and the correlation length is taken to be the average of each class extrema diameters giving $L_c^{\{1,2,3\}} = \{12, 6, 3\}^2$, respectively. With regards to the union set theory, volume fractions of each excursion set will have to be targetted higher than the wanted value. In this case, they are computed as follows:

$$\Phi_{\text{target}}^1 = \Phi^1 = 0.25\Phi \quad (1.63a)$$

$$\Phi_{\text{target}}^2 = \frac{\Phi^2}{1 - \Phi^1} = \frac{0.5\Phi}{1 - 0.25\Phi} \quad (1.63b)$$

$$\Phi_{\text{target}}^3 = \frac{\Phi^3}{(1 - \Phi^1 - \Phi^2)} = \frac{0.25\Phi}{(1 - 0.75\Phi)} \quad (1.63c)$$

Three realizations of this morphology can be seen in FIG. (1.20).

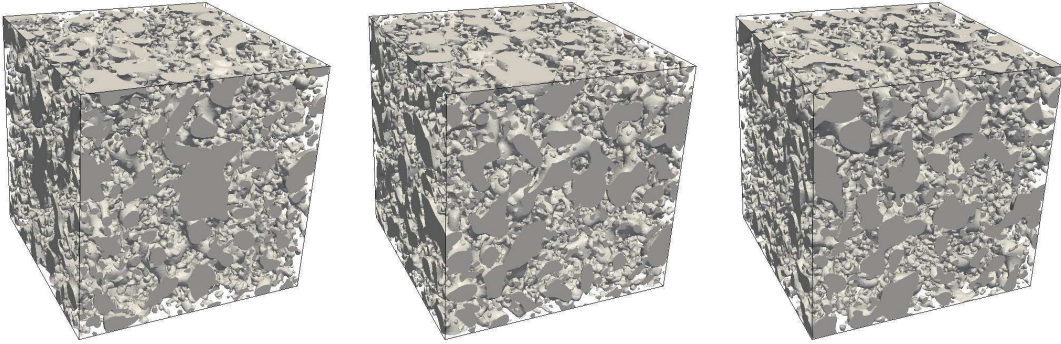


Figure 1.20: Three realizations of 40% volume fraction excursion sets of correlation lengths $\{12, 6, 3\}$.

In the second chapter of this thesis, a mechanical framework, using the Finite Element Method, explicitly takes into account those kinds of morphology. Due to the mesh thickness that representation of 2 mm particle implies, another morphology in which the total volume fraction is lower (30%) and the characteristic lengths are higher $L_c^{\{1,2,3\}} = \{15, 7, 5\}$ is used. Three realizations are shown in FIG. (1.21).

²Lengths in mm .

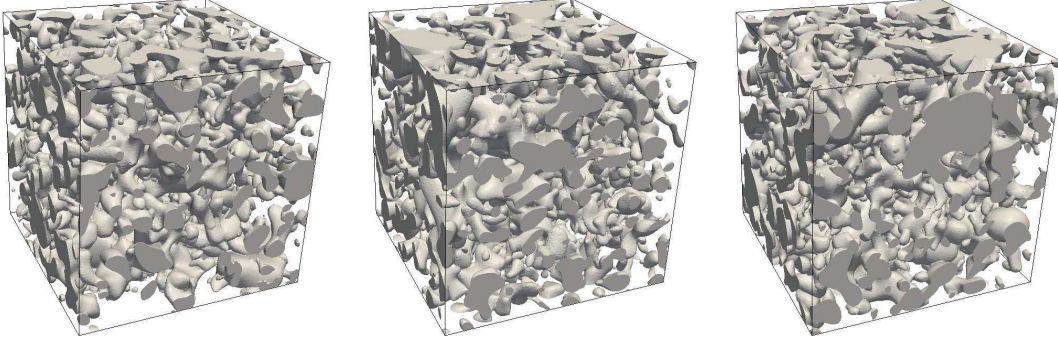


Figure 1.21: Three realizations of 30% volume fraction excursion sets of correlation lengths $\{15, 7, 5\}$.

4.2 Micro-scale modeling of cement paste

Up to this point it has been shown how excursion sets can be used to model aggregates (inclusions) within a cement paste matrix, the latter being considered as homogeneous. However, once seen at a much smaller scale than the microscopic scale (from nm to μm), its porous aspect has to be represented. The purpose here is to show that these completely different morphologies (topologically speaking) can also be modeled using excursion sets. Two applications of this strategy are presented. Both are based on the previously developed theory and are parts of two ongoing Ph.D. thesis (Mahban Hosseini and Mateusz Bogdan). Herein, only the morphological aspect is considered.

4.2.1 Porous media

As stated before, the hitting set chosen to perform any RF excursion has a major role on the resulting morphology. Herein, attention is focused on the sponge-like ones (see FIG. (1.9(a))) that are adapted to model porous media such as cement paste. In order to show this ability, a cement paste which has been investigated through mercury intrusion is chosen. The total porosity is near 31% and the total pore area is almost $31 m^2.g^{-1}$. The former is directly linked to the third Lipschitz-Killing curvature $\mathbb{E}\{\mathcal{L}_3(E_s(\kappa))\}/a^3$ and leads to define the corresponding threshold $\kappa = -0.51$ for a centered and reduced Gaussian field using equation EQ. (1.49d). Moreover, assuming a density equal to $2.5 g.cm^{-3}$, the latter leads to the definition of $\mathbb{E}\{\mathcal{L}_2(E_s(\kappa))\}/a^3$ and, afterwards for determining the underlying correlation length L_c using equation EQ. (1.49c).

FIG. (1.22) shows a realization of an excursion set computed with those parameters. The whole domain is a cube $C = 1 \times 1 \times 1 \mu m^3$. For computational reasons the choice of $L_c = 10^{-2} \mu m$ is retained. It leads to a high-pass filter with a cutoff pore size corresponding to 20% HR. The total porous volume represented in the excursion (see FIG. (1.22)) is thus $6.10^4 mm^2.mm^{-3}$ which is 60% of the total volume measured by mercury intrusion.

This morphological modeling strategy has many advantages and may lead to several

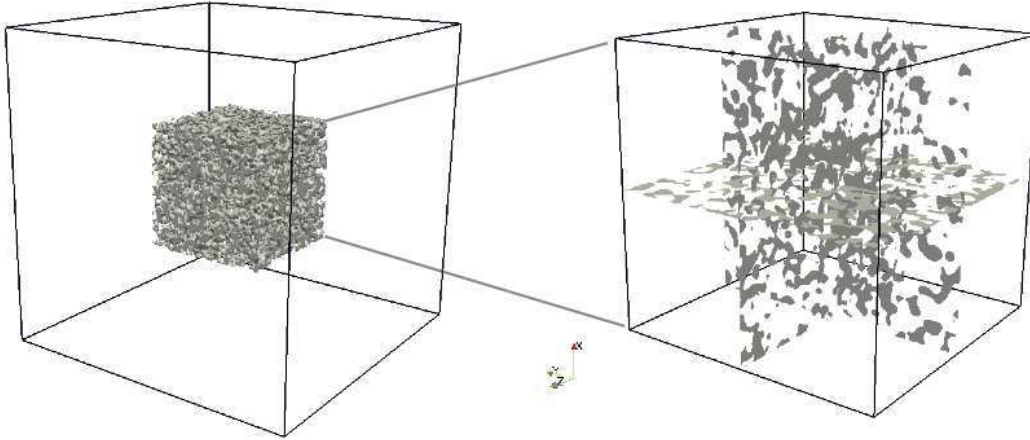


Figure 1.22: Excursion set for modeling the porous space of a cement paste.

applications at the cement paste scale. Among them the Ph.D. thesis of Mahban Hosseini focuses on the modeling of adsorption — desorption process which is a key point for the study of cementitious material durability.

4.2.2 A simple hydration model

In this section a simple hydration model for concrete-like material is presented. It has to be seen more as an opportunity to present some additional features (or extensions) of the excursion set morphological model than an actual attempt to describe the full complexity of early age cement based material processes. However, in order to depict this phenomenon, a physical *evolution of more than two phases* is to be considered. A simplified version of the Powers hydration model [Powers and Brownyard, 1947] is chosen to set up the evolution rules. It takes into account three phases only: anhydrous cement, hydration products and free water which initial state and evolutions are controlled in terms of volume fractions (noted Φ_c , Φ_h and Φ_w , respectively) as defined SYS. (1.64).

$$p = \frac{w/c}{w/c + \rho_w/\rho_c}, \quad (1.64a)$$

$$\Phi_c = (1 - p)(1 - \alpha_{\text{hyd}}), \quad (1.64b)$$

$$\Phi_h = 2.12(1 - p)\alpha_{\text{hyd}} \quad \text{and} \quad (1.64c)$$

$$\Phi_w = 1 - \Phi_c - \Phi_h. \quad (1.64d)$$

in which p is the initial porosity, w/c and ρ_w/ρ_c are the ratio water/cement in mass and in density, respectively and α_{hyd} ($0 \leq \alpha_{\text{hyd}} \leq 1$) the hydration degree.

As a first step, the modeling of three phases is considered. This problematic occurs to be easily implementable in the presented framework and does not involve new principles, hypothesis or equations. The basic idea is to introduce an additional level set. As one level set defined a border between two phases, two can naturally define two borders between

three phases. Hence, three hitting sets H_s^1, H_s^2 and H_s^3 can characterize three phases E_s^1, E_s^2 and E_s^3 , respectively. Using the previous notations, it can be written (using χ_1^2 distributions):

$$H_s^1 = \{x \in M \mid 0 \leq x < \kappa_1\} = [0 \ \kappa_1[\quad (1.65a)$$

$$H_s^2 = \{x \in M \mid \kappa_1 \leq x \leq \kappa_2\} = [\kappa_1 \ \kappa_2] \quad (1.65b)$$

$$H_s^3 = \{x \in M \mid \kappa_2 > x\} =]\kappa_2 \ \infty[\quad (1.65c)$$

Depicted in FIG. (1.23) in the one-dimensional case, this principle can be applied in the same manner for any dimension.

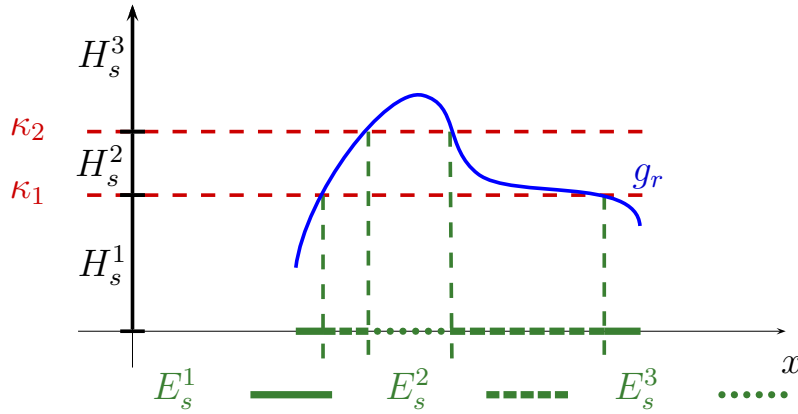


Figure 1.23: Three phase morphology using excursion set framework in one-dimension.

Herein, the three-dimensional space is considered. The morphological aspect of each phase implies to assign the right hitting set to the right material. Since hydration products are created around nearly disconnected anhydrous cement grains, forming a frontier with the free water, the hitting set repartition is set as noted in TAB. (1.5). *Remark: The topological denomination given in this table has to be seen in a three-dimensional space. Due to the complexity of topological concepts, the meaning of this denomination is not necessary applicable to other dimensions (and especially not to the one-dimensional case FIG. (1.23))*. An example of this morphology is given in FIG. (1.24) where the three

Phase	Hitting set	Topological denomination (in three dimensions)
Anhydrous cement	$]\kappa_2 \ \infty[$	Disconnected components
Free water	$[0 \ \kappa_1[$	Connected media (sponge-like)
Hydration product	$[\kappa_1 \ \kappa_2]$	Border

Table 1.5: Repartition of hitting sets according to the phase topology.

phases are represented (anhydrous cement in grey, hydration products in brown and free water in blue).

The second step is to make each phase evolve through “time” following the chemical model summarized by SYS. (1.64). From a physical point of view, evolution is controlled

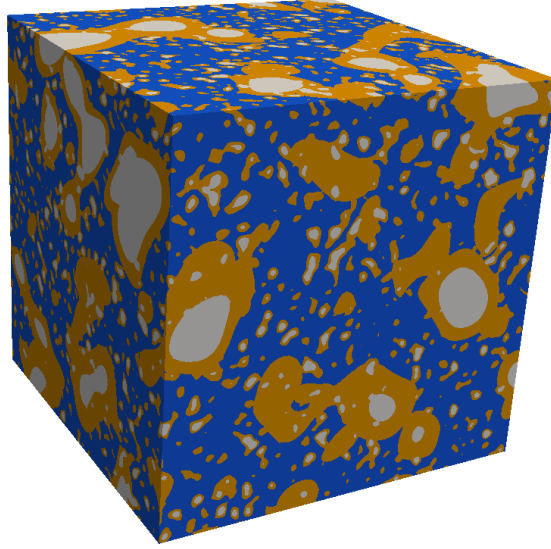


Figure 1.24: Example of a three-dimensional morphology with three phases.

by the hydration degree α_{hyd} (not the time) and for a given value, the volume fraction of each phase is defined by EQ. (1.64b), (1.64c) and (1.64d). First, at the hydration onset ($\alpha_{\text{hyd}} = 0$), only two phases are present, the water filling the voids left by anhydrous cement grains ($\Phi_c = 1 - p$, $\Phi_h = 0$ and $\Phi_w = p$). Then, as the process progresses (α_{hyd} increases), volume fractions evolve and hydration productions replace both water and anhydrous cement. It tends to a *theoretical* two phases end ($\alpha_{\text{hyd}} = 1$) when all the cement has reacted ($\Phi_c = 0$, $\Phi_h = 2.12(1 - p)$ and $\Phi_w = 1 - \Phi_h$). Depending on the initial porosity ($p < 0.53$), this stage can lead to a physical absurdity when Φ_h is greater than 100%. Those evolutions are drawn for $p = 0.61$ in FIG. (1.25(a)).

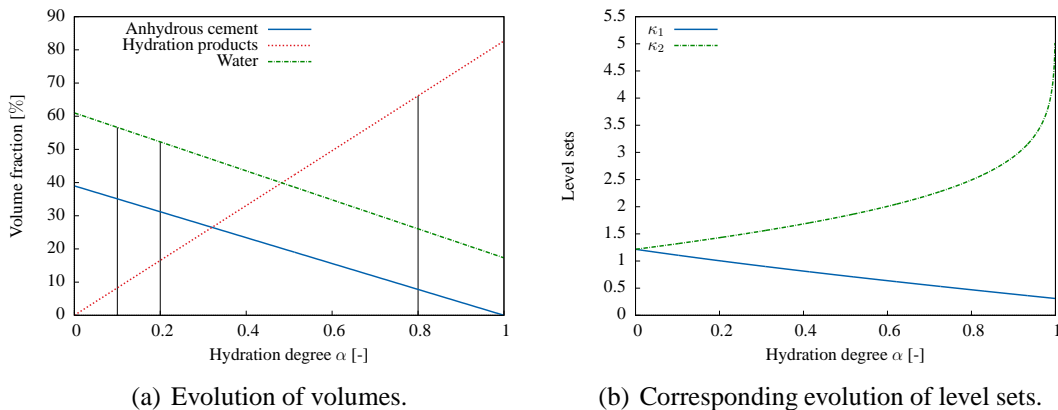


Figure 1.25: Evolution of the volume fraction of each phase for $p = 0.61$.

The link between volume evolution and the excursion set framework is directly made by the mean of the level sets κ_1 and κ_2 . Indeed, equation EQ. (1.47) gives the knowledge

of the volume fraction phase for a given hitting set, *e.g.* a given level set. Furthermore, always related to the underlying tail probability function, this equation can easily be inverted giving an expression of level sets in terms of volume. Henceforth, an analytical link is made between given volumes and level sets. In the simple case of χ_1^2 excursion with one correlation length, the equation can be inverted, giving an explicit relationship between Φ_w and κ_1 on the one hand, and Φ_c and κ_2 on the other hand (SYS. (1.66b)). Finally, by injecting the Powers evolution rules SYS. (1.64) in it, $\kappa_1(\alpha_{\text{hyd}})$ and $\kappa_2(\alpha_{\text{hyd}})$ are directly known. Those relationships are drawn in FIG. (1.25(b)).

$$\kappa_1 = 2\sigma^4 \left(\text{erf}^{-1}(1 - \Phi_w(\alpha_{\text{hyd}})) \right)^2 \quad \text{and} \quad (1.66a)$$

$$\kappa_2 = 2\sigma^4 \left(\text{erf}^{-1}(\Phi_c(\alpha_{\text{hyd}})) \right)^2. \quad (1.66b)$$

The more realistic approach of union of excursion sets is used in order to yield the initial state ($\alpha_{\text{hyd}} = 0$) where the only constraint is a volume fraction of nearly disconnected components $1 - p$. The results of the presented method are shown in FIG. (1.26) for four hydration degrees.

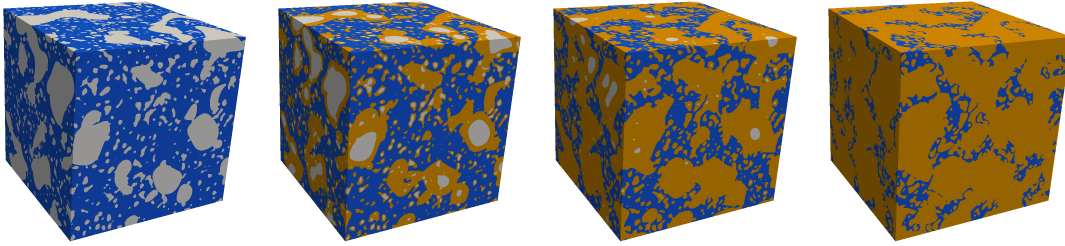


Figure 1.26: Evolution of morphologies through an hydration process with $\alpha_{\text{hyd}} = 0, 0.1, 0.2$ and 0.8 .

On the one hand, a way of representing three-dimensional morphologies with three phases has been presented. Notice that an additional number of phases (4, 5 . . .) can be implemented the same way. For each supplementary phase, an additional level set is needed. However, this simple representation introduces a major drawback regarding morphological aspect of each phase. Using the presented methodology only produces a disconnected topology (cement grains), a sponge-like media (water) and a frontier between them (hydration products). For example, if two phases representing disconnected components is considered, another approach implying more than hitting sets repartition (not developed here) is necessary.

On the other hand, a handful use of analytical results on expected characteristics of excursion sets (volumes) makes those phases evolve through time following given rules. Herein, it has been depicted using a simplified Powers hydration model.

This section has presented several applications of the excursion set theory for the explicit modeling of concrete-like material heterogeneities. Several features such as grain

size repartition or evolution of geometrical characteristics have been developed in order to show the possibilities that the framework enables. The problematics related to the two following sections are rather different. The same theoretical background is used to propose original approaches to common issues related to brittle and quasi brittle failure that are *size effect* and *percolation theory*.

5 Analytical model for size effect of brittle material

In this section another approach using expected values of excursion set characteristics is proposed. Up to this point, this mathematical tool has been used in order to yield actual morphologies and predict their geometrical and topological characteristics. The continuum aspect of correlated RFs was concealed by the thresholding method used (level set) which led to discrete fields (excursion sets). Herein, RFs directly represent a material property (ultimate stress field) and the excursion set theory is used in order to catch statistical information on its extrema.

A theoretical method for size effect modeling of brittle heterogeneous materials is proposed. In this field, the main result comes from the early studies of [Weibull, 1951] based on the theory of the weakest link. The authors proposed an analytical solution for the global failure criterion, considering a discrete structure of independent brittle links with a specific distribution probability of local failure criterion. With no spatial correlation between each link, this theory leads inevitably to large scale size effect. The two current theories of Zdeněk P. Bažant and Alberto Carpinteri, trying to describe the size effect for the missing scales, are the main results of the extensive literature existing on this topic. The former tends, in many ways, to describe the size effect using both non-local model and stochastic approach [Sab and Lalaai, 1993], or more recently using the so-called energetic-statistical size effect mixing strength redistribution theory in a fracture process zone and Weibull's theory [Bažant, 2004]. The latter considers material heterogeneities with a fractal model in order to represent size effects for quasi-brittle materials [Carpinteri et al., 2003]. On the other hand, numerical simulations have been made using stochastic integrations and correlated RFs in order to describe material properties [Colliat et al., 2007]. These methods are quickly time consuming and the underlying numerical implementation brings an inevitable limitation regarding the observation scale.

The idea behind this method is to extend the Weibull theory to lower scales by adding the spatial structure of *correlated* RFs. A continuum representation of the spatial variability through scales can theoretically be made by defining a ratio α (as in EQ. (1.50)) between the spatial parameter of the correlated RF covariance function L_c and the size of its definition domain a . As already stated just above, heterogeneities modeling is directly made through a variation of material properties (and not by through definition of different phases). The continuum aspect of correlated RFs statistically represents a local ultimate failure stress $\sigma_y(\mathbf{x}, \omega)$ on a structure M . RFs are here used in a direct way, even if the discrete aspect of excursion set and their expected Euler characteristic are used in

order to define the global failure stress σ_f of the structure. The whole framework has to be seen on a purely theoretical and analytical point of view. Contrary to stochastic integration methods, the knowledge of expected information on RFs avoids generating actual RF realizations. Hence, there is no scale limitation.

5.1 Correlation lengths as scale parameters

As it has been pointed out during this chapter, the correlation length L_c can be seen as a size parameter of a correlated RF. Herein, a constant value of L_c is chosen, fixing the average size of the heterogeneities considered. The dimension of the domain M (where the RF is defined) represents the size of the whole structure. If a is the characteristic length of M (for example: the length of a segment in the one-dimensional space, the length of the side of a square in a two-dimensional space...), its value determines the observation scale. In order to let the heterogeneity size unspecified, the ratio $\alpha = L_c/a$ is taken into consideration. Nonetheless, L_c still has to be seen as a constant and a a variable. Realizations of RFs for different ratios α are shown in FIG. (1.27) on a two-dimensional square.

For $\alpha \gg 1$

The structure is very small compared to the heterogeneity size. The RF tends to be a constant field and is equivalent to a single RV with no spatial information. It represents the material scale, the validity domain of continuum damage mechanics (CDM) where the failure stress does not depend on the size of the structure (see FIG. (1.27(a))).

For $\alpha \ll 1$

The structure is very large compared to the heterogeneity size. The RF tends to be equivalent to a white noise (completely uncorrelated), leading to a loss of spatial structures. It represents the scale of big structures as the Weibull theory does, retrieving the linear fracture mechanic (LFM) domain of expertise (see FIG. (1.27(c))).

For $\alpha \approx 1$

The RF represents the missing scale range where the continuum statistical information of correlated RFs for various α can link together material and big structure scales. Hence, it can model size effect for civil engineering structures (see FIG. (1.27(b))).

5.2 One-dimensional case

In this study, a one-dimensional bar in tension is considered. The source of uncertainty is modeled by a statistical representation of the local failure criterion $\sigma_y(x, \omega)$. Due to the positiveness of stress fields in tension, the *log-normal* distribution is used. Since log-normal distribution is Gaussian related, the results of the previous section are applicable

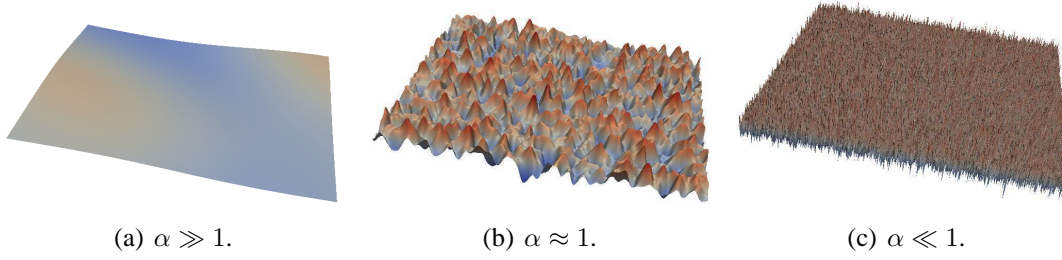


Figure 1.27: Realization of two-dimensional correlated RFs for various α ratios.

by a simple transformation of the hitting set $S = \exp$. The spatial structure representation is done by using correlated RF with Gaussian covariance function of correlation length L_c . The continuum domain represented is a one-dimensional bar M of length a . For this specific case, the global brittle failure of a bar M is assumed to occur when, at least, the minimum value of $\sigma_y(x, \omega)$ is reached by the stress field. If $\sigma_f(\omega)$ is this criterion, it can be defined for a realization i by:

$$\sigma_f(\omega_i) = \inf_{x \in M_i} (\sigma_y(x, \omega_i)). \quad (1.67)$$

It occurs that this equation can directly be linked with the Euler characteristic χ of an excursion sets. Let $E_s(\sigma) = \{x \in M \mid 0 \leq \sigma_y(x, \omega) \leq \sigma\}$ be an excursion set where the constant stress state of the bar can be seen as a level set. With this definition, the excursion set represents the part of the bar (subset of M) where the stress is above the local failure criterion $\sigma_y(x, \omega)$. The global failure criterion of EQ. (1.67) can therefore be seen in terms of excursion set; σ_f being the stress state when, with increasing σ , $E_s(\sigma)$ changes from being a void subset of M ($\chi = 0$) to a single connected component ($\chi = 1$).

A result of [Adler, 2008] on statistical thresholding technics links the probability of reaching these minima and the expected Euler characteristic as follows:

$$P \left\{ \inf_{x \in M} (\sigma_y(x, \omega)) \leq \sigma \right\} \approx \mathbb{E} \{ \chi(E_s(\sigma)) \} \quad \text{“for low } \sigma\text{”}. \quad (1.68)$$

The major improvement that EQ. (1.68) provides is the knowledge of statistical information on $\sigma_f(\omega)$, and with it, the need of Monte Carlo simulations with actual realizations i as suggested by EQ. (1.67). Then, the initial failure criterion of the structure can be reformulated in terms of probability q . This leads to:

$$\sigma_f(q) = \left\{ \sigma \mid P \left\{ \inf_{x \in M} (\sigma_y(x, \omega)) \leq \sigma \right\} = q \right\}. \quad (1.69)$$

The expected value of the Euler characteristic being analytically known, EQ. (1.68) and EQ. (1.69) allow the ultimate stress criterion of the bar to be analytically determined, for a given failure probability q .

In order to scan every observation scales possible, EQ. (1.69) is solved for a large scale range $10^{-9} \leq \alpha \leq 10^3$. Since L_c is fixed by the heterogeneity size, the different

scales are therefore represented by defining a single $\sigma_y(x, \omega)$ (with the same covariance function) for various a as represented in FIG. (1.28). The mean and the variance of the log-normal correlated RF have physical meaning and can be determined depending on the material characteristics. While the mean value of $\sigma_y(x, \omega)$ determines the value of the structural failure stress of small scales ($\alpha \gg 1$), its variance indicates the decreasing rate of the size effect for large scales ($\alpha \ll 1$).

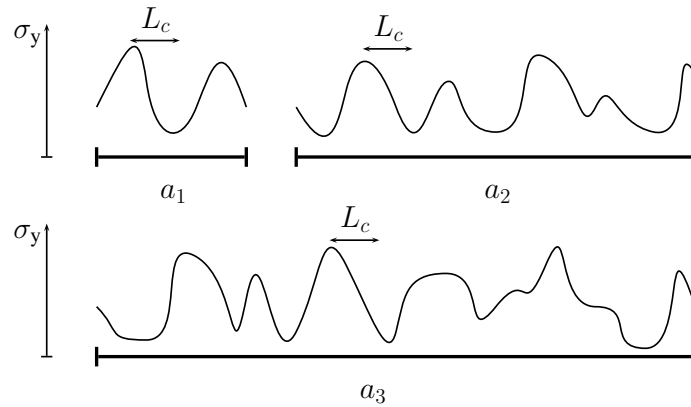


Figure 1.28: Illustration of the local failure stress repartition on structures of various sizes.

5.3 Validation, results and comments

In order to validate the theoretical framework, results of the same problem solved using a Monte-Carlo stochastic integration method are also given. On the one hand, the stochastic integration provides a full empirical distribution of $\sigma_f(\omega)$ (defined by EQ. (1.67)) for several ratios α . On the other hand, the analytical results of $\sigma_f(q)$ depends directly on the probability parameter q that, by definition of the ultimate stress EQ. (1.69), is directly linked with quantiles of the previous empirical distribution. For example, $q = 1/2$ corresponds to the 2-quantile, *i.e.* the median.

FIG. (1.29(a)) shows the resulting global failure stresses σ_f for ratio $\beta = \alpha^{-1}$ from 10^{-3} to 10^2 with the Monte-Carlo method (in order to show results in the most commonly used manner, scales are represented by the inverse ratio $\beta = \alpha^{-1} = a/L_c$). The inspection of larger scales is rapidly limited by the inconvenient resource consuming aspect of stochastic integrations. On the strength of its analytical base, the excursion set theory every scale can be inspected, here for β varying from 10^{-3} to 10^9 . The Monte-Carlo integration results of global the failure stress distribution is given for the 2, 10, and 100-quantile, corresponding to $q = 1/2$, $1/10$, and $1/100$, respectively. In both method, the mean and the variance of the *log-normal* distribution are both taken to be 10. The RANDOMFIELDS package [Schlather, 2012] of the R environment [Team, 2012] has been used in order to do the stochastic integration, using 10 000 integration points for each length.

As expected, no size effect is observed at the small scale, $\beta < 10^{-2}$. For $q = 1/2$, the value of the failure stress corresponds to the *log-normal* distribution median (that is, due

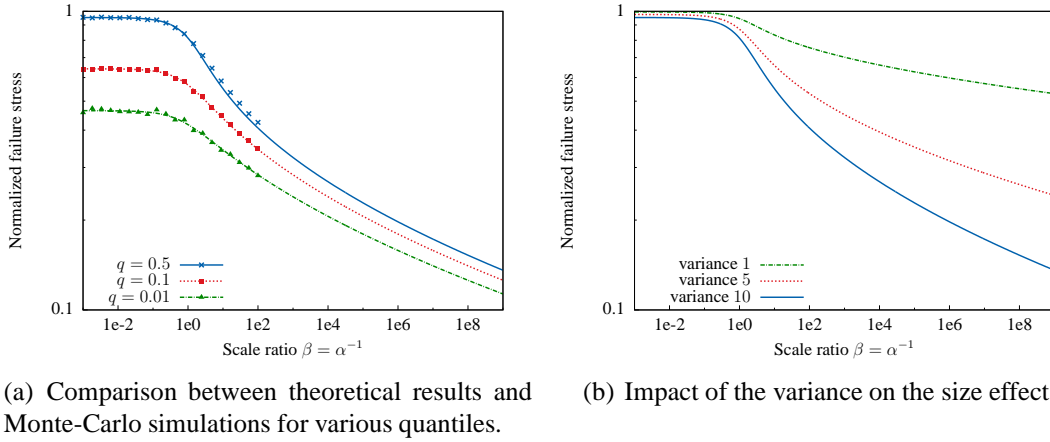


Figure 1.29: Representation of the size effect through a failure stress criterion estimated for various scales.

to the skewness of the distribution, a little less than the mean). As β grows, the decrease of σ_f representing the size effect can be seen. As for the impact of q , results show the good behavior. Indeed, for a safety probability of 90% (meaning a failure probability of $q = 0.1$), the failure stress is higher than for a safety of 99% ($q = 0.01$). The three curves drawn in FIG. (1.29(b)) represent the impact of the variance on size effect for a failure probability $q = 1/2$. While L_c is the parameter of the correlated RF that represents the geometry of the heterogeneities, the variance can be seen as a description of the mechanical property discrepancy. Results show the natural principle that higher variations are, lower the values and larger the drop of σ_f are.

6 Continuous percolation on finite size domains

Percolation theory deals with connectivity issues on random stochastic patterns. First expressed by [Broadbent and Hammersley, 1957] as a statistical-geometry model, percolation was used to study a fluid flow through a rock where it was assumed to be a network of channels randomly open or close. These problems are often treated with lattice discretization of the space. Arbitrary rules (often referred as bond or site percolation) can be set in order to define clusters (open path) on those lattices. Accordingly, elements of the lattice have two states: *open* or *close*. For example, the *bond percolation* in two-dimensional spaces models a path between two vertices by a Bernoulli distribution of parameter p . Hence, each edge is independent and has a probability p to be open and $1 - p$ to be close. The quantity of interest in order to define whether a lattice is percolated or not is defined by a critical probability p_c which has the two followings properties:

$$\text{If } p < p_c$$

There is a probability one chance that all clusters are finite. The lattice is not percolated.

If $p > p_c$

There is a positive probability that a given point of the lattice is in an infinite cluster.
The lattice is percolated.

This first approach carries a lot of issues. First, most of the literature considers infinite size problems (which is mathematically correct, but is only an approximation of what happens in real cases). Second, the definition of a percolation cluster (a subset of connected bonds) is also made on infinite size problems. It is usually defined by the presence of an unbounded cluster, or by a continuous path from the origin to an infinitely distant point. Again, in finite size problems, these definitions have to be revised. Furthermore, these problems are subjected to lattice dependency. However, the latter problem can be dealt with by defining volumes around edges (or vertices) in order to phase out the discrete aspect of lattices. It is the first step into the continuum percolation field where instead of looking at the critical probability p_c , a critical volume fraction Φ_c (which has the same properties) is considered. First expressed in [Scher and Zallen, 1970] it is admitted that in a three-dimensional space:

$$\Phi_c \approx 16\%. \quad (1.70)$$

Most of the time, no analytical solution is known to solve these problems leading to an expensive need of numerical resources.

Given that it has been established that the topological information carried by the Euler characteristic is intrinsically linked with percolation, a link can be made with excursion sets using the theoretical framework of Robert Adler. In the early nineties, it has been highlighted by [Tomita and Murakami, 1994] and [Okun, 1990] where a critical volume fraction is deduced for infinite size problems analytically. This section proposes the same approach but with the bound corrections introduced by [Worsley, 1996], aptly representing finite size domains. A side effect can then be observed giving the possibility of defining a statistical Representative Volume Element (RVE) for percolation.

6.1 Accounting for side effects

Herein, excursion sets are defined by Gaussian correlated RF over a three-dimensional cube M of finite size a . Among the four LKCs that characterize the excursion morphology, only the Euler characteristic $\chi = \mathcal{L}_0$ and the volume fraction $\Phi = \mathcal{L}_3/a^3$ are considered. Expected values of these measures are given EQ. (1.49). As for the previous cases, the domain size has to be compared to the excursion set correlation length L_c . Hence, analysis is still made in terms of the ratio $\alpha = L_c/a$.

The link between percolation and the Euler characteristic is stated to be when the latter switch signs. Most of the time it occurs two times and represents two different percolation states as depicted in FIG. (1.30). The two underlying level sets are noted κ_{p+} and κ_{p-} and correspond to the followings situations:

Percolation of the excursion set at $\chi(\kappa_{p+}) = 0$

By considering a high level set value, the corresponding excursion set is made of

small disconnected components. As the level set value decreases, those components grow and others appear making the Euler characteristic increase up to a certain maximum point. It corresponds to the coalescence of the biggest components. The critical point of interest κ_{p+} is for a level set value just below the latter states, where the χ is null. It is stated that at this stage, the excursion set is percolated.

Percolation of the voids at $\chi(\kappa_{p-}) = 0$

The same reasoning can be made in order to define the other percolation point. This time, increasing level sets starting at a very low value has to be considered. The percolation point κ_{p-} is also for the first null value of the Euler characteristic and corresponds to the percolation of the voids.

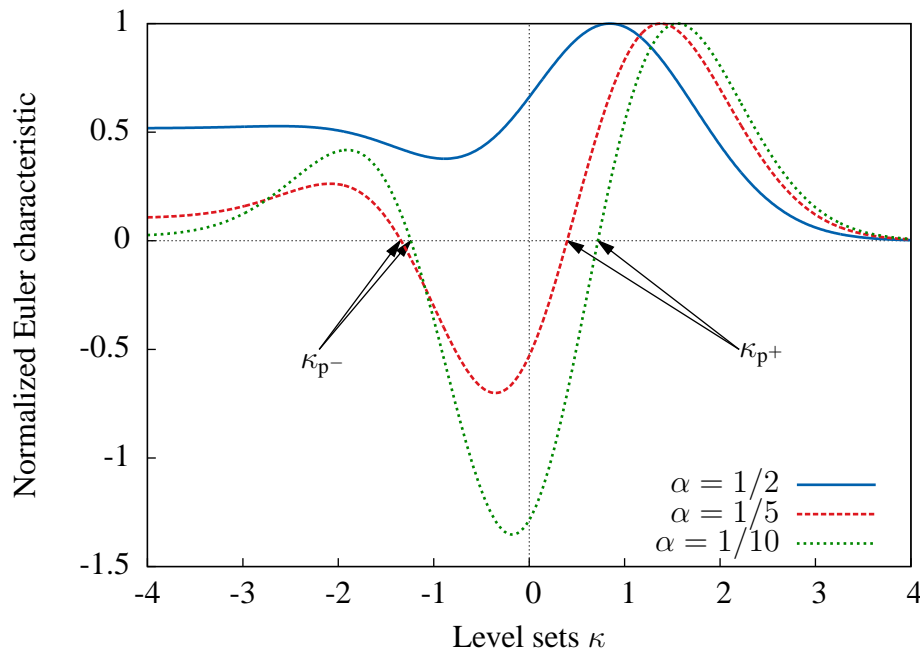


Figure 1.30: Expected values of the Euler characteristics in terms of level sets for Gaussian excursion sets of unit variance and different ratios α .

As already remarked in FIG. (1.12), for several values of α , percolation cannot be defined ($\alpha = 1/2$ for example). Since the Euler characteristic is always positive, the volumes considered are too small to bring any relevant statistical information in terms of percolation states. However, in the other cases (for smaller α) attention is drawn to the corresponding critical volume fractions $\Phi(\kappa_{p+})$ and $\Phi(\kappa_{p-})$. As FIG. (1.13) shows the first only, FIG. (1.31) shows both in terms of α . A frontier is created between two states, one with positive values of χ (outside) and the another with negative values (inside). The fact that the two curves go away from their asymptotic values ($\alpha \ll 1$) and finally meet is a direct representation of side effects. It is analytically taken into account by the bound corrections [Worsley, 1996]. As the topology of an excursion can be determined whether it is inside or

outside, this graph can be seen as a *phase diagram*. Unfortunately, the Euler characteristic does not give information whether positive values are due to holes in the excursion or to components (see EQ. (1.29)). For example, an additional topological measure that counts the number of disconnected components of the excursion could define a third frontier, giving three topological states: disconnected excursion set and percolated voids ($\chi > 0$ due to components), both voids and excursion percolated ($\chi < 0$) or percolated excursion set and disconnected voids ($\chi > 0$ due to voids).

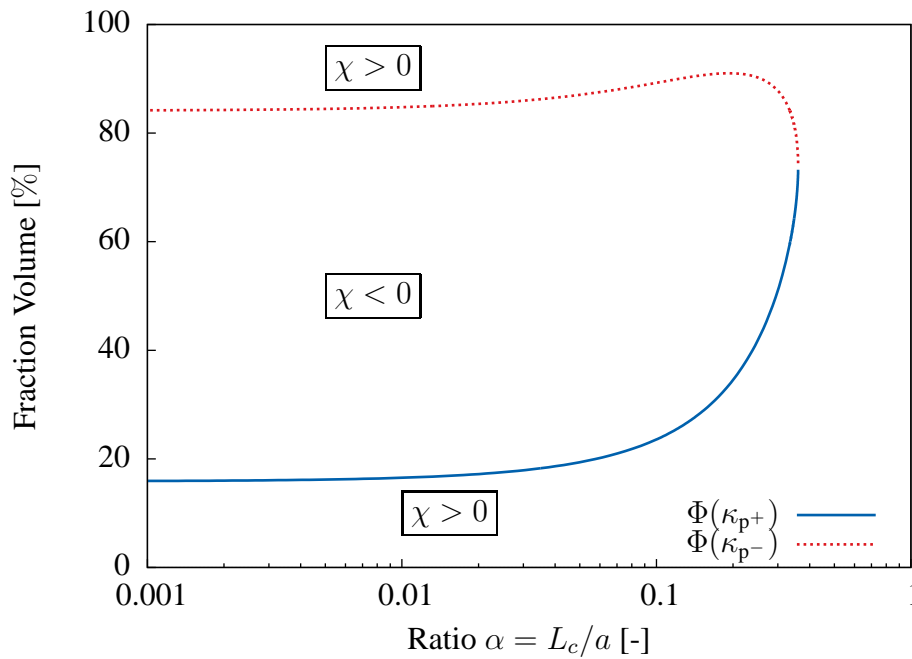


Figure 1.31: Critical volume fractions with side effects for percolation of both excursion set and voids.

It can be seen that the asymptotic values that correspond to infinite domains are consistent with values from the literature obtained first by computer simulations [Skal et al., 1973] or by speculation on lattice problems [Zallen, 1979] and with the basic underlying symmetrical assumption:

$$\lim_{\alpha \rightarrow 0} \Phi(\kappa_{p+}) = \Phi_c \approx 16\% \quad \text{and} \quad \lim_{\alpha \rightarrow 0} \Phi(\kappa_{p-}) = 1 - \Phi_c. \quad (1.71)$$

Then, as α grows, the critical volume fraction of the excursion set increases. This rather unintuitive feature can be interpreted by the fact that, in a finite size domain, there are less possible paths to link two distant points than in an infinite one. Hence, a higher volume fraction is needed. Furthermore, these stages lead to the loose of the relation $\Phi(\kappa_{p+}) + \Phi(\kappa_{p-}) = 1$, meaning that the symmetry hypothesis that exists on infinite size problems does not apply anymore.

In regards to these results, morphological RVE for percolation is now defined.

6.2 Representative Volume Element for percolation

Traditional approaches to define a RVE are based upon a certain number of realizations of a random media and the average properties measured for each realization. Theoretically, if the domain M is a RVE for a given property, the discrepancy of the results must vanish to zero. However, these RVE are usually too large to be handled numerically. Smaller realizations are thus made and from average values over all the realizations, lower and upper bounds can be defined [Huet, 1990, Hazanov and Huet, 1994]. Herein, this statistical approach is embedded in the theoretical framework that gives the excursion set *expected* characteristics. Hence, no actual realization is computed.

Due to its monotonic shape, the RVE is defined in regards to the critical volumes of excursion set percolation $\Phi(\kappa_{p+})$ (and not the one corresponding to the voids), the reference value being Φ_c . The relative error between both (EQ. (1.72)) gives the RVE precision. Its evolution through scales is plotted in FIG. (1.32).

$$\epsilon = \frac{\Phi(\kappa_{p+}) - \Phi_c}{\Phi_c}. \quad (1.72)$$

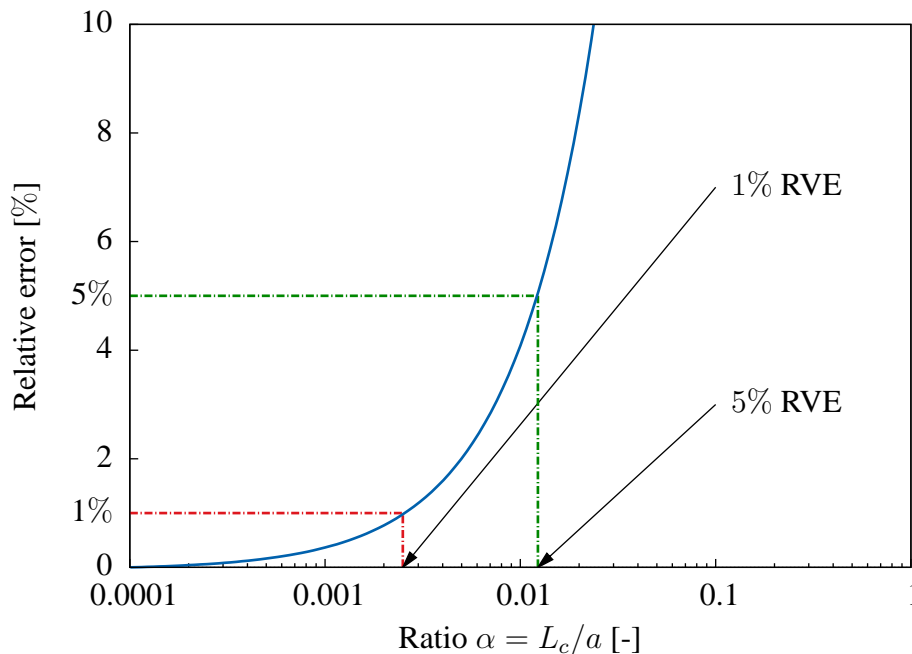


Figure 1.32: Relative error between critical percolated volumes of finite and infinite size domains.

Hence, a value of α can be determined for a given error. Results of TAB. (1.6) show that, for a given heterogeneity size L_c , a domaine size of more than 80 times L_c is needed for a 5% RVE and 400 times for 1%.

ϵ	0%	1%	5%
$\Phi(\kappa_{p+})$	15.87	16.03	16.67
α	0	0.0025	0.012

Table 1.6: Size (α) and corresponding volume fraction (Φ) of 1% and 5% error RVE.

Since, as far as the authors can tell, no RVE for percolation can be found in the literature. However, it can be compared to classical mechanical problems linked with percolation issues such as diffusivity phenomena or permeation in cement paste material. On these matters, results are rather consistent and tend to define RVE corresponding to a scale ratio of $\alpha = 1/100$. Among the vast literature on that subject, in [Zhang et al., 2011] the authors define a cement paste RVE for water diffusivity of $100 \mu m^3$ with heterogeneities represented by a polydisperse spheres from $1 \mu m$ to $50 \mu m$. The RVE is then smaller than what the theory predicts. Several consideration can explain this difference. First, the property of interest differs. When the latter RVE is based on mechanical property (diffusivity), the theory only takes into consideration the topological aspect of the morphology. Secondly, a size distribution of spheres is compared to an excursion set with one characteristic lengths.

7 Concluding remarks

In this chapter, a morphological model based on excursion set of correlated RFs that produces complex randomly shaped morphologies has been presented. Original formulae [Adler, 2008] that statistically control the geometrical and topological characteristics of these excursion sets — volume, surface area, Euler characteristic — in terms of the RF parameters — correlation length, variance — has been adapted in order to model cementitious material heterogeneities at different observation scales. It has led to several problematics such as describing matrix-inclusion topology or porous media, reaching high fraction volumes, representing grain size distributions or adding several phases to the modeling. Finally, advantages of these analytical formulae has been highlighted by presenting two models for finite-size problems. First, to represent the size effect and second, to determine a RVE for percolation.

As it has been pointed out, the main issue with this methodology is to reach high volume fractions while keeping a disconnected topology. Even if the use of another distribution — χ_1^2 rather than Gaussian — helped double it, the maximal compacity obtained with a single characteristic length in a representative volume is about 30 %. However, it is shown that by only considering a certain part of a grain size distribution (mainly gravels) and using union of excursion sets, relevant modeling can be obtained. Nonetheless, as presented during the introduction of this chapter, this value is lower than what an efficient packing sphere algorithm can produce. On that matter, a further work on hitting sets can be done. An idea is to extend the principle of χ^2 distribution to higher order, yielding

vectors valued RF. Thus, hitting sets could be based on spherical harmonics functions. Hence, as transforming the one-dimensional open hitting set $[\kappa, \infty[$ into the complementary ball of the same dimension doubled the volume fraction, working with hitting sets in higher dimensions should increase it as well.

An improvement of the method can also be made by considering all the excursion set characteristics. In this chapter, attention has mainly be focused on the volume fraction and the Euler characteristic, which seem the more relevant characteristics to control first. In order to model the heterogeneity more accurately, it is recalled that in the three-dimensional space, information on two and one-dimensional measures such as surface area and calliper diameter, respectively, are also available. An analysis of the link between the latter and the correlation length could be an interesting research area.

Finally, even though it as just been theoretically presented, it is recalled that the use of other covariance function classes, such as the Matérn class, can be used to control a thinner detail of the resulting geometry, namely the surface aspect. Adapting expectation formulae to these classes only require a change of the second spectral moment which can easily be calculated. Even though not presented here applications in the two-dimension space has been made in order to analyse fracture surfaces of mortar specimens. An identification of their correlation length and the Matérn parameter ν on these surfaces characterized their tortuosity and their roughness, respectively.

Chapter 2

Unified numerical implementation of quasi-brittle behavior for heterogeneous material through the Embedded Finite Element Method

Contents

1	Introduction	62
2	Kinematics of strain and displacement discontinuity	65
2.1	Jump in the strain field	67
2.2	Jump in the displacement field	68
2.3	Strong discontinuity analysis	70
3	Variational formulation	71
3.1	Three-field variational formulation	71
3.2	Assumed strain and double enhancement	73
3.3	Finite Element interpolation	76
4	Discrete model at the discontinuity	78
4.1	Localization	79
4.2	Traction-separation law	80
5	Resolution methodology	81
5.1	Integration and linearization with constant strain elements	82
5.2	Solving the system	84
5.3	Application to spatial truss and spatial frame	86
5.4	Application to volume Finite Elements	97
6	Concluding remarks	103

1 Introduction

The objective is to develop a numerical model for quasi-brittle materials at a scale where heterogeneities play a significant role. For concrete-like material this scale is referred to as the meso-scale where aggregates inclusions are embedded within a cement-paste matrix. Therefore, the framework main features are the explicit representation of heterogeneities within a FE context and modeling of the failure mechanism at the meso-scale. Both are made possible through kinematical enhancements of the finite element interpolation basis. Firstly, thanks to the non-adapted meshing strategy implemented through a *weak* kinematic enhancement. Secondly, according to the choice of *strong* enhancement in the model that addresses a major challenge, namely the cracking representation phenomenon. This chapter presents a uniform and general numerical method called the Embedded Finite Element Method (E-FEM) handling these problematics.

At the so-called meso-scale, numerical methods based upon spatial meshes are quickly confronted to the fundamental problematic of its construction regarding heterogeneities. The standard methodology to address this issue— known as *adapted* meshing — consists of three steps. First, the interfaces between the heterogeneities are considered, corresponding to a surface meshing for a three-dimensional problem. For that matter, several technics have been developed whether the morphology is known (CAD) or not (Marching cube [Lorensen and Cline, 1987]). Second, the rest of domain is considered, corresponding to a volume meshing of several homogeneous phases. Thus, a two-phase morphology leads to two kinds of elements, each having their nodes in a single phase, leading to a simple FE implementation. Despite the number of studies of this method, their time consuming aspect makes them rather irrelevant regarding to geometrical variability. In addition treating interface debonding problems involves the introduction of zero thickness elements — or *cohesive zone* — [Barenblatt, 1962]. Herein, the choice is made to turn to another method.

The method referred as *non-adapted* consists in a unique “homogeneous” mesh with nodes placed independently from the morphology and thus from the interfaces — hereafter referred as the *original mesh* (see FIG. (2.1(a))). Hence, for a given geometry, a set of elements are split into two parts by a physical interface. These elements are decomposed into two subdomains that inherit of each material phase properties. In order to introduce this contrast of property in the classical linear elements, an enhancement of the kinematics is performed by means of a jump within the strain field — this being known as a *weak discontinuity*. The pioneer work on that matter goes back to the end of the 80’s [Ortiz et al., 1987] for the modeling of localization bands. The application of weak discontinuities in the context of material heterogeneities modeling has been introduced later in [Sukumar et al., 2001].

In the case of a two-phase material (matrix-inclusion for instance), the non-adapted meshing method leads to two types of elements: the elements that are completely within the matrix or within the inclusions, and the elements with a part in the matrix and another in an inclusion. Only the latter type of element is enhanced by the weak discontinuity.

Hence, the meshing process, referred to as morphological projection, consists in assigning their type to the original elements of the mesh, *i.e.* defining the distribution of element types. It occurs that this light implementation is linearly dependent on the number of elements of the original mesh. In addition, with the one-time volume meshing of the original mesh, this methodology ensures a swift and efficient process well suited for morphological probabilistic studies based on Monte-Carlo procedures (see Chapter 3 on RVE determination). The work presented here is a development, from a theoretical point of view, of Damijan Markovič Ph.D. thesis where two-dimensional Constant Strain Triangles were considered [Markovic et al., 2005] and from a numerical point of view, of Nathan Benkemoun Ph.D. thesis where a three-dimensional discretization of a heterogeneous media was done by means of a spatial lattice model [Benkemoun, 2010, Benkemoun et al., 2010].

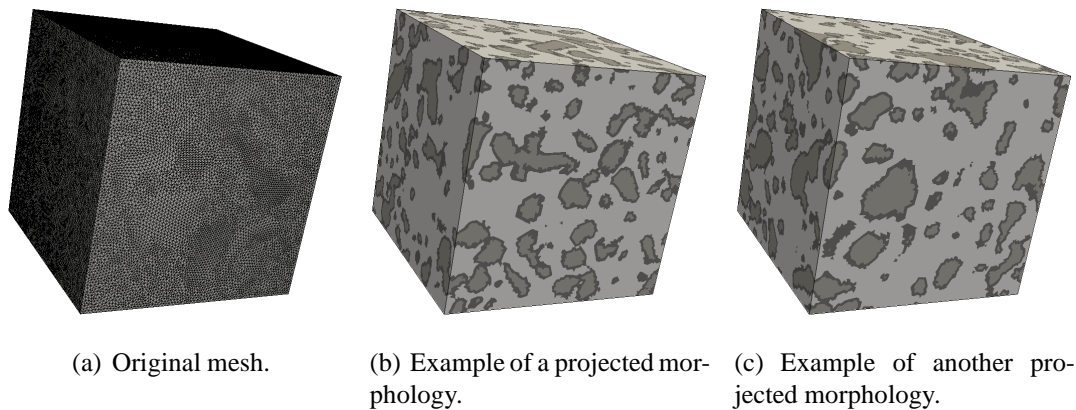


Figure 2.1: Projection of two-phase morphologies on a mesh.

Furthermore, this methodology can be applied to three-dimensional random shapes (not analytically defined), allowing the morphological model based on excursion set (Chapter 1) to fit this context as depicted in FIG. (2.1(b)) and (2.1(c)) (where matrix, inclusion and interface elements are represented in light, medium and dark grey, respectively).

Finally, this distribution of element types brings a very useful additional tool concerning interface modeling. Indeed, for a mechanical problem, the numerical implementation within a FEM context of rigid parts in order to represent *perfect interface* is clearly not a trivial task [Zienkiewicz and Taylor, 2001]. On the contrary, the non-adapted methodology has all the necessary ingredients to achieve this behavior. Indeed, the meshing procedure, through the morphology projection, plays the role of surface locator while weak discontinuities provide a perfect interface behavior.

Crack representation is one of the crucial issue for brittle or quasi-brittle heterogeneous material. Physically speaking, a crack is a discontinuous hypersurface (dimension $n-1$) within a continuum domain of dimension n , herein, a surface in a three-dimensional body. Its growing (or opening) leads to a progressive decay of the traction vector introduced within a FE context by softening laws. The loss of uniqueness of the solution is then

inherent of this softening effect. From this two-dimensional localization of the strain in a band of three-dimensional elements arises the classical problematic of dissipated energy depending on the mesh size. Among the large amount of FE solutions that can be found in the literature, often referred as *localization limiter* or *regularization*, the most popular are: the smeared crack models [Hillerborg, 1991], the gradient approaches [Mindlin and Eshel, 1968], the non-local models [Pijaudier-Cabot and Bažant, 1987] and more recently the kinematics enhancements — weak-strong discontinuity — approaches [Ortiz et al., 1987, Simo et al., 1993]. The key point of localization limiters of the latter kind is that the energy is dissipated onto the two-dimensional surface only, through a specific *kinematical enhancement* of the Finite Elements, eventually leading to a total dissipated energy independent from the mesh size. Henceforth, these approaches offer an overall solution for the two main problems raised by FE cracking modeling namely numerical localization and physical representation (opening and orientation), surely explaining the increasing interest in strong discontinuities over the last decades.

The use of kinematics enhancements within a FE context is a well known problem initially introduced in order to address the crack modeling concern. The natural evolution of this field leads to a broader range of applications, such as material property contrast (heterogeneity) representation for instance. Their implementation can be classified into two main categories known as *global* (nodal) and *local* (element) enhancement approaches. The Extended Finite Elements (X-FEM) [Moës et al., 1999] and Embedded Finite Elements (E-FEM) [Ortiz et al., 1987] are among them the best-known techniques. Studies between these two families of methods have not been the subject of a great deal of researches. However, Oliver [Oliver et al., 2006] recently enlightened the community with an exhaustive review on specific test cases. Conclusions of this study reveal that the two methods produce very similar results, giving a slight advantage to E-FEM regarding computation time. This phenomenon is explained by the inherent local aspect of the latter approach which can be summarized by two key features: light local equation solving (often behavior laws) within each element for fixed global unknowns (displacements) and condensation of the latter information in order to perform the global resolution. On the contrary, by adding global unknowns, X-FEM violates the local-global duality. This deviation from the original FEM spirit leads to adverse effects such as: increase of the global system size and both conditioning — crack representation and structural equilibrium equations of different nature — and structural — sparsity — degradation of the stiffness matrix properties. However, for a small number of enhanced elements, these negative effects can be considered to be negligible but otherwise, may have severe consequences.

Due to the complex shape pattern, implying a large number of enhanced elements, inherent of cement based cracking process and notwithstanding the widespread popularity of X-FEM, the several advantages of the E-FEM approaches and their simple implementation within a FEM context bring the authors to the choice of the latter method to perform this study.

Historically speaking, embedded discontinuities have significantly evolved. As depicted in FIG. (2.2) on triangle elements, weak and strong discontinuities are used in or-

der to represent the kinematics of crack and material property contrast (heterogeneities). On the one hand, regarding the former problematic, the first attempt to model a crack by a *band localization* was made by Michael Ortiz through a single weak discontinuity within several neighbor elements [Ortiz et al., 1987]. Shortly after, in order to represent this band, Ted Belytschko embedded two weak discontinuities within a single element [Belytschko et al., 1988] (see FIG. (2.2(b))). Finally, *localization lines* were introduced by Eduardo N. Dvorkin in [Dvorkin et al., 1990], giving a first solution intrinsically insensitive to mesh size (see FIG. (2.2(c))). On the other hand, in [Hautefeuille et al., 2009], the authors show that a single weak discontinuity gives the possibility for an enhanced element to represent a material heterogeneity.

Following [Benkemoun et al., 2010], the general spirit of the present strategy is to couple both crack and material heterogeneity representation to a coherent framework using embedded elements with strong and weak discontinuities (see FIG. (2.2(d))).

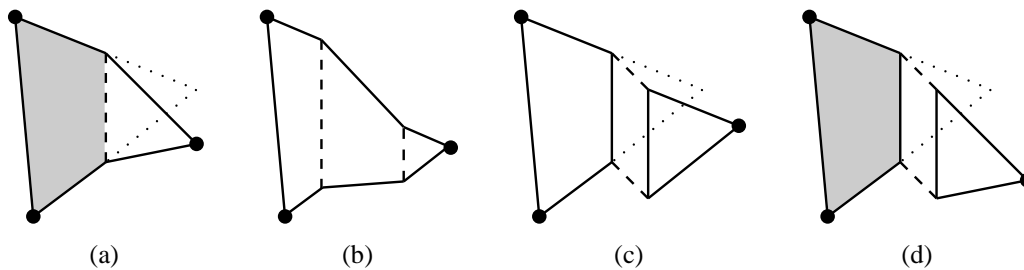


Figure 2.2: From [Jirásek, 2000], element with embedded discontinuity: (a) one weak discontinuity, (b) two weak discontinuities, (c) one strong discontinuity and (d) both weak and strong discontinuity.

In order to present the theoretical basis and the numerical implementation of the present model, this chapter is organized as follows. The first two parts give details on the mathematical representation of the two discontinuities and their integrations in a special variational formulation based on three independent fields. Then the local governing law modeling the crack opening is presented. Finally, the resolution methodology and some explicit applications of the theoretical framework are shown: several FE kinematics developed in this study and their performances are illustrated through representative tension-compression test results.

2 Kinematics of strain and displacement discontinuity

The key point related to the framework presented here is to deal with two kinds of discontinuities: one in the strain field (weak discontinuity), representing material heterogeneity, and one in the displacement field (strong discontinuity), representing a crack — with its orientation and opening — and hence, modeling the degradation mechanism. If the domain Ω represents the whole body considered for the problem, both discontinuities

can be set up anywhere in Ω and, of course, at several places. Naturally, the weak discontinuity is defined by the heterogeneities positions and shapes — and so their geometry is a pure geometrical issue linked to Chapter 1 — whereas the strong discontinuity is not known prior to any calculation and is triggered following a localization criterion. As the whole framework lies into a FE discretization, an interpolation mesh paving Ω is considered and referred to as Ω^h . Finally, in order to use light notations, a single element within the mesh is noted Ω_e (instead of Ω_e^h).

If the failure mechanism is triggered within an element, leading to a crack opening, Ω_e is split in two parts by a discontinuity surface Γ_{du} . In this case, a strong discontinuous kinematics has to be defined. Moreover, because a non-adapted meshing method is used here, another case has to be considered in which the element is taken “near” a material heterogeneity (interface element): the element is still split in two by a discontinuity surface $\Gamma_{d\varepsilon}$ but defined this time by the phase morphology. This leads to a weak discontinuous kinematics modeling. Whatever the type of discontinuity considered (weak, strong or both) in an element, it is assumed that it follows a single discontinuity surface $\Gamma_d = \Gamma_{du} = \Gamma_{d\varepsilon}$ dividing Ω_e into two sub-domains Ω_e^\oplus and Ω_e^\ominus (with $\Omega_e = \Omega_e^\oplus \cup \Omega_e^\ominus$). These points are summarized in FIG. (2.3) in two dimensions, where \mathbf{n} represents the direction vector of the interface. Starting from this vector, an orthonormal basis $(\mathbf{n}, \mathbf{m}, \mathbf{t})$ attached to the surface (often referred to as the local basis) can be built.

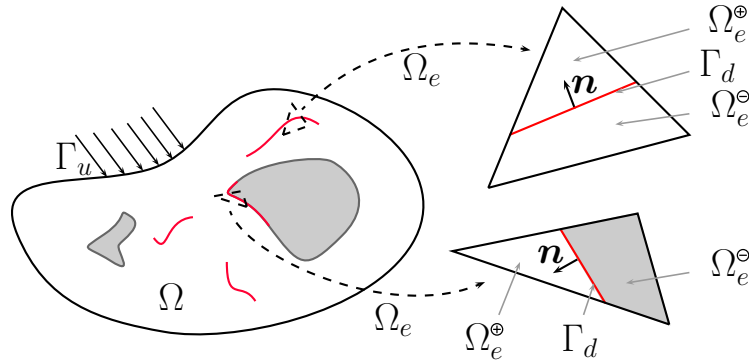


Figure 2.3: Body split by several discontinuity interfaces.

Kinematics relationships that describe both discontinuities are based on generalized functions such as Heaviside or Dirac-delta. These mathematical tools link discontinuous and continuous analysis. Hence, the domain Ω^h can be considered with a traditional variational principal. Both kinematics are handled by strain enhancement and each contribution, supposed independent, is simply added to the standard strain field taken as the symmetric gradient of the displacement field:

$$\varepsilon = \underbrace{\nabla^s \bar{\mathbf{u}}}_{\text{regular}} + \underbrace{\tilde{\varepsilon}}_{\text{weak}} + \underbrace{\hat{\varepsilon}}_{\text{strong}}. \quad (2.1)$$

Thereafter, notation $\tilde{\bullet}$ (resp. $\hat{\bullet}$) refers to weak (resp. strong) discontinuity. Moreover $(\bullet)^\oplus$ (resp. $(\bullet)^\ominus$) means $(\bullet)(\mathbf{x})$, $\mathbf{x} \in \Omega^\oplus$ (resp. Ω^\ominus).

Additionally to the inner difference between the two enhancements, it is important for the physical understanding of the framework to note that, in the case of material heterogeneities presence, the interface is defined by purely geometrical characteristics. It is assumed that, if cracking takes place near those zones, crack opening follows the interface. Considering an homogeneous part of the material, crack orientation is defined along a particular localization criterion (built mainly upon stress considerations).

Since it is assumed that enhanced contributions to the strain field are independent, each kinematics can be treated separately. The next two sections give details on strain and displacement discontinuity kinematics.

2.1 Jump in the strain field

In this section focus is made on the strain field enhancement in order to represent strain discontinuity. This idea can be found in the literature in the pioneer work of [Ortiz et al., 1987] (used to model band localization), in [Sukumar et al., 2001] with the X-FEM method or in [Markovic et al., 2005] with the E-FEM method. In order to represent the kinematics of these problems, the shape of the enhanced part of the strain field labelled as $\tilde{\epsilon}$ is determined with physical considerations on $\tilde{\mathbf{u}}$, the corresponding displacement of $\tilde{\epsilon}$ and its derivatives at the discontinuity interface. Naturally definition of $\tilde{\mathbf{u}}$ depends on the considered sub-domain. Hence both $\tilde{\mathbf{u}}^\oplus$ and $\tilde{\mathbf{u}}^\ominus$ have to be taken into account. At this stage, physical consideration of continuity of this displacement enhancement at the interface vector has to be respected. This yields to:

$$\tilde{\mathbf{u}}^\oplus = \tilde{\mathbf{u}}^\ominus \quad \forall \mathbf{x} \in \Gamma_d. \quad (2.2)$$

A second less trivial consideration is taken on the smoothness of this displacement field. Physically, a discontinuity of the displacement derivatives has to be taken into account only when crossing the interface, following its direction vector \mathbf{n} . In opposition, no discontinuity is present along Γ_d . This leads to the next three conditions at the interface:

$$\begin{cases} \nabla(\tilde{\mathbf{u}}^\oplus) \cdot \mathbf{n} & \neq \nabla(\tilde{\mathbf{u}}^\ominus) \cdot \mathbf{n} \\ \nabla(\tilde{\mathbf{u}}^\oplus) \cdot \mathbf{m} & = \nabla(\tilde{\mathbf{u}}^\ominus) \cdot \mathbf{m} \\ \nabla(\tilde{\mathbf{u}}^\oplus) \cdot \mathbf{t} & = \nabla(\tilde{\mathbf{u}}^\ominus) \cdot \mathbf{t} \end{cases} \quad \forall \mathbf{x} \in \Gamma_d. \quad (2.3)$$

Considerations are now taken on the enhanced displacement field $\tilde{\epsilon}$ and especially its jump $\tilde{\epsilon}^\oplus - \tilde{\epsilon}^\ominus$. The latter can be calculated by taking the symmetrical gradient of the corresponding displacement $\tilde{\mathbf{u}}$. In the local base, it is written:

$$\tilde{\epsilon} = \nabla^s(\tilde{\mathbf{u}}) = \begin{bmatrix} \tilde{u}_{1,n} & \frac{1}{2}(\tilde{u}_{1,m} + \tilde{u}_{2,n}) & \frac{1}{2}(\tilde{u}_{1,t} + \tilde{u}_{3,n}) \\ \text{sym} & \tilde{u}_{2,m} & \frac{1}{2}(\tilde{u}_{2,t} + \tilde{u}_{3,m}) \\ \text{sym} & \text{sym} & \tilde{u}_{3,t} \end{bmatrix}_{(n,m,t)}. \quad (2.4)$$

Following conditions EQ. (2.3), it can be seen that only derivatives of the first component of the displacement ($\tilde{u}_{1,\bullet}$) of $\tilde{\epsilon}^\oplus$ differs from that of $\tilde{\epsilon}^\ominus$. Hence, the strain jump shape

(and especially the number of independent scalar parameters needed to represent it) can be determined by taking the difference between both fields. Henceforth, the strain jump can be expressed:

$$\tilde{\varepsilon}^{\oplus} - \tilde{\varepsilon}^{\ominus} = \begin{bmatrix} [\varepsilon]_n & [\varepsilon]_m & [\varepsilon]_t \\ [\varepsilon]_m & 0 & 0 \\ [\varepsilon]_t & 0 & 0 \end{bmatrix}. \quad (2.5)$$

These discontinuities can therefore be represented by a set of only three parameters $[[\varepsilon]] = \{[\varepsilon]_n \ [\varepsilon]_m \ [\varepsilon]_t\}^T$. Using this set of parameters and respecting EQ. (2.2), the enhanced part of the displacement field can be yielded. The choice is made here to take $\tilde{\mathbf{u}}$ as a first order displacement field [Markovic et al., 2005], hence:

$$\tilde{\mathbf{u}} = \Theta \mathbf{n} \cdot (\mathbf{x} - \boldsymbol{\xi}) ([\varepsilon]_n \mathbf{n} + [\varepsilon]_m \mathbf{m} + [\varepsilon]_t \mathbf{t}) \quad \text{with} \quad \Theta = \begin{cases} \Theta^{\oplus} & \forall \mathbf{x} \in \Omega_e^{\oplus} \\ \Theta^{\ominus} & \forall \mathbf{x} \in \Omega_e^{\ominus} \end{cases}, \quad (2.6)$$

where $\boldsymbol{\xi}$ represents the position of Γ_d and Θ is a still undefined function of Ω_e . Hence, different forms of $\tilde{\mathbf{u}}$ whether it is evaluated in Ω_e^{\oplus} or Ω_e^{\ominus} can be represented. Finally, by taking the symmetrical gradient of EQ. (2.6), the shape of the tensor $\tilde{\varepsilon}$ can be obtained:

$$\tilde{\varepsilon} = \nabla^s(\tilde{\mathbf{u}}) = \Theta \left([\varepsilon]_n \mathbf{n} \otimes \mathbf{n} + \frac{[\varepsilon]_m}{2} (\mathbf{n} \otimes \mathbf{m})^s + \frac{[\varepsilon]_t}{2} (\mathbf{n} \otimes \mathbf{t})^s \right). \quad (2.7)$$

The form of the weak part of EQ. (2.1) is now known, however Θ still has to be exactly defined according to additional statical considerations. It can already noticed that the enhancement brings three parameters — stored in the so-called weak discontinuities vector $[[\varepsilon]]$ — that are future unknowns of the mechanical problem.

2.2 Jump in the displacement field

As for the weak discontinuity kinematics, the strong discontinuity can be constructed separately. Hence, in this section, only a jump in the displacement field is considered. Kinematics of these jumps has been introduced in [Simo et al., 1993] within a FEM framework and further developments can be found in [Simo and Oliver, 1994, Oliver, 1996a, Wells and Sluys, 2001] where numerical implementations are made in two and three-dimensional spaces.

An element Ω_e is still considered to be split by a discontinuity surface Γ_d , representing this time a jump in the displacement field. As for the weak discontinuity, strain enhancement comes from considerations on the displacement field. If $\bar{\mathbf{u}}$ is taken to be a smooth function over Ω_e representing the regular part of the displacement field and $[[\mathbf{u}]]$ a piece-wise constant function representing the displacement jump, this discontinuity can be modeled by decomposing a theoretical displacement field \mathbf{u} into a regular and an enhanced part such as follows:

$$\mathbf{u} = \bar{\mathbf{u}} + \mathcal{H}_{\Gamma_d} [[\mathbf{u}]], \quad (2.8)$$

where \mathcal{H}_{Γ_d} is the Heaviside function centered on Γ_d (unit valued in Ω_e^\oplus and null in Ω_e^\ominus). In a finite element context, interpolation function of this enhancement inevitably leads to ill formulation regarding displacement boundary conditions. Following [Oliver, 1996b] the introduction of an arbitrary continuous function φ_e of unit value at each node in Ω_e^\oplus and null at each node in Ω_e^\ominus can be introduced to overcome this difficulty. By establishing an arbitrary displacement function $\hat{\mathbf{u}}$ as

$$\hat{\mathbf{u}} = \bar{\mathbf{u}} + \varphi_e [|\mathbf{u}|], \quad (2.9)$$

the theoretical displacement field EQ. (2.8) can be re-written:

$$\mathbf{u} = \hat{\mathbf{u}} + (\mathcal{H}_{\Gamma_d} - \varphi_e) [|\mathbf{u}|]. \quad (2.10)$$

EQ. (2.8) and EQ. (2.10) are strictly equivalent. Nevertheless, using the latter eventually leads to an interpolation of $(\mathcal{H}_{\Gamma_d} - \varphi_e)$, which can be done with functions of zero nodal values. Furthermore, the displacement unknowns are $\hat{\mathbf{u}}$ whose nodal values carry the displacement jump information (through φ_e). An example in one dimension with φ_e taken as a linear function is depicted on the following graphs where FIG. (2.4(a)) shows the construction of enhanced part interpolation function and FIG. (2.4(b)) shows the decomposition of the discontinuous displacement \mathbf{u} .

Remarks on strain enhancement: It should be retained that, in this framework, \mathbf{u} is purely theoretical and simply helps the determination of enhanced strain shapes. In a first place, the actual displacement field has been noted $\bar{\mathbf{u}}$, but since strong discontinuity enhancement has implied the introduction of a modified field using φ_e , it is now referred to as $\hat{\mathbf{u}}$ for the rest of the dissertation.

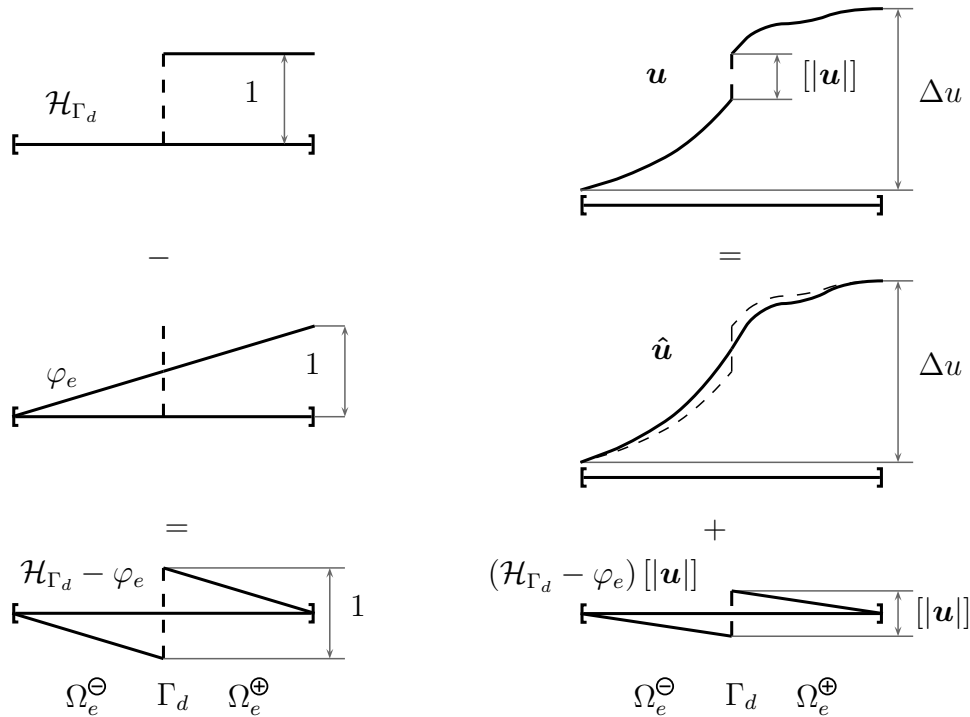
The corresponding strain field can be obtained by taking the symmetric gradient of EQ. (2.10). Non trivial development is made in [Simo and Oliver, 1994] showing that the resulting enhanced strain field can be decomposed into a bounded part $\hat{\boldsymbol{\varepsilon}}_b$ and an unbounded one $\hat{\boldsymbol{\varepsilon}}_u$, using the Dirac-delta distribution δ centered at the interface:

$$\nabla^s \mathbf{u} = \boldsymbol{\varepsilon} = \underbrace{\nabla^s \hat{\mathbf{u}}}_{\text{regular}} + \underbrace{(\mathcal{H}_{\Gamma_d} - \varphi_e) \nabla^s (|\mathbf{u}|) - (|\mathbf{u}| \otimes \nabla \varphi_e)^s}_{\text{bounded enhancement}} + \underbrace{\delta_{\Gamma_d} (|\mathbf{u}| \otimes \mathbf{n})^s}_{\text{unbounded enhancement}}. \quad (2.11)$$

Finally, $|\mathbf{u}|$ is taken to be a constant function. Under this consideration it can therefore be seen as a vector containing the displacement discontinuity components (*i.e.* the crack). Moreover, it leads to a simplified version of the previous equation, EQ. (2.12), giving the explicit kinematics form of the enhanced strain field. Hereafter, this enhancement is referred to as *Kinematically Enhanced Strain* (KES).

Kinematically Enhanced Strain (KES)

$$\hat{\boldsymbol{\varepsilon}} = \hat{\boldsymbol{\varepsilon}}_b + \hat{\boldsymbol{\varepsilon}}_u = -(|\mathbf{u}| \otimes \nabla \varphi_e)^s + \delta_{\Gamma_d} (|\mathbf{u}| \otimes \mathbf{n})^s. \quad (2.12)$$



(a) Decomposition of the enhancement function (b) Decomposition of the discontinuous displacement function

Figure 2.4: From [Oliver, 1996b]: one dimensional representation of discontinuous displacement decomposition.

The bounded part of the strain has been explicitly defined using the arbitrary function φ_e . However the variational formulation hypothesis based on a statical point of view (see next section) leads to another shape referred to as *Enhanced Assumed Strain* (EAS). Hence, whether considerations are made on a statical or kinematics point of view, strong discontinuity strain enhancement differs. In order to avoid any mix-up, it is already stated that: in the variational formulation, *actual* strain field is enhanced using KES in order to represent meaningful kinematics whereas that of the *virtual* is enhanced using the EAS method. Discussions on that point and impact on modeling properties (robustness, mesh dependency, *etc.*) are made later. Anyway, the kinematics representation of displacement discontinuity leads to another set of unknowns stored in the vector $[[u]]$ representing the crack opening. Due to its physical meaning, this vector is a main component of the failure mechanism. It is presented below how it models a local brittle behavior through a so-called *traction-separation law*.

A first remark can be made regarding the *unbounded* part of the strong enhancement. In these cases, properties such as continuity of the traction vector at the interface seem impossible to fulfill. Nevertheless, several possibilities for their numerical implementation within a FE context are available. The next section briefly lists these solutions.

2.3 Strong discontinuity analysis

The term *strong discontinuity analysis* seems to appear for the first time in [Simo et al., 1993] and then in [Armero and Garikipati, 1996]. The concept of this analysis is to ensure that the constitutive models used are still *consistent* once strong discontinuities are enabled. Several requirements can be imposed on the stress field. Among them:

- (1) the stress field has to be bounded over Ω_e
- (2) continuity of the traction vector has to be respected on the surface Γ_d

In view of these statements, two main solutions can be found in the literature:

Continuum Strong Discontinuity Approach (CSDA)

The main idea of this class of solutions is to keep using continuum constitutive laws (plasticity, damage, *etc.*) over Ω_e . Inspired by the *discontinuous Galerkin* Finite Element Methods, the Dirac-delta distribution is k -regularized in order to keep interpolation functions smooth enough. In [Simo et al., 1993], authors also change the mathematical basis of the softening law, making the plastic softening modulus a distribution itself. They show that when $k \rightarrow 0$ (computer limit), the finite element approximation has the same structure as in a standard Galerkin procedure but with modified shape functions. Full development can be found in [Oliver, 1996b, Oliver et al., 2002].

Discrete Strong Discontinuity Approach (DSDA)

It has been shown in [Oliver, 2000] and [Brancherie, 2003] that a continuum model equipped with strong discontinuity induces an underlying complete discrete model at the discontinuity. A so-called *traction-separation* law, linking the traction vector to the crack-opening can be defined on Γ_d whereas a standard continuum relationship between strain and stress fields runs the behavior in $\Omega_e \setminus \Gamma_d$. Introduced by [Armero and Garikipati, 1996] this method has spread around and can also be seen in [Wells and Sluys, 2001, Dias-da Costa et al., 2009a, Dias-da Costa et al., 2009b]. It is in this specific framework that the presented study stands.

Both weak and strong discontinuity kinematics have been treated in this section leading to a global shape of the strain enhancement EQ. (2.1). However several components of this representation still remain to be determined. The form of Θ and $\hat{\gamma}_b$ (which is the bounded part of the *virtual* strain field strong enhancement) are determined so that it respects some assumptions made through the variational formulation of the next section. Additional unknowns provided by this modeling, $[[\varepsilon]]$ and $[[\mathbf{u}]]$, are additional unknowns of the mechanical problem. Therefore, compared to standard formulations, additional equations are needed. The unified three-field variational principle [Washizu, 1982] is used in this framework and applied to this specific enhancement in the following section.

3 Variational formulation

Since it has been seen many times in the literature, it is the author choice to keep the writing as light and simple as possible, emphasizing only the several strong assumptions made and their consequences, for the sake of the reading.

3.1 Three-field variational formulation

In contrast to standard displacement formulations, where the equilibrium equation is expressed in its weak form, the Hu-Washizu [Washizu, 1982] three-field variational formulation provides a suitable unified mathematical statement for enhanced FE kinematics. The main idea is to consider displacement, stress and strain field — noted $\hat{\mathbf{u}}$, $\boldsymbol{\sigma}$ and $\boldsymbol{\varepsilon}$, respectively — as independent. Hence, each fundamental equations of the mechanical problem are formulated in their weak form, using three corresponding virtual fields — noted $\hat{\boldsymbol{\eta}}$, $\boldsymbol{\tau}$ and $\boldsymbol{\gamma}$, respectively. The variational statement of the *equilibrium equation* of the stress field, the *kinematics relationship* between the strain and displacement field and *constitutive model* — EQ. (2.13a), EQ. (2.13b) and EQ. (2.13c), respectively — are expressed as follows:

Three-field variational formulation

Find $(\hat{\mathbf{u}}, \boldsymbol{\varepsilon}, \boldsymbol{\sigma}) \in (\mathcal{V}, \mathcal{E}, \mathcal{T})$ so that $\forall (\hat{\boldsymbol{\eta}}, \boldsymbol{\gamma}, \boldsymbol{\tau}) \in (\mathcal{V}_0, \mathcal{E}, \mathcal{T})$:

$$\text{HW}_{\hat{\mathbf{u}}}(\hat{\mathbf{u}}, \boldsymbol{\varepsilon}, \boldsymbol{\sigma}; \hat{\boldsymbol{\eta}}) = \int_{\Omega} \nabla^s \hat{\boldsymbol{\eta}} : \boldsymbol{\sigma} \, d\Omega - \int_{\Omega} \hat{\boldsymbol{\eta}} \cdot \rho \mathbf{b} \, d\Omega - \int_{\Gamma_t} \hat{\boldsymbol{\eta}} \cdot \underline{\mathbf{t}} \, d\partial\Omega = 0, \quad (2.13a)$$

$$\text{HW}_{\boldsymbol{\sigma}}(\hat{\mathbf{u}}, \boldsymbol{\varepsilon}, \boldsymbol{\sigma}; \boldsymbol{\tau}) = \int_{\Omega} \boldsymbol{\tau} : (\nabla^s \hat{\mathbf{u}} - \boldsymbol{\varepsilon}) \, d\Omega = 0, \quad (2.13b)$$

$$\text{HW}_{\boldsymbol{\varepsilon}}(\hat{\mathbf{u}}, \boldsymbol{\varepsilon}, \boldsymbol{\sigma}; \boldsymbol{\gamma}) = \int_{\Omega} \boldsymbol{\gamma} : (\check{\boldsymbol{\sigma}}(\boldsymbol{\varepsilon}) - \boldsymbol{\sigma}) \, d\Omega = 0, \quad (2.13c)$$

with

$$\begin{aligned} \mathcal{V} &= \{\hat{\mathbf{u}} \mid \hat{\mathbf{u}} \in H^1(\Omega), \hat{\mathbf{u}} = \underline{\mathbf{u}} \text{ on } \Gamma_u\}, \mathcal{V}_0 = \{\hat{\mathbf{u}} \mid \hat{\mathbf{u}} \in H^1(\Omega), \hat{\mathbf{u}} = \mathbf{0} \text{ on } \Gamma_u\} \\ \mathcal{E} &= \{\boldsymbol{\varepsilon} \mid \boldsymbol{\varepsilon} \in L^2(\Omega)\} \text{ and } \mathcal{T} = \{\boldsymbol{\sigma} \mid \boldsymbol{\sigma} \in L^2(\Omega)\}, \end{aligned}$$

where $\underline{\mathbf{t}}$ is the traction vector imposed on the Neumann surface Γ_t , $\rho \mathbf{b}$ the internal force and $\check{\boldsymbol{\sigma}}$ a stress field that respects the constitutive law on Ω . Notice that in usual displacement formulations both kinematics relationship and constitutive model are supposed to be verified in a strong sense, *i.e.* $\boldsymbol{\sigma} = \check{\boldsymbol{\sigma}}(\boldsymbol{\varepsilon})$ and $\boldsymbol{\varepsilon} = \nabla^s \hat{\mathbf{u}}$, making EQ. (2.13b) and EQ. (2.13c) irrelevant.

On the one hand, additional unknowns have been brought by kinematics enhancements and on the other hand, the presented formulation brings additional equations to the system. However, it remains many ways to solve it. Since literature is well documented

on the matter, the different possibilities are simply enunciated, focusing only on the critical points. Full description of the methods can be found in [Jirásek, 2000] and in the other citations that follow.

Two major solutions of enhancement (based on the one hand, on statical considerations and on the other hand, on kinematics considerations) assist in the resolution of the Hu-Washizu formulation system. Notice that at this stage, a discretization is necessary and equations have to be considered within a finite element context.

Statically Optimal Symmetric Formulation (SOS)

First SOS formulation can be found in [Belytschko et al., 1988]. Then, this work has been enhanced by a great deal of contributions over the next decades. Among them: [Larsson et al., 1996, Armero and Garikipati, 1996, Sluys and Berends, 1998]. The main idea of this method is to consider that the interpolation of the displacement field is *not* enhanced. Basically, it results in a compatibility condition between the stress interpolation matrix and the enhanced strain. An important assumption of L_2 -orthogonality is made between the virtual strain field and the actual stress field. Under this assumption, the latter vanishes from the formulation, eventually leading to a so-called zero mean condition onto the enhanced part of the strain field $\int_{\Omega} \tilde{\varepsilon} d\Omega = \mathbf{0}$ and $\int_{\Omega} \hat{\varepsilon} d\Omega = \mathbf{0}$. Hence, the still unknown shape of the enhanced part can be determined. Based on purely statical considerations (patch test), a construction of the interpolation matrix of strain enhancement respecting the zero mean condition brings continuity to the stress field. Furthermore and due to the fact that strain fields and their variations are interpolated the same way, the resulting matrix of the system is proved to be symmetrical. The major drawback of this enhancement construction is the lack of kinematical meaning. Indeed, no discontinuities (weak nor strong) are kinematically represented.

Kinematically Optimal Symmetric Formulation (KOS)

The lack of kinematical representation can be dealt with by modifying the enhanced interpolation process. Although for SOS it directly derives from the three-field formulation, KOS proposes to construct it regarding only a meaningful description of discontinuity kinematics [Lotfi and Shing, 1995]. Hence, displacement field is enhanced by a suitable interpolation matrix. The corresponding strain is therefore deduced, applying the symmetrical kinematics operator ∇^s . It occurs that the resulting system is strictly identical to the one obtained by using SOS formulation (stress field deleted from the equations and symmetric matrix system). The only differences reside in the construction of the enhanced strain part interpolation. Herein, the zero mean condition is *not* respected but kinematics of discontinuities are well represented.

Statically and Kinematically Optimal Nonsymmetric Formulation (SKON)

First brought out in [Dvorkin et al., 1990], followed by Simo in [Simo and Oliver, 1994] and fully developed by Oliver in [Oliver, 1996a] (but not called so at the time), the SKON formulation takes the advantages of both methods. Actual and

virtual strain fields are not interpolated the same way. When the latter respects the zero mean condition of SOS formulation, the suitable representation of discontinuity kinematics is chosen for standard enhanced strain field (KOS). Leading inevitably to a non symmetrical system.

In the next section, the three-field formulation system is described using the *Enhanced Assumed Strain method* developed in [Simo and Rifai, 1990] and adapted here to the double enhancement framework.

3.2 Assumed strain and double enhancement

Following the spirit of mixed formulations, the presented framework is build using the *Enhanced Assumed Strain method* (EAS). In [Wilson and Ibrahimbegović, 1990], the displacement field is enhanced, eliminating the compatibility restriction. It was one of the pioneer work using the relaxed restriction of the patch test [Irons and Razzaque, 1972, Strang and Fix, 1973] over displacement compatibility. The authors added then a correction matrix to the resulting enhanced strain in order to pass the zero mean condition. Herein, following [Ibrahimbegović and Wilson, 1991] and SOS/KOS formulation, enhancement is made directly into the strain field. It is shown that, by making the enhancement part orthogonal to virtual stress field, SKON formulation can be retrieved. This section describes the method with both weak and strong discontinuities recently introduced by [Benkemoun et al., 2010].

The formulation derives from the three-field formulation of Hu-Washizu SYS. (2.13). As in SOS formulation only strain fields are enhanced. The first assumption is that both actual and variational fields are enhanced the same way, by adding to standard kinematics operator an enhanced part for each discontinuity EQ. (2.14). As fairly reminded in [Simo and Rifai, 1990], *in a finite element context, the enhanced part of ε is not subject to any inter element continuity requirements*. Hence, strain fields can be yielded as follows:

$$\varepsilon = \underbrace{\nabla^s \hat{u}}_{\text{standard}} + \underbrace{\tilde{\varepsilon}}_{\text{weak}} + \underbrace{\hat{\varepsilon}}_{\text{strong}} \quad \text{and} \quad \gamma = \underbrace{\nabla^s \hat{\eta}}_{\text{standard}} + \underbrace{\tilde{\gamma}}_{\text{weak}} + \underbrace{\hat{\gamma}}_{\text{strong}}, \quad (2.14)$$

enhancement
enhancement

where $(\hat{u}, \tilde{\varepsilon}, \hat{\varepsilon})$ (resp. $(\hat{\eta}, \tilde{\gamma}, \hat{\gamma})$) are taken to be independent variables. Note that the $\hat{\gamma}$ follows the global shape of $\hat{\varepsilon}$ defined EQ. (2.12). Then, by substituting EQ. (2.14) into

SYS. (2.13) the system of equations SYS. (2.15) can easily be casted:

$$\int_{\Omega} \nabla^s \hat{\boldsymbol{\eta}} : \boldsymbol{\sigma} \, d\Omega - \int_{\Omega} \hat{\boldsymbol{\eta}} \cdot \rho \mathbf{b} \, d\Omega - \int_{\Gamma_t} \hat{\boldsymbol{\eta}} \cdot \underline{\mathbf{t}} \, d\partial\Omega = 0, \quad (2.15a)$$

$$\int_{\Omega} \boldsymbol{\tau} : \tilde{\boldsymbol{\varepsilon}} \, d\Omega = 0, \quad (2.15b)$$

$$\int_{\Omega} \boldsymbol{\tau} : \hat{\boldsymbol{\varepsilon}} \, d\Omega = 0, \quad (2.15c)$$

$$\int_{\Omega} \nabla^s \hat{\boldsymbol{\eta}} : (\check{\boldsymbol{\sigma}} (\nabla^s \hat{\mathbf{u}} + \tilde{\boldsymbol{\varepsilon}} + \hat{\boldsymbol{\varepsilon}}) - \boldsymbol{\sigma}) \, d\Omega = 0, \quad (2.15d)$$

$$\int_{\Omega} \tilde{\boldsymbol{\gamma}} : (\check{\boldsymbol{\sigma}} (\nabla^s \hat{\mathbf{u}} + \tilde{\boldsymbol{\varepsilon}} + \hat{\boldsymbol{\varepsilon}}) - \boldsymbol{\sigma}) \, d\Omega = 0, \quad (2.15e)$$

$$\int_{\Omega} \hat{\boldsymbol{\gamma}} : (\check{\boldsymbol{\sigma}} (\nabla^s \hat{\mathbf{u}} + \tilde{\boldsymbol{\varepsilon}} + \hat{\boldsymbol{\varepsilon}}) - \boldsymbol{\sigma}) \, d\Omega = 0. \quad (2.15f)$$

EQ. (2.15b) and (2.15c) show the need of enhancement parts to be constructed L_2 -orthogonally to the virtual stress, as mentioned previously. It is recalled that assumption is made that virtual enhancement is constructed the same way as the actual one. Therefore $\tilde{\boldsymbol{\gamma}}$ and $\hat{\boldsymbol{\gamma}}$ are taken L_2 -orthogonal to $\boldsymbol{\sigma}$ leading to a simplification of EQ. (2.15e) and EQ. (2.15f) making the stress vanishes from the whole system. These considerations lead to the following modified three-field variational formulation:

$$\int_{\Omega} \nabla^s \hat{\boldsymbol{\eta}} : \check{\boldsymbol{\sigma}} (\nabla^s \hat{\mathbf{u}} + \tilde{\boldsymbol{\varepsilon}} + \hat{\boldsymbol{\varepsilon}}) \, d\Omega - \int_{\Omega} \hat{\boldsymbol{\eta}} \cdot \rho \mathbf{b} \, d\Omega - \int_{\Gamma_t} \hat{\boldsymbol{\eta}} \cdot \underline{\mathbf{t}} \, d\partial\Omega = 0, \quad (2.16a)$$

$$\int_{\Omega_e} \tilde{\boldsymbol{\gamma}} : \check{\boldsymbol{\sigma}} (\nabla^s \hat{\mathbf{u}} + \tilde{\boldsymbol{\varepsilon}} + \hat{\boldsymbol{\varepsilon}}) \, d\Omega = 0, \quad (2.16b)$$

$$\int_{\Omega_e} \hat{\boldsymbol{\gamma}} : \check{\boldsymbol{\sigma}} (\nabla^s \hat{\mathbf{u}} + \tilde{\boldsymbol{\varepsilon}} + \hat{\boldsymbol{\varepsilon}}) \, d\Omega = 0. \quad (2.16c)$$

Since no inter element continuity is required, the L_2 -orthogonal conditions are applied on each elements independently. Hence, the last two equations are evaluated on Ω_e for each element $e = [1..n_{el}]$. To keep the notation as light as possible, the geometrical properties of each element is noted without this e subscript. For example, V refers to the volume of Ω_e and not V_e as it should be.

The third idea of EAS is to insure that an enhanced element still satisfies the patch test (ensuring convergence of the method) after imposing the orthogonal condition. Hence, the stress field must at least include piece-wise constant function [Simo and Rifai, 1990]. Mathematically speaking, it implies the following zero mean conditions onto the virtual strain enhancement:

$$\int_{\Omega_e} \tilde{\boldsymbol{\gamma}} \, d\Omega = 0 \quad \text{and} \quad \int_{\Omega_e} \hat{\boldsymbol{\gamma}} \, d\Omega = 0. \quad (2.17)$$

Even though kinematics of jumps into strain and displacement fields have been defined in the previous section, several parameters remained unknown such as the shape of Θ or

$\hat{\gamma}_b$. They can now be defined regarding the zero mean conditions of SYS. (2.17). Starting with the weak enhancement, the condition is written:

$$\int_{\Omega_e^\oplus} \tilde{\gamma}^\oplus d\Omega + \int_{\Omega_e^\ominus} \tilde{\gamma}^\ominus d\Omega = \mathbf{0}. \quad (2.18)$$

Further development can be done by considering the kinematics definition made EQ. (2.7). Assumption is made that the interface Γ_d is flat — meaning that \mathbf{n} is constant — over Ω_e and that $\tilde{\gamma}^\oplus$ (resp. $\tilde{\gamma}^\ominus$) is constant by part over Ω_e^\oplus (resp. Ω_e^\ominus). Integration can therefore easily be done, giving condition on Θ :

$$\Theta^\oplus V^\oplus + \Theta^\ominus V^\ominus = 0. \quad (2.19)$$

The choice made here is to take

$$\Theta^\oplus = \frac{V^\ominus}{V} \quad \text{and} \quad \Theta^\ominus = -\frac{V^\oplus}{V}. \quad (2.20)$$

Integration of the zero mean condition applied to EQ. (2.12) gives the shape of the bounded part of the strong enhancement. Also, it is recalled that for a smooth enough function ϕ : $\int_{\Omega} \delta_{\Gamma} \phi d\Omega = \int_{\Gamma} \phi d\Gamma$. Hence, the condition on $\hat{\gamma}$ can be written:

$$\int_{\Omega} \hat{\gamma}_b d\Omega + \int_{\Gamma_d} ([[\boldsymbol{\eta}]] \otimes \mathbf{n})^s d\Omega = \mathbf{0}. \quad (2.21)$$

The same assumption of constant value of \mathbf{n} is also made, giving the possibility of integration. It finally gives the bounded part of EAS:

$$\hat{\gamma}_b = -\frac{A}{V} ([[\boldsymbol{\eta}]] \otimes \mathbf{n})^s. \quad (2.22)$$

The complete shape of the strong discontinuity can now be given by adding to $\hat{\gamma}_b$ the unbounded part defined EQ. (2.12). This leads to:

Enhanced Assumed Strain (EAS)

$$\hat{\gamma} = \left(\delta_{\Gamma_d} - \frac{A}{V} \right) ([[\boldsymbol{\eta}]] \otimes \mathbf{n})^s. \quad (2.23)$$

In this section, a modified three-field formulation has been obtained (SYS. (2.16)) in a double strain enhancement context following the EAS method. This leads to a form of both weak and strong enhancement strain defining explicitly $\tilde{\gamma}$ through Θ EQ. (2.19) and $\hat{\gamma}$ through its bounded part $\hat{\gamma}_b$ EQ. (2.23). Notice that these results come from zero mean conditions on virtual fields. It is assumed that the weak enhanced part of actual field $\tilde{\boldsymbol{\varepsilon}}$ is constructed in the same way whereas that of the strong enhancement $\hat{\boldsymbol{\varepsilon}}$ is constructed using KES EQ. (2.12). Hence, the method fits in the SKON framework. At this point it is not necessary to push further SYS. (2.16). Specific developments with discretized fields are now made in the Embedded Finite Element context.

3.3 Finite Element interpolation

The presented approach is based on DSDA (presented §2.3). Hence, the actual discretized strain field ε (now in Voigt notation) is defined by only keeping the bounded part of the enhancement. On the contrary, due to its different role in the formulation, the virtual field is kept fully enhanced (and therefore unbounded). It is recalled that no k -regularization is made but since the unbounded part does not involve strains-stress relationship $\check{\sigma}(\varepsilon)$ the system can be solved due to integral properties of the Dirac-delta distribution. It occurs that enhancing both actual and virtual strain fields this way gives useful information on the traction vector at the discontinuity surface.

The enhanced strain fields are discretized as follows:

$$\varepsilon = \{\varepsilon_{xx} \ \varepsilon_{yy} \ \varepsilon_{zz} \ 2\varepsilon_{xy} \ 2\varepsilon_{yz} \ 2\varepsilon_{xz}\}^T = \underbrace{\mathbf{B} \mathbf{d}}_{\nabla^s \hat{\mathbf{u}}} + \underbrace{\mathbf{G}_w [|\varepsilon|]}_{\hat{\varepsilon}} + \underbrace{\mathbf{G}_s [|\mathbf{u}|]}_{\hat{\varepsilon}_b}, \quad (2.24a)$$

$$\gamma = \{\gamma_{xx} \ \gamma_{yy} \ \gamma_{zz} \ 2\gamma_{xy} \ 2\gamma_{yz} \ 2\gamma_{xz}\}^T = \underbrace{\mathbf{B} \boldsymbol{\delta}}_{\nabla^s \hat{\boldsymbol{\eta}}} + \underbrace{\mathbf{G}_w [|\gamma|]}_{\hat{\gamma}} + \underbrace{\mathbf{G}_s^* [|\boldsymbol{\eta}|]}_{\hat{\gamma}}, \quad (2.24b)$$

where several interpolation matrices introduced correspond to: \mathbf{B} ($= \partial \mathbf{N}$) the standard strain interpolation matrix, \mathbf{G}_w the actual and virtual field corresponding to the weak discontinuity, \mathbf{G}_s the actual field corresponding to the strong discontinuity (bounded) and \mathbf{G}_s^* the virtual field corresponding to the strong discontinuity part (unbounded). The star notation (*) refers to EAS where no up-script refers to KES. The vector \mathbf{d} contains the nodal displacements and $[|\varepsilon|]$ (resp. $[|\mathbf{u}|]$) corresponds to the additional unknowns brought by the kinematics enhancement of weak (resp. strong) discontinuities.

Regarding EQ. (2.7), \mathbf{G}_w can be decomposed into Θ and a constant part \mathbf{H}_w that only carry information on the interface vector \mathbf{n} :

$$\mathbf{G}_w = \begin{cases} \mathbf{G}_w^\oplus = \Theta^\oplus \mathbf{H}_w = \frac{V^\ominus}{V} \mathbf{H}_w & \text{in } \Omega_e^\oplus \\ \mathbf{G}_w^\ominus = \Theta^\ominus \mathbf{H}_w = -\frac{V^\oplus}{V} \mathbf{H}_w & \text{in } \Omega_e^\ominus \end{cases}, \quad (2.25)$$

The KES interpolation matrix \mathbf{G}_s can be constructed by explicitly defining the arbitrary function φ_e of EQ. (2.12). The idea is to construct a function that links the displacement at the discontinuity only to one side in order to “separate” nodes in Ω_e^\oplus from nodes in Ω_e^\ominus . It can be seen as a rigid body motion (within an element) of a sub-domain along the direction of the crack opening. The function φ_e can be defined with unit values at each nodes of Ω_e^\oplus , and zero at the others. Hence, it can be constructed with standard first order interpolation shape functions:

$$\varphi_e(\mathbf{x}) = \sum_{a=1}^{n_{\text{en}}} \mathbf{N}_a p_a \quad \text{with} \quad p_a = \begin{cases} 1 & \text{if node number } a \in \Omega_e^\oplus \\ 0 & \text{if node number } a \in \Omega_e^\ominus \end{cases}, \quad (2.26)$$

where n_{en} is the number of nodes in the element and p_a the nodal values of φ_e . \mathbf{G}_s is therefore the equivalent symmetric operator $(\bullet \otimes \nabla(\varphi_e))^s$ in the Voigt notation of EQ. (2.24a).

Finally, from the definition of EAS EQ. (2.23), \mathbf{G}_s^* can be decomposed in a bounded $\mathbf{G}_{s,b}^*$ and an unbounded $\mathbf{G}_{s,u}^*$ part. Thus leads to:

$$\mathbf{G}_s^* = \mathbf{G}_{s,b}^* + \mathbf{G}_{s,u}^* = \left(-\frac{A}{V} + \delta_{\Gamma_d} \right) \mathbf{H}_s^*, \quad (2.27)$$

where \mathbf{H}_s^* is the equivalent symmetric operator $(\bullet \otimes \mathbf{n})^s$ in the Voigt notation of EQ. (2.24b).

The behavior in $\Omega_e \setminus \Gamma_d$ (within a finite element e) remains elastic and since material properties can differ whether evaluated in Ω_e^\oplus or Ω_e^\ominus , the behavior law is written:

$$\check{\boldsymbol{\sigma}}(\mathbf{d}, [|\boldsymbol{\varepsilon}|], [|\mathbf{u}|]) = \begin{cases} \mathbf{C}^\oplus \boldsymbol{\varepsilon}^\oplus = \mathbf{C}^\oplus \left(\mathbf{B}\mathbf{d} + \mathbf{G}_w^\oplus [|\boldsymbol{\varepsilon}|] + \mathbf{G}_s [|\mathbf{u}|] \right) & \text{in } \Omega_e^\oplus, \\ \mathbf{C}^\ominus \boldsymbol{\varepsilon}^\ominus = \mathbf{C}^\ominus \left(\mathbf{B}\mathbf{d} + \mathbf{G}_w^\ominus [|\boldsymbol{\varepsilon}|] + \mathbf{G}_s [|\mathbf{u}|] \right) & \text{in } \Omega_e^\ominus. \end{cases} \quad (2.28)$$

By injecting EQ. (2.24b) and EQ. (2.28) in SYS. (2.16) SKON formulation is retrieved. After a little work on EQ. (2.16c),

$$\begin{aligned} & \int_{\Omega_e} \mathbf{G}_s^{*,T} \check{\boldsymbol{\sigma}}(\mathbf{d}, [|\boldsymbol{\varepsilon}|], [|\mathbf{u}|]) d\Omega, \\ &= \int_{\Omega_e \setminus \Gamma_d} \mathbf{G}_{s,b}^{*,T} \check{\boldsymbol{\sigma}}(\mathbf{d}, [|\boldsymbol{\varepsilon}|], [|\mathbf{u}|]) d\Omega + \int_{\Omega_e} \mathbf{G}_{s,u}^{*,T} \check{\boldsymbol{\sigma}}(\mathbf{d}, [|\boldsymbol{\varepsilon}|], [|\mathbf{u}|]) d\Omega, \\ &= \int_{\Omega_e \setminus \Gamma_d} \mathbf{G}_{s,b}^{*,T} \check{\boldsymbol{\sigma}}(\mathbf{d}, [|\boldsymbol{\varepsilon}|], [|\mathbf{u}|]) d\Omega + \int_{\Gamma_d} \mathbf{H}_s^{*,T} \check{\boldsymbol{\sigma}}(\mathbf{d}, [|\boldsymbol{\varepsilon}|], [|\mathbf{u}|]) d\partial\Omega, \\ &= \int_{\Omega_e \setminus \Gamma_d} \mathbf{G}_{s,b}^{*,T} \check{\boldsymbol{\sigma}}(\mathbf{d}, [|\boldsymbol{\varepsilon}|], [|\mathbf{u}|]) d\Omega + \int_{\Gamma_d} \mathbf{T}(\mathbf{d}, [|\boldsymbol{\varepsilon}|], [|\mathbf{u}|]) d\partial\Omega, \end{aligned}$$

where

$$\mathbf{T} = \underbrace{\check{\boldsymbol{\sigma}} \cdot \mathbf{n}}_{\text{matrix notation}} = \underbrace{\mathbf{H}_s^{*,T} \check{\boldsymbol{\sigma}}}_{\text{Voigt notation}}, \quad (2.29)$$

is the traction vector, and by considering the variational system of the discretized FE framework applied to n_{el} elements, the system SYS. (2.30) can be obtained.

Discretized system

$$\left. \begin{aligned} & \sum_{e=1}^{n_{el}} \{ \mathbf{f}_{int}^e - \mathbf{f}_{ext}^e \} = \mathbf{0} \quad \text{with} \quad \mathbf{f}_{int}^e = \int_{\Omega_e} \mathbf{B}^T \check{\boldsymbol{\sigma}}(\mathbf{d}, [|\boldsymbol{\varepsilon}|], [|\mathbf{u}|]) d\Omega, \end{aligned} \right\} \quad (2.30a)$$

$$\left. \begin{aligned} & \mathbf{h}_{[|\boldsymbol{\varepsilon}|]} = \int_{\Omega_e} \mathbf{G}_w^T \check{\boldsymbol{\sigma}}(\mathbf{d}, [|\boldsymbol{\varepsilon}|], [|\mathbf{u}|]) d\Omega = \mathbf{0} \quad \forall e \in [1 .. n_{el}], \end{aligned} \right\} \quad (2.30b)$$

$$\left. \begin{aligned} & \mathbf{h}_{[|\mathbf{u}|]} = \int_{\Omega_e \setminus \Gamma_d} \mathbf{G}_{s,b}^{*,T} \check{\boldsymbol{\sigma}}(\mathbf{d}, [|\boldsymbol{\varepsilon}|], [|\mathbf{u}|]) d\Omega + \int_{\Gamma_d} \mathbf{T} d\partial\Omega = \mathbf{0} \quad \forall e \in [1 .. n_{el}]. \end{aligned} \right\} \quad (2.30c)$$

The EAS method presented above leads to a Dirac-delta distribution within the enhanced virtual strain field $\hat{\gamma}$ and imposing the zero mean condition grants, in a weak sense, to the traction vector continuity condition EQ. (2.30c). Virtual strain field has therefore been formulated from *statical* considerations. It is well known that, FE calculation involving strain softening are sensitive to mesh alignment. However, as it is discussed in [Jirásek, 2000] the kinematical based enhancement (KES) overcomes this problem. Herein, a relative displacement between nodes in Ω_e^\oplus and Ω_e^\ominus is taken into account by interpolating the actual field $\hat{\varepsilon}$ with φ_e . The counterpart of this consideration is that zero mean condition usually fails in these cases. Combining advantages of both EAS and KES is the spirit of the SKON formulation presented in this section.

At the moment, the development of SYS. (2.30) is stopped. Linearization, resolution method and applications to specific FE kinematics are concerns of the last section of this chapter. In the next section, attention is placed on the discrete model used at the interface.

4 Discrete model at the discontinuity

The mechanical description of meso-scale relies on the phenomenological law governing the failure mechanism. In this framework, a continuum model that represents localization zone of high strain by introducing a discontinuity is used. As presented above, this discontinuity leads to an element split into two sub domains ($\Omega_e = \Omega_e^\oplus \cup \Omega_e^\ominus$) separated by an interface Γ_d . This separation is described by a discontinuity within the displacement field (mathematically speaking: an Heaviside). Hence, it naturally represents material degradation through a crack opening mechanism. As the whole framework fits in the Discrete Strong Discontinuity Approach, two behaviors have to be considered. First regarding continuum parts. Ω_e^\oplus and Ω_e^\ominus are considered elastic which is a rather strong assumption justified by the general spirit of simple meso-scale modeling. Even if not done here, more complex behaviors such as plasticity or damage can be implemented (see [Oliver, 1996a] for details). The second part of the modeling is located at the discontinuity surface. A governing law that links the traction vector $\mathbf{T} = \boldsymbol{\sigma}|_{\Gamma_d} \cdot \mathbf{n}$ defined on the surface with the crack opening $[|\mathbf{u}|]$ performs the non linear failure mechanism. These laws are often referred to as *traction-separation* laws.

In order to fit the general spirit of *simple* meso-scale modeling, a very basic single tensile criterion and brittle softening is used here. This section describe its main characteristics.

4.1 Localization

As in many failure models, the inelastic behavior occurs after the stress field reaches a certain amount. This limit value is here referred to as *yield stress* (noted σ_y). It has to be seen has a material characteristic of the meso-scale. Within the multi-scale framework, this *local* characteristic must not be confused with the macroscopic *effective* strength of

a homogenized material. Only full calculation until global failure can provide these up-scaled values. EQ. (2.31) defines a *localization criterion* noted Φ_1 . A negative value of the criterion means an elastic behavior while a positive leads to localization and trigger the crack opening.

$$\Phi_1 = \sigma_{\text{eq}} - \sigma_y. \quad (2.31)$$

From the latter equation, it can be seen that the stress state is represented by a scalar referred to as the *equivalent stress* σ_{eq} . In order to catch a meaningful representation, its definition has to be tackled with careful attention. Two cases have to be considered. First, if the localization occurs “far” from an heterogeneity — *matrix element* — no geometrical information are given on the crack orientation. The choice is made here to use the major principal stress as the equivalent stress: $\sigma_{\text{eq}} = \sigma_1$. This principal component is simply the first eigenvalue of the stress tensor. Furthermore, the corresponding eigenvector \mathbf{n}_1 represents its direction. The physical meaning of eigenvalue problems naturally leads to the choice of this vector in order to represent the crack orientation $\mathbf{n} \leftarrow \mathbf{n}_1^{\text{localization}}$. It is assumed that, in contrast to rotating crack problems, the orientation is determined at the localization and does not change. A choice justified by the unusual vision of macroscopic crack as a coalescence of cracked element (a notion developed in Chapter 3). Secondly, if localization occurs “near” a material discontinuity, it is assumed that the crack follows the interface, thus corresponding to debonding. Then, the main difference is that \mathbf{n} is defined by geometrical characteristics and is therefore independent from any stress state. Traction vector is defined prior localization and therefore used in the criterion. Herein, its projection on the interface direction is used $\sigma_{\text{eq}} = \mathbf{n} \cdot \mathbf{T}$. *Note that, in the simplified kinematics of degenerated Timoshenko beams developed in the next section, the approximation that \mathbf{n} follows the beam direction is also made. Further details are given in the corresponding section. Nevertheless, the global spirit described above is the same.*

The choices made here reflect, in a physical way, the tension-based localization criterion at meso-scale, keeping it as simple as possible. Having defined the so-called localization step, the traction-separation law governing the opening after localization is now introduced.

4.2 Traction-separation law

Traction-separation law is the governing equation that links crack opening to the stress at the discontinuity. Integration of this law within the E-FEM context comes from [Oliver, 2000] and can also be seen in [Wells and Sluys, 2001, Brancherie, 2003, Benkemoun et al., 2010, Benkemoun, 2010]. It has been shown that a model on the discontinuity can be yielded using the same thermodynamical way as continuum ones — free energy, internal variables, evolution laws, load/unloading functions, *etc.* It is not the will of the author to develop this part since no major improvement is made here and full explanations can easily be found in the literature. However the principal characteristics are developed.

Still for sake of simplicity, a single opening criterion Φ_o is considered in order to govern the traction separation law, linking an equivalent stress σ_{eq} to the opening magnitude

of the crack $[u]$ through a hardening function q :

$$\Phi_o = \sigma_{\text{eq}} - (\sigma_y - q). \quad (2.32)$$

For quasi-brittle materials like concrete, it has been shown that the hardening function should follow a simple decreasing exponential with respect to the magnitude crack (see EQ. (2.33)). A second material parameter \mathcal{G}_f is the fracture energy. It governs the amount of energy necessary to create a fully opened crack — zero magnitude of traction vector and very large distance between the two remaining solid parts — per meter square. Making it tending toward 0 (resp. ∞) leads to more fragile (resp. ductile) behavior. As for the yield stress σ_y , the fracture energy introduced here has to be seen as a local parameter of the material.

$$q = \sigma_y \left(1 - \exp \left(-\frac{\sigma_y}{\mathcal{G}_f} [u] \right) \right). \quad (2.33)$$

Positive values of the opening criterion indicates a need for the crack to go further in the opening process in order to get a plastically admissible stress state ($\Phi_o = 0$), whereas negative values mean elastic load or unloading. As the localization and the crack opening mechanism are uncorrelated, the equivalent stress does not have to be necessary the same, nevertheless it involves necessary the traction vector defined at the interface \mathbf{T} (details are given later). Because both q and σ_{eq} are depending on $[u]$ a non linear way EQ. (2.32) has to be differentiated in order to solve the problem. It is a concern that have to kept in mind while choosing σ_{eq} . Finally, the global behavior in Ω_e can be summarized as in FIG. (2.5). An elastic relationship links strain and stress fields in Ω_e^\oplus and Ω_e^\ominus where, after localization, the two parts of the split body are linked together by the interface through a relationship between crack opening magnitude and traction vector that models the degradation process.

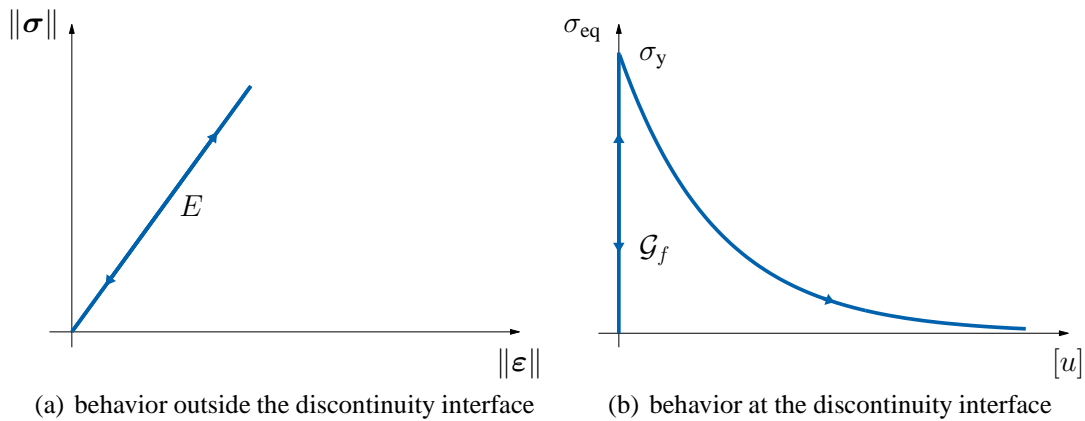


Figure 2.5: Continuum/discrete constitutive model.

As the criterion is single valued (one scalar equation), herein, the traction separation law can only determine the crack magnitude $[u]$. Hence, it has to be projected onto the

three-dimensional space following a given vector (noted \mathbf{n}_p). This leads to the following definition of the crack vector $[[\mathbf{u}]]$:

$$[[\mathbf{u}]] = [u] \mathbf{n}_p. \quad (2.34)$$

Depending on the element kinematics, several choices are proposed for \mathbf{n}_p , based on displacement or stress considerations.

This section has been the occasion to describe the non linear behavior used in this work. Keeping in mind the spirit of *simple* modeling, a single tensile criterion with quasi-brittle phenomenological behavior linking stress state at the discontinuity to the crack opening is chosen. Several aspects such as the equivalent stress and the crack projection will be specified in due time.

5 Resolution methodology

In this section, attention is drawn to the resolution of SYS. (2.30) where EQ. (2.30a) is the global equilibrium and EQ. (2.30b) and (2.30c) are the two local equations corresponding respectively to the weak and the strong enhancement. The latter ensure continuity of the traction vector at the discontinuity interface. As seen above, it is first activated according to a stress criterion, then a quasi-brittle behavior is introduced linking the crack opening magnitude to the traction vector. Hence, a non linear system has to be solved. First, linearization of the equations is presented, then both local and global levels of resolution are discussed. Finally, application of the theoretical framework is made using two different FE. One with a simple kinematics using degenerated Timoshenko beams and another using 4-node tetrahedra.

5.1 Integration and linearization with constant strain elements

Application is made here with constant strain elements. Hence, integration over Ω_e can be performed easily. Because weak discontinuity can be present, those integrations have to be decomposed on Ω_e^\oplus and Ω_e^\ominus . Equations will be developed by explicitly separating each variables: on the one hand the displacements \mathbf{d} and on the other hand the internal variables corresponding to weak and strong discontinuities respectively $[[\boldsymbol{\varepsilon}]]$ and $[[\mathbf{u}]]$. It is recalled that, giving the statement EQ. (2.34), the latter vector valued variable may simply be expressed as a scalar variable $[u]$.

The notations used for the linearization are as follows: let Y be an equation depending on n_{var} variables $\{X_i\}$, at each time step n (subscript) it is necessary to iterate a certain number of time (k) (superscript) using a standard Newton procedure. It is noted:

$$\text{Lin}(Y) = Y \Big|_{n+1}^{(k)} + \sum_{i=1}^{n_{\text{var}}} \frac{\partial Y}{\partial X_i} \Big|_{n+1}^{(k)} \Delta X_i \Big|_{n+1}^{(k+1)} = 0. \quad (2.35)$$

5.1.1 Linearization of the equilibrium equation

Integration of $\mathbf{f}_{\text{int}}^e$ gives:

$$\begin{aligned} \mathbf{f}_{\text{int}}^e &= \int_{\Omega_e} \mathbf{B}^T \check{\boldsymbol{\sigma}}(\mathbf{d}, [|\boldsymbol{\varepsilon}|], [|\mathbf{u}|]) d\Omega = \underbrace{\mathbf{B}^T \left(V^\oplus \mathbf{C}^\oplus + V^\ominus \mathbf{C}^\ominus \right) \mathbf{B} \mathbf{d}}_{\mathbf{K}_{\text{bb}}} \\ &\quad + \underbrace{\frac{V^\oplus V^\ominus}{V} \mathbf{B}^T \left(\mathbf{C}^\oplus - \mathbf{C}^\ominus \right) \mathbf{H}_w [|\boldsymbol{\varepsilon}|]}_{\mathbf{K}_{\text{bw}}} \\ &\quad + \underbrace{\mathbf{B}^T \left(V^\oplus \mathbf{C}^\oplus + V^\ominus \mathbf{C}^\ominus \right) \mathbf{G}_s \mathbf{n}_p [u]}_{\mathbf{K}_{\text{bs}}}, \end{aligned}$$

therefore, linearization of global equilibrium EQ. (2.30a) can be written as:

$$\mathbb{A}_{e=1}^{n_{\text{el}}} \left\{ \mathbf{K}_{\text{bb}} \Delta \mathbf{d} \Big|_{n+1}^{(k+1)} + \mathbf{K}_{\text{bw}} \Delta [|\boldsymbol{\varepsilon}|] \Big|_{n+1}^{(k+1)} + \mathbf{K}_{\text{bs}} \Delta [u] \Big|_{n+1}^{(k+1)} \right\} = - \mathbb{A}_{e=1}^{n_{\text{el}}} \left\{ \mathbf{f}_{\text{int}}^e \Big|_{n+1}^{(k)} - \mathbf{f}_{\text{ext}}^e \right\}. \quad (2.36)$$

Notice that, the same equation can be applied for matrix element (no weak discontinuity) since $\mathbf{K}_{\text{bw}} = \mathbf{0}$ if $\mathbf{C}^\oplus = \mathbf{C}^\ominus$, leading to standard E-FEM formulation with only strong discontinuities. The same remark can be made for the next equations.

5.1.2 Linearization of weak discontinuity equation

Integration of EQ. (2.30b) gives:

$$\begin{aligned} \mathbf{h}_{[|\boldsymbol{\varepsilon}|]} &= \int_{\Omega_e} \mathbf{G}_w^T \check{\boldsymbol{\sigma}}(\mathbf{d}, [|\boldsymbol{\varepsilon}|], [|\mathbf{u}|]) d\Omega = \underbrace{\frac{V^\oplus V^\ominus}{V} \mathbf{H}_w^T \left(\mathbf{C}^\oplus - \mathbf{C}^\ominus \right) \mathbf{B} \mathbf{d}}_{\mathbf{K}_{\text{wb}}} \\ &\quad + \underbrace{\frac{V^\oplus V^\ominus}{V^2} \mathbf{H}_w^T \left(V^\ominus \mathbf{C}^\oplus + V^\oplus \mathbf{C}^\ominus \right) \mathbf{H}_w [|\boldsymbol{\varepsilon}|]}_{\mathbf{K}_{\text{ww}}} \\ &\quad + \underbrace{\frac{V^\oplus V^\ominus}{V} \mathbf{H}_w^T \left(\mathbf{C}^\oplus - \mathbf{C}^\ominus \right) \mathbf{G}_s \mathbf{n}_p [u]}_{\mathbf{K}_{\text{ws}}}, \end{aligned}$$

which can be linearized as follows:

$$\mathbf{K}_{\text{wb}} \Delta \mathbf{d} \Big|_{n+1}^{(k+1)} + \mathbf{K}_{\text{ww}} \Delta [|\boldsymbol{\varepsilon}|] \Big|_{n+1}^{(k+1)} + \mathbf{K}_{\text{ws}} \Delta [u] \Big|_{n+1}^{(k+1)} = - \mathbf{h}_{[|\boldsymbol{\varepsilon}|]} \Big|_{n+1}^{(k)}. \quad (2.37)$$

5.1.3 Linearization of strong discontinuity equation

Strong discontinuity is handled with equation EQ. (2.30c), only giving an explicit value of the traction vector. Hence, the traction-separation law EQ. (2.32) is incorporated within the system [Ibrahimbegović et al., 1998].

The integration of the traction vector over the discontinuity surface leads to a factor A . Since $\mathbf{G}_{s,b}^*$ is also proportional to this area surface, it is only natural that it does not appear in the end. Actually, the traction vector appears to be an average value of $\check{\boldsymbol{\sigma}}^\oplus$ and $\check{\boldsymbol{\sigma}}^\ominus$ weighted by volumes. Indeed:

$$\mathbf{h}_{[u]} = \int_{\Omega_e} \mathbf{G}_{s,b}^{*,T} \check{\boldsymbol{\sigma}}(\mathbf{d}, [|\boldsymbol{\varepsilon}|], [u]) d\Omega + \int_{\Gamma_d} \mathbf{T} d\Omega = \mathbf{0} \quad (2.38)$$

leads to:

$$\mathbf{T} = \frac{1}{V} \mathbf{H}_s^{*,T} (V^\oplus \check{\boldsymbol{\sigma}}^\oplus + V^\ominus \check{\boldsymbol{\sigma}}^\ominus). \quad (2.39)$$

It can be verified that if no weak discontinuity is present in the element, usual value of the traction vector is retrieved: $\mathbf{T} = \mathbf{H}_s^{*,T} \check{\boldsymbol{\sigma}}$. From the last two equations, the traction vector can be written in terms of $(\mathbf{d}, [|\boldsymbol{\varepsilon}|], [u])$:

$$\begin{aligned} \mathbf{T} &= \underbrace{\frac{1}{V} \mathbf{H}_s^{*,T} (V^\oplus \mathbf{C}^\oplus + V^\ominus \mathbf{C}^\ominus)}_{\mathbf{K}_{s^*b}} \mathbf{B} \mathbf{d} \\ &+ \underbrace{\frac{V^\oplus V^\ominus}{V^2} \mathbf{H}_s^{*,T} (\mathbf{C}^\oplus - \mathbf{C}^\ominus)}_{\mathbf{K}_{s^*w}} \mathbf{H}_w [|\boldsymbol{\varepsilon}|] \\ &+ \underbrace{\frac{1}{V} \mathbf{H}_s^{*,T} (V^\oplus \mathbf{C}^\oplus + V^\ominus \mathbf{C}^\ominus)}_{\mathbf{K}_{s^*s}} \mathbf{G}_s \mathbf{n}_p [u]. \end{aligned}$$

Now, focus is placed on the opening criterion equation EQ. (2.32) that links \mathbf{T} to $[u]$. In order to stay in a rather general framework, it is assumed that $\sigma_{\text{eq}} = f(\mathbf{T})$ and $\frac{\partial \sigma_{\text{eq}}}{\partial \mathbf{T}}$ is known but not explicitly defined. Φ_o can be decomposed into two parts: $\sigma_{\text{eq}}(\mathbf{T})$ and $q([u])$. Hence, an increment of Φ_o can be written:

$$\Delta \Phi_o = \frac{\partial \sigma_{\text{eq}}}{\partial \mathbf{T}} \Delta \mathbf{T} + \frac{\partial q}{\partial [u]} \Delta [u],$$

giving, as a function of increment of \mathbf{d} , $[[\boldsymbol{\varepsilon}]]$ and $[u]$:

$$\begin{aligned} \Delta\Phi_o &= \underbrace{\frac{\partial\sigma_{\text{eq}}}{\partial\mathbf{T}} \frac{1}{V} \mathbf{H}_s^{*,T} \left(V^{\oplus} \mathbf{C}^{\oplus} + V^{\ominus} \mathbf{C}^{\ominus} \right) \mathbf{B} \Delta\mathbf{d}}_{\mathbf{K}_{s^*b}} \\ &+ \underbrace{\frac{\partial\sigma_{\text{eq}}}{\partial\mathbf{T}} \frac{V^{\oplus} V^{\ominus}}{V^2} \mathbf{H}_s^{*,T} \left(\mathbf{C}^{\oplus} - \mathbf{C}^{\ominus} \right) \mathbf{H}_w \Delta[[\boldsymbol{\varepsilon}]]}_{\mathbf{K}_{s^*w}} \\ &+ \underbrace{\frac{\partial\sigma_{\text{eq}}}{\partial\mathbf{T}} \frac{1}{V} \mathbf{H}_s^{*,T} \left(V^{\oplus} \mathbf{C}^{\oplus} + V^{\ominus} \mathbf{C}^{\ominus} \right) \mathbf{G}_s \mathbf{n}_p \Delta[u]}_{\mathbf{K}_{s^*s}} \\ &+ \underbrace{\frac{\sigma_y^2}{\mathcal{G}_f} e^{-\sigma_y[u]/\mathcal{G}_f} \Delta[u]}_{\mathbf{K}_q}, \end{aligned}$$

which finally leads to the following linearization of $\Phi_o = 0$:

$$\mathbf{K}_{s^*b} \Big|_{n+1}^{(k)} \Delta\mathbf{d} \Big|_{n+1}^{(k+1)} + \mathbf{K}_{s^*w} \Big|_{n+1}^{(k)} \Delta[[\boldsymbol{\varepsilon}]] \Big|_{n+1}^{(k+1)} + (\mathbf{K}_{s^*s} + \mathbf{K}_q) \Big|_{n+1}^{(k)} \Delta[u] \Big|_{n+1}^{(k+1)} = -\Phi_o \Big|_{n+1}^{(k)}. \quad (2.40)$$

5.2 Solving the system

Finally the system EQ. (2.36), EQ. (2.37) and EQ. (2.40) can be cast in the following matrix format:

Linearized system

$$\left[\begin{array}{ccc} \mathbf{K}_{bb} & \mathbf{K}_{bw} & \mathbf{K}_{bs} \\ \mathbf{K}_{wb} & \mathbf{K}_{ww} & \mathbf{K}_{ws} \\ \mathbf{K}_{s^*b} & \mathbf{K}_{s^*w} & \mathbf{K}_{s^*s} + \mathbf{K}_q \end{array} \right]_{n+1}^{(k)} \left\{ \begin{array}{c} \Delta\mathbf{d} \\ \Delta[[\boldsymbol{\varepsilon}]] \\ \Delta[u] \end{array} \right\}_{n+1}^{(k+1)} = \left\{ \begin{array}{c} -\sum_{e=1}^{n_{el}} \{ \mathbf{f}_{\text{int}}^e - \mathbf{f}_{\text{ext}}^e \} \\ -\mathbf{h}_{[[\boldsymbol{\varepsilon}]]} \\ -\Phi_o \end{array} \right\}_{n+1}^{(k)}. \quad (2.41)$$

The resolution procedure of SYS. (2.41) is performed at two levels. A global one corresponding to EQ. (2.36) and a local one corresponding to EQ. (2.37) and EQ. (2.40). Following the spirit of the *operator split* method, internal variables $[[\boldsymbol{\varepsilon}]]$ and $[u]$ are computed for a fixed value of \mathbf{d} . It can be seen as a *local* resolution within each FE. And because $\Phi_o = 0$ is a non linear equation, a standard Newton procedure is implemented in the element routine, in order to solve the local system:

$$\mathbf{h}_{[[\boldsymbol{\varepsilon}]]} = \mathbf{0}, \quad (2.42a)$$

$$\Phi_o = 0. \quad (2.42b)$$

Once the SYS. (2.42) is solved for each element, appropriate values of $[\boldsymbol{\varepsilon}] \Big|_{n+1}^{(k+1)}$ and $[u] \Big|_{n+1}^{(k+1)}$ are known, leading to null residuals $\mathbf{h}_{[\boldsymbol{\varepsilon}]} \Big|_{n+1}^{(k)}$ and $\Phi_o \Big|_{n+1}^{(k)}$. Then, following [Wilson, 1974], a *static condensation* is made on the local variables, leading to a global system written with a modified stiffness matrix \mathbf{K}_{sc} . The basic idea is to write the internal variables in terms of displacements. Since SYS. (2.42) is supposed to be solved, from the two last equations of SYS. (2.41), it is assumed that:

$$\begin{bmatrix} \mathbf{K}_{ww} & \mathbf{K}_{ws} \\ \mathbf{K}_{s^*w} & K_{s^*s} + Kq \end{bmatrix}_{n+1}^{(k)} \begin{Bmatrix} \Delta [\boldsymbol{\varepsilon}] \\ \Delta [u] \end{Bmatrix}_{n+1}^{(k+1)} = - \begin{bmatrix} \mathbf{K}_{wb} \\ \mathbf{K}_{s^*b} \end{bmatrix}_{n+1}^{(k)} \Delta \mathbf{d} \Big|_{n+1}^{(k+1)},$$

giving a direct expression of internal variables in terms of nodal displacements:

$$\begin{Bmatrix} \Delta [\boldsymbol{\varepsilon}] \\ \Delta [u] \end{Bmatrix}_{n+1}^{(k+1)} = - \left(\begin{bmatrix} \mathbf{K}_{ww} & \mathbf{K}_{ws} \\ \mathbf{K}_{s^*w} & K_{s^*s} + Kq \end{bmatrix}_{n+1}^{(k)} \right)^{-1} \begin{bmatrix} \mathbf{K}_{wb} \\ \mathbf{K}_{s^*b} \end{bmatrix}_{n+1}^{(k)} \Delta \mathbf{d} \Big|_{n+1}^{(k+1)}. \quad (2.43)$$

Then, the first equation can be extracted from SYS. (2.41) and written in terms of all the variables:

$$\mathbf{K}_{bb} \Delta \mathbf{d} \Big|_{n+1}^{(k+1)} + \begin{bmatrix} \mathbf{K}_{bw} & \mathbf{K}_{bs} \end{bmatrix} \begin{Bmatrix} \Delta [\boldsymbol{\varepsilon}] \\ \Delta [u] \end{Bmatrix}_{n+1}^{(k+1)} = - \underset{e=1}{\overset{n_{el}}{\mathbb{A}}} \{ \mathbf{f}_{int}^e - \mathbf{f}_{ext}^e \} \Big|_{n+1}^{(k)}.$$

Finally, by injecting EQ. (2.43) in the latter equation, the global equilibrium can be written just in terms of displacement unknowns:

Discretized using a static condensation

$$\mathbf{K}_{sc} \Big|_{n+1}^{(k)} \Delta \mathbf{d} \Big|_{n+1}^{(k+1)} = - \underset{e=1}{\overset{n_{el}}{\mathbb{A}}} \{ \mathbf{f}_{int}^e - \mathbf{f}_{ext}^e \} \Big|_{n+1}^{(k)}, \quad (2.44)$$

where

$$\mathbf{K}_{sc} \Big|_{n+1}^{(k)} = \mathbf{K}_{bb} - \begin{bmatrix} \mathbf{K}_{bw} & \mathbf{K}_{bs} \end{bmatrix} \left(\begin{bmatrix} \mathbf{K}_{ww} & \mathbf{K}_{ws} \\ \mathbf{K}_{s^*w} & K_{s^*s} + Kq \end{bmatrix}_{n+1}^{(k)} \right)^{-1} \begin{bmatrix} \mathbf{K}_{wb} \\ \mathbf{K}_{s^*b} \end{bmatrix}_{n+1}^{(k)}.$$

Even though the stiffness matrix has been changed due to kinematics enhancement, its size is unchanged. Hence, no matter how many heterogeneities are represented or how many elements have starting to fail, the global size of the problem is preserved. In terms of numerical resources, the memory needed only depends on the mesh size (number of nodes). Naturally, local Newton algorithms slow down the global calculation as the number of strong discontinuity activated increases. By using the static condensation, a standard FE problem is retrieved, where increments of \mathbf{d} have to be found in order to respect the global equilibrium equation EQ. (2.44).

The most common method used to solve those problems in case of non linearity are the so-called *Newton* methods. However, it requires full calculation of full stiffness matrix at each iteration, and since morphological modeling requires rather fine meshes, a *quasi-Newton* algorithm coupled with an iterative solver is used here. Among the huge diversity of those algorithms, the *BFGS* (Broyden-Fletcher-Goldfarb-Shanno) algorithm is retained. It makes the number of arithmetical operations to fall down from $\mathcal{O}(n^3)$ to $\mathcal{O}(n^2)$. The price to pay is that quasi-linear convergence is obtained (instead of quadratic). Full details are given in the original papers: [Broyden, 1970b, Broyden, 1970a, Fletcher, 1970, Goldfarb, 1970, Shanno, 1970]. Moreover numerical implementation details are in [Matthies and Strang, 1979]. Added to the quasi-Newton BFGS, a *line-search* method is also used, modulating the incremental displacement norm for each iterations by a factor s :

$$\mathbf{d}^{(k+1)} = \mathbf{d}^{(k)} + s^{(k+1)} \Delta \mathbf{d}^{(k+1)}.$$

See [Dahlquist, 2003] for details on the computation of s . It is recalled that powerful algorithm adapted to the E-FEM such as [Oliver et al., 2008] and not implemented here can significantly increase the computation performance.

In the last two sections, the resolution methodology has been presented in a general framework, the only strong specification being the use of constant strain FE. In the next two sections those equations are applied to three different FE types: first to a spatial truss with one-dimensional *bar elements* then to a spatial frame with one-dimensional *beam elements* and finally to standard mesh with volume FE, namely *4-node tetrahedra*.

5.3 Application to spatial truss and spatial frame

One of the choice made for the numerical modeling is the use of a three-dimensional spatial truss (resp. frame) made of one-dimensional bars (reps. beams). Since the pioneer work of [Hrennikoff, 1941], the so-called *framework method* has been developed in many fields in two and three dimensions. Its inner discrete characteristic makes it a handy tool for crack modeling [Jirásek and Bažant, 1995, Man and van Mier, 2008]. Herein, it is the FE discretization that is based on these frames. However, it has to be constructed with attention, especially regarding the area assigned to each element. Indeed, it has been shown in the literature that a constant section fails to represent uniform strain under uniform loading [Jirásek and Bažant, 1995, Bolander and Saito, 1998, Yip et al., 2005]. Following Bolander recommendations, an irregular frame is constructed upon the Delaunay triangulation (which is dual to the Voronoi paving of the domain). In concrete terms, the two vertices of an element are defined by the centers of two neighbor Voronoi polyhedra while its area is the one of those polyhedra common face.

The numerical implementation of the frame construction has been a part of the Ph.D. thesis of Nathan Benkemoun. Details on the algorithm can be found (in French) in [Benkemoun, 2010]. In a FE context, the latter work shows that frames give relevant results in homogeneous elasticity. Indeed, convergence of global characteristics are shown with regards to the vertex density.

Using this frame construction as a FE discretization basis, two kinds of element's kinematics are presented within the double enhancement background. The first one (not developed), referred to as *bar element* involves a very simple kinematics only in the element principal direction (one dimension). In this case, the element assembly is referred to as truss (not frame). The second one, involves *beam element* with a more complex kinematics that ables to represent local shearing.

5.3.1 Remind of previous results concerning uniaxial compression and tension test on spatial truss

This subsection presents the main results of Nathan Benkemoun Ph.D. thesis: [Benkemoun et al., 2010] and [Benkemoun, 2010] (in French). Since a similar model is developed afterwards and in order to minimize repetitions, a very succinct presentation is made here, emphasizing only advantages and drawbacks of the method. It can be seen as motivations for the further development made.

As it was the pioneer work of the presented meso-model, the idea was to begin by using the most simple local kinematics. Only strain and stress in the principal direction of the bar are taken into account. Hence, both fields are scalar functions over each elements, linked together by the Young modulus. The failure mechanism presented previously can be applied in this context with no other choice than taking the equivalent stress as the scalar stress itself. Henceforth, only mode I opening can be represented. However, this simple local representation leads to much more complex global results at the macro-scale. Meaningful results on an uniaxial tension and uniaxial compression are now briefly presented. Macroscopic responses of both solicitations are presented on the same graph FIG. (2.6) where macroscopic axial stress (response) is plotted with respect to the macroscopic axial strain (solicitation). Furthermore, cracks' patterns are shown in FIG. (2.7).

Regarding the tension test, it can be observed that a single macroscopic crack perpendicular to the solicitation occurs, leading to the specimen failure. Even though it is not represented by the local failure model, a lost of stiffness before failure can be seen. It can be explained by the development of several micro-cracks spread all over the specimen. It is the coalescence of these broken elements (or activated) that forms the macroscopic crack. This first observation shows how a structural effect induced by explicit material heterogeneity modeling brings several complex features such as: loss of stiffness, global failure, complex macro-cracks' pattern, *etc.* Failure mechanisms that occur during the compression test are even more interesting. Indeed, in this case, the global failure is not in mode I. Displacement incompatibilities due to the heterogeneities added to the underlying truss Poisson effect lead to a local mode I failure model ables to represent much more complex global mechanisms. Eventually, both tests can be compared revealing an asymmetric response reflected in several ways: regarding the strength, the ductility and the cracks' patterns.

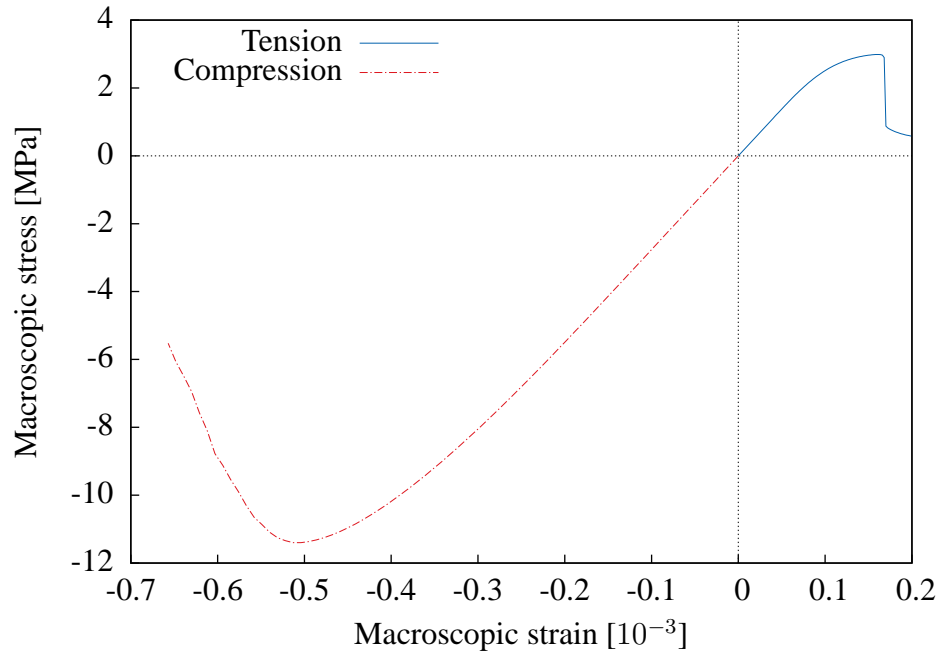


Figure 2.6: Stress-strain response for uniaxial compression and tension with bar elements.

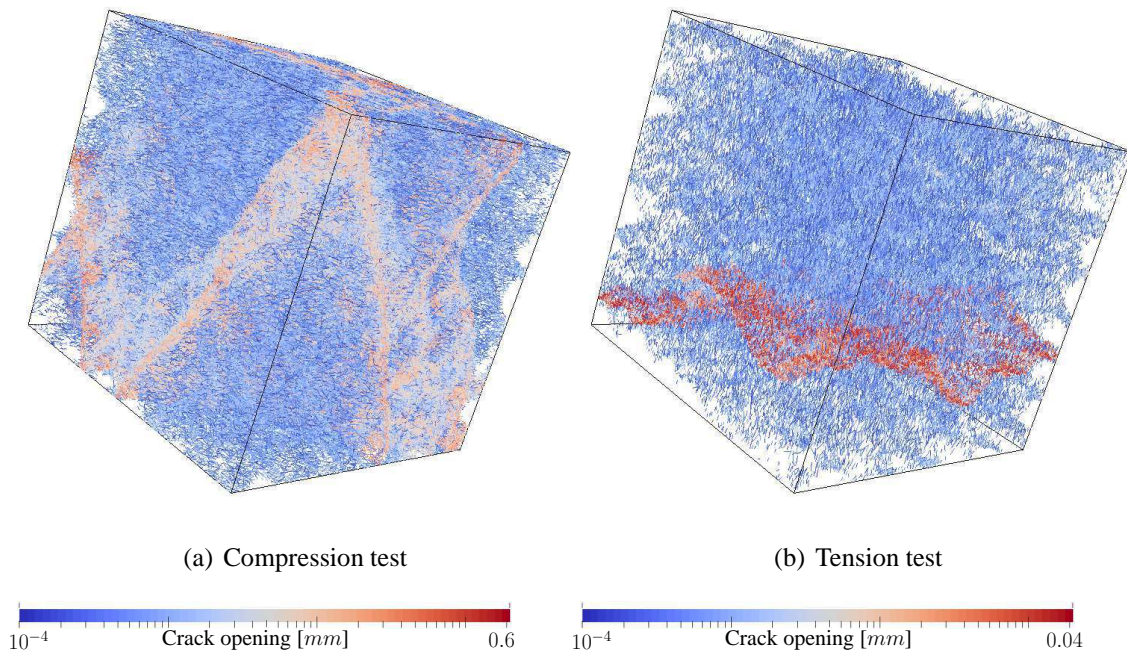


Figure 2.7: Cracks' pattern in uniaxial compression and tension with bar elements.

Several major drawbacks can be reported. First, the ratio between compressive and

tensile strength is rather low. Experiences have shown that it increases as the volume fraction of aggregates increases. However, it has not been possible to reach more than a ratio of 4. Furthermore, the compression cracks' pattern is rather odd and does not represent well the reality. The conclusion is that the local model is too simple. By representing displacements in the other directions, shear could be taken into account at the meso-scale and therefore mode II failure too. It is in this spirit that degenerated Timoshenko beams are used in the same context.

5.3.2 Degenerated Timoshenko beam element

A beam of length l projected onto a three-dimensional space is considered. Its direction is noted \mathbf{n} and \mathbf{m}, \mathbf{t} are defined so that $(\mathbf{n}, \mathbf{m}, \mathbf{t})$ is an orthonormal basis of \mathbb{R}^3 . (x, y, z) represents the coordinates in each direction, respectively. The displacement field is decomposed in the basis into three components u, v, w . θ_v and θ_w are rotations around axis \mathbf{m} and \mathbf{t} , respectively. Timoshenko kinematics implies the followings relationships between displacements, rotations and strain field:

$$\varepsilon = \frac{\partial u(x)}{\partial x}, \quad \gamma_v = \frac{\partial v(x)}{\partial x} - \theta_v(x), \quad \gamma_w = \frac{\partial w(x)}{\partial x} - \theta_w(x),$$

$$\kappa_v = \frac{\partial \theta_v(x)}{\partial x}, \quad \text{and} \quad \kappa_w = \frac{\partial \theta_w(x)}{\partial x},$$

where ε represents the axial strain, γ_v and γ_w sliding and κ_v and κ_w curving. The simplified kinematics called *degenerated* is based on the assumption that all rotations are blocked ($\theta_v = 0$ and $\theta_w = 0$). This choice is made here in order to exclude any additional parameter that would need to be identified, namely: the second moment of area. It leads to a strain field that can be put in the following matrix format:

$$\boldsymbol{\varepsilon} = \begin{bmatrix} \varepsilon & \gamma_v & \gamma_w \\ \gamma_v & 0 & 0 \\ \gamma_w & 0 & 0 \end{bmatrix}. \quad (2.45)$$

If K and G are the bulk and the shear moduli, respectively, the stress field is defined by:

$$\boldsymbol{\sigma} = \begin{bmatrix} \sigma_n & \tau_m & \tau_t \\ \tau_m & 0 & 0 \\ \tau_t & 0 & 0 \end{bmatrix} = \begin{bmatrix} (K + 4G/3)\varepsilon & 2G\gamma_v & 2G\gamma_w \\ 2G\gamma_v & 0 & 0 \\ 2G\gamma_w & 0 & 0 \end{bmatrix}, \quad (2.46)$$

assuming that $\sigma_{22}, \sigma_{23}, \sigma_{33}$ are equal to zero. Since only three components remain in order to define both strain and stress fields, a special vector notation is used EQ. (2.47). Let $K_{\text{eq}} = K + 4G/3$ and $G_{\text{eq}} = 2G$ be equivalent moduli and \mathbf{C} the Hooke operator. The elastic behavior relationship written $\check{\boldsymbol{\sigma}} = \mathbf{C}\boldsymbol{\varepsilon}$ means in this context:

$$\begin{Bmatrix} \sigma_n \\ \tau_m \\ \tau_t \end{Bmatrix} = \begin{bmatrix} K_{\text{eq}} & 0 & 0 \\ 0 & G_{\text{eq}} & 0 \\ 0 & 0 & G_{\text{eq}} \end{bmatrix} \begin{Bmatrix} \varepsilon \\ \gamma_v \\ \gamma_w \end{Bmatrix}. \quad (2.47)$$

The FE interpolation is made following EQ. (2.24a). Each components are now specified for the Timoshenko beam. Standard order one shape functions $N_1(x)$, $N_2(x)$ are used for 2-node elements. Respecting kinematics relationships set above, the interpolation matrix of the strain field \mathbf{B} and the displacement nodal values vector \mathbf{d} lead to a regular part of the strain of the form:

$$\mathbf{B}\mathbf{d} = \frac{\mathbf{u}_d}{l} \quad \text{with} \quad \mathbf{u}_d = \begin{Bmatrix} u_2 - u_1 \\ v_2 - v_1 \\ w_2 - w_1 \end{Bmatrix}. \quad (2.48)$$

In case of discontinuity, the beam is split into Ω_e^\oplus and Ω_e^\ominus of size l^\oplus and l^\ominus . It is recalled that each element beam has a section A constant over l giving an easy computation of the volumes:

$$V = Al, \quad V^\oplus = Al^\oplus \quad \text{and} \quad V^\ominus = Al^\ominus. \quad (2.49)$$

As depicted in FIG. (2.8), it is assumed that the discontinuity interface direction is always

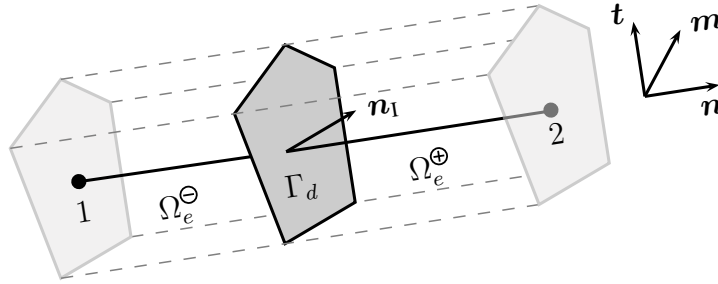


Figure 2.8: Beam element.

the one of the beam, \mathbf{n} . This rather strong assumption leads to a predictive orientation, depending only on the truss geometry and not, for example, the stress state as it usually is. However, it leads to several major simplifications such as working on the local basis: $\mathbf{n} = \{1 \ 0 \ 0\}^T$. Regarding the weak discontinuity, \mathbf{G}_w becomes a simple scalar function and Θ can be expressed in terms of length ratio rather than volumes. The same simplification can be made for the strong discontinuity. It implies that the two scalar functions \mathbf{G}_s and \mathbf{G}_s^* respectively corresponding to EAS and KES enhancement are identical:

$$\mathbf{H}_w = 1, \quad \mathbf{G}_w^\oplus = \frac{l^\ominus}{l} \quad \text{and} \quad \mathbf{G}_w^\ominus = \frac{-l^\oplus}{l}, \quad (2.50a)$$

$$\mathbf{H}_s = 1 \quad \text{and} \quad \mathbf{G}_s = \mathbf{G}_s^* = -\frac{1}{l}. \quad (2.50b)$$

Then from EQ. (2.47), the stress field can now be explicitly defined as follows:

$$\check{\boldsymbol{\sigma}}^\oplus = \mathbf{C}^\oplus \left(\mathbf{u}_d + l^\ominus [|\boldsymbol{\varepsilon}|] - \mathbf{n}_p[u] \right) / l, \quad (2.51a)$$

$$\check{\boldsymbol{\sigma}}^\ominus = \mathbf{C}^\ominus \left(\mathbf{u}_d - l^\oplus [|\boldsymbol{\varepsilon}|] - \mathbf{n}_p[u] \right) / l. \quad (2.51b)$$

It is interesting for the rest of the reasoning to express $\mathbf{h}_{[[\varepsilon]]}$ by taking into account the new features presented for this special case and solving $\mathbf{h}_{[[\varepsilon]]} = \mathbf{0}$. It leads to an explicit value of $[[\varepsilon]]$ as a function of the displacements \mathbf{u}_d and the crack magnitude $[u]$:

$$[[\varepsilon]] = - \left(l^\ominus \mathbf{C}^\oplus + l^\oplus \mathbf{C}^\ominus \right)^{-1} \left(\mathbf{C}^\oplus - \mathbf{C}^\ominus \right) (\mathbf{u}_d - \mathbf{n}_p[u]). \quad (2.52)$$

It can be pointed out that if no material discontinuity is present within the element, $\mathbf{C}^\oplus = \mathbf{C}^\ominus$ and naturally, $[[\varepsilon]] = \mathbf{0}$. Furthermore, because \mathbf{C} is diagonal, by injecting EQ. (2.52) in the previous system SYS. (2.51), it can be shown that both stress fields are identical:

$$\check{\boldsymbol{\sigma}} = \check{\boldsymbol{\sigma}}^\oplus = \check{\boldsymbol{\sigma}}^\ominus = \mathbf{C}^\oplus \mathbf{C}^\ominus \left(l^\ominus \mathbf{C}^\oplus + l^\oplus \mathbf{C}^\ominus \right)^{-1} (\mathbf{u}_d - \mathbf{n}_p[u]). \quad (2.53)$$

Actually, this conclusion is completely natural and could have been brought up sooner. Indeed, the fact that the stress field is defined by only three components and since the discontinuity interface is oriented in the local basis $(\mathbf{n}, \mathbf{m}, \mathbf{t})$, the vector $\check{\boldsymbol{\sigma}}$ is nothing else than the traction vector \mathbf{T} itself. Notice that this results can be retrieved from the traction vector definition EQ. (2.39). Thus leading to:

$$\mathbf{T} = \check{\boldsymbol{\sigma}} = \check{\boldsymbol{\sigma}}^\oplus = \check{\boldsymbol{\sigma}}^\ominus. \quad (2.54)$$

Projection of the crack has still to be determined. Choice is made here to consider it in terms of displacements. As it is not constant over the beam, its difference between each nodal values is taken into account, *i.e.* \mathbf{u}_d . The projection is made following the same direction but with unit norm. It physically reflects how the crack will open, letting mode I, mode II or both possible:

$$[[\mathbf{u}]] = [u] \frac{\mathbf{u}_d}{\|\mathbf{u}_d\|}. \quad (2.55)$$

The traction vector can now be written:

$$\mathbf{T} = \mathbf{C}^\oplus \mathbf{C}^\ominus \left(l^\ominus \mathbf{C}^\oplus + l^\oplus \mathbf{C}^\ominus \right)^{-1} \mathbf{u}_d \left(1 - \frac{[u]}{\|\mathbf{u}_d\|} \right), \quad (2.56)$$

leading to the interesting feature being that, the chosen projection brings all components of the traction vector to zero at a total failure state. When $[u]$ reaches the magnitude of the imposed displacement, the elastic part of the strain field cancels exactly the strong discontinuity enhancement part. Furthermore, if $\mathbf{h}_{[[\varepsilon]]} = \mathbf{0}$ is respected, it can easily be seen that $[[\varepsilon]] = \mathbf{0}$, leading to a null stress field within the whole beam.

It has been noticed that in this case, the stress field is equal in Ω^\oplus and Ω^\ominus . Hence, it is relevant to consider the stress tensor $\boldsymbol{\sigma}$ in order to define the equivalent stress σ_{eq} . For both localization and opening criterion, the first eigenvalue σ_I of $\boldsymbol{\sigma}$ is chosen. A common choice for quasi-brittle material since, among other characteristics, shear is taken into account during the failure mechanism. Hence, criterion are given by:

$$\Phi_1 = \sigma_I - \sigma_y \quad \text{and} \quad \Phi_0 = \sigma_I - (\sigma_y - q). \quad (2.57)$$

Due to the choice of the interface vector as the principal direction of the element and the kinematics approximation of degenerated Timoshenko beams, the principal stress can be analytically expressed as follows:

$$\sigma_I = \frac{1}{2} \left(\sigma_n + \sqrt{\sigma_n^2 + 4(\tau_m^2 + \tau_t^2)} \right). \quad (2.58)$$

In order to make this criterion fitting into the general framework presented above, derivatives of σ_I by all components of the traction vector have to be calculated. It can also be analytically expressed:

$$\frac{\partial \sigma_{\text{eq}}}{\partial \mathbf{T}} = \left\{ \frac{\partial \sigma_I}{\partial \sigma_n} \quad \frac{\partial \sigma_I}{\partial \tau_m} \quad \frac{\partial \sigma_I}{\partial \tau_t} \right\}, \quad (2.59)$$

with

$$\begin{aligned} \frac{\partial \sigma_I}{\partial \sigma_n} &= \frac{1}{2} + \frac{\sigma_n}{\sqrt{2(\sigma_n^2 + 4(\tau_m^2 + \tau_t^2))}}, \\ \frac{\partial \sigma_I}{\partial \tau_m} &= \frac{2\tau_m}{\sqrt{2(\sigma_n^2 + 4(\tau_m^2 + \tau_t^2))}} \quad \text{and} \\ \frac{\partial \sigma_I}{\partial \tau_t} &= \frac{2\tau_t}{\sqrt{2(\sigma_n^2 + 4(\tau_m^2 + \tau_t^2))}}. \end{aligned}$$

For some particular cases, an analytical solution of $\mathbf{h}_{[u]} = 0$ is presented. Herein, σ_{eq} is not a linear combination of the stress components, hence derivatives of σ_{eq} by the traction vector depend on σ components. An iterative Newton resolution is needed in the element procedure.

Remark: During numerical implementation, the author noticed that the choice of the opening projection \mathbf{n}_p had a major impact on the criterion shape $\Phi_o([u])$. Among all the possibilities ($\mathbf{n}_p = \mathbf{n}$, $\mathbf{n}_p = \mathbf{n}_l$, $\mathbf{n}_p = \mathbf{u}_d / \|\mathbf{u}_d\|$, etc.), it appeared that only the latter grants a solution for $\Phi_o = 0$ for any solicitations. It is the author interpretation that this feature comes from the suitable physical modeling of crack opening that projection onto the displacement brings. Added to the fact that this choice leads to a total failure state, it is strongly advised to use this criterion.

It has been seen in this section that \mathbf{C} being diagonal leads to practical simplifications. It is the consequence of the simple relationship between strain and stress components, each one being respectively independent. Both failure criterion and crack projection represent mode I and mode II failure mechanisms and take into account tension and shear stresses. Furthermore, displacement considerations for the crack projection on this particular simple kinematics lead to a total failure state where all the stress components tend to zero. At this stage, the system SYS. (2.41) is completely defined. Presentation of some features of this model are now illustrated through numerical examples.

5.3.3 Up-scaling relationship in homogeneous linear elasticity

A first step considering frames discretization is to validate kinematic approximations at meso-scale. The aim of this section is to show: firstly, that the presented discretization converges towards theoretical elastic properties as the frame node density increases and secondly the relationship linking meso-scale and macro-scale material characteristic.

In this section, homogeneous and linear elastic material is considered. Several domains are considered with different node densities (hereafter identified by their number of degrees of freedom (dof)). A first result is that, considering a given solicitation, macroscopic results converge with the total number of dof, validating the frame convergence.

The elastic material properties are described through the bulk and the shear moduli. They have to be considered at the meso-scale (FE parameters) and at the macro-scale (up-scaled values). They are noted (K^m, G^m) and (K^M, G^M) , respectively. In this context, the Kinematics Uniform Boundary Conditions (KUBC, [Hill, 1967]) are imposed. Hence, Dirichlet conditions depend on the position \boldsymbol{x} as follows:

$$\boldsymbol{u}|_{\Gamma_u} = \boldsymbol{\varepsilon}_{\text{KUBC}} \cdot \boldsymbol{x}, \quad (2.60)$$

where $\boldsymbol{\varepsilon}_{\text{KUBC}}$ is the mean macroscopic strain tensor. Under the assumption of isotropic effective response, two specific solicitations are considered:

$$\boldsymbol{\varepsilon}_{\text{KUBC}} = \boldsymbol{\varepsilon}_K = \frac{1}{3} \begin{bmatrix} 1 & 0 & 0 \\ 0 & 1 & 0 \\ 0 & 0 & 1 \end{bmatrix} \quad \text{and} \quad \boldsymbol{\varepsilon}_{\text{KUBC}} = \boldsymbol{\varepsilon}_G = \frac{1}{2} \begin{bmatrix} 0 & 1 & 0 \\ 1 & 0 & 0 \\ 0 & 0 & 0 \end{bmatrix}. \quad (2.61)$$

By considering macroscopic fields as mean values of mesoscopic results over the cube Ω , the following relationships between the elastic characteristics can be retrieved:

$$K^M = \frac{1}{3}K^m + \frac{4}{9}G^m, \quad (2.62a)$$

$$G^M = 0.18K^m + 0.89G^m. \quad (2.62b)$$

If the assumption of homogeneous repartition of beams orientations over space is made, EQ. (2.62a) can be found analytically. Unfortunately, simulations are needed in order to cast EQ. (2.62b). This system can easily be inverted leading to the knowledge of mesoscopic characteristics in terms of those of the macro-scale.

In order to illustrate both frame convergence and up-scaling relationship accuracy, an elastic homogeneous material is considered with given macroscopic characteristics. The equivalent mesoscopic moduli are yielded by inverting SYS. (2.62). All these parameters are given TAB. (2.1). Notice that it corresponds to a macroscopic Young modulus of 10 GPa and a Poisson ratio of 0.2.

In FIG. (2.9), it can be observed: on the left, both bulk and shear moduli calculated for several dof (dashed curves) compared to the theoretical values and on the right, the error between them. Those simulations validate both the frame convergence and the up-scaling relationship SYS. (2.62) consistency.

Macroscopic properties [MPa]		Mesoscopic properties [MPa]	
Bulk modulus	$K^M = 5555$	Bulk modulus	$K^m = 14137$
Shear modulus	$G^M = 4167$	Shear modulus	$G^m = 1789$

Table 2.1: Macroscopic and equivalent mesoscopic elastic moduli.

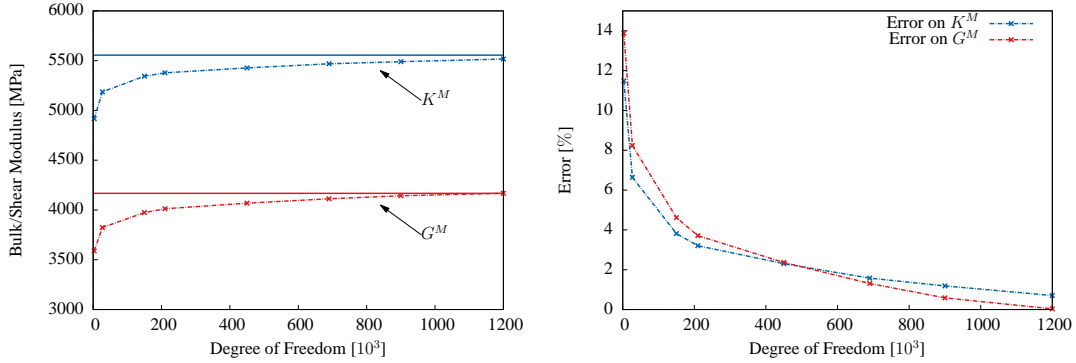


Figure 2.9: Global convergence of elastic characteristic using frame discretization.

In order to conclude this first introduction on frame validation, it is recalled that, in this context, two meso-scale elastic parameters grant a control of the usual two macro-scale material properties. Furthermore, a relationship between them has been determined leading to a predictable up-scaled behavior. Hence, no identification is necessary which is an improvement compared to the truss model. The non-linear features of the model are now presented and compared to the truss discretization.

5.3.4 Uniaxial compression and tension tests on spatial frame

Degenerated Timoshenko beams are now tested for the same uniaxial compression and tension tests that have been performed on the spatial truss. The macroscopic responses for both tests are plotted in FIG. (2.10).

The same features as above can be observed. However some improvements are worth noticing:

- The behavior in tension is more brittle along with, in compression, a larger loss of rigidity region. These two opposite effects show that the changes in the behavior are induced by the new kinematics and not the material parameters (fracture energy). Thus, results are more consistent with experimental observations.
- The strength ratio is higher, reaching almost 5.5. An expected behavior of the model since, with a local mode II failure and a criterion also based on the principal stress, more energy can be dissipated. In contrast to the cracks' pattern results, the macroscopic response shows that the tensile strength is predominantly affected

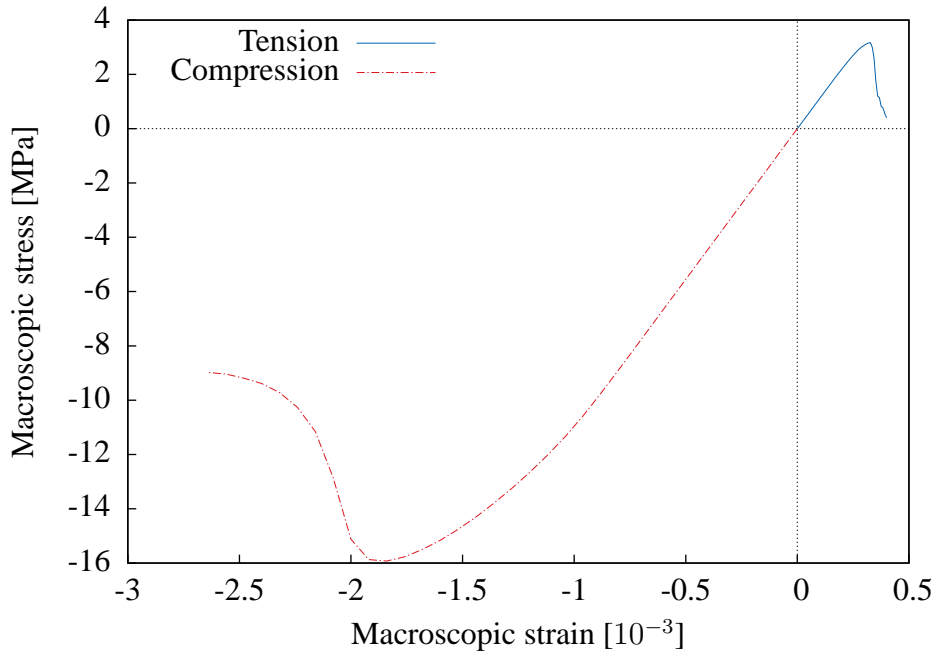


Figure 2.10: Stress-strain response for uniaxial compression and tension with beam elements.

by the new kinematics, making the specimen fail sooner while the compressive strength is approximately the same. *Herein, mesoscopic material properties have been set in order to reach the same tensile strength.*

Those differences are highlighted in FIG. (2.11) where results of both truss and frame discretization are plotted. Notice that the macroscopic strains have been rescaled in order to simplify the comparison.

From the cracks' pattern shown in FIG. (2.12), it can be noted that the tension failure mode is sensitively the same as above. Indeed a single localized macroscopic crack perpendicular to the solicitation direction splits the specimen in two. A diffuse micro-cracking is present in the rest of the material. However the compression test exhibits a significant difference. Indeed, where the truss model produced an odd cracks' pattern with one principal macroscopic crack oriented in a diagonal direction, herein, the pattern is a complex network of plans parallel to the solicitation direction. These more realistic geometrical representations of the failure behavior explain the better macroscopic response of the specimen observed in FIG. (2.10).

5.3.5 Comments on the spatial truss and frame discretization

The performances of the FE implementation of the meso-model presented in this section using a *framework discretization* (with bar and beam elements) have been briefly presented. Uniaxial compression and tension tests revealed several generic features of

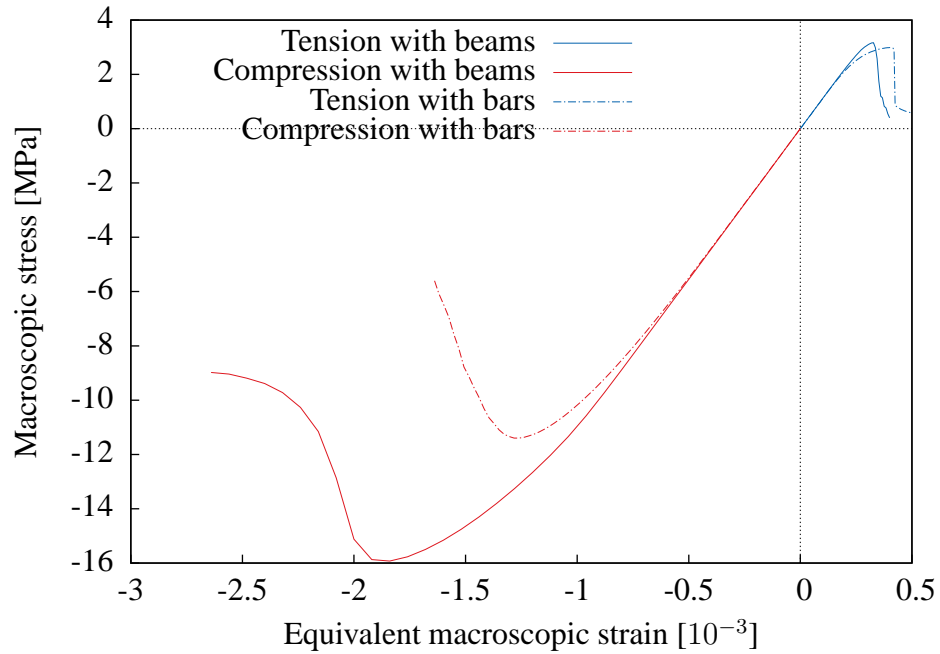


Figure 2.11: Comparison between bar and beam elements on uniaxial compression and tension.

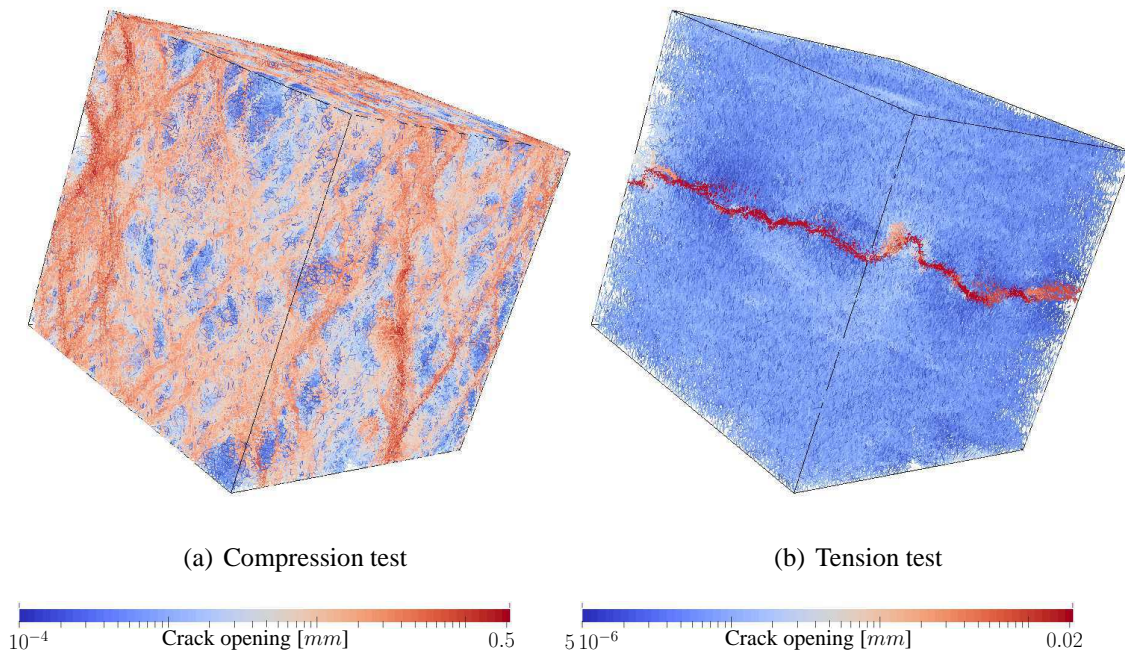


Figure 2.12: Cracks' pattern in uniaxial compression and tension with beam elements.

this two-scale model where heterogeneities of concrete at the meso-scale are geomet-

rically represented and the two resulting phases (aggregates and mortar matrix) follow simple mechanical behaviors. Indeed, it leads to a structural effect which induces a complex global behavior in terms of both macroscopic response and cracks' pattern. It has also been remarked how a more accurate element kinematics enhances the performances comparing to a realistic modeling.

However, several major drawbacks can be noticed. On a purely numerical point of view, in addition to frame convergence problematic, the one dimension aspect of the FE discretization prevents the model from producing a volumetric representation of the stress field. Henceforth, local analysis are often impossible to compute. In addition, even though significant improvements are made using degenerated Timoshenko beams, several characteristics of the macroscopic response — such as the strength ratio — remain rather unrealistic compared to experimental observations.

It is for these reasons that an implementation based upon volume FE with full kinematics representation is made after.

5.4 Application to volume Finite Elements

Another choice of interpolation, using 4-node tetrahedron elements, is now presented. Compared to frame, this volume discretization brings several advantages. First, an exact representation is made regarding the volume tessellation of the mesh, leading to exact representation of constant stress problems. Therefore, the problematic of mesh convergence presented in the previous section is irrelevant in this context. Furthermore, a complete kinematics can now be represented. Hence, both geometrical construction and mechanical behavior are more accurately depicted. Unfortunately, this more complex modeling leads to several major drawbacks inherent to the enhancement layout.

5.4.1 Interpolation matrices

Exact implementation of the classic kinematics relationship can be represented with 4-node tetrahedron FE (considering small deformations) leading to full strain and stress matrices of six components. As displacement interpolation shape functions are linear, the stress yielded is constant over the whole element. Hence, it complies with the necessary integration conditions of system SYS. (2.30). For sake of convenience, fields are represented in their Voigt notation. Hence, each enhancement matrices are developed in this format. Now, attention is focused on making explicit these matrices.

The standard part of the deformation strain is computed from the displacement field

using the differential operator ∇^s . Conventions of Voigt notation are as follows:

$$\begin{Bmatrix} \varepsilon_{xx} \\ \varepsilon_{yy} \\ \varepsilon_{zz} \\ 2\varepsilon_{xy} \\ 2\varepsilon_{yz} \\ 2\varepsilon_{xz} \end{Bmatrix} = \begin{bmatrix} \frac{\partial}{\partial x} & 0 & 0 \\ 0 & \frac{\partial}{\partial y} & 0 \\ 0 & 0 & \frac{\partial}{\partial z} \\ \frac{\partial}{\partial y} & \frac{\partial}{\partial x} & 0 \\ 0 & \frac{\partial}{\partial z} & \frac{\partial}{\partial y} \\ \frac{\partial}{\partial z} & 0 & \frac{\partial}{\partial x} \end{bmatrix} \begin{Bmatrix} u \\ v \\ w \end{Bmatrix}. \quad (2.63)$$

Hence, the interpolation matrix of node a shape function derivatives is:

$$\mathbf{B}_a = \begin{bmatrix} \frac{\partial N_a}{\partial x} & 0 & 0 \\ 0 & \frac{\partial N_a}{\partial y} & 0 \\ 0 & 0 & \frac{\partial N_a}{\partial z} \\ \frac{\partial N_a}{\partial y} & \frac{\partial N_a}{\partial x} & 0 \\ 0 & \frac{\partial N_a}{\partial z} & \frac{\partial N_a}{\partial y} \\ \frac{\partial N_a}{\partial z} & 0 & \frac{\partial N_a}{\partial x} \end{bmatrix}, \quad a = [1..4]. \quad (2.64)$$

Then strain field is written using the following shorthand notation:

$$\nabla^s(\hat{\mathbf{u}}) = \mathbf{B}\mathbf{d} \leftrightarrow \nabla^s(\hat{\mathbf{u}}) = \sum_{a=1}^4 \mathbf{B}_a \mathbf{d}_a, \quad (2.65)$$

where \mathbf{d}_a is the nodal displacement vector at node a .

In case of discontinuity within an element, the tetrahedron is split into two sub volumes Ω^\oplus and Ω^\ominus delimited by the interface Γ_d of direction vector \mathbf{n} (see FIG. (2.13)). It is recalled that this surface is assumed to be flat (\mathbf{n} is constant over Ω). Numerical implementation of this geometrical construction is not trivial and several cases have to be taken into account depending on the surface orientation. Indeed, Ω^\oplus and Ω^\ominus can be polyhedra of respectively 6 and 4, 5 and 5 or 4 and 6 nodes. And since the formulation involves only the volumes V^\oplus and V^\ominus (not the interface area), it has to be considered with utmost attention. When dealing with interface elements (with weak discontinuity), the discontinuity surface is constructed regarding geometrical properties of the excursion. It leads to a predictive computation of volumes (V^\oplus and V^\ominus) and interface orientation \mathbf{n} independent to the stress state. It is recalled that the interpolation matrix \mathbf{G}_w can be decomposed into Θ , a piece-wise function that depends on the sub domain and \mathbf{H}_w a matrix that contains interface orientation information (see EQ. (2.25)). In order to respect orthogonal condition between stress and enhanced strain field, the choice of Θ shape is still:

$$\Theta = \begin{cases} \Theta^\oplus = \frac{V^\ominus}{V} & \text{in } \Omega^\oplus \\ \Theta^\ominus = -\frac{V^\oplus}{V} & \text{in } \Omega^\ominus \end{cases} \quad (2.66)$$

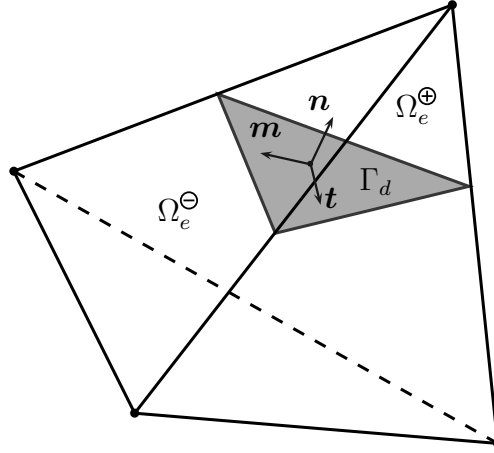


Figure 2.13: 4-node tetrahedron element.

Following the same Voigt convention, \mathbf{H}_w can be constructed so that the vector format strain enhancement matches its tensor definition EQ. (2.7). The interface orientation vector is written in the global coordinate system $\mathbf{n} = \{n_x \ n_y \ n_z\}^T$, leading to the following interpolation matrix format:

$$\mathbf{H}_w = \begin{bmatrix} n_x^2 & n_x m_x & n_x t_x \\ n_y^2 & n_y m_y & n_y t_y \\ n_z^2 & n_z m_z & n_z t_z \\ 2n_x n_y & n_x m_y + n_y m_x & n_x t_y + n_y t_x \\ 2n_y n_z & n_y m_z + n_z m_y & n_y t_z + n_z t_y \\ 2n_x n_z & n_x m_z + n_z m_x & n_x t_z + n_z t_x \end{bmatrix}. \quad (2.67)$$

This time, regarding strong discontinuities, EAS and KES have to be considered separately. It is recalled that the EAS enhancement is based on the tensor operator $(\bullet \otimes \mathbf{n})^s$ that equivalence in Voigt notation is noted \mathbf{H}_s^* . Still respecting conventions EQ. (2.63), EAS enhancement interpolation matrix of the bounded part is written:

$$\mathbf{G}_{s,b}^* = -\frac{A}{V} \mathbf{H}_s^* \quad \text{with} \quad \mathbf{H}_s^* = \begin{bmatrix} n_x & 0 & 0 \\ 0 & n_y & 0 \\ 0 & 0 & n_z \\ n_y & n_x & 0 \\ 0 & n_z & n_y \\ n_z & 0 & n_x \end{bmatrix}. \quad (2.68)$$

Even though EAS interpolation matrix $\mathbf{G}_{s,b}^*$ includes the interface area, its computation is unnecessary. Indeed, since, $\mathbf{G}_{s,b}^*$ appears only in the strong discontinuity equation $\mathbf{h}_{[|u|]}$, the area can be simplified along with that of the interface integration of the Dirac-delta function. Hence it does not appear in the system anymore. It is the reason why the general

system has been standardized in terms of \mathbf{H}_s^* and not $\mathbf{G}_{s,b}^*$. It is important to be aware that this property comes directly from the choice of EAS enhancement of the virtual strain.

Since it comes from the same operator, the KES is quite similar, substituting geometrical information A, V and \mathbf{n} by the displacement considerations within φ_e EQ. (2.26). Actually kinematics carries geometrical information too since φ_e is constructed considering which nodes are in Ω^\oplus . \mathbf{G}_s is written:

$$\mathbf{G}_s = - \begin{bmatrix} \frac{\partial \varphi_e}{\partial x} & 0 & 0 \\ 0 & \frac{\partial \varphi_e}{\partial y} & 0 \\ 0 & 0 & \frac{\partial \varphi_e}{\partial z} \\ \frac{\partial \varphi_e}{\partial y} & \frac{\partial \varphi_e}{\partial x} & 0 \\ 0 & \frac{\partial \varphi_e}{\partial z} & \frac{\partial \varphi_e}{\partial y} \\ \frac{\partial \varphi_e}{\partial z} & 0 & \frac{\partial \varphi_e}{\partial x} \end{bmatrix}. \quad (2.69)$$

Remark: Even if not explicitly revealed, the kinematics formulation is related to a length factor through derivation of shape functions. While EAS gives a simple one-dimensional measure through the ratio A/V , KES gives a more sophisticated length-scale strongly depending on the interface orientation. It can easily be shown that if the interface is parallel to one face of the tetrahedron, both enhancement are proportional: $\mathbf{G}_s \propto \mathbf{G}_{s,b}^*$ (see [Wells, 2001]).

All components of the enhanced strain field are now explicitly defined. The stress field outside the discontinuity is given using the standard elastic Hooke operator \mathbf{C} :

$$\check{\boldsymbol{\sigma}} = \mathbf{C}\boldsymbol{\varepsilon} = \begin{Bmatrix} \sigma_{xx} \\ \sigma_{yy} \\ \sigma_{zz} \\ \sigma_{xy} \\ \sigma_{yz} \\ \sigma_{xz} \end{Bmatrix} = \frac{E}{1+\nu} \begin{bmatrix} \frac{1-\nu}{1-2\nu} & \frac{\nu}{1-2\nu} & \frac{\nu}{1-2\nu} & 0 & 0 & 0 \\ \frac{\nu}{1-2\nu} & \frac{1-\nu}{1-2\nu} & \frac{\nu}{1-2\nu} & 0 & 0 & 0 \\ \frac{\nu}{1-2\nu} & \frac{\nu}{1-2\nu} & \frac{1-\nu}{1-2\nu} & 0 & 0 & 0 \\ 0 & 0 & 0 & \frac{1}{2} & 0 & 0 \\ 0 & 0 & 0 & 0 & \frac{1}{2} & 0 \\ 0 & 0 & 0 & 0 & 0 & \frac{1}{2} \end{bmatrix} \begin{Bmatrix} \varepsilon_{xx} \\ \varepsilon_{yy} \\ \varepsilon_{zz} \\ 2\varepsilon_{xy} \\ 2\varepsilon_{yz} \\ 2\varepsilon_{xz} \end{Bmatrix}. \quad (2.70)$$

In case of material discontinuities, two elastic tensors are defined \mathbf{C}^\oplus and \mathbf{C}^\ominus respectively defined by Young modulus and Poisson ratio E^\oplus, ν^\oplus and E^\ominus, ν^\ominus . In contrast to beam element presented above, the stress fields in Ω^\oplus and Ω^\ominus can be different. Only projections on \mathbf{n} are equals. Hence, the traction vector has to be defined as in EQ. (2.39).

5.4.2 Localization and opening criterion

Since the discontinuity surface orientation is constructed with geometrical properties for interface elements and with stress consideration otherwise, the two cases have to be treated separately.

It is recalled that in the first case both strain and displacement discontinuity have the same physical interface. Being defined by the heterogeneities, its orientation \mathbf{n} is known

prior to any mechanical calculation. Hence, the traction vector is computable and has a physical meaning before localization. It can therefore be used in the criterion. In order to represent the interface orientation as the weakest direction, the equivalent stress for localization is defined as the projection of the traction vector on it:

$$\Phi_1 = \sigma_{\text{eq}} - \sigma_y = \mathbf{n} \cdot \mathbf{T} - \sigma_y = T_n - \sigma_y, \quad (2.71)$$

with

$$\mathbf{T} = \frac{1}{V} \mathbf{H}_s^{*,T} (V^{\oplus} \check{\boldsymbol{\sigma}}^{\oplus} + V^{\ominus} \check{\boldsymbol{\sigma}}^{\ominus}). \quad (2.72)$$

On the contrary, if no material discontinuity can define an interface, strong discontinuity appears with stress state consideration. It can be noted that in this case, a constant stress tensor is given for the whole element since it is free of material discontinuity. Its orientation is defined by the principal direction of the stress tensor. If σ_1 is its first (larger) eigenvalue then:

$$\Phi_1 = \sigma_{\text{eq}} - \sigma_y = \sigma_1 - \sigma_y. \quad (2.73)$$

When localization occurs, *i.e.* $\Phi_1 > 0$, the corresponding eigenvector \mathbf{n}_1 is recorded and set as the interface orientation: $\mathbf{n} \leftarrow \mathbf{n}_1^{\text{localization}}$. It is assumed that its value remains constant over the whole calculation. Afterwards, the traction vector is defined by:

$$\mathbf{T} = \mathbf{H}_s^{*,T} \check{\boldsymbol{\sigma}}, \quad (2.74)$$

which follows its previous definition with $\check{\boldsymbol{\sigma}}^{\oplus} = \check{\boldsymbol{\sigma}}^{\ominus} = \check{\boldsymbol{\sigma}}$.

In both cases, after localization the discontinuity surface and its orientation \mathbf{n} are defined. In order to model the same failure mechanism whether an interface element is considered or not, the opening criterion Φ_o is assumed to be identical. The equivalent stress is taken as the projection of the traction vector on \mathbf{n} :

$$\Phi_o = \mathbf{n} \cdot \mathbf{T} - (\sigma_y - q) = T_n - (\sigma_y - q). \quad (2.75)$$

Notice that a much more complex criterion is used for beam elements. This difference is justified by the fact that shear cannot be taken into account by using the latter criterion with the simple kinematics representation of beams, where all modes are independent. Herein, due to the full stress and strain tensors representation, T_n has the necessary shear components for the present problematic.

Furthermore, it leads to a very simple written expression of the equivalent stress derivatives:

$$\frac{\partial \sigma_{\text{eq}}}{\partial \mathbf{T}} = \mathbf{n}. \quad (2.76)$$

It occurs that in this special case, an analytical solution exists in order to solve the local system SYS. (2.42). Following the notations of the previous section $\mathbf{h}_{[|\varepsilon|]}$ is written

$$\mathbf{K}_{\text{wb}} \mathbf{d} + \mathbf{K}_{\text{ww}} [|\varepsilon|] + \mathbf{K}_{\text{ws}} [u] = \mathbf{0}, \quad (2.77)$$

and $\mathbf{h}_{[u]}$

$$\mathbf{K}_{s^*b}\mathbf{d} + \mathbf{K}_{s^*w}[[\varepsilon]] + K_{s^*s}[u] - \sigma_y \exp\left(-\frac{\sigma_y}{\mathcal{G}_f}[u]\right) = 0. \quad (2.78)$$

From the linear equation EQ. (2.77), $[[\varepsilon]]$ can be expressed in terms of \mathbf{d} and $[u]$ and by injecting it in EQ. (2.78). Thus yields:

$$\underbrace{(\mathbf{K}_{s^*b} - \mathbf{K}_{s^*w}\mathbf{K}_{ww}^{-1}\mathbf{K}_{wb})}_{T_e}\mathbf{d} + \underbrace{(K_{s^*s} - \mathbf{K}_{s^*w}\mathbf{K}_{ww}^{-1}\mathbf{K}_{ws})}_M[u] - \sigma_y \exp\left(-\frac{\sigma_y}{\mathcal{G}_f}[u]\right) = 0. \quad (2.79)$$

Because \mathbf{n} is constant and σ_{eq} depends on \mathbf{T} in a linear way, \mathbf{K}_{s^*b} and K_{s^*s} do not depend on $[u]$. The solution to the equation

$$T_e + M[u] = \sigma_y \exp\left(-\frac{\sigma_y}{\mathcal{G}_f}[u]\right) \quad (2.80)$$

is represented in FIG. (2.14).

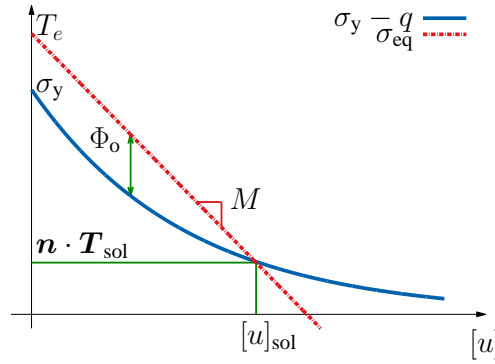


Figure 2.14: Graphical representation of the strong discontinuity equation.

With $M < 0$, the equivalent stress decreases as the crack grows. Hence, since T_e represents the equivalent stress for $[u] = 0$, a solution always exists if $T_e > \sigma_y$. Fortunately, this condition is always fulfilled since this equation has to be solved after localization ($\Phi_1 > 0$). The solution for this equation is given through the main real branch of the Lamber W function W_0 by:

$$[u]_{sol} = \frac{\mathcal{G}_f}{\sigma_y} \left(W_0 \left(\frac{\sigma_y^2 \exp\left(\frac{\sigma_y T_e}{\mathcal{G}_f M}\right)}{\mathcal{G}_f M} \right) - \frac{\sigma_y T_e}{\mathcal{G}_f M} \right). \quad (2.81)$$

Then, once $[u]_{sol}$ is determined, $\mathbf{h}_{[[\varepsilon]]}$ can directly be solved, giving the value of $[[\varepsilon]]_{sol}$:

$$[[\varepsilon]]_{sol} = -\mathbf{K}_{ww}^{-1}(\mathbf{K}_{wb}\mathbf{d} + \mathbf{K}_{ws}[u]_{sol}) \quad (2.82)$$

This leads to a really simple and light local framework where no Newton algorithm is necessary in order to find proper internal variable values that match the opening criterion.

The framework using 4-node tetrahedron is now completely defined. Concluding remarks are now proposed prior to move on to the next chapter where numerical examples of this implementation are given.

6 Concluding remarks

In this second chapter, the E-FEM has been presented in the context of the modeling of quasi-brittle materials. First kinematics of weak and strong discontinuities have been detailed. Then the mathematical framework based upon a three-field variational formulation have been explained and the author has shown how weak and strong kinematics are introduced into this formulation leading to the problem to be solved. After that several FE discretization with different types of finite elements (bars, Timoshenko beams and 4-node tetrahedra) have been introduced. Some comparisons between bars and Timoshenko beams results have been performed justifying the interest of the step beyond in the local kinematics made by the author. Nevertheless no result dealing with 4-node tetrahedra has been shown. This is the concern of the next chapter of this work in which focus is made only on computational results with 4-node tetrahedra. First some mechanical results are presented in the context of uniaxial and cyclic tension and compression tests. Then the author turns to RVE determination in the context of linear and non-linear properties. Finally a multi-physics problem is treated modeling the delayed Ettringite Formation (DEF).

Prior to any numerical results (chapter 3), several comments are made on the latter volume element implementation.

On a purely geometrical point of view, using tetrahedra instead one-dimensional elements increases the mesh node density needed in order to accurately represent a morphology. Basically, it is due to the fact that one tetrahedron is made of six one-dimensional bars. This principle is depicted (in two dimensions) in FIG. (2.15) where the same simple morphology (in grey) is projected on a frame and a mesh based on the same geometry.

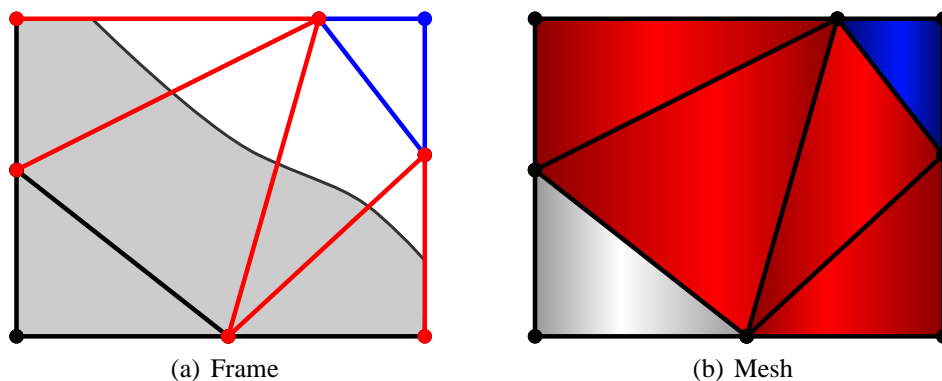


Figure 2.15: Two-dimensional illustration of morphological projection onto frames and meshes.

In this example, where the same number of nodes is used, it can be seen that the matrix is represented by 3 elements in the case of bar elements and by 1 in the case of tetrahedra (in blue). Hence frame discretization has two supplementary elements which can behave “independently”. Considering the interface (in red), the difference is less important but still falls from 5 to 4 elements, respectively. However, since no failure mechanism occurs in the aggregates, although the phase more coarsely discretized, a full kinematics can still be considered as an advantage for mesh discretization. Eventually, there is an inherent trade-off between geometrical and kinematical representations. Notice that the gap between these two methods increases in the three-dimensional context.

On a numerical point of view, some difficulties embedded within the volumetric element design are worth noticing. It has been shown that the strain enhancement is based on kinematics (KES EQ. (2.12)) and statical (EAS EQ. (2.23)) considerations for the actual and virtual field, respectively, leading to a non symmetrical formulation (SKON). It can be proved that if the discontinuity surface is perpendicular to one face of the tetrahedron, both KES and EAS are identical [Jirásek, 2012]. In the frame context, due to the one-dimensional aspect of elements, this condition is always fulfilled leading to a more simple general formulation. Furthermore, the unstable aspect of the kinematics function φ_e leads to several numerical concerns. However, solutions can be found in the literature that leads to more complex but robust implementation. Detailed discussion on that matter is made in [Wells, 2001]. Finally, due to its full kinematics representation, the local failure implemented in volume elements only affects one part of the stress tensor. In contrast to bar or beam element, it prevents the model from representing a local ruined state. However, multi-criteria failure [Simo and Hughes, 2008] or introduction of a damage behavior (usually done in this context [Oliver, 1996a]) can be of help on that matter. Herein, following [Wells and Sluys, 2001], a discrete damage-type based model is performed on the traction vector in order to drive a shear degradation through the crack opening.

Chapter 3

Applications to cementitious materials modeling

Contents

1	Introduction	106
2	One-dimensional macroscopic loading paths	108
2.1	Analysis of the asymmetric macroscopic response for traction and compression loading paths	108
2.2	Transversal strain	118
2.3	Dissipated energy	120
2.4	Induced anisotropy	122
2.5	Uniaxial cyclic compression loading	124
3	Representative Volume Element for elastic and failure properties	129
3.1	Experimental protocol	130
3.2	Young moduli analysis	131
3.3	Tensile and compressive strength	133
3.4	Comments	135
4	Application to the Delayed Ettringite Formation	136
4.1	Numerical simulation	137
4.2	Homogeneous mortar expansion	138
4.3	Residual Young modulus	139
5	Concluding remarks	140

1 Introduction

In this last chapter, the meso-model — based on the morphological representation and the Embedded Finite Element Method presented in Chapter 1 and 2, respectively — is subjected to several tests in the context of cementitious materials behavior. This will be an opportunity to show and comment on the different advantages of the methods. These tests can be broadly classified into three categories, which constitute this chapter outline.

In section 2, attention is focused on the capability of the model to represent the main features of cementitious materials by means of mechanical loading only. First uniaxial tension and compression loading are performed, the aim being: on the one hand, to show the emergence of the typical asymmetry of the respective macroscopic responses and on the other hand, to make a complete review of the cracks' patterns. The observations highlight the close relationship between these two phenomena. In addition, non proportional loadings are performed in order to analyze any anisotropic behavior that could be induced by the failure process. This study is carried out on the previous uniaxial tension and compression tests by means of a damage indicator — linear post-analysis on Young modulus degradation — as well as residual strength — non linear post-analysis on tensile strength degradation. Finally, by submitting the model to cyclic compression loading, information such as the shared responsibility of reversible damage and irreversible plasticity in the failure process, can be revealed. Consistency of the meso-model results are compared to the extent possible with experimental results on both macroscopic responses (see FIG. (1)) and geometrical cracks' pattern aspects.

Then, a statistical study is conducted in the section 3, by means of Representative Volume Element (RVE) determination, illustrating the capacity of the model to be used as a homogenization tool. Carried out within a Monte-Carlo procedure the study provides RVE for linear and non linear properties. First, RVE of linear properties — Young modulus — are computed. Then, innovative results on RVE of non-linear properties — tensile strength — are evaluated. These results are discussed and the limits of the computations are explained along with interesting perspectives.

In section 4, a multi-physic example related to concrete durability is addressed. In addition to the major industrial challenge associated with these problematics, it can be seen as an opportunity to depict an underlying significant advantage of meso-models, namely an accurate knowledge of physically meaningful mesoscopic information. Herein, this information is the crack opening. Schematically speaking, mesoscopic results (*i.e.* crack opening values) from a first damaging physical process (*e.g.* mechanical, chemical, thermal, *etc*) are the starting point of secondary calculations designed to determine macroscopic (homogenized) material properties. These degraded properties can also be based on different physical principles (*e.g.* mechanic, diffusion, transfer, *etc*). An example of chemo-mechanical coupling in the case of Delayed Ettringite Formation (DEF) is illustrated through the corresponding effect on mechanical properties such as Young modulus and strengths.

Each numerical example given in this chapter is made on a heterogeneous $100 \times$

$100 \times 100 \text{ mm}^3$ cubical specimen where two phases are modeled using the morphological framework presented in Chapter 1. Based on unions of excursion sets, this method explicitly represents aggregates of different sizes melted within a matrix that is, roughly speaking a mortar. The latter are modeled with three average diameters of 15, 7 and 5 mm representing respectively 25, 50 and 25 % of the total 30 % volume fraction (see FIG. (1.21)). Following the *non-adapted* mesh spirit, once projected onto the FE discretized space, this morphology is represented by two kinds of elements: those which are completely included within the matrix or an aggregate and those close to an interface that are split by a weak discontinuity. In order to catch the geometrical information of the smallest heterogeneities, the mesh used to compute the following examples has about $550 \cdot 10^3$ nodes. FIG. (3.1) shows a projection of a morphology onto the mesh in which only interface and aggregates elements are represented in light and dark grey, respectively. Finally, in order to be consistent in the several calculations, the material properties of each phase of the meso-scale materials given TAB. (3.1) are kept identical for the first two sections. Unless otherwise indicated, it is recalled that, numerical implementation is made with 4-node tetrahedron Finite Element. Thus the numerical results of this chapter reflect the interest of going further into the complexity of the FE kinematics regarding the bar or Timoshenko beams presented in the previous chapter.

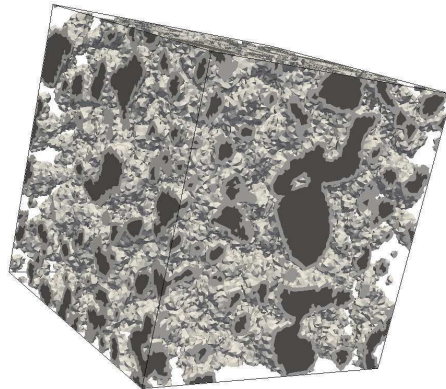


Figure 3.1: Projection of the meso-scale morphology onto a FE mesh.

Phase	E [GPa]	ν [-]	σ_y [MPa]	\mathcal{G}_f [$J.m^{-2}$]
Aggregates	100	0.2	-	-
Mortar	20	0.2	9	0.1

Table 3.1: Meso-scale material characteristic of each phase.

Finally, the numerical implementation has been made, following a component-oriented programming spirit, with COFEAP [Kassiotis and Hautefeuille, 2008], a module of the FE code FEAP [Taylor, 2003], assigned to treat mechanical, thermal and chemical problems, using CTL as the middleware [Niekamp, 1995]. A choice based, on the one hand, on the

suitable architecture of FEAP in regards to the non-intrusive implementation that E-FEM requires, and on the other hand, the practical aspect the component-oriented programming of COFEAP in regards to coupled problems. Details on the different aspects of this specific numerical strategy can be found in [Colliat, 2010].

2 One-dimensional macroscopic loading paths

As a first illustration of the mechanical model's basic features, the numerical application presented in this section deals with simple one-dimensional macroscopic loading paths (simple tension and compression). Computations are performed under *displacement control* according to the first spatial axis (X -direction). The four faces in the perpendicular direction are stress free. Hereafter, a value corresponding to the X -direction is referred to as *axial* whereas those of the *transversal* are assumed to be an average value according to the Y and Z -direction.

Material characteristics are set at the meso-scale, therefore, each phase possesses specific data. It is recalled that the model contains two elastic and two failure parameters respectively being, the Young modulus E , the Poisson ratio ν , the yield stress σ_y and the fracture energy \mathcal{G}_f . The attributed values are summarized in TAB. (3.1).

It is worth noting that:

- Aggregates are assumed to remain elastic and so no crack may initiate at those points.
- Enhanced elements do not require any specific characteristics in the elastic regime. Indeed, as presented in the previous chapter, they model a perfect interface with infinite rigidity. This point is a major advantage of the E-FEM method compared to other strategies such as the introduction of cohesive zones that require some values for the normal and tangential rigidities.

2.1 Analysis of the asymmetric macroscopic response for traction and compression loading paths

Two *independent* tests — tension and compression — are performed on the specimen (see FIG. (3.1)). FIG. (3.2) shows the macroscopic axial stress obtained for both tests along the macroscopic axial strain. Clearly, both loading paths are leading to a macroscopic softening behavior, which can be interpreted as two macroscopic failures. This point is a major result, already obtained by [Benkemoun et al., 2010] dealing with truss elements. Indeed, the use of a single failure criterion at meso-scale, which is triggered in tension, shows the emergence of a complex behavior at macro-scale due to the high number of elements and to the morphology of the heterogeneities. Yet, FIG. (3.2) also shows that the two macroscopic responses are much more different than in [Benkemoun et al., 2010].

Dealing with both cases, a common pattern can still be identified. It is made of three parts: first, an elastic regime — no cracking — is observed from the stress free point O up to a yielding point A . It is followed by a loss of rigidity (more noticeable in compression) up to the critical failure peak B . Then a softening behavior is represented corresponding to the progressive ruin of the specimen at C . Those steps are now referred as: $[OA]$ the elastic region, $[AB]$ the diffuse cracking region, B the localization and $[BC]$ the post-localization. Even though they are present in both tests, their characteristic values differ notably from tension to compression. An analysis of the two behaviors is now proposed first from a quantitative point of view based on upscaled values and then from a qualitative point of view based on the cracks' pattern.

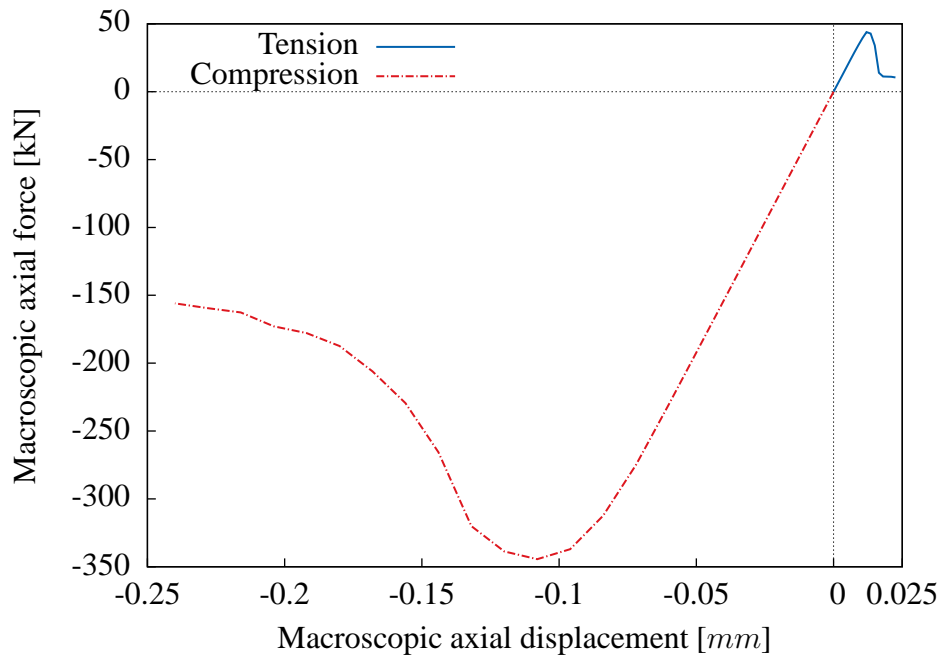


Figure 3.2: Macroscopic response for tension and compression tests.

2.1.1 Upscaled material properties

After FE calculation, macroscopic characteristics can be determined from those results. It is recalled that, due to the sequential multi-scale framework, those quantities shall be based on a set of independent realizations of the morphology and thus on a set of FE computations. This point is investigated in section 3 of this chapter, in which effective macroscopic properties according to a simple Monte-Carlo process are computed.

Here, attention is focused on a single realization only. Investigation on the macroscopic values are made for: the macroscopic Young modulus E^M , the macroscopic tensile and compressive strengths σ_f^M , the macroscopic failure strains ε_f^M and finally, the total dissipated energy D^p , the latter being calculated by integration of the macroscopic axial

force over the axial displacement. The different upscaled characteristics are summarized in TAB. (3.2) (comments on the Poisson ratio ν^M are given in the next section along with other transversal behavioral quantities).

Loading path	E^M [GPa]	ν^M [-]	σ_f^M [MPa]	ε_f^M [-]	\mathcal{D}^p [J]
Compression	37.8	0.202	34.4	$1.08 \cdot 10^{-3}$	50
Tension	37.8	0.202	4.4	$1.2 \cdot 10^{-4}$	0.5

Table 3.2: Macroscopic upscaled material properties for both tension and compression.

As expected the initial elastic behavior is strictly symmetric. Moreover, the model provides a value of the macroscopic Young modulus E^M that fits inside the Hashin-Shtrikman range [Hashin and Shtrikman, 1963]. Even though it is quite difficult to observe the end of the purely elastic region on the curves, it can safely be assumed that, for compression, the transition with the non linear behavior occurs for a more important macroscopic stress than for tension. This non-symmetrical elastic domain is the first feature that emerges from the multi-scale framework. Clearly it is mainly due to the structural effect brought by the heterogeneous character of the mesoscale. From a phenomenological modeling point of view, this feature would require the introduction of (for example) two yield surfaces, one for tension and another one for compression. It is recalled that herein, only one mesoscopic yield stress σ_y is used. Actually, this comment can be made (but will not be) for all the other features presented below.

Regarding the energy \mathcal{D}^p needed to reach the specimen ruin, it can be noted that both are greater than the mesoscopic fracture energy \mathcal{G}_f (in $J.m^{-2}$) assigned to the mortar (corresponding values of \mathcal{D}^p in tension and compression are 50 and 5 000 $J.m^{-2}$, respectively). Furthermore, the fact that this energy is significantly greater in compression highlight the more brittle behavior of concrete-like materials when solicited in tension. It is naturally linked with the asymmetric strength values and their corresponding failure strains which ratios of compression to tension are respectively 7.8 and 9.

2.1.2 Cracks' pattern analysis

The additional analysis now proposed is based on the cracks' patterns. It directly benefits from the multi-scale framework, giving a quantitative link between the meso-scale failure process and the macroscopic material behavior. It can be seen as an illustration and explanation of the macroscopic asymmetries described just above. From a practical point of view, the local spirit of the numerical implementation, using the E-FEM as presented in the previous chapter, provides the knowledge of the crack opening of each element (tetrahedron). Since, no non-local governing laws are implemented, each FE is "independent" and can potentially represent a micro-crack. Henceforth, in order to visualize the cracks' pattern, focus is placed on the only representation of tetrahedron with a non-null crack opening value. Hereafter, those elements are referred as *activated elements*.

FIG. (3.3) shows those activated elements at the different stages of the macroscopic

tension test, and the color scale representing the crack opening in mm . First, after the elastic region FIG. (3.3(a)), it can be seen that barely opened micro cracks are scattered all over the cube. It corresponds to a *diffuse cracks' pattern* responsible for the loss of rigidity. Then, by increasing the imposed macroscopic displacement, the localization occurs FIG. (3.3(b)). It still corresponds to a diffuse cracks' pattern with more activated elements but with a zone where micro cracks are more dense and start to coalesce. It is the ignition of a *macroscopic crack* that eventually leads to a softening behavior. During the post-localization FIG. (3.3(c)), the macro crack has completely percolated through the cube splitting it apart. It roughly forms a plan perpendicular to the axial direction, crinkling around the aggregates. However, it can be noted that regarding the diffuse cracks' pattern, hardly anything has changed. The conclusion can be drawn that the energy is only dissipated at the macro crack and that the rest of the domain is mainly unloading. Finally a last remark can be made on the non symmetrical aspect of the cracks' pattern.

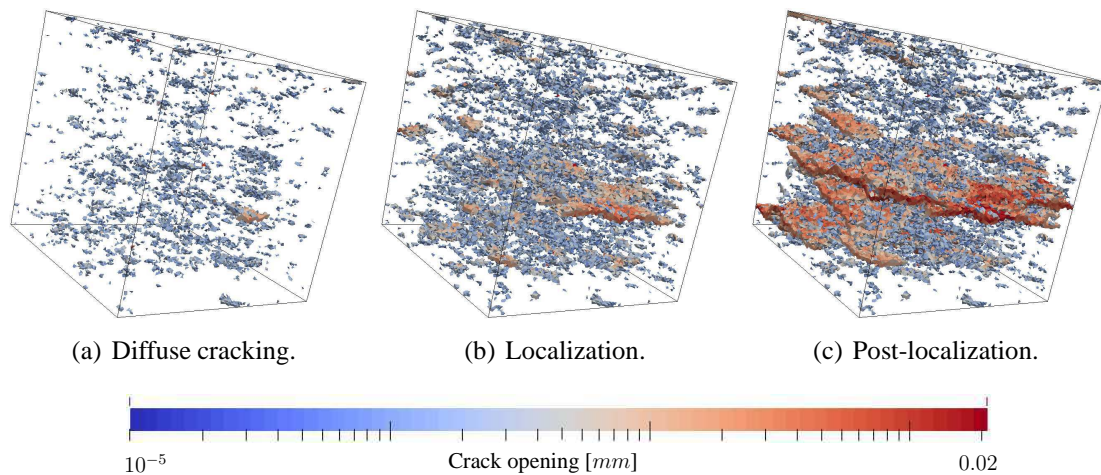


Figure 3.3: Cracks' pattern evolution for a tension test.

This pattern can also be seen on the displacement field contours. The three states are shown in FIG. (3.4) in which the axial macroscopic displacement is represented in mm . It can be seen that the diffuse cracking does not appear distinctly. However, the localization and the failure can clearly be detected depicting the discrete aspect of macroscopic cracking.

On the other hand, it can be seen in FIG. (3.5), in which the same steps as above are shown, that the compression cracks' pattern is rather different. At the beginning, a diffuse cracking also occurs. However, it rapidly differs from the tension test since small micro cracks coalesce between the aggregates, forming several paths with no privileged direction FIG. (3.5(a)). It leads to a more important loss of rigidity noticeable on the macroscopic response curve FIG. (3.2). At the localization point, every crack is connected forming a macroscopic crack network which goes around the aggregates all over the specimen. Finally during the post-localization, this network grows and nearly all the elements within the mortar are activated. Depending on their crack opening, those elements are

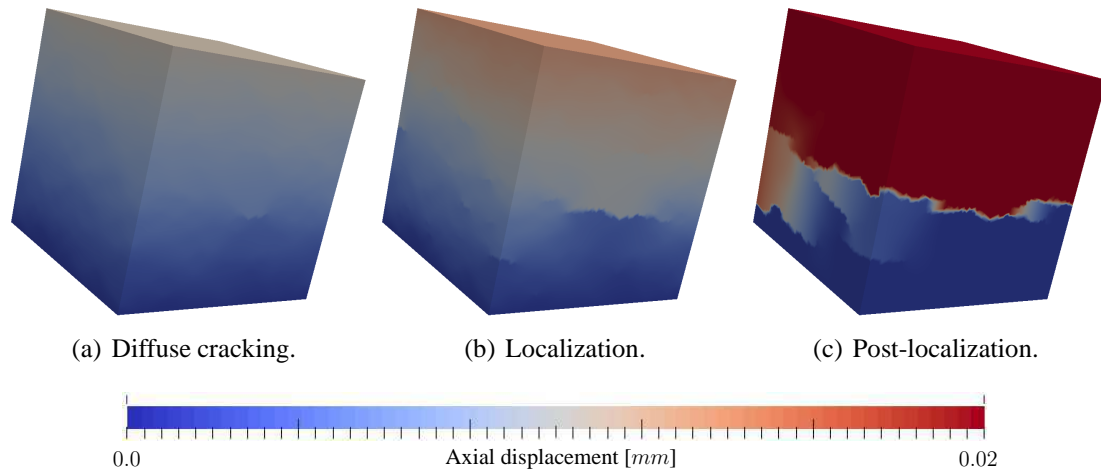


Figure 3.4: Axial displacement field during a tension test.

roughly forming a skeleton made of several planes parallel to the axial macroscopic displacement. The main differences between tension and compression cracks' pattern are that: first, before the localization, the latter does not show any specific propagation direction. And secondly, it eventually leads to a failure process more homogeneous and uniformly distributed all over the specimen. It can be pointed out that in this case, the term “localization” is not necessary suitable since cracks propagation does not occur in a specific place. Nevertheless, this term is still used and has to be seen as a stage when enough localizations occurs to cause a macroscopic softening (interpreted as the specimen failure).

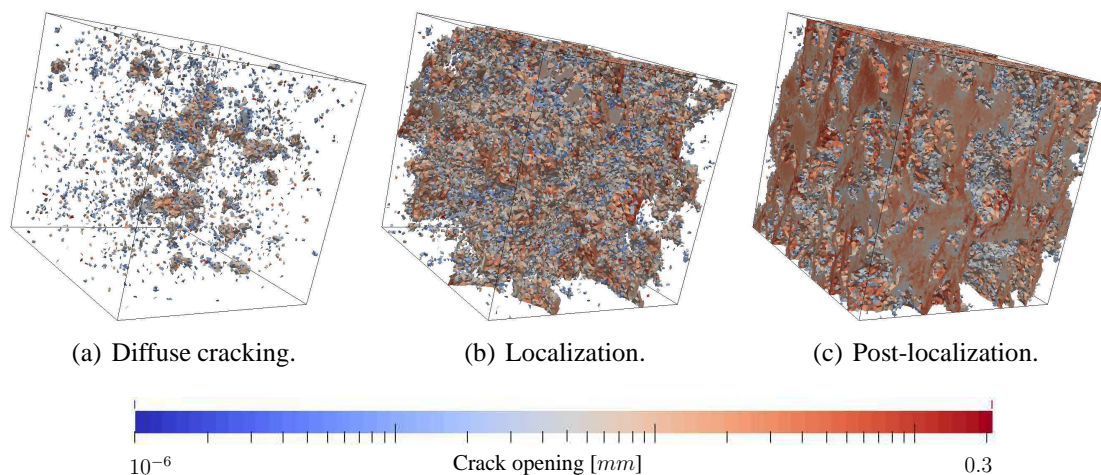


Figure 3.5: Cracks' pattern evolution for a compression test.

The features presented just above can also be depicted through the displacement field contours. Herein, focus is placed on the displacement along each direction. Prior to the

localization step, due to the “homogeneous” repartition of cracks, the non linear behavior is hardly noticeable on the displacement fields hence, it has not been represented. However it is shown (with different scale ranges) after the localization in FIG. (3.7) where, from left to right, the pictures represent the axial displacement X , and the two transversal displacements Y and Z . A discontinuous zone can be observed on the axial field. However, this time, it does not draw a frontier as clear as for the tension test. Indeed, several borders following the axial direction can be seen. It shows a *sliding* effect due to a mode II opening of some macroscopic the cracks. Besides, the visualization of the network of those perpendicular cracks is improved when looking at the two transversal displacements where two and three planes perpendicular to the solicitation can be detected.

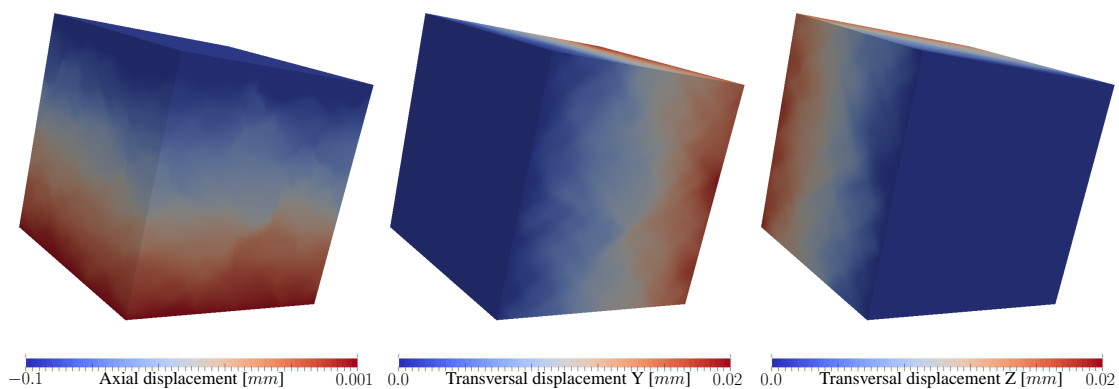


Figure 3.6: Displacement fields during a compression test at the localization.

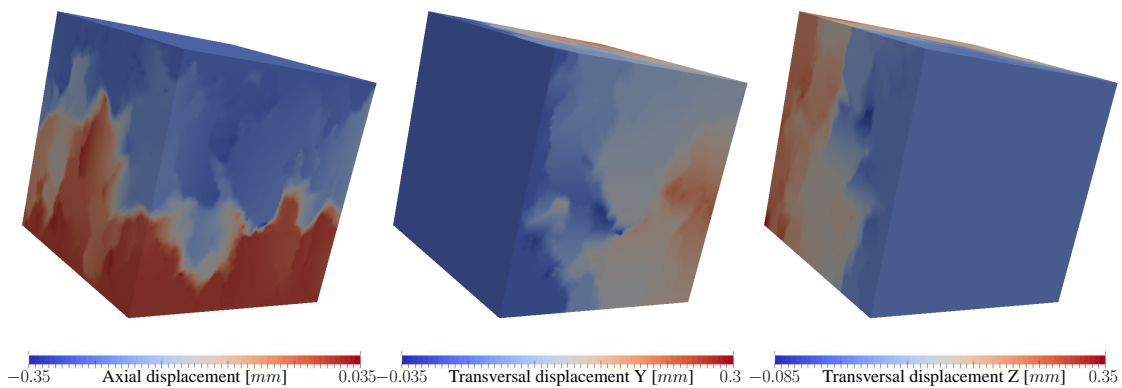


Figure 3.7: Decomposition of the displacement field after localization in compression.

2.1.3 Crack coalescence versus path continuity

The question of the geometrical representation of a macroscopic crack using a local method such as the Embedded Finite Element is not trivial. For example, in the two-dimensional case, using constant triangular elements, it has been shown (see [Jirásek,

2012] for details) that the best way to produce a suitable crack trajectory and avoid numerical issues such as locking is to combine two methods. First a non local formulation of the smeared crack approach, giving crack orientation in each element. Then a tracking algorithm enforcing the crack path continuity between each element.

The major drawback of this implementation is that the *local* nature of the E-FEM (directly inherited from the FEM itself) is lost. Indeed, in addition to non local damage, path continuity enforcement implies, for an element, a crack position that depends on those of its neighbors. Furthermore, since the displacement of activated elements is intrinsically discontinuous, there is no theoretical reason to enforce path continuity. Moreover, in the three-dimensional case, continuity of flat plane (crack) is often impossible.

Herein, the E-FEM implementation has to be placed within the multi-scale context. In this case, a single fractured element is not considered to be representative of any specific macroscopic feature. However, it is when a large number of those activated elements are merging that it may be considered that they model a continuous macroscopic crack. It is for those reasons that no specific efforts has been taken in the path continuity enforcement.

FIG. (3.8) shows, for the same morphology, both compression and tension cracks' patterns after localization with the aggregates. Those pictures depict the consequences of the multi-scale framework presented in this work. The actual modeling of the material heterogeneities and the completely local behavior of each element confer a *natural autonomy* to the model. It leads to complex cracks' patterns that find their way around the aggregates.

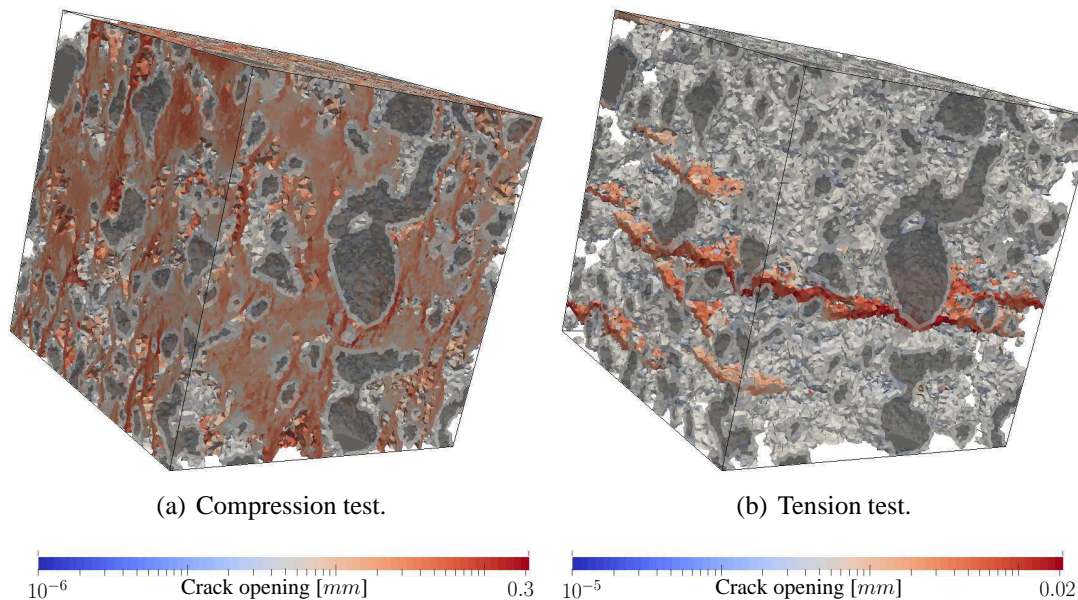


Figure 3.8: Illustration of the macroscopic crack path around the aggregates.

Features like multi-cracking or branching which usually require a complex local numerical implementation (within an element), are herein omitted at the meso-scale. How-

ever, as shown in FIG. (3.9) (which is a zoom of FIG. (3.8(b))) due to the morphological modeling, it can be retrieved at the macro-scale. This picture shows a crack that splits in two branches; a main branch (on the top) with larger opening values and a second branch that eventually vanishes. Generally, these branchings come from an aggregates blocking the way of the crack propagation direction.

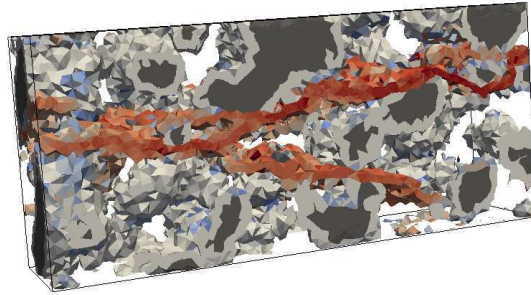


Figure 3.9: Natural branching behavior of the macroscopic crack path around the aggregates.

2.1.4 Consistency of the cracks' pattern in compression

A qualitative comparison between experimental and numerical results is now proposed for the uniaxial compression test. Prior to that, it seems important to mention some basic experimental issues regarding this test such as the friction fit. Often the mechanical characteristic of the compression testing machine part mating the specimen are very different than that of the latter. Hence, the resulting frictions induce a transversal deformation restraint of the specimen. Not only does it leads to an overestimation of the specimen strength [Schickert, 1973] but it also significantly changes the cracks' pattern. Indeed, the uniaxial compression characteristic pattern made of plans parallel to the solicitation (columns) changes in a pyramidal structure if no attention is taken. Since from a numerical point of view, the boundary conditions are "perfect" (meaning that no friction is modeled), it is important to compare those results with those of an experimental set up that tends to minimize this detrimental effect. In addition, the specimen geometry imposes a unit slenderness ratio, preventing the comparison to be made with normalized cylindrical $16\text{ cm} \times 32\text{ cm}$ specimen where the monitored area is far from the boundaries.

For that matter, the comparison is made with experimental results of [Torrenti, 1987] (on cubical specimen of 100 mm length) where the loading is applied by means of steel branches, reducing significantly the maximum induced shear stress prior to the specimen failure [van Mier, 1984]. These results are sketched (from actual ruined specimens) in FIG. (3.10) (a) and (c) in three and two dimensions (face), respectively. They are compared to (b) and (d) and (e) where the last two are two-dimensional slices of the specimen cut in two perpendicular plans parallel to the solicitation direction. The numerical results are a representation of the micro-cracks (activated elements) where the lowest opening values have been faded in order to reveal the network more clearly.

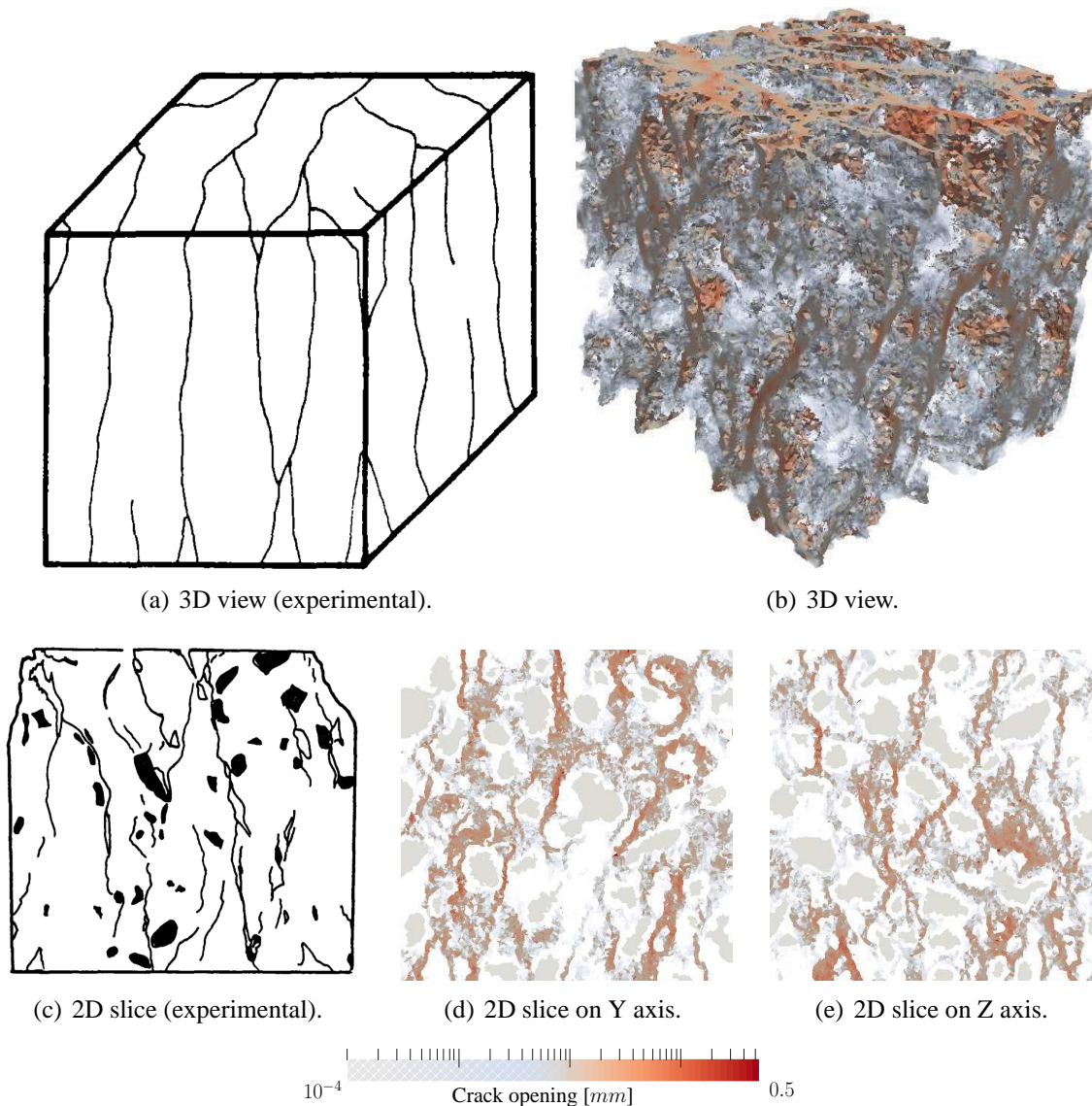
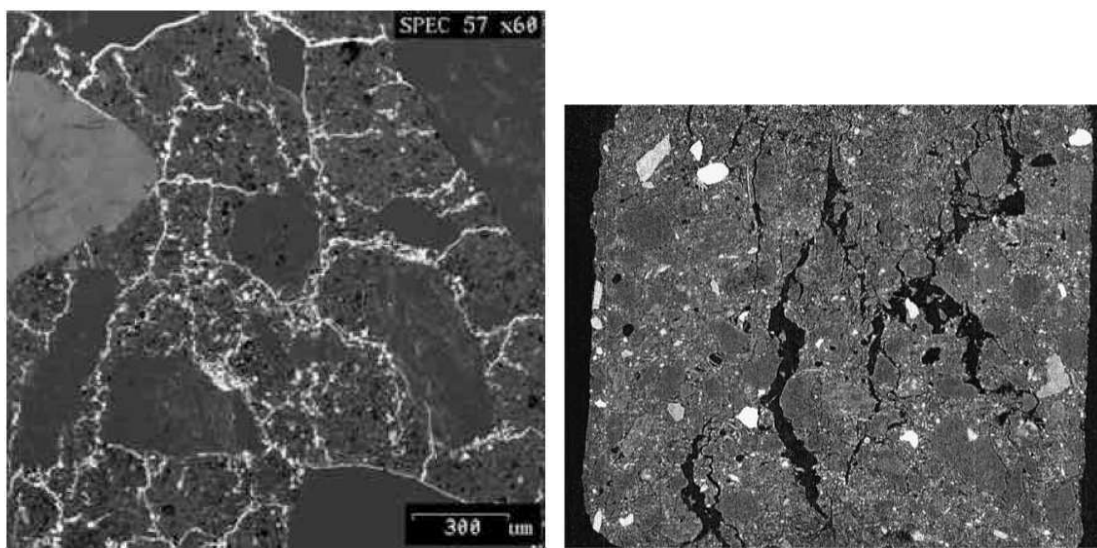


Figure 3.10: Comparison between numerical and experimental cracks' pattern in uniaxial compression (from [Torrenti, 1987]).

The three-dimensional views shows that the column shaped crack network is well represented as for its crack-branching node density, *i.e.* the number of crack. The two-dimensional slices show the complex trajectories, not necessarily going through the specimen from top to bottom.

It is clear that compared to current crack analysis, this comparison seems rather coarse. However, numerically speaking, meso-models still struggle with crack representation, especially in compression. It occurs that herein, results exhibit interesting features that show the model crack representation consistency. Thus it partially justifies the implementation choices, namely the strong local aspect of embedded discontinuities.

In addition, in view of these encouraging results, many different perspectives can be considered. For example in [Nemati et al., 1998], the authors make a statistical analysis of the crack network of damaged mortar specimens (micro-scale) under uniaxial compression using scanning electron microscopy (SEM) (see FIG. (3.11(a))). Geometrical information such as crack orientation distribution, branching-node topology could be compared to results of the numerical model applied to micro-scale morphologies. Another analysis on crack growing made through X-ray microtomography [Landis et al., 2003] where scans were made at different increments could also be an interesting comparison process easily adaptable to the numerical framework.



(a) From [Nemati et al., 1998]: Cracks' pattern of mortar under uniaxial compression using SEM. (b) From [Landis et al., 2003]: Cracks' pattern of mortar under uniaxial compression after localization using X-ray microtomography.

Figure 3.11: Perspective of cracks' pattern modeling at thinner scale (micro-scale).

In this section, a initial analysis of the macroscopic response has been made. It revealed the emergence, at macro-scale, of some complex behavior that was not included in the meso-scale model. It mainly deals with the asymmetric behavior in tension and compression (macroscopic strengths and dissipated energy) which is a major feature of concrete-like materials. Then an enlightened analysis of the cracks' pattern gave an illustration of the mesoscopic mechanisms responsible for the macroscopic behavior. This qualitative description showed complex cracks paths with interesting topological properties (diffuse cracking, coalescence, multi cracking, branching). These initial results are a persuasive illustration of the important role of morphological modeling and more generally, of multi-scale frameworks.

A more advanced analysis based on transversal information is now proposed.

2.2 Transversal strain

Now attention is focused on the macroscopic transversal strains. It is recalled that the axial direction X corresponds to the imposed displacement direction and transversal values are defined as the average of those along Y and Z . The results presented here are still based on the same one-dimensional macroscopic tests (tension/compression) mentioned above.

The macroscopic Poisson ratio can be determined using the transversal strains by:

$$\nu^M = -\frac{\varepsilon_{tr}^M}{\varepsilon_{ax}^M}. \quad (3.1)$$

Herein, this *elastic* property is extended to the diffuse cracking region in order to illustrate the mechanism that leads to the specimen loss of rigidity - see FIG. (3.12) where it is plotted in terms of axial strain for both tension and compression tests. First, the elastic phase shows that the macroscopic Poisson ratio is of the same order as for the meso-scale: $\nu^M = 0.202$ in both cases. Afterwards those values are diverging. First, in tension, the ignition of diffuse cracking cause local strain release and thus make the macroscopic strain decrease along with the Poisson ratio. On the contrary, in compression, this local strain release causes a heightening of the transversal mechanism leading to a significant increase of the Poisson ratio.

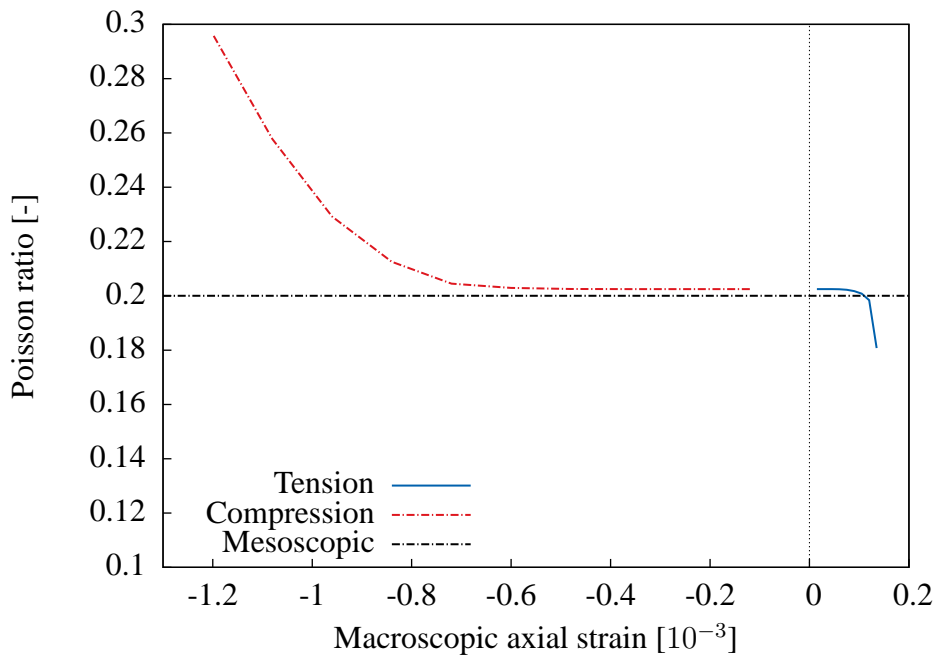


Figure 3.12: Poisson ratio for tension and compression tests vs. axial strain.

Since the meaning of the Poisson ratio is highly contestable with strongly non-linear failure behavior, the post-localization analysis is only based on transversal strains. For

that matter, FIG. (3.13) and FIG. (3.14) show the macroscopic response up to the specimen ruin in terms of the axial strain ε_{ax}^M (solid curve) and of the transversal direction ε_{tr}^M (dashed curve). Regarding the tension test, during the post-peak phase the transversal strain decreases and tends to vanish (see FIG. (3.13)). It represents the unloading that occurs in the specimen - at a macroscopic scale - after the main crack localization. In contrast, during a compression test, the transversal strain still increases after the peak (see FIG. (3.14)). As already mentioned, for this loading path, the cracks' pattern is more a network of several macroscopic cracks than a single localization zone. The dilatancy observed here is the direct result of this *diffuse* cracking process. Besides, it is the same mechanisms that explained the Poisson ratio increase.

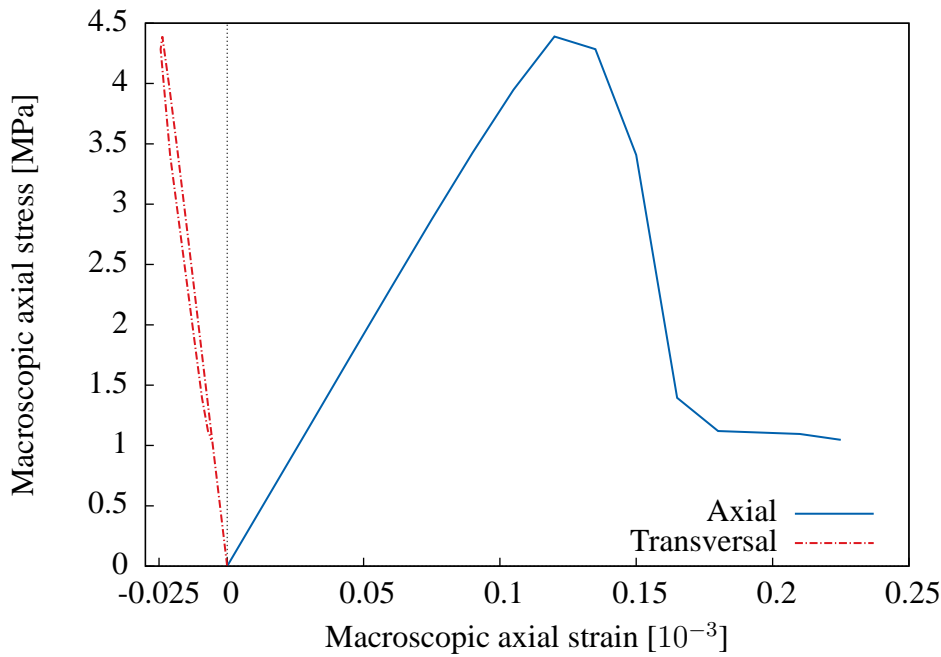


Figure 3.13: Macroscopic response for tension in terms of axial and transversal strain.

The dilatancy δ of the specimen can also be computed by considering the trace of the macroscopic strain tensor. Thus, the relative variation of the volume, drawn in FIG. (3.15), is:

$$\delta = \frac{\Delta V}{V_0} = \varepsilon_{ax}^M + \varepsilon_{tr_Y}^M + \varepsilon_{tr_Z}^M \quad (3.2)$$

Notice that the same dilatancy rate magnitude is observed in tension and in compression regarding the elastic region: a result in conformity with the identical Poisson ratio value. Naturally a tension test produces a volumetric expansion ($\delta > 0$) while compression produces a contraction ($\delta < 0$). However, the cracking process increases the dilatation rate for both tests. Hence, when in tension the slope is increased, in compression, the contraction tendency is slowed down. The localization is characterized by: in

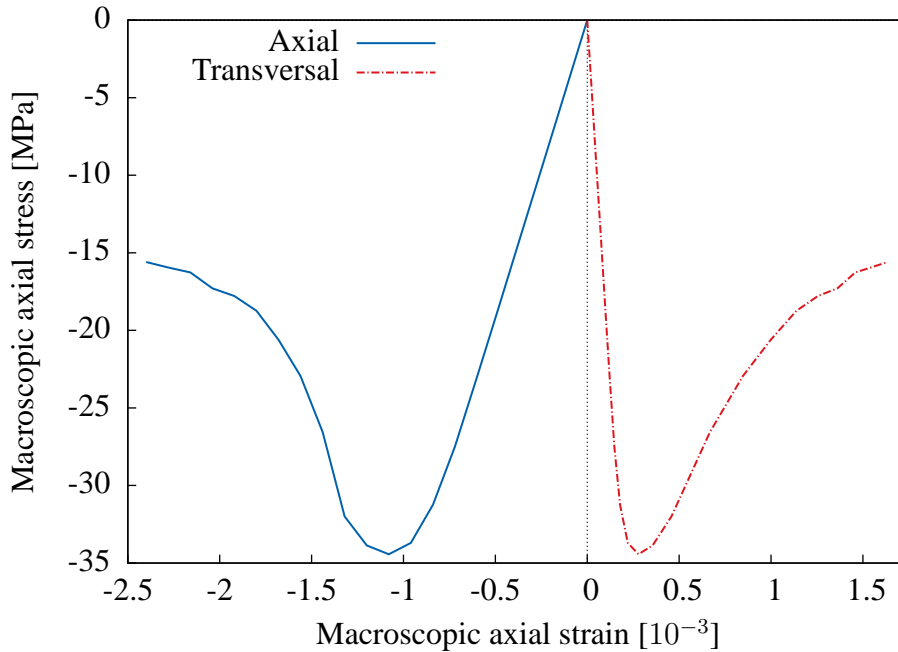


Figure 3.14: Macroscopic response for compression in terms of axial and transversal strain.

tension a sudden rate increase and in compression a dilatancy minima. Afterwards, the dilatancy shows an interesting feature in compression. Indeed, the tendency is reversed in the post-localization region. Eventually, the positive transversal strains reach the axial strain magnitude leading to a specimen volume equal to the original value V_0 ($\delta = 0$). This characteristic is reached for $\varepsilon_{ax}^M \approx -1.5 \cdot 10^{-3}$. More important loading even leads to a positive relative variation of the volume.

These observations of volumetric variations are rather consistent with experimental results. In [Torrenti, 1987] the interpretation is made that, in compression, the contraction corresponds to a predominant elastic effect where the following expansion reveals an important cracking stage. However, experiences revealed a volumetric strain which switches sign prior to the localization (see ε_V in FIG. (1)).

2.3 Dissipated energy

As an integration of the reaction over the displacement, a total energy can be calculated from the macroscopic response shown in FIG. (3.2) for each step. Furthermore, considering a fictitious elastic unloading until zero load level, a distinction can be made between the elastic and the dissipated part. Thus it gives an additional mean to quantify the failure mechanism and compare tension and compression behaviors. The three energies — elastic, dissipated and total — are plotted in FIG. (3.16) as a function of the axial imposed displacement for both loadings.

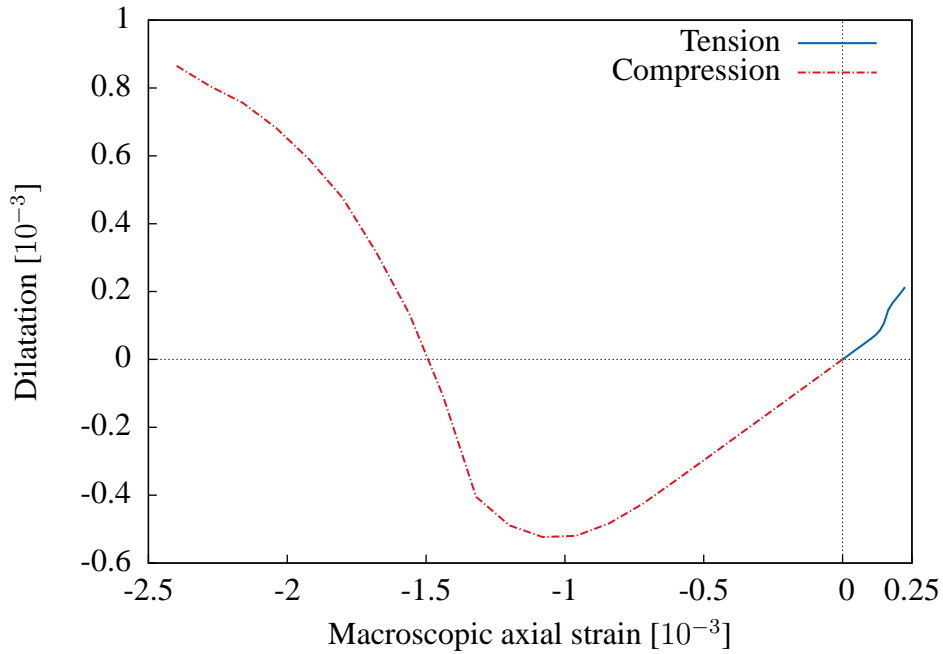


Figure 3.15: Dilatancy for tension and compression.

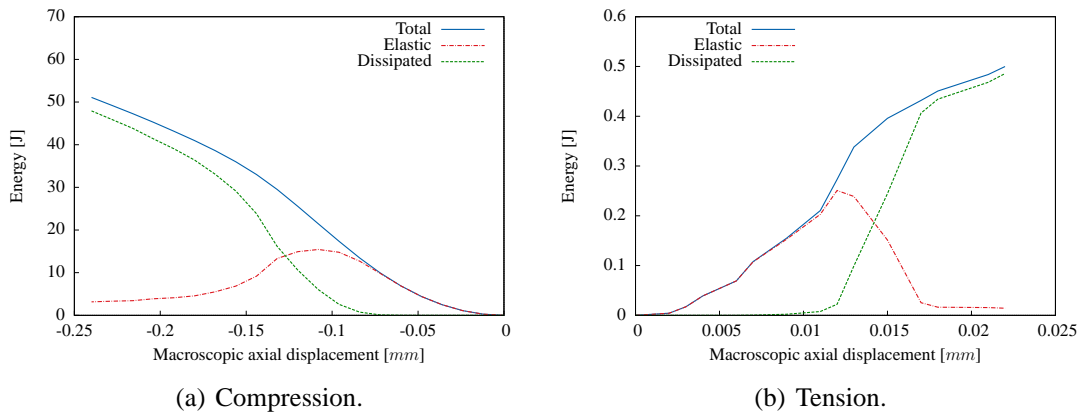


Figure 3.16: Energies calculated for each step of the loading.

These curves give a clear representation of the elastic and dissipated mechanisms that occurs during the loadings, which are typical of a softening behavior. It can be observed that at the beginning, nearly all the energy is elastic and then, at the localization, the energy dissipated increases significantly. The more brittle failure in tension than in compression can be seen and the fall of the elastic energy to a nearly zero value represents well the relaxation phenomena and the fact that all the energy is dissipated in the macroscopic cracks.

2.4 Induced anisotropy

After having shown the macroscopic response of the model to simple radial macroscopic loading paths, focus is now placed on non proportional cases. Here, our objective is to show the emergence, at macro-scale, of some features related to any anisotropic behaviors. This anisotropy shall be related to the non proportionality of the loading path. Hence, it is referred to as *induced anisotropy*.

Considering a tension or a compression test with monotonic loading, the failure mechanism that leads to the specimen ruin induces a strong anisotropy of cracks' pattern. On the basis of this simple observation, an analysis of the macroscopic material properties — e.g Young modulus, tensile strength, etc. — for each step of the previous monotonic loading tests (in both tension and compression) is now proposed. Hereafter, the two first parts of the macroscopic loading path (tension or compression) are referred as *principal* calculations. In order to yield residual material properties, additional calculations, that are inherited from the principal, are performed. They are referred as *secondary* calculations. Basically, the inheritance from principal to secondary calculation is made through the non linear features, *i.e.* the set of meso-scale cracks with their orientations and opening values.

2.4.1 Anisotropic induced damage

Here the residual property of concern is the Young modulus. In order to display the anisotropy, it is independently calculated for each direction X , Y and Z . Hence, for each step of the principal calculation, three secondary ones are performed in the three directions. It gives three macroscopic Young moduli: an axial \tilde{E}_{ax}^M value and two transversal ones \tilde{E}_{trY}^M and \tilde{E}_{trZ}^M . The results are displayed by defining “damage” variables d_{ax} , d_{trY} and d_{trZ} , respectively. They are built to compare the upscaled residual Young moduli to those corresponding to the initial state E^M (which are the same for all direction):

$$d_{ax} = \frac{E^M - \tilde{E}_{ax}^M}{E^M}, \quad d_{trY} = \frac{E^M - \tilde{E}_{trY}^M}{E^M} \quad \text{and} \quad d_{trZ} = \frac{E^M - \tilde{E}_{trZ}^M}{E^M}. \quad (3.3)$$

Theoretically, in the elastic region of the principal test, those variables are null and then, tend to increase along with the specimen failure state. Notice that this unusual approach is clearly opposed to standard damage mechanic where the calculation of a damage variable d gives an effective Young modulus: $\tilde{E} = (1 - d)E$. Herein, the Young moduli upscaled values \tilde{E}_{ax}^M and \tilde{E}_{tr}^M yield the damage variables d_{ax} and d_{tr} (EQ. (3.3)).

The results in tension are given in FIG. (3.17) where the two damage variables are plotted in terms of the macroscopic axial strain of the principal calculation. It can be observed that the axial damage d_{ax} is growing much faster than that of the transversal d_{tr} . Moreover, the former reaches a value of ≈ 0.85 which corresponds to a highly damaged state when the latter hardly reaches 0.15. Hence, the elastic property is far more spoiled in the axial direction. This result reflects the characteristic morphology of the cracks' pattern, splitting the specimen in two by a plan perpendicular to the axial axis. As the macroscopic crack grows, the “link” between each part of the specimen becomes weaker,

leading to a decrease of the upscaled Young modulus in this direction. On the contrary, there remain several non broken paths on the transversal directions that gives the specimen a higher rigidity.

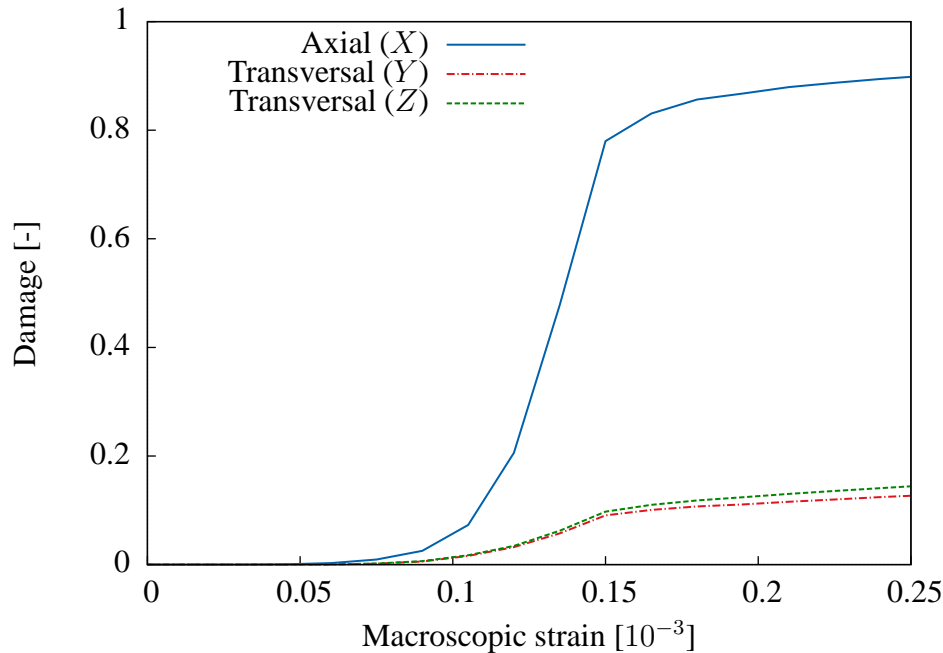


Figure 3.17: Evolution of axial and transversal damage variables for a tension test.

Regarding the compression test, FIG. (3.18) shows the opposite effect. Indeed, here the transversal damage is more important than the axial one. It may be explained by cracks' patterns that form planes parallel to the axial direction and leading to a higher loss of rigidity in the transversal directions. Furthermore, the more diffuse aspect of the crack repartition makes the difference between axial and transversal damage less important.

Finally, for both tension and compression cases, it can be noted that the two transversal damages are of the same order of magnitude, representing isotropic behavior in these two directions. Somehow, it could be said that the macroscopic elastic behavior is shifting from an isotropic case to a transverse isotropic one. More numerical investigations for the second step of those non proportional loading paths may determine the complete elasticity tensor for this case.

2.4.2 Induced anisotropy for tensile strengths

Still dealing with both tension and compression tests, interest is taken now in the *residual tensile strength* of the specimen for each direction. As the previous section computed an elastic property, herein, non-linear calculations are performed at each step of the principal test in order to yield these failure properties. The results are plotted in terms of

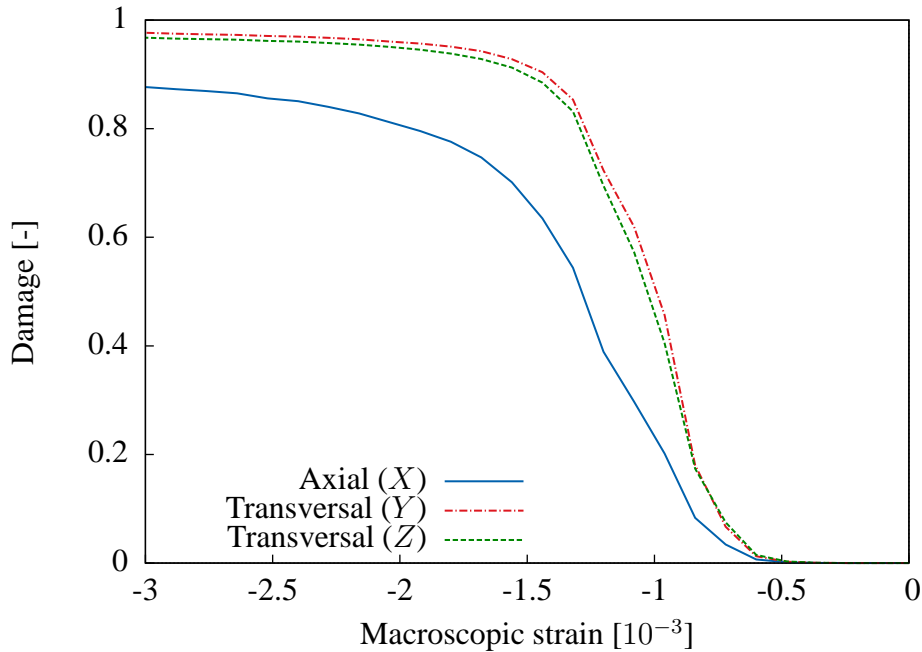


Figure 3.18: Axial and transversal damage variables evolutions for a compression test.

residual strengths defined by the ratio between actual tensile strengths f_{ax} , f_{trY} and f_{trZ} and the initial state one f (which is the same for each direction):

$$r_{ax} = \frac{f_{ax}}{f}, \quad r_{trY} = \frac{f_{trY}}{f} \quad \text{and} \quad r_{trZ} = \frac{f_{trZ}}{f} \quad (3.4)$$

Theoretically, these residual values are unit valued in the elastic domain and null whether the specimen is ruined. Their evolution through tension and compression failure are drawn as a function of the principal calculation axial strain FIG. (3.19) and FIG. (3.20), respectively.

The results show approximatively the same behavior as those for the elastic moduli. Regarding the tension failure, a more important decrease of the tensile strength is observed in the axial direction than along the transversal directions. The ratios are also the same order of magnitude. Indeed, when the specimen lost $\approx 80\%$ of its strength in the former direction, it only lost $\approx 20\%$ in the last two. Regarding the compression test, the specimen seems to follow a rather isotropic behavior. Nevertheless, the transversal residual strengths are a little smaller. Notice that at these failure states, the specimen lost $\approx 90\%$ of its tensile strength.

2.5 Uniaxial cyclic compression loading

It is widely admitted that the behavior of concrete is highly dependent upon its load-history. Modeling this behavior under cyclic compression loading is a complex matter

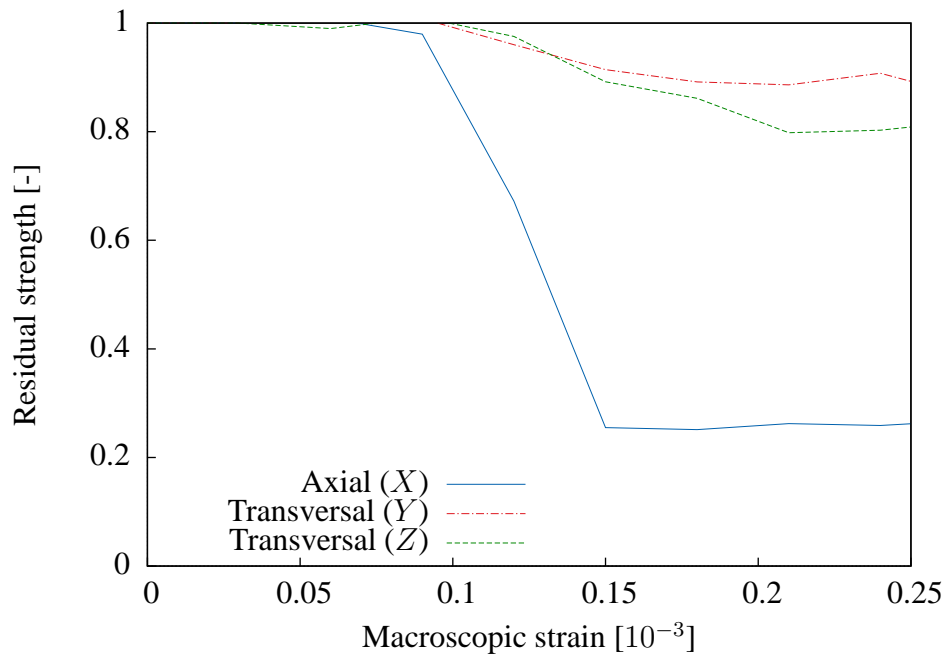


Figure 3.19: Residual tensile strength evolution during failure process in tension.

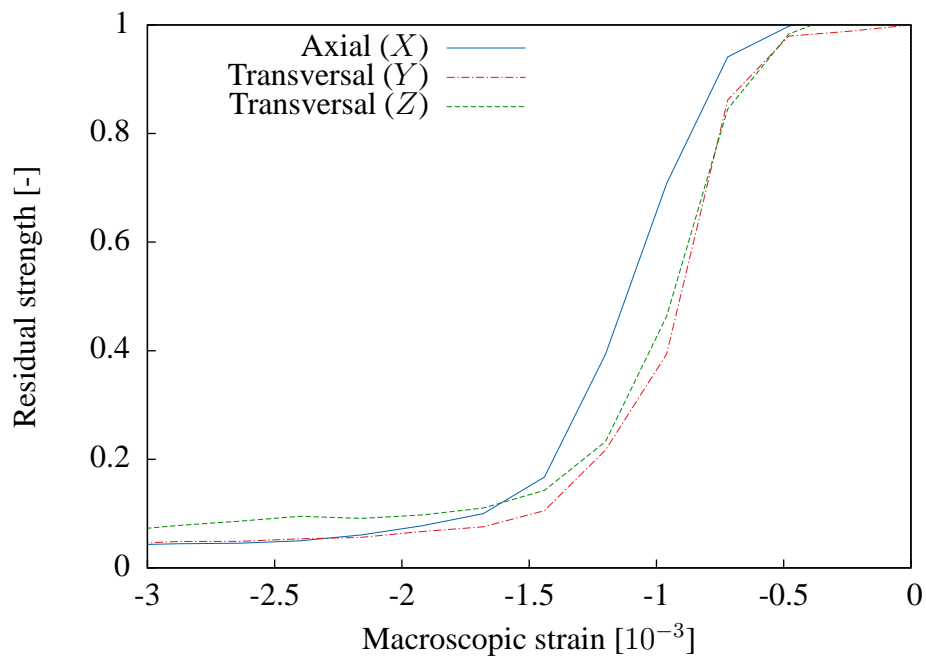


Figure 3.20: Residual tensile strength evolution during failure process in compression.

due to the highly non linear strain-stress relationship and the multiple effects that must be taken into account. Nonetheless, a great number of studies, from phenomenological

models [Ollivier et al., 2012] to empirical formulae [Bahn and Hsu, 1998], have shown consistent results. However, it inevitably leads to a high number of parameters not necessarily easily measurable. Herein, the performances of the meso-model are now tested with this kind of loading. Furthermore, it is an occasion to reveal several details of the different mechanisms that take place during the specimen failure — for example, the emergence of macroscopic plasticity and damage — which are concealed by the previous simple monotonic tests. Henceforth, the model is now submitted to a more complex test following a *uniaxial cyclic compression loading path*.

The same cubic specimen as above of size $100\text{ mm} \times 100\text{ mm} \times 100\text{ mm}$ is tested in compression with a series of loading/unloading cycles. The boundary conditions are the same: the upper and lower faces are controlled by a negative imposed axial displacement (Dirichlet) and the others are left free of any stress (Neumann), simulating a simple compression test. The loading paths, drawn in FIG. (3.21), consists of four cycles of maximal displacement -0.06 , -0.12 , -0.18 and -0.24 mm . The unloading paths correspond to a displacement of -0.024 , -0.036 , -0.084 and -0.12 mm , respectively, leading to a rather important stress release.

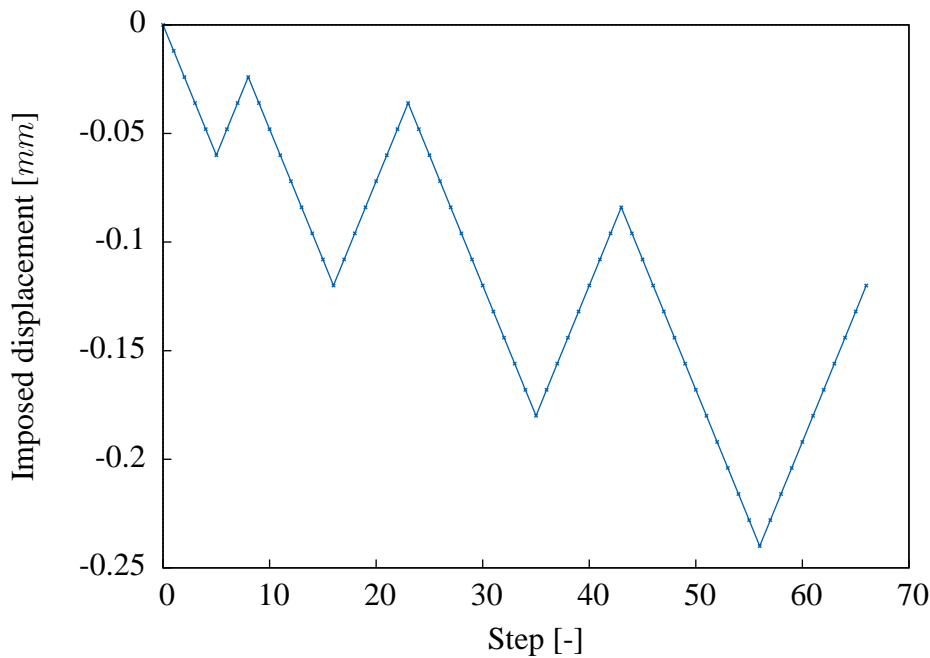


Figure 3.21: Loading path: axial displacement for each calculation time steps.

The macroscopic response along axial, transversal and volumetric strain is drawn in FIG. (3.22) (with inverted axis). Among the four cycles, only the last three are visible since the former is performed in the linear region. The same features as for the monotonic loading are naturally observed, among them being the contraction at the beginning and the eventual expansion of the specimen in the post-localization region (positive volumetric

strain). On these points, the model remains pretty consistent with experimental results (see FIG. (1(a)) for example). Though it can be pointed out that the behavior is more brittle and a rather small amount of energy is dissipated during the unloading/reloading phases (more visible on the transversal curve).

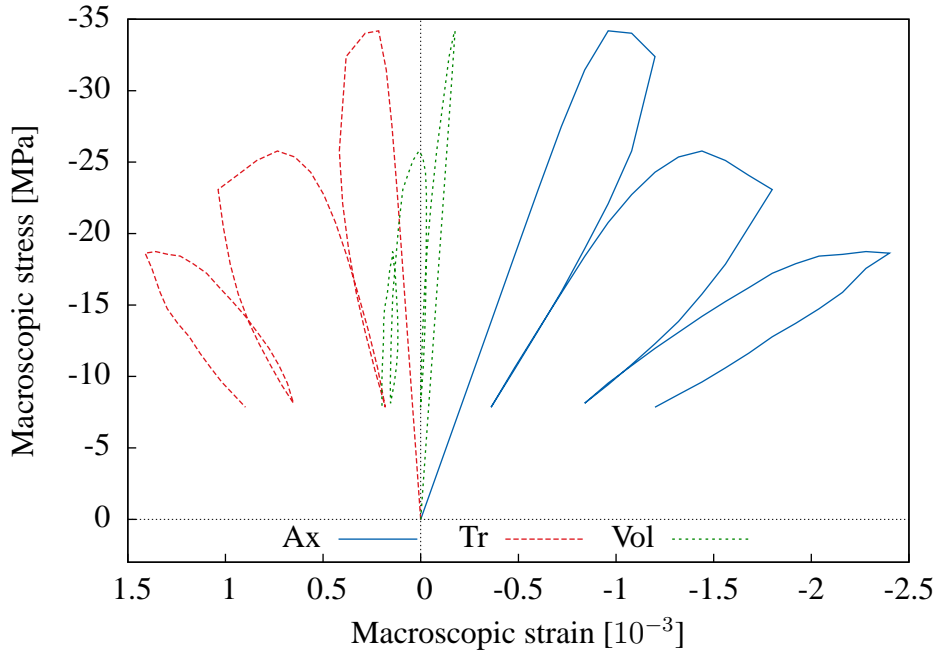


Figure 3.22: Macroscopic response under loading/unloading cycles in terms of axial, transversal and volumetric strain.

The unloading trajectory of the macroscopic response gives a quantitative description of the different mechanisms that take place during the specimen failure. For that matter the macroscopic response versus macroscopic axial strain is plotted in FIG. (3.23) along with the unloading stress-strain path (assumed linear). These previous (linear) paths give the part of macroscopic plastic or damage effects in the failure process. Their slope and the strains for near-zero stress level (intersection with the abscissa axis) correspond to the damaged Young modulus \tilde{E}_i^M and the residual plastic deformation ε_i^p , respectively, for $i = [0..3]$. Considering two extreme cases: on the one hand, if non-linearity is due only to plastic mechanisms (irreversible dissipated energies), the unloading path should have the same slope as that of the elastic loading. On the other hand, if non-linearity is due only to reversible crack opening, unloading should lead, following a damaged path to the initial zero-zero strain-stress point (perfect crack closure).

Of course, it is worth recalling that the numerical framework does not take into account for any damage at the meso-scale. Only a softening behavior is modeled through the so-called traction-separation law. However, data on plastic or damage phenomenon that occur at the *macroscopic scale* (see TAB. (3.3)) shows that both play their part in the

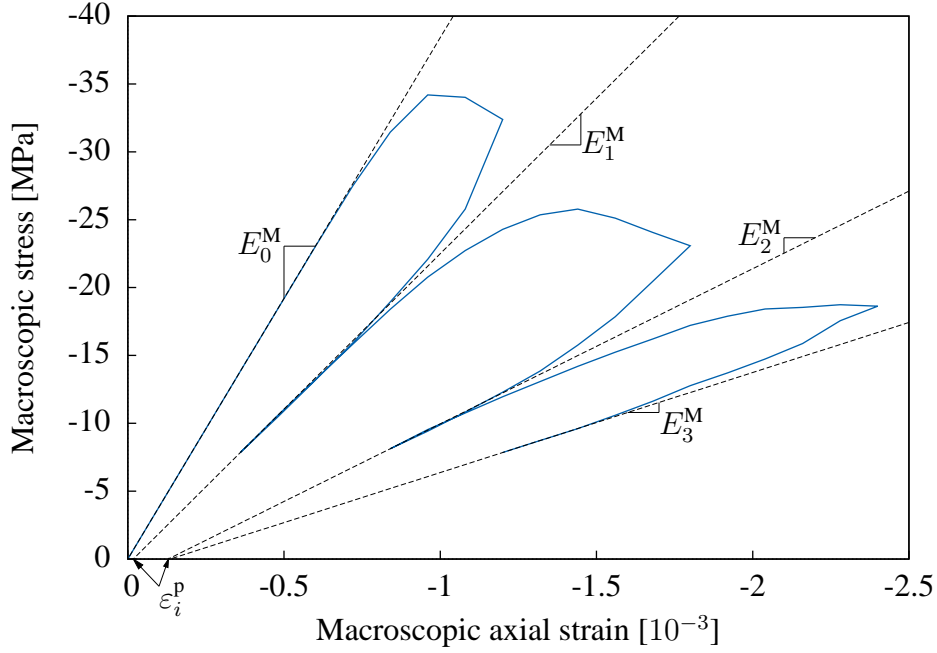


Figure 3.23: Illustration of the plasticity and damage repartition during the cyclic loading.

modeled failure mechanism. An interpretation of this upscale feature is that the resulting incompatible displacement of morphological modeling induces asymmetrical local deformations during loading. Henceforth, with regards to its opening, the crack closure is not necessarily symmetrical during unloading, representing a historically dependent behavior.

As for the induced anisotropy analysis and in order to quantify the damage, equivalent variables d_i are defined with upscaled Young moduli:

$$d_i = \frac{\tilde{E}_i^M - E_0^M}{E_0^M}, \quad (3.5)$$

with $i = [0..3]$ and where $E_0^M = \tilde{E}_0^M$ is the initial Young modulus of the non-damaged specimen.

Notice that the first visible cycle is made just after macroscopic localization. At this stage, it can be observed that the specimen lost almost half of its initial stiffness $d_1 = 0.4$ by a crack opening process almost reversible and $\epsilon_1^p = 0.017 \cdot 10^{-3}$. The plastic effects appear to be gaining importance along with the specimen degradation $\epsilon_2^p = 0.128 \cdot 10^{-3}$. And eventually, the failure irreversibility stops increasing at the last cycle while the specimen stiffness continues to decrease up to a nearly completely damaged state $d_3 = 0.8$.

The nearly non existent plastic effect in the early stages of the specimen degradation are rather odd compared to experimental observations (see FIG. (1(a))). Among the several reasons that can explain this results, the fact that no actual plasticity is modeled within the meso-scale behavior is one of the most important. Indeed irreversible effects

Cycle	Young modulus	Damage	Plastic deformation
i	\tilde{E}_i^M [GPa]	d_i [-]	ε_i^p [10^{-3}]
0	38	0	0
1	23	0.4	0.017
2	11	0.7	0.128
3	7	0.8	0.135

Table 3.3: Proportion of plasticity and damage at each cycles.

are here only induced by morphological displacement incompatibilities, leading to crack opening even during the unloading paths. In addition, unloading cycles prior to localization, not done in this study, could reveal an interesting part of the behavior. Finally, the quantitative results (TAB. (3.3)) have to be considered with caution since unloading paths are not necessary linear and only actual strain values near a zero stress level could give accurate information on the residual plastic part — hardly computable within a numerical displacement control context.

3 Representative Volume Element for elastic and failure properties

In order to predict statistically relevant effective properties of heterogeneous media, the determination of a Representative Volume Element (RVE) is a crucial matter. As shown in [Kanit et al., 2003], a RVE depends on four main features: a *material property* Z , a *precision* ϵ , a *contrast* c between each phase and the *number of realizations* computed n . The last two are closely related. Indeed, to be statistically relevant, n must increase along with c . Since herein, the contrast — based on the Young modulus of each phase — is rather small $c = 100\,000/20\,000 = 5$ and the calculations are time consuming, the choice is made to consider the smallest number of realizations so that it can be statistically considered as “infinite”, *i.e.* $n = 100$. With this number of realizations, it can be assumed that the material properties $\{Z_i\}$ follow a normal distribution. Hence the confidence interval at 95 % is

$$I_{95\%} = \left[\bar{Z} - \frac{1.96\sigma_Z}{\sqrt{n}} ; \bar{Z} + \frac{1.96\sigma_Z}{\sqrt{n}} \right], \quad (3.6)$$

where σ_Z is the standard deviation and \bar{Z} the mean of the property Z . From this interval, the sample theory gives a relative error of the mean value of Z defined by:

$$\epsilon = \frac{1.96\sigma_Z}{\bar{Z}\sqrt{n}}. \quad (3.7)$$

This unit-less error is usually used in order to set the precision. Notice that it is proportional, for a given n , to the coefficient of variation. Naturally, along with the mean and the

standard deviation, this error depends on the specimen volume considered. Henceforth, a RVE is defined for a given absolute error ϵ . Herein, attention is drawn to a RVE at 1 %, defined by the unique volume:

$$V_Z^{\text{REV}} = \{V \mid \epsilon(V) = 0.01\}. \quad (3.8)$$

Finally, only the mechanical properties Z of concern remain to be determined.

3.1 Experimental protocol

It is recalled that a set of 100 realizations is produced in order to preform the statistical study. Hence, the same number of morphologies have to be yielded and projected onto FE meshes of different volumes. The specimen volume range considered goes from $V = 10^3 \text{ mm}^3$ to 10^6 mm^3 , corresponding to a cube size range that goes from $a = 10 \text{ mm}$ to 100 mm . The morphology characteristics are the same as above: 30 % volume fraction of disconnected random shaped aggregates, whose characteristic lengths are distributed around 5, 7 and 15 mm , are included within a mortar matrix.

Both tension and compression tests are performed up to the ruin of the specimen (the same conditions as above are applied). In addition to the *Young modulus* (elastic property), full non-linear calculations enable the statistical study of failure properties such as *tensile* or *compressive strength*. In FIG. (3.24), the envelope (area between minimal and maximal value) of the 100 macroscopic responses of both tension and compression are plotted for two specimens of size 40 and 100 mm , respectively. A initial qualitative analysis can be made in view of these curves. Firstly, it can be observed that, for a smaller volume, the behavior seems to be less predictable than for a that of a larger one. Indeed the macroscopic responses are more spread around the mean value, *i.e.* the variance of the response is higher. A logical result that also stands for the elastic region. However, this behavior appears to be more pronounced in compression. Secondly, the compressive behavior shows a size effect, making the large specimen weaker than the other. This is an integral feature of meso-models that shows the strength of their underlying spirit.

The statistical analysis is preformed through the error defined EQ. (3.7) which is made a function of specimen volumes V . It occurs that the discrete results obtained are well fitted by a decreasing exponential of the specimen one-dimensional *size* $a = V^{1/3}$:

$$f_\epsilon(V) = \alpha_1 \exp\left(- (V/\alpha_2)^{1/3}\right) + \alpha_3, \quad (3.9)$$

where α_1 and α_3 can be seen as initial and offset errors, respectively, and α_2 as a volume which characterizes the error decreasing rate. The higher α_2 is, the slower the error decrease.

Then, after an identification of the fitting parameters α_i , it is possible to compute the RVE volume for a given property following EQ. (3.8), which gives:

$$V_Z^{\text{REV}} = \alpha_2 \ln\left(\frac{\alpha_1}{1 - \alpha_3}\right)^3. \quad (3.10)$$

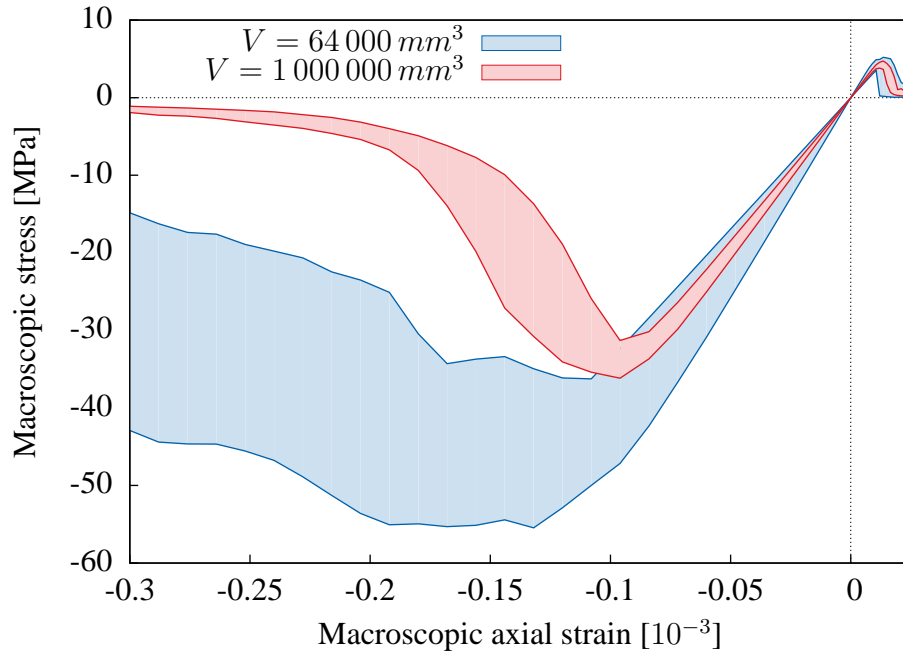


Figure 3.24: Envelope of 100 macroscopic responses in tension and compression for two specimen volumes.

A quantitative analysis of Young moduli, tensile and compressive strengths is now proposed leading to the definition of as many RVEs.

3.2 Young moduli analysis

In this section, the mechanical property studied is the Young modulus *in simple tension*. As an elastic characteristic, the results are the same in tension and in compression. Hence, no distinction has been made. It is simply calculated by the ratio between macroscopic axial stress and axial strain at the first step of the calculation. At this stage of the calculation, the specimen is still free of any microscopic cracks. In FIG. (3.25), the Young moduli over specimens of volume $V = 1\,000, 8\,000, 27\,000, 64\,000, 216\,000, 343\,000, 512\,000, 729\,000$ and $1\,000\,000\text{ mm}^3$ are plotted along with the confidence interval $I_{95\%}$ defined EQ. (3.6). The equivalent volume of the larger aggregates is also represented.

Notice the smallest specimen seems to give an odd value, substantially below the others. It can be explained by the fact that this volume is, in fact, smaller than the volume of the larger aggregate. This value should be ignored as a relevant upscaled Young modulus. However, it can be remarked that the confidence interval has the same order of magnitude than for larger volumes. Beyond a volume of $8\,000\text{ mm}^3$, the Young modulus converges rapidly to a value just below $40\,000\text{ MPa}$ while the size of the confidence interval monotonically decreases. Quantitative results of this decrease are drawn in FIG. (3.26) through the relative error defined EQ. (3.7) (represented in %).

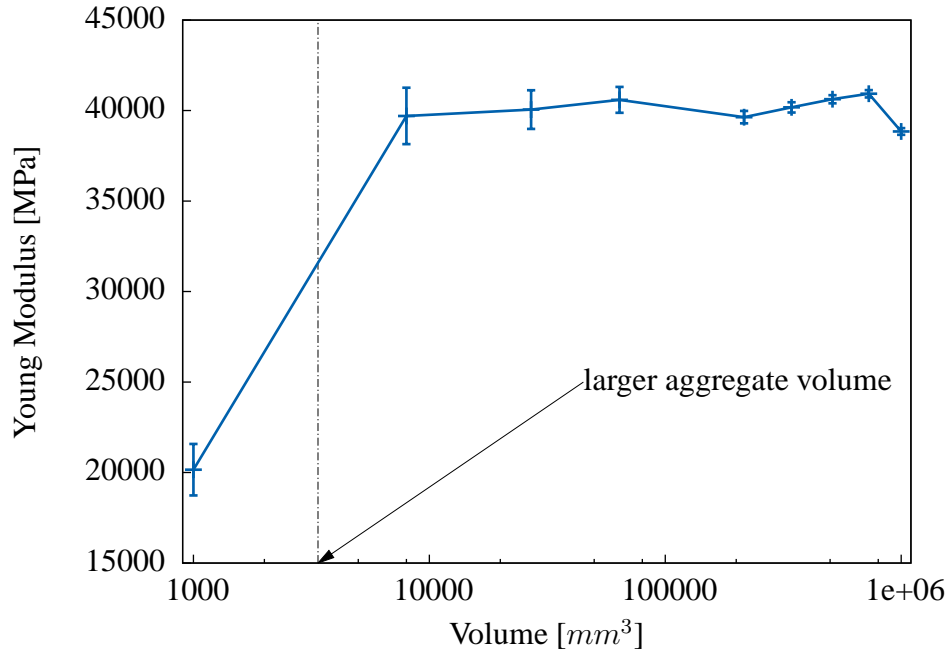


Figure 3.25: Young modulus for several volumes with a confidence interval of 95 %.

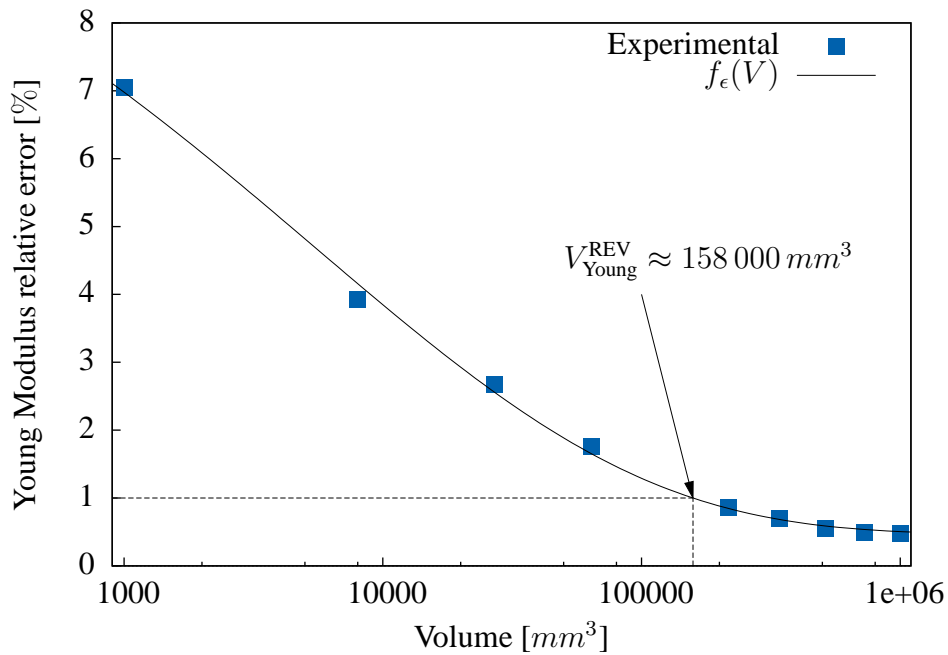


Figure 3.26: Relative error of Young modulus for several volumes.

Results on the identification of EQ. (3.9) and corresponding RVE value defined EQ. (3.10) are given (along with those of the next section) in TAB. (3.4). Herein, considering the

Young modulus and an error of 1 %, the RVE is

$$V_{\text{Young}}^{\text{REV}} \approx 158\,000 \text{ mm}^3, \quad (3.11)$$

which corresponds to a cube size $a \approx 54 \text{ mm}$.

3.3 Tensile and compressive strength

In this section, the tensile and compressive strength of the specimen are considered. The same procedure as for the Young modulus is applied. However, a full calculation up to failure is performed in tension and in compression for each realization in order to measure the two macroscopic strengths. Their mean values and confidence interval at 95 % are plotted in FIG. (3.27) and FIG. (3.28), respectively, for specimens of volumes $V = 1\,000, 64\,000, 216\,000$ and $1\,000\,000 \text{ mm}^3$. They both approximately show the same behavior. Indeed, a global decrease of the strength can be observed, representing a *size effect*. Due to this typical feature of heterogenous quasi-brittle materials, the strengths do not seem to converge to an asymptotic value, which makes a major difference to the latter result on elastic properties.

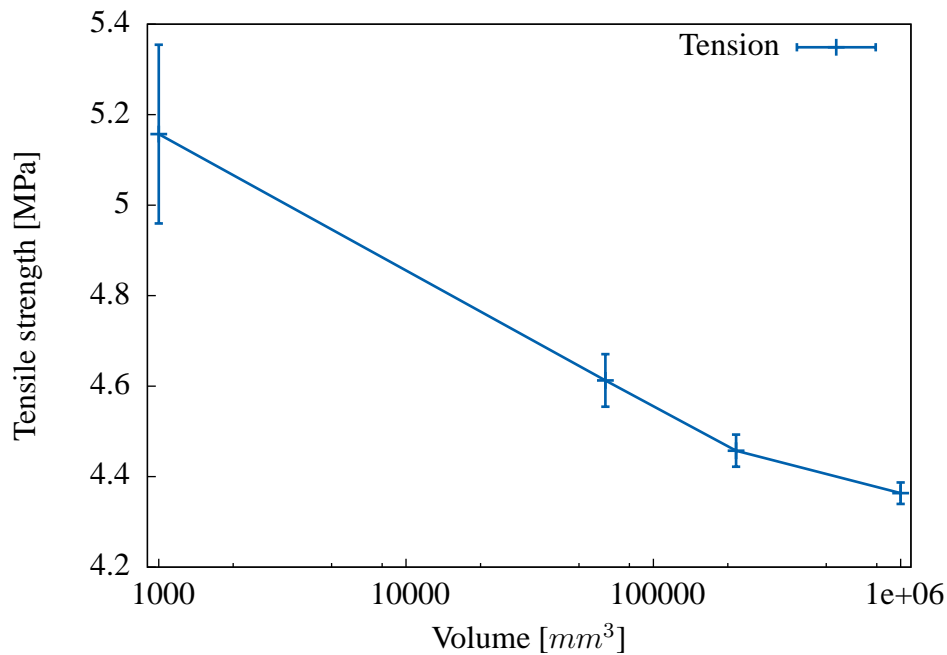


Figure 3.27: Tensile strength for several volumes with a confidence interval of 95 %.

The two last figures show the logical decrease of the confidence interval $I_{95\%}$. It is quantified by the error in EQ. (3.7) whose fitting function parameters are summarized in TAB. (3.4). Along with the calculation results, this function is drawn in FIG. (3.29) for both tensile and compressive strengths.

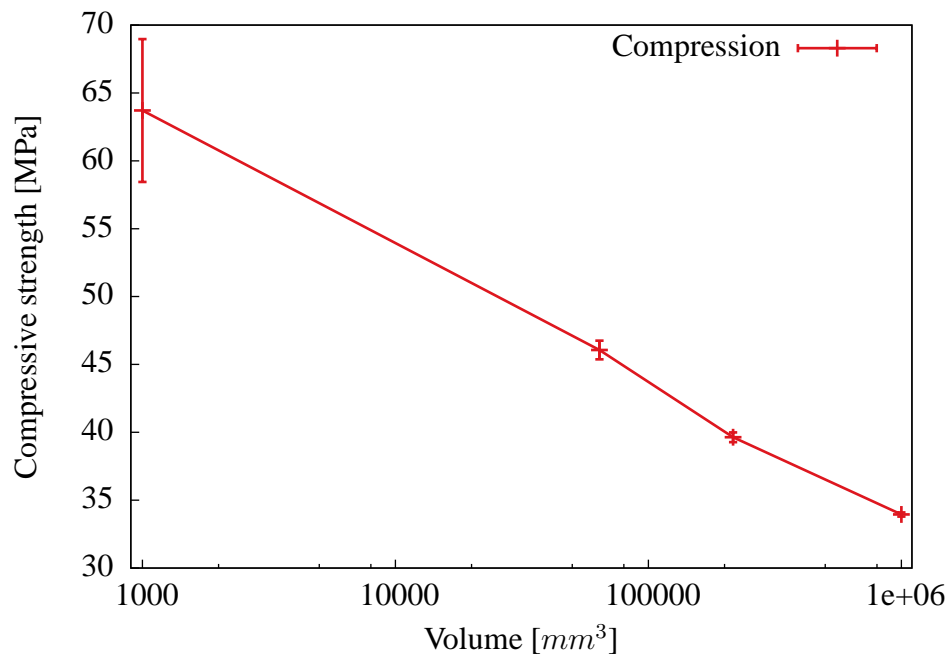


Figure 3.28: Compressive strength for several volumes with a confidence interval of 95 %.

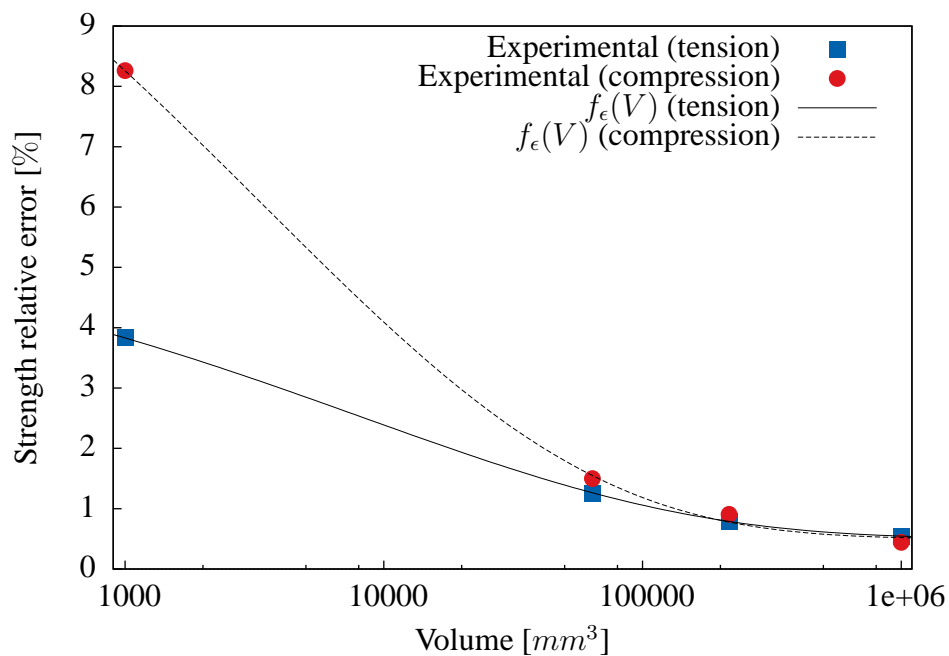


Figure 3.29: Relative error of both tensile and compressive strength for several volumes.

These curves depict several interesting features. Firstly, the more important error of

small volume compressive strength ($< 50\,000\text{ mm}^3$) shows that a statistically non representative morphology leads to a more unpredictable failure behavior in compression than in tension. It can be explained by the cracks' pattern analysis made in the previous section. Indeed, in compression, a complex network of several macroscopic cracks is formed around the aggregates where in tension just one is created perpendicularly to the solicitation. It can be easily imagined how, for small volumes, the first pattern can hardly be obtained. Hence, it can be assumed that in compression the failure mechanism is more closely related to the morphology than in tension. This hypothesis is supported by the results which show that, for the smallest volume $V = 1\,000\text{ mm}^3$, a factor 2 on the error is observed. However, since the compressive strength decrease rate is higher than that of the tensile strength, this difference is rapidly reduced as the volumes increase. It is quantified by the fitting parameter α_2 which is more than two times higher in tension than in compression (see TAB. (3.4)). In order to explain this difference, a new principle referred to as *cracks' pattern stabilization* is introduced. This characterization of the failure mechanism aims to qualify the geometrical difference between a resulting cracks' pattern and that observed on representative volumes. Herein, it is assumed that a single perpendicular macroscopic crack and a network of parallel planes are representative of tension and compression tests, respectively. Hence, they can be referred to as stabilized cracks' patterns. Naturally, this denomination is to be seen only in terms of volume variations. The difference between the two decreasing rates of the error can be explained by this stabilization process. An initial error (for $V = 1\,000\text{ mm}^3$) higher in compression than in tension represents a more unusual failure mechanism in compression than in tension. Hence, in the former case, the stabilization of the cracks' pattern as the morphology becomes representative is more important. Finally both errors seem to converge to an identical value below the 1% error.

Just as the Young modulus RVE has been calculated, EQ. (3.8) applied to this case gives the two following RVE for tensile and compressive strength (f_T and f_C):

$$V_{f_T}^{\text{REV}} \approx 115\,000 \text{ and } V_{f_C}^{\text{REV}} \approx 135\,000\text{ mm}^3, \quad (3.12)$$

which correspond to cube sizes of $a \approx 49$ and 51 mm , respectively. Compressive strength RVE is just a bit larger than that of the tensile strength. This difference in the geometrical complexity of the cracks' pattern can be explained in the same manner as above.

Material property Z	$V_Z^{\text{REV}} [\text{mm}^3]$	α_1 [%]	α_2 [mm^3]	α_3 [%]
Young modulus	158 000	11.5	5470	0.48
Tensile strength	115 000	5.4	8350	0.51
Compressive strength	135 000	15.1	3370	0.50

Table 3.4: VER size and coefficients of the fitting function $f_\epsilon(V)$ for the elastic and failure material properties.

3.4 Comments

When elastic and failure material characteristics are compared, the statistical analysis made here reveals some unexpected features. Firstly, the three error functions considered (Young modulus, tensile and compressive strengths) have the same order of magnitude. Actually, the former fits between the last two for small volumes ($< 10\,000\text{ mm}^3$). Secondly, the decreasing rate α_2 is also within the same range, which eventually produces a RVE at 1 % of an elastic property larger than that of failure properties (strengths).

It was the author's expectation that non-linear properties such as material strengths would be more spread around the mean value than the elastic modulus. An interpretation of this result is that the failure mechanisms that take place here are initiated by highly localized phenomenon induced by the morphology leading to small RVE. Furthermore, the low error value of tensile strength can be seen as a strong geometrical stability of this mode I failure mechanism — with a single macroscopic crack — almost not influenced by the morphological distribution. Beyond a certain volume, the same reasoning can be made for compression. Indeed, this study shows that even if being more sensitive to small volumes, the compression cracks' pattern — network of parallel planes — is eventually quite stable.

However, this study has to be seen as being at its early stage. Since, as far as the author can tell, no RVE on failure characteristics such as strength can be found in the literature, the aim here is to determine a trend and provide a basis for a future study. On that matter, the several weak points that undermine the results accuracy and that must be treated are listed just below. Basically, they are related to the fact that the necessity of failure calculation is time consuming.

- 1) Full failure calculations have to be made for the same number of volumes as for the elastic modulus. Herein, the fitting function of three parameters is based on four points. Henceforth, the value of one mean strength highly influences the RVE size.
- 2) The Monte Carlo integration methods are known to be slow to converge (\sqrt{n}). Herein, the number n of realizations seems too small even for the elastic modulus.
- 3) Finally, an investigation of larger scale and different morphologies could provide more information on the asymptotic aspect of the three error functions and the size effect observed on the strengths.

4 Application to the Delayed Ettringite Formation

Delayed Ettringite Formation (DEF) is a harmful phenomenon typical of concrete-like material. The underlying cement paste expansion affects the long term behavior of massive large civil engineering structures such as power plants, dams or bridges. Ettringite is

the principal phase of hydration products. Its formation at early ages along with its role in the resulting concrete behavior is well known [Moore and Taylor, 1970]. However, under certain conditions, its formation occurs after the classical stabilization of the hydration process. Two main conditions can be retrained: concrete subject to high temperatures [Divet and Randriambololona, 1998] or humidity [Collepari, 1997]. Hence, in view of the important economic impact of DEF (monitoring, repairing, *etc*), the modeling of this behavior and its impact on material characteristics is a serious issue.

It is admitted that most parts of the degradation take their origin at the meso-scale where local stress concentrations due to heterogeneities (displacement incompatibilities) leads to a diffuse micro cracks' pattern. Hence, on the strength of its explicit morphological modeling, the presented meso-model seems well suited for this problematic, improving the capability of more usual homogeneous based representations (phenomenological models).

4.1 Numerical simulation

The DEF process can be represented by a progressive expansion [Taylor et al., 2001] of the cement matrix. Furthermore, observations reveal a heterogeneous repartition of the ettringite precipitation. In this context, since the different phases of the matrix are not represented, a simplified expansion is modeled by an *homogeneous strain solicitation* within the matrix Finite Elements.

Following the tests developed by Pavoine [Pavoine et al., 2006a, Pavoine et al., 2006b], simulations are performed on $110\text{ mm} \times 220\text{ mm}$ concrete cores cylinders. Aggregates are represented by non-intersecting polydisperse spheres of radii varying uniformly from 2 to 20 mm randomly placed over the specimen, as represented in FIG. (3.30(a)).

Prior to an analysis of the impact of DEF on Young moduli, a validation of the expansion modeling through volumetric variation of the specimen is made.

4.2 Homogeneous mortar expansion

It is assumed that DEF is accurately represented by an homogeneous matrix expansion of 1 %. The impact of this local (mortar) deformation is now analyzed at the macroscopic level (concrete). Numerically speaking, the latter expansion is calculated in order to be consistent with experimental measure. Hence, it is assumed that the longitudinal expansion calculated with radial displacement extracted from three axial segments (see FIG. (3.30(b))) is representative of the total volumetric variation. In FIG. (3.31), this concrete expansion is drawn as a function of the mortar deformation (strain solicitation) from 0 to 1 %. Two calculations are performed, the first where all phases are elastic and the second where the mortar can fail, generating micro-cracking. A logical linear behavior is observed in the first case. Since the aggregate volume is constant then the macroscopic expansion rate is less than 1. Actually, this rate approximately corresponds to the mortar volume fraction which is almost 60 %. Now, considering the second case, two linear

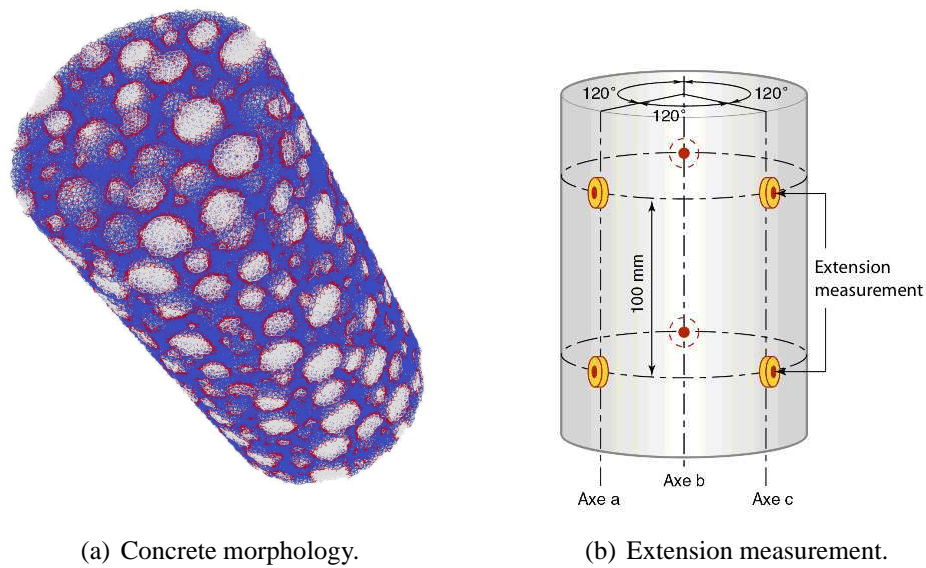


Figure 3.30: $110\text{ mm} \times 220\text{ mm}$ cylinder specimen.

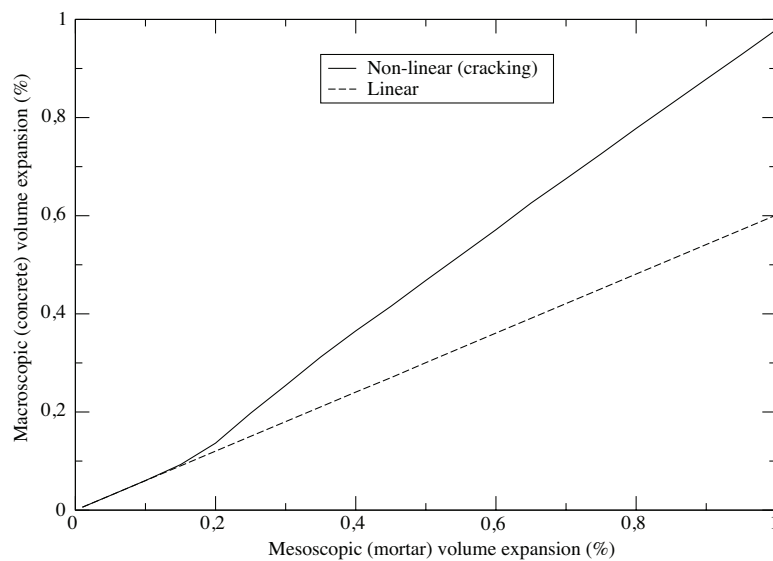


Figure 3.31: Concrete expansion as a function of mortar expansion.

regimes can be identified. The first corresponds to low solicitations — less than 0.13% — where the induced stress concentrations are smaller than the mortar strength. Hence, the behavior is identical to the elastic case. However, for more important solicitations, crack-

ing occurs, leading to a more important macroscopic expansion than previously observed. Eventually, it nearly reaches the mortar expansion, 1 %.

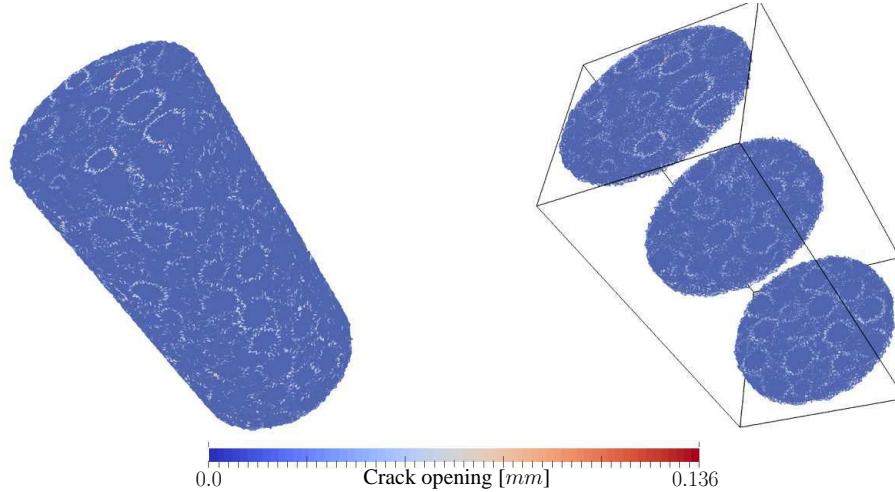


Figure 3.32: Cracks' pattern at the final 1 % mortar expansion.

The numerical responses are rather consistent with experimental observations for several reasons. Firstly: with regard to the cracks' pattern (represented in FIG. (3.32)), initiation of the process takes place at the interfaces, then coalescence of meso-cracks spreads to the mortar matrix. Secondly, the larger crack opening $140 \mu m$ is near to those measured $100 - 300 \mu m$. These results enhance the position and the role of the meso-scale strategy as a consistent modeling asset.

4.3 Residual Young modulus

Now that the DEF modeling has been presented, its impact on the degradation of material property is considered. Numerically speaking, the failure state of the specimen at each step of the DEF simulation can be stored through the crack opening. Hence, it is simple to perform as many parallel calculations in order to determine a material property (as for the induced anisotropy presented above). Herein, focus is placed on the *residual tangent Young modulus* of the specimen. Displacements are imposed on both upper and lower faces and the lateral surface is left stress free, simulating a pure tension test. The upscale value of this residual Young modulus is easily obtained with the resulting macroscopic response.

In FIG. (3.33), the results are plotted in terms of relative Young modulus (ratio between residual and initial modulus) along with the concrete (macroscopic) expansion for each numerical step of the DEF simulation. A natural monotonic decreasing shape of the relative ratio can be observed eventually leading to a loss of 50 % of the initial stiffness for a concrete expansion of almost 1 %.

A this stage, since experimental results are usually based on dynamic measure (ultra-sonic) Young modulus, the comparison is rather difficult. However, it can be remarked

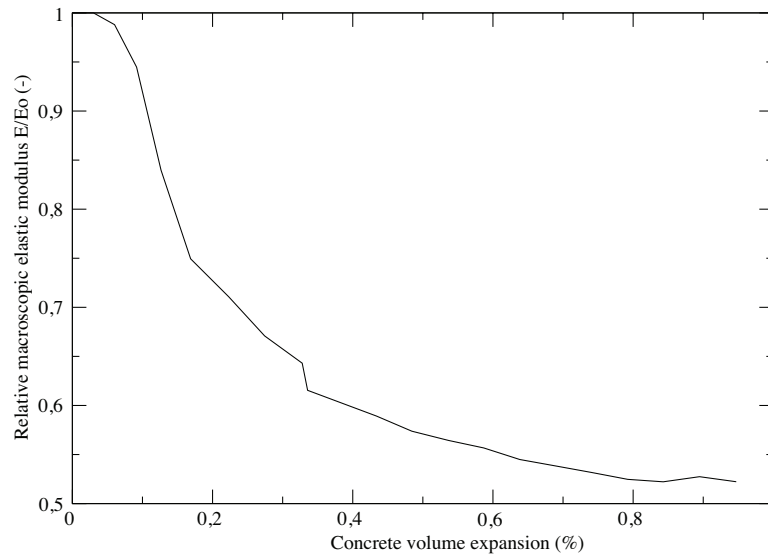


Figure 3.33: Evolution of the macroscopic Young modulus along with concrete expansion.

that the global shape depicted in FIG. (3.33) along with the final value are pretty consistent. Indeed, it is experimentally shown after a decreasing part, the dynamic Young modulus of the specimen falls to 50 % of its original value.

This numerical analysis of DEF based on meso-scale is a part of a more general study of this degradation process. The latter has been conducted by M. Al Shamaa during his Ph.D. thesis [Al Shamaa, 2012]. More specifically, several experiments have been conducted, varying the granulometry of the concrete. An ongoing numerical study of this influence is a major perspective of meso-scale models presented here.

5 Concluding remarks

In this last chapter, performances of the meso-model have been presented. First, attention has been drawn to macroscopic responses under uniaxial loadings (especially in tension and compression). It revealed that the structural effect induced by the explicit material heterogeneity representation leads to relevant complex asymmetric macroscopic behavior both in terms of stress-strain relationships and cracks' patterns. Then, a statistical analysis has been performed in order to define RVE for the elastic modulus, the tensile and the compressive strengths. Finally, coupled modeling of the Delayed Ettringite Formation has been presented, showing the impact degradation due to mortar expansion on the Young modulus.

The examples selected in this chapter have been chosen for their representative aspects. However, the diversity of this meso-model — and of meso-models in general — is far broader. Herein, computation has been performed on a single set of morphological parameters (except for the DEF application). Even though the impact of different geometrical characteristics (fraction volume, aggregate size, *etc*) has been “observed” during the numerical implementation of the framework, no actual analysis has been made and it was the author’s choice not to draw premature conclusions. However, due to the model’s capacity to represent the structural effect, it seems relevant to enhance the application spectrum by performing such an analysis. A good starting point could be an analysis of the tensile and compressive strengths according to aggregate sizes. Experimental results show a significant drop of the former (in compression) as the aggregate size increases [Szczesniak et al., 2013].

Regarding the cracks’ pattern analysis, a good perspective would be to compare our results with statistical studies which have been performed on specimens at different loading states [Nemati et al., 1998]. This would give a quantitative characterisation of cracks in terms of orientation, number of intersections, branching topology and surface area. A comparison on the same basis could be performed on numerical results by developing a post-treatment procedure taking into account both geometrical and topological information of cracks’ patterns. In addition, a brittle behavior could be implemented within the aggregates in order to depict their tendency to fail as the mortar strength increase.

Another perspective could be to consider cementitious materials at thinner scales. A good starting point could be to perform non-linear analysis on a mortar paste (micro-scale). Smaller aggregates, additional phases (pores) and different topologies could lead to interesting analysis. However, taking into account these heterogeneity sizes at the macroscopic scale requires major improvement of the resolution methodology, using parallel computation [Hautefeuille et al., 2009].

Finally, it is worth pointing out that the methodology described in DEF modeling can be extended to other coupling problems such as the effect of drying shrinkage incompatibilities between aggregates and mortar [Lagier et al., 2011] or permeability problems [Jourdain et al., 2011]. This is a major feature of the strong discontinuity methodology.

Conclusions and perspectives

The work presented in this document is part of an approach that attempts to represent the quasi-brittle behavior of heterogeneous materials such as cementitious ones. The guideline followed fits into a sequenced multi-scale framework for which descriptions of the material are selected at a thin scale (mesoscopic or microscopic) and information is transferred to a larger scale (macroscopic). It is shown how the explicit representation of heterogeneities offers interesting prospects of identification, understanding and modeling of macroscopic behaviors. In practice, from a simple description of each phase and interface behavior, a structural effect that leads to more complex macroscopic behavior is observed.

The work is therefore focusing on two main problematics: on the one hand, the morphological representation of the heterogeneities, and on the other hand, the FE implementation of both heterogeneity and local behaviors.

It is shown how the spatial structure of correlated Random Field intrinsically represents the morphological variability of material heterogeneities and thus is a relevant asset to address the former problematic. In addition to the light implementation that this methodology grants, its generalized aspect leads to the possibility of representing different kinds of morphologies. Thus cementitious material can be modeled at the meso-scale (matrix-inclusion) or the micro-scale (porous media). Finally, since thresholding process of these fields produces random shaped morphologies — excursion sets — whose geometry and topology can be statistically controlled, this model possesses a suitable predictive aspect (statistically speaking).

The numerical implementation of the meso-scale behavior is based on the introduction of kinematics enhancements of two kinds within the FE context. The first, referred to as weak, leads to a non-adapted mesh strategy. Morphologies are projected onto an unstructured mesh being created regardless of any physical surface. The second, referred to as strong, models discontinuities in the displacement field that are viewed as micro-cracks. Their openings are directly linked with local fracture energy and tensile strength leading to a model with only two meaningful non-linear parameters. These two enhancements provide the model with a significant capacity to represent the failure mechanisms in a continuum region (mortar matrix) as well as on its interfaces. Furthermore, the E-FEM integrates both within a single unified variational statement.

Finally, coupling both parts of the problematic, the model has been tested by modeling cementitious materials at the meso-scale mainly under uniaxial loadings. It revealed an emergent macroscopic response that exhibits several features such as asymmetry of the tension-compression stress-strain relationship, cracks' patterns or historical-dependency which are typical of concrete-like materials. However, several weak points are worth noticing regarding the macroscopic response such as a rather low ratio compressive to

tension strength or a too brittle behavior in compression. Up to this point, the author did not manage to produce more realistic results while keeping a representative local configuration. It is recalled that the latter is only based on physical considerations. Henceforth, improving the framework automatically leads to more in-depth analysis than parameters identification.

On the one hand, the mechanical behavior modeled at the meso-scale could be enhanced. Adding plasticity or damage outside strong discontinuities could provide a better macroscopic behavior. Implementation of this type of modeling are common and known to produce efficient results within a phenomenological context.

On the other hand, keeping the same governing laws, the physics of the modeling can be considered more accurately. It is well known that the early age phase of cementitious materials has a major impact on its resulting characteristics. A large number of phenomena occur during this stage, *e.g.* drying shrinkage, leading to a complex damaged state not represented in this study. In addition, a more accurate representation of the material heterogeneities could also improve the results. This corresponds to an investigation in thinner scales and a representation of more phases. Many ingredients such as pores, sand or water could increase the significance of the macroscopic responses. However, it would necessitate adding a nested aspect to this complex system, transferring information from the micro to the meso and then to the macro-scale.

Considering this latter point of view, the author considers that the future development of this model lies in retaining the spirit of the *physical significance of thin scales*.

Appendix A

Gaussian Minkowski Functionals

1 Volume of the unit ball

A closed ball is defined in the Euclidean space \mathbb{R}^N , for $N > 0$ and $k > 0$:

$$\mathcal{B}_k^N = \left\{ (x_1, x_2, \dots, x_n) \in \mathbb{R}^N \mid \sum_{i=1}^N \|x_i\|_k \leq 1 \right\} \quad (\text{A.1})$$

For example, \mathcal{B}_2^2 is a disk of radius 1 and \mathcal{B}_∞^2 a square of size 2.

For the specific case $k = 2$, which is of interest here, the volume of the unit ball of dimension $N \geq 1$ is:

$$\omega_N = \frac{\pi^{N/2}}{\Gamma(1 + N/2)} \quad (\text{A.2})$$

The values of the first four volumes are:

$$\omega_0 = 1 \quad (\text{A.3a})$$

$$\omega_1 = 2 \quad (\text{A.3b})$$

$$\omega_2 = \pi \quad (\text{A.3c})$$

$$\omega_3 = 4\pi/3 \quad (\text{A.3d})$$

2 Probabilist Hermite polynomials

Hermite polynomials are a sequence of orthogonal polynomials. Several manners of “scaling” them can be used. The so called Probabilist Hermite polynomials are defined as follows:

$$H_n(x) = (-1)^n e^{x^2/2} \frac{d^n}{dx^n} e^{-x^2/2} \quad (\text{A.4})$$

The order of the n^{th} is n . The first four polynomials are:

$$H_0(x) = 1 \quad (\text{A.5a})$$

$$H_1(x) = x \quad (\text{A.5b})$$

$$H_2(x) = x^2 - 1 \quad (\text{A.5c})$$

$$H_3(x) = x^3 - 3 \quad (\text{A.5d})$$

3 Gaussian volumes of spherical set in \mathbb{R}^k

The aim of this appendix is to compute the Gaussian measure γ_k of this specific hitting set:

$$\tilde{H}_s = \mathbb{R}^k \setminus \mathcal{B}_{\mathbb{R}^k}(0, \tilde{\kappa}). \quad (\text{A.6})$$

It is defined by EQ. (1.34), leading to:

$$\gamma_k(\tilde{H}_s) = \frac{1}{\sigma^k (2\pi)^{k/2}} \int_{\tilde{H}_s} e^{-\|\mathbf{x}\|^2/2\sigma^2} d\mathbf{x} \quad (\text{A.7})$$

The spherical coordinates in dimension k are as defined below.

$$\begin{cases} \|\mathbf{x}\| &= r \\ x_1 &= r \cos(\theta_1) \\ x_2 &= r \sin(\theta_1) \cos(\theta_2) \\ x_3 &= r \sin(\theta_1) \sin(\theta_2) \cos(\theta_3) \\ \vdots & \\ x_{k-1} &= r \sin(\theta_1) \sin(\theta_2) \cdots \sin(\theta_{k-2}) \cos(\theta_{k-1}) \\ x_k &= r \sin(\theta_1) \sin(\theta_2) \cdots \sin(\theta_{k-2}) \sin(\theta_{k-1}) \end{cases}$$

An volume element being:

$$\begin{aligned} dV &= \left| \det \frac{\partial x_i}{\partial (r, \theta_j)} \right| dr d\theta_1 \cdots d\theta_{k-1} \\ &= r^{k-1} \sin^{k-2}(\theta_1) \sin^{k-3}(\theta_2) \cdots \sin(\theta_{k-2}) dr d\theta_1 \cdots d\theta_{k-1} \end{aligned}$$

the Gaussian volume can be computed, using $(r, \{\theta_i\})$:

$$\begin{aligned} \gamma_k(\tilde{H}_s) &= \frac{1}{\sigma^k (2\pi)^{k/2}} \int_{r=\tilde{\kappa}}^{\infty} r^{k-1} e^{-r^2/2\sigma^2} dx \\ &\quad \times \underbrace{\int_0^\pi \sin^{k-2}(\theta_1) d\theta_1 \int_0^{2\pi} \sin^{k-3}(\theta_2) d\theta_2 \cdots \int_0^{2\pi} d\theta_{k-1}}_{2\pi^{k/2}/\Gamma(k/2) \text{ (} k-1\text{-dimensional volume of unit sphere)}} \\ &= \frac{1}{\sigma^k 2^{k/2-1} \Gamma(k/2)} \int_{r=\tilde{\kappa}}^{\infty} r^{k-1} e^{-r^2/2\sigma^2} dr \end{aligned}$$

In order to simplify the previous equation, one can make the following variable substitution:

$$t = r^2/2\sigma^2 \rightarrow r = \sqrt{2t}\sigma$$

$$dt = r dr / \sigma^2 \rightarrow dr = \sqrt{1/2t}\sigma dt$$

leading to :

$$\gamma_k(\tilde{H}_s) = \frac{1}{\sigma^k \Gamma(k/2) 2^{k/2-1}} \int_{r=\tilde{\kappa}^2/2\sigma^2}^{\infty} (\sqrt{2t}\sigma)^{k-1} e^{-t} \frac{\sigma}{\sqrt{2t}} dt$$

And finally, after obvious simplifications:

$$\gamma_k(\tilde{H}_s) = \frac{1}{\Gamma(k/2)} \int_{r=\tilde{\kappa}^2/2\sigma^2}^{\infty} t^{k/2-1} e^{-t} dt = \bar{\Gamma}(k/2, \tilde{\kappa}^2/2\sigma^2) \quad (\text{A.11})$$

The exact same reasoning can be made for other similar hitting set. Solution are given in the followings formulae:

$$\gamma_k(\mathcal{B}_{\mathbb{R}^k}(0, \tilde{\kappa})) = \bar{\gamma}(k/2, \tilde{\kappa}^2/2\sigma^2) \quad (\text{A.12a})$$

$$\gamma_k(\mathbb{R}^k \setminus \mathcal{B}_{\mathbb{R}^k}(0, \tilde{\kappa})) = \bar{\Gamma}(k/2, \tilde{\kappa}^2/2\sigma^2) \quad (\text{A.12b})$$

$$\gamma_k(\mathcal{B}_{\mathbb{R}^k}(0, \tilde{\kappa}_1) \cup (\mathbb{R}^k \setminus \mathcal{B}_{\mathbb{R}^k}(0, \tilde{\kappa}_2))) = \bar{\gamma}(k/2, \tilde{\kappa}_1^2/2\sigma^2) + \bar{\Gamma}(k/2, \tilde{\kappa}_2^2/2\sigma^2) \quad (\text{A.12c})$$

$$\gamma_k(\mathbb{R}^k \setminus (\mathcal{B}_{\mathbb{R}^k}(0, \tilde{\kappa}_1) \cup (\mathbb{R}^k \setminus \mathcal{B}_{\mathbb{R}^k}(0, \tilde{\kappa}_2)))) = 1 - \bar{\gamma}(k/2, \tilde{\kappa}_1^2/2\sigma^2) - \bar{\Gamma}(k/2, \tilde{\kappa}_2^2/2\sigma^2) \quad (\text{A.12d})$$

Appendix B

Correlated Random Fields

1 Orthogonal decomposition of correlated random fields

The aim of this appendix is to present the “big picture” of correlated random field orthogonal decomposition. Full development and proof of the theorem can be found in [Adler and Taylor, 2007]. A brief description of the ingredients that leads to the decomposition are described, hopefully helping understand the Karhunen-Loève decomposition.

The theory is valid for a large range of space but, for simplicity, a bounded region M of the Euclidean space \mathbb{R}^N is considered here. The *reproducing kernel Hilbert space*, RKHS of a correlated Gaussian random field of covariance function \mathcal{C} is define EQ. (B.4). It is a set of functions which share the same regularity as $\mathcal{C}(\mathbf{x}, \mathbf{y})$ for a given \mathbf{x} (or \mathbf{y}). First one can define:

$$S = \left\{ u : M \mapsto \mathbb{R} : u(\cdot) = \sum_{i=1}^n a_i \mathcal{C}(\mathbf{x}_i, \cdot), a_i \in \mathbb{R}, \mathbf{x}_i \in M, n \geq 1 \right\} \quad (\text{B.1})$$

From \mathcal{C} properties (like its positive definiteness), one can define the following inner product:

$$\langle u, v \rangle_H = \sum_{i=1}^n \sum_{j=1}^m a_i b_j \mathcal{C}(\mathbf{x}_i, \mathbf{y}_j). \quad (\text{B.2})$$

that possess the following reproducing kernel property:

$$\langle u, \mathcal{C}(\mathbf{x}, \cdot) \rangle_H = u(\mathbf{x}) \quad (\text{B.3})$$

This inner product can naturally define a norm of the space S , $\|u\|_H = \sqrt{\langle u, u \rangle_H}$. Hence S can be completed, creating the RKHS $H(\mathcal{C})$ as follows:

$$H(\mathcal{C}) = \left\{ u : M \mapsto \mathbb{R} : u(\cdot) = \sum_{i=1}^{\infty} a_i \mathcal{C}(\mathbf{x}_i, \cdot), a_i \in \mathbb{R}, \mathbf{x}_i \in M \right\} \quad (\text{B.4})$$

$H(\mathcal{C})$ is a separable space since $S \subset H(\mathcal{C})$ is a dense and countable space. This result comes from the separability of M and the continuity of \mathcal{C} . The idea now is to find a base to this space that will be the decomposition base. One need to define, first a linear span of the random variables $g(\mathbf{x})$, $\mathcal{H} = \text{Vect}\{g(\mathbf{x}, \mathbf{x} \in M)\}$ and then, a linear application $\Theta : S \rightarrow \mathcal{H}$ so that:

$$\Theta(u) = \Theta \left(\sum_{i=1}^n a_i \mathcal{C}(\mathbf{x}_i, \cdot) \right) \triangleq \sum_{i=1}^n a_i g(\mathbf{x}_i). \quad (\text{B.5})$$

Knowing that each linear combination of Gaussian random variables is a Gaussian random variable, one can clearly see that $\Theta(u)$ is Gaussian and keeps its norm. Furthermore, $H(\mathcal{C})$ is separable, leading to a possibility to extend it by Θ . The complementary of \mathcal{H} is then constructed with the remaining Gaussian limits. This extension is an isomorphism and make \mathcal{H} separable too. By taking $\{\varphi_n\}$ an orthonormal base of $H(\mathcal{C})$, and $\xi_n = \Theta(\varphi_n)$, $\{\xi_n\}$ is a base of \mathcal{H} and:

$$g(\mathbf{x}) = \sum_{n=1}^{\infty} \xi_n \langle g(\mathbf{x}), \xi_n \rangle_{\mathcal{H}} = \sum_{n=1}^{\infty} \xi_n \mathbb{E}\{g(\mathbf{x})\xi_n\} \quad (\text{B.6})$$

where $\xi_n \sim \mathcal{N}(0, \sigma^2)$ and therefore $\mathbb{E}\{\xi_i \xi_j\} = \delta_{ij}$. Since Θ is an isometry (equivalence of the inner product), using EQ. (B.3), one can conclude that:

$$\mathbb{E}\{g(\mathbf{x})\xi_n\} = \langle \mathcal{C}(\mathbf{x}, \cdot), \varphi_n \rangle_H = \varphi_n(\mathbf{x}) \quad (\text{B.7})$$

EQ. (B.6) and EQ. (B.7) gives directly the wanted decomposition:

$$g(\mathbf{x}) = \sum_{n=1}^{\infty} \varphi_n(\mathbf{x}) \xi_n \quad (\text{B.8})$$

2 Finite Element discretization of the Fredholm problem

The continuum Fredholm problem is written:

$$\int_M \mathcal{C}(\mathbf{x}, \mathbf{y}) \psi(\mathbf{y}) d\mathbf{y} = \lambda \psi(\mathbf{x}) \quad (\text{B.9})$$

Its weak formulation can be written:

$\forall w(\cdot) \in H^1(M)$, find $(\lambda, \psi(\cdot))$ so that:

$$\int_M w(\mathbf{x}) \int_M \mathcal{C}(\mathbf{x}, \mathbf{y}) \psi(\mathbf{y}) d\mathbf{y} d\mathbf{x} = \int_M w(\mathbf{x}) \lambda \psi(\mathbf{x}) d\mathbf{x} \quad (\text{B.10})$$

If M is a cube discretized in a regular mesh with $n \times n \times n$ nodes, one can define:

$$\begin{aligned} \boldsymbol{\psi}_a &= [\psi_1 \dots \psi_{n^3}]^T \\ \mathbf{w}_a &= [w_1 \dots w_{n^3}]^T \\ \mathbf{N}(\cdot) &= [N_1(\cdot) \dots N_{n^3}(\cdot)]^T \end{aligned} \quad (\text{B.11})$$

leading to the following finite element discretization:

$$\begin{aligned} w(\cdot) &= \mathbf{N}^T(\cdot) \mathbf{w}_a \\ \psi(\cdot) &= \mathbf{N}^T(\cdot) \boldsymbol{\psi}_a \\ \mathcal{C}(\cdot, *) &= \mathbf{N}^T(\cdot) \mathbf{C}_{ab} \mathbf{N}(\cdot) \end{aligned} \quad (\text{B.12})$$

Which leads to:

$$\begin{aligned} &\int_M \mathbf{w}_a^T \mathbf{N}(\mathbf{x}) \int_M \mathbf{N}^T(\mathbf{x}) \mathbf{C}_{ab} \mathbf{N}(\mathbf{y}) \mathbf{N}^T(\mathbf{y}) \boldsymbol{\psi}_a d\mathbf{y} d\mathbf{x} = \int_M \mathbf{w}_a^T \mathbf{N}(\mathbf{x}) \lambda \mathbf{N}^T(\mathbf{x}) \boldsymbol{\psi}_a d\mathbf{x} \\ \Rightarrow \mathbf{w}_a^T &\underbrace{\int_M \mathbf{N} \mathbf{N}^T d\mathbf{x}}_M \mathbf{C}_{ab} \int_M \mathbf{N} \mathbf{N}^T d\mathbf{y} \boldsymbol{\psi}_a = \mathbf{w}_a^T \lambda \int_M \mathbf{N} \mathbf{N}^T d\mathbf{x} \boldsymbol{\psi}_a \\ \Rightarrow \mathbf{M} \mathbf{C} \mathbf{M} \boldsymbol{\psi} &= \lambda \mathbf{M} \boldsymbol{\psi} \end{aligned} \quad (\text{B.13})$$

3 The turning band method

Let g be an isotropic, stationary, zero mean correlated random field define over M , a bounded region of \mathbb{R}^3 and $\mathcal{C}_3(\mathbf{x}, \mathbf{y}) = \mathcal{C}_3(\|\mathbf{x} - \mathbf{y}\|)$ be its covariance function. Let $\{z_i\}$, $i = [1..Z]$ be Z unidimensional random fields defined over Z segments (bands) b_i which direction vectors \mathbf{n}_i are uniformly distributed over the unit sphere. The covariance function is assumed to be the same for each random field z_i and is called \mathcal{C}_1 . The three dimensional random field is constructed at each point as the average value of each z_i evaluated at the corresponding projection point:

$$g(\mathbf{x}) = \frac{1}{\sqrt{Z}} \sum_{i=1}^Z z_i(\mathbf{x} \cdot \mathbf{n}_i) \quad (\text{B.14})$$

In order to yield a three dimensional random field with a given covariance function \mathcal{C}_3 , a link can be made with the unidimensional one \mathcal{C}_1 .

$$\begin{aligned} \mathcal{C}_3(\mathbf{x}, \mathbf{y}) &= \mathcal{C}_3(\|\mathbf{x} - \mathbf{y}\|) \\ &= \mathbb{E}\{g(\mathbf{x})g(\mathbf{y})\} \\ &= \mathbb{E}\left\{\frac{1}{Z} \sum_{i=1}^Z \sum_{j=1}^Z z_i(\mathbf{x} \cdot \mathbf{n}_i) z_j(\mathbf{y} \cdot \mathbf{n}_j)\right\} \\ &= \frac{1}{Z} \sum_{i=1}^Z \sum_{j=1}^Z \mathbb{E}\{z_i(\mathbf{x} \cdot \mathbf{n}_i) z_j(\mathbf{y} \cdot \mathbf{n}_j)\} \end{aligned}$$

Since z_i are Z independent random fields, $\mathbb{E}z_i z_j = 0 \forall i \neq j$. Therefore:

$$\mathcal{C}_3(\|\mathbf{x} - \mathbf{y}\|) = \frac{1}{Z} \sum_{i=1}^Z \mathbb{E}\{z_i(\mathbf{x} \cdot \mathbf{n}_i) z_i(\mathbf{y} \cdot \mathbf{n}_i)\}$$

Following the law of large number, if it is assumed that $Z \rightarrow \infty$:

$$\begin{aligned} \mathcal{C}_3(\|\mathbf{x} - \mathbf{y}\|) &= \mathbb{E}\{\mathcal{C}_1((\mathbf{x} - \mathbf{y}) \cdot \mathbf{n})\} \\ &= \oint_{\text{unit sphere}} \mathcal{C}_1((\mathbf{x} - \mathbf{y}) \cdot \mathbf{n}) f(\mathbf{n}) d\mathbf{n} \end{aligned}$$

where \mathbf{n} represents the random unit vector uniformly distributed over the unit sphere. It is recalled that its distribution function is $f(\mathbf{n}) = \frac{1}{4\pi}$ in the three dimensional case. Using spherical coordinates leads to a simplification of the equation. $(\mathbf{x} - \mathbf{y}) \cdot \mathbf{n} = r \cos \phi$, $d\mathbf{n} = \sin \phi d\phi d\theta$. Following [Glimm and Sharp, 1991] leads to, if $\zeta \leftarrow r \cos \phi$:

$$\mathcal{C}_3(r) = \frac{1}{r} \int_0^r \mathcal{C}_1(\zeta) d\zeta \quad (\text{B.18})$$

leading to the inverse equation:

$$\mathcal{C}_1(r) = \frac{d}{dr}(r\mathcal{C}_3(r)) \quad (\text{B.19})$$

If one is interested in yielding a random field with Gaussian covariance then the following unidimensional covariance function should be used:

$$\mathcal{C}_3(r) = \sigma^2 e^{-r^2/L_c^2} \Rightarrow \mathcal{C}_1(r) = \sigma^2 \left(1 - \frac{2r^2}{L_c^2}\right) e^{-r^2/L_c^2} \quad (\text{B.20})$$

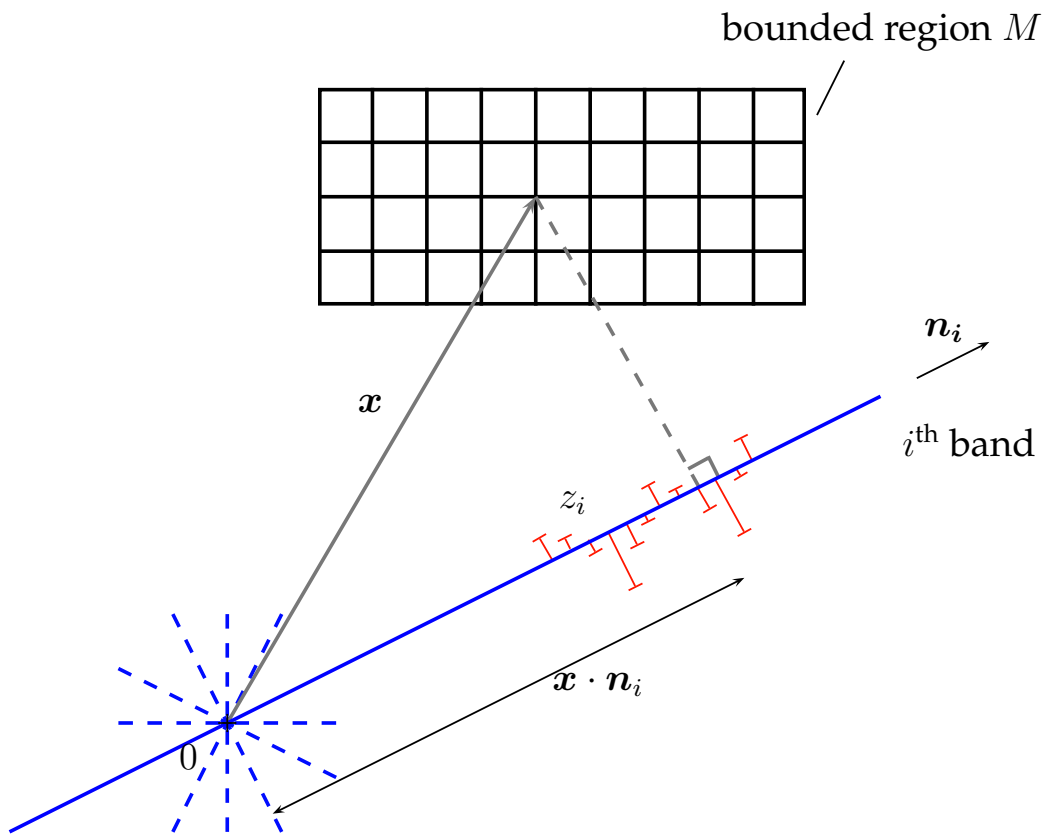


Figure B.1: Representation of the turning band method in two dimensions

Bibliography

- [Adler, 1981] Adler, R. (1981). *The geometry of random fields*. Classics in applied mathematics. Society for Industrial and Applied Mathematics (SIAM, 3600 Market Street, Floor 6, Philadelphia, PA 19104).
- [Adler, 2008] Adler, R. (2008). Some new random field tools for spatial analysis. *Stochastic Environmental Research and Risk Assessment*, 22(6):809–822.
- [Adler and Taylor, 2007] Adler, R. J. and Taylor, J. E. (2007). *Random Fields and Geometry*, volume XVII of *Springer Monographs in Mathematics*. Springer, New York.
- [Adler et al., 2010] Adler, R. J., Taylor, J. E., and Worsley, K. J. (2010). *Applications of Random Fields and Geometry: Foundations and Case Studies*.
- [Ahmed et al., 2005] Ahmed, E., Elgazzar, A., and Hegazi, A. (2005). An overview of complex adaptive systems. *arXiv preprint nlin/0506059*.
- [Al Shamaa, 2012] Al Shamaa, M. (2012). *Étude du risque de développement d'une réaction sulfatique interne et de ses conséquences dans les bétons de structure des ouvrages nucléaires*. PhD thesis, IFSTTAR/MAT - Département Matériaux.
- [Armero and Garikipati, 1996] Armero, F. and Garikipati, K. (1996). An analysis of strong discontinuities in multiplicative finite strain plasticity and their relation with the numerical simulation of strain localization in solids. *International Journal of Solids and Structures*, 33(20-22):2863 – 2885.
- [Bahn and Hsu, 1998] Bahn, B. Y. and Hsu, C.-T. T. (1998). Stress-strain behavior of concrete under cyclic loading. *ACI Materials Journal*, 95:178–193.
- [Barenblatt, 1962] Barenblatt, G. (1962). The mathematical theory of equilibrium cracks in brittle fracture. *Advances in applied mechanics*, 7(1):55–129.
- [Bargieł and Mościński, 1991] Bargieł, M. and Mościński, J. (1991). C-language program for the irregular close packing of hard spheres. *Computer Physics Communications*, 64(1):183–192.
- [Bargieł and Tory, 2001] Bargieł, M. and Tory, E. M. (2001). Packing fraction and measures of disorder of ultradense irregular packings of equal spheres. II. transition from dense random packing. *Advanced Powder Technology*, 12(4):533–557.
- [Barker and Grimson, 1989] Barker, G. C. and Grimson, M. J. (1989). Sequential random close packing of binary disc mixtures. *Journal of Physics: Condensed Matter*, 1(17):2779–2789.

- [Bažant, 2004] Bažant, Z. P. (2004). Probability distribution of energetic-statistical size effect in quasibrittle fracture. *Probabilistic Engineering Mechanics*, 19(4):307–319.
- [Bažant et al., 1990] Bažant, Z. P., Tabbara, M. R., Kazemi, M. T., and Pijaudier-Cabot, G. (1990). Random particle model for fracture of aggregate or fiber composites. *Journal of Engineering Mechanics*, 116(8):1686–1705.
- [Belytschko et al., 1988] Belytschko, T., Fish, J., and Engelmann, B. E. (1988). A finite element with embedded localization zones. *Computer Methods in Applied Mechanics and Engineering*, 70(1):59–89.
- [Benkemoun, 2010] Benkemoun, N. (2010). *Contribution aux approches multi-échelles séquencées pour la modélisation numérique des matériaux à matrice cimentaire*. PhD thesis, ENS Cachan.
- [Benkemoun et al., 2010] Benkemoun, N., Hautefeuille, M., Colliat, J.-B., and Ibrahimbegović, A. (2010). Failure of heterogeneous materials: 3D meso-scale FE models with embedded discontinuities. *International Journal for Numerical Methods in Engineering*, 82(13):1671–1688.
- [Bezrukov et al., 2002] Bezrukov, A., Bargieł, M., and Stoyan, D. (2002). Statistical analysis of simulated random packings of spheres. *Particle & Particle Systems Characterization*, 19(2):111.
- [Bezrukov and Stoyan, 2006] Bezrukov, A. and Stoyan, D. (2006). Simulation and statistical analysis of random packings of ellipsoids. *Particle & Particle Systems Characterization*, 23(5):388–398.
- [Bolander and Saito, 1998] Bolander, J. E. and Saito, S. (1998). Fracture analyses using spring networks with random geometry. *Engineering Fracture Mechanics*, 61(120):569 – 591.
- [Brancherie, 2003] Brancherie, D. (2003). *Modèles continus et “discrets” pour les problèmes de localisation et de rupture fragile et/ou ductile*. PhD thesis, ENS Cachan, Cachan.
- [Broadbent and Hammersley, 1957] Broadbent, S. R. and Hammersley, J. M. (1957). Percolation process, i and II. *Proc. Cambridge Philos. Soc.*, 53:629 – 645.
- [Broyden, 1970a] Broyden, C. G. (1970a). The convergence of a class of double-rank minimization algorithms: 1. general considerations. *IMA Journal of Applied Mathematics*, 6(1):76–90.
- [Broyden, 1970b] Broyden, C. G. (1970b). The convergence of a class of double-rank minimization algorithms: 2. the new algorithm. *IMA Journal of Applied Mathematics*, 6(3):222–231.

- [Caffisch, 1998] Caffisch, R. E. (1998). Monte carlo and quasi-monte carlo methods. *Acta numerica*, 1998:1–49.
- [Carpinteri et al., 2003] Carpinteri, A., Chiaia, B., and Cornetti, P. (2003). On the mechanics of quasi-brittle materials with a fractal microstructure. *Eng. Frac. Mech*, 70:2321–2349.
- [Chatfield, 2004] Chatfield, C. (2004). *The analysis of time series: an introduction*. Texts in statistical science. Chapman & Hall/CRC, Boca Raton, FL, 6th ed edition.
- [Colleparidi, 1997] Colleparidi, M. (1997). A holistic approach to concrete damage induced by delayed ettringite formation. In *Proceedings of the Mario Colleparidi Symposium” Advances in Concrete Science and Technology”, Editor PK Mehta*, page 373–396.
- [Colliat, 2010] Colliat, J.-B. (2010). Modélisation numérique des matériaux hétérogènes: Applications aux matériaux à matrice cimentaire. Technical report, École normale supérieure de Cachan-ENS Cachan, Cachan, France.
- [Colliat et al., 2007] Colliat, J.-B., Hautefeuille, M., Ibrahimbegović, A., and Matthies, H. G. (2007). Stochastic approach to size effect in quasi-brittle materials. *Comptes Rendus Mécanique*, 335(8):430 – 435.
- [Cullum and Willoughby, 2002] Cullum, J. K. and Willoughby, R. A. (2002). *Lanczos Algorithms for Large Symmetric Eigenvalue Computations: vol I: The theory*. Classics in Applied Mathematics. SIAM.
- [Dahlquist, 2003] Dahlquist, G. (2003). *Numerical methods*. Dover Publications, Mineola, N.Y.
- [Dias-da Costa et al., 2009a] Dias-da Costa, D., Alfaiate, J., Sluys, L. J., and Júlio, E. (2009a). A discrete strong discontinuity approach. *Engineering Fracture Mechanics*, 76(9):1176 – 1201.
- [Dias-da Costa et al., 2009b] Dias-da Costa, D., Alfaiate, J., Sluys, L. J., and Júlio, E. (2009b). Towards a generalization of a discrete strong discontinuity approach. *Computer Methods in Applied Mechanics and Engineering*, 198(47-48):3670 – 3681.
- [Divet and Randriambololona, 1998] Divet, L. and Randriambololona, R. (1998). Delayed ettringite formation: The effect of temperature and basicity on the interaction of sulphate and c-s-h phase. *Cement and Concrete Research*, 28(3):357 – 363.
- [Dvorkin et al., 1990] Dvorkin, E. N., Cuitino, A. M., and Gioia, G. (1990). Finite elements with displacement interpolated embedded localization lines insensitive to mesh size and distortions. *International Journal for Numerical Methods in Engineering*, 30(3):541–564.

- [Federer, 1959] Federer, H. (1959). Curvature measures. *Transactions of the American Mathematical Society*, 93(3):pp. 418–491.
- [Fletcher, 1970] Fletcher, R. (1970). A new approach to variable metric algorithms. *The Computer Journal*, 13(3):317–322.
- [Glimm and Sharp, 1991] Glimm, J. and Sharp, D. (1991). A random field model for anomalous diffusion in heterogeneous porous media. *Journal of Statistical Physics*, 62(1-2):415–424.
- [Goldfarb, 1970] Goldfarb, D. (1970). A family of variable-metric methods derived by variational means. *Mathematics of Computation*, 24(109):23–26.
- [Hashin and Shtrikman, 1963] Hashin, Z. and Shtrikman, S. (1963). A variational approach to the theory of the elastic behaviour of multiphase materials. *Journal of the mechanics and physics of solids*, 11:127–140.
- [Hautefeuille et al., 2009] Hautefeuille, M., Melnyk, S., Colliat, J., and Ibrahimbegovic, A. (2009). Failure model for heterogeneous structures using structured meshes and accounting for probability aspects. *Engineering Computations*, 26(1/2):166–184.
- [Hazanov and Huet, 1994] Hazanov, S. and Huet, C. (1994). Order relationships for boundary conditions effect in heterogeneous bodies smaller than the representative volume. *Journal of the Mechanics and Physics of Solids*, 43(42):1995–2011.
- [Heimbs, 2009] Heimbs, S. (2009). Virtual testing of sandwich core structures using dynamic finite element simulations. *Computational Materials Science*, 45(2):205 – 216.
- [Hill, 1963] Hill, R. (1963). Elastic properties of reinforced solids: some theoretical principles. *J. Mech. Phys. Solids*, 11:357–372.
- [Hill, 1967] Hill, R. (1967). The essential structure of constitutive laws for metal composites and polycrystals. *Journal of the Mechanics and Physics of Solids*, 15(2):79 – 95.
- [Hillerborg, 1991] Hillerborg, A. (1991). Application of the fictitious crack model to different types of materials. *International Journal of Fracture*, 51:95–102.
- [Hrennikoff, 1941] Hrennikoff, A. (1941). Solution of problems of elasticity by the framework method. *Journal of Applied Mechanics*, 8:169–175.
- [Huet, 1990] Huet, C. (1990). Application of variational concepts to size effects in elastic heterogeneous bodies. *Journal of the Mechanics and Physics of Solids*, 21(43):813–841.

- [Ibrahimbegović et al., 1998] Ibrahimbegović, A., Gharzeddine, F., and Chorfi, L. (1998). Classical plasticity and viscoplasticity models reformulated: theoretical basis and numerical implementation. *International Journal for Numerical Methods in Engineering*, 42(8):1499–1535.
- [Ibrahimbegović and Wilson, 1991] Ibrahimbegović, A. and Wilson, E. L. (1991). A modified method of incompatible modes. *Communications in Applied Numerical Methods*, 7(3):187–194.
- [Irons and Razzaque, 1972] Irons, B. and Razzaque, A. (1972). *Experience with the patch test for convergence of finite element methods*. Mathematical Foundations of the Finite Element Method. A.K. Aziz, aziz A.K (ed.) edition.
- [Jirásek, 2000] Jirásek, M. (2000). Comparative study on finite elements with embedded discontinuities. *Computer Methods in Applied Mechanics and Engineering*, 188:307 – 330.
- [Jirásek, 2012] Jirásek, M. (2012). Modeling of localized inelastic deformation.
- [Jirásek and Bažant, 1995] Jirásek, M. and Bažant, Z. P. (1995). Particle model for quasibrittle fracture and application to sea ice. *Journal of Engineering Mechanics*, 121(9):1016–1025.
- [Jodrey and Tory, 1979] Jodrey, W. S. and Tory, E. M. (1979). Simulation of random packing of spheres. *Simulation*, 32(1):1–12.
- [Jodrey and Tory, 1985] Jodrey, W. S. and Tory, E. M. (1985). Computer simulation of close random packing of equal spheres. *Phys. Rev. A*, 32(4):2347–2351.
- [Jourdain et al., 2011] Jourdain, X., Colliat, J.-B., De Sa, C., Benboudjema, F., and Gatuingt, F. (2011). Upscaling permeability for fractured concrete: meso-macro numerical approach coupled to strong discontinuities. *Submitted to International Journal for Numerical and Analytical Methods in Geomechanics*.
- [Kanit et al., 2003] Kanit, T., Forest, S., Galliet, I., Mounoury, V., and Jeulin, D. (2003). Determination of the size of the representative volume element for random composites: statistical approach. *International Journal of Solids and Structures*, 40:3647–3679.
- [Kassiotis and Hautefeuille, 2008] Kassiotis, C. and Hautefeuille, M. (2008). coFeap’s manual. http://www.lmt.ens-cachan.fr/cofeap/files/cofeap_manual.pdf.
- [Kerscher et al., 2001] Kerscher, M., Mecke, K., Schuecker, P., Böhringer, H., Guzzo, L., Collins, C. A., Schindler, S., De Grandi, S., and Cruddace, R. (2001). Non-gaussian morphology on large scales: Minkowski functionals of the REFLEX cluster catalogue. *Astronomy and Astrophysics*, 377(1):1–16.

- [Lagier et al., 2011] Lagier, F., Jourdain, X., De Sa, C., Benboudjema, F., and Colliat, J. (2011). Numerical strategies for prediction of drying cracks in heterogeneous materials: Comparison upon experimental results. *Engineering Structures*, 33(3):920–931.
- [Landis et al., 2003] Landis, E. N., Nagy, E. N., and Keane, D. T. (2003). Microstructure and fracture in three dimensions. *Engineering Fracture Mechanics*, 70(7):911–925.
- [Larsson et al., 1996] Larsson, R., Runesson, K., and Sture, S. (1996). Embedded localization band in undrained soil based on regularized strong discontinuity—theory and FE-analysis. *International Journal of Solids and Structures*, 33(20–22):3081 – 3101.
- [Lorensen and Cline, 1987] Lorensen, W. E. and Cline, H. E. (1987). Marching cubes: A high resolution 3D surface construction algorithm. *SIGGRAPH Comput. Graph.*, 21(4):163–169.
- [Lotfi and Shing, 1995] Lotfi, H. R. and Shing, P. B. (1995). Embedded representation of fracture in concrete with mixed finite elements. *International Journal for Numerical Methods in Engineering*, 38(8):1307–1325.
- [Loève, 1978] Loève, M. (1978). *Probability theory*, volume II of *Graduate Texts in Mathematics*. Springer-Verlag, 4 edition.
- [Man and van Mier, 2008] Man, H.-K. and van Mier, J. G. (2008). Influence of particle density on 3D size effects in the fracture of (numerical) concrete. *Mechanics of Materials*, 40(6):470–486.
- [Markovic et al., 2005] Markovic, D., Niekamp, R., Ibrahimbegović, A., Matthies, H. G., and Taylor, R. L. (2005). Multi-scale modelling of the heterogeneous structures with inelastic constitutive behaviour. part i – physical and mathematical aspects. *Engineering Computations*, 22:664–683.
- [Matheron, 1966] Matheron, G. (1966). Genese et signification energetique de la loi de darcy. *Revue Inst. Franc. Petrole*, 21:1697.
- [Matheron, 1973] Matheron, G. (1973). The intrinsic random functions and their applications.
- [Matheron, 1975] Matheron, G. (1975). *Random sets and integral geometry*. Wiley series in probability and mathematical statistics: Probability and mathematical statistics. Wiley.
- [Matthies and Strang, 1979] Matthies, H. and Strang, G. (1979). The solution of nonlinear finite element equations. *International Journal for Numerical Methods in Engineering*, 14(11):1613–1626.
- [Matérn, 1960] Matérn, B. (1960). Spatial variation. stochastic models and their application to some problems in forest surveys and other sampling investigations. *Meddelanden fran statens Skogsforskningsinstitut*, 49(5).

- [Mecke and Wagner, 1991] Mecke, K. and Wagner, H. (1991). Euler characteristic and related measures for random geometric sets. *Journal of Statistical Physics*, 64(3-4):843–850.
- [Mecke et al., 1994] Mecke, K. R., Buchert, T., and Wagner, H. (1994). Robust morphological measures for large-scale structure in the universe. *Astronomy & Astrophysics*, 288:697–704.
- [Mindlin and Eshel, 1968] Mindlin, R. and Eshel, N. (1968). On first strain-gradient theories in linear elasticity. *International Journal of Solids and Structures*, 4(1):109–124.
- [Moore and Taylor, 1970] Moore, A. E. and Taylor, H. F. W. (1970). Crystal structure of ettringite. *Acta Crystallographica Section B*, 26(4):386–393.
- [Moës et al., 1999] Moës, N., Dolbow, J., and Belytschko, T. (1999). A finite element method for crack growth without remeshing. *International Journal for Numerical Methods in Engineering*, 46:131 – 150.
- [Mościński et al., 1989] Mościński, J., Bargieł, M., Rycerz, Z. A., and Jacobs, P. W. M. (1989). The force-biased algorithm for the irregular close packing of equal hard spheres. *Molecular Simulation*, 3(4):201–212.
- [Nemati et al., 1998] Nemati, K. M., Monteiro, P. J., and Scrivener, K. L. (1998). Analysis of compressive stress-induced cracks in concrete. *ACI Materials Journal*, 95:617–630.
- [Niekamp, 1995] Niekamp, R. (1995). Component template library. <http://www.wire.tu-bs.de/forschung/projekte/ctl/>.
- [Okun, 1990] Okun, B. L. (1990). Euler characteristic in percolation theory. *Journal of Statistical Physics*, 59(1/2):523–527.
- [Oliver, 1996a] Oliver, J. (1996a). Modelling strong discontinuities in solid mechanics via strain softening constitutive equations. part 1: fundamentals. *Int. J. Num. Meth. Eng.*, 39(21):3575 – 3600.
- [Oliver, 1996b] Oliver, J. (1996b). Modelling strong discontinuities in solid mechanics via strain softening constitutive equations. part. 1: fundamentals. part. 2: numerical simulation. *Int. J. Num. Meth. Eng.*, 39(21):3575 – 3623.
- [Oliver, 2000] Oliver, J. (2000). On the discrete constitutive models induced by strong discontinuity kinematics and continuum constitutive equations. *International Journal of Solids and Structures*, 37(48-50):7207 – 7229.
- [Oliver et al., 2008] Oliver, J., Huespe, A., and Cante, J. (2008). An implicit/explicit integration scheme to increase computability of non-linear material and contact/friction problems. *Computer Methods in Applied Mechanics and Engineering*, 197(21):1865–1889.

- [Oliver et al., 2002] Oliver, J., Huespe, A. E., Pulido, M. D. G., and Chaves, E. (2002). From continuum mechanics to fracture mechanics: the strong discontinuity approach. *Engineering Fracture Mechanics*, 69(2):113 – 136.
- [Oliver et al., 2006] Oliver, J., Huespe, A. E., and Sánchez, P. J. (2006). A comparative study on finite elements for capturing strong discontinuities: E-FEM vs x-FEM. *Computer Methods in Applied Mechanics and Engineering*, 195(37–40):4732 – 4752.
- [Ollivier et al., 2012] Ollivier, J., Torrenti, J.-M., and Carcasses, M. (2012). *Physical Properties of Concrete and Concrete Constituents*. ISTE. Wiley.
- [Ortiz et al., 1987] Ortiz, M., Leroy, Y., and Needleman, A. (1987). A finite element method for localized failure analysis. *Comput. Methods Appl. Mech. Eng.*, 61(2):189–214.
- [Pavoine et al., 2006a] Pavoine, A., Divet, L., and Fenouillet, S. (2006a). A concrete performance test for delayed ettringite formation: Part i optimisation. *Cement and Concrete Research*, 36(12):2138 – 2143.
- [Pavoine et al., 2006b] Pavoine, A., Divet, L., and Fenouillet, S. (2006b). A concrete performance test for delayed ettringite formation: Part II validation. *Cement and Concrete Research*, 36(12):2144 – 2151.
- [Pijaudier-Cabot and Bažant, 1987] Pijaudier-Cabot, G. and Bažant, Z. P. (1987). Non-local damage theory. *Journal of Engineering Mechanics (ASCE)*, 113:1512–1533.
- [Powers and Brownyard, 1947] Powers, T. and Brownyard, T. (1947). Studies of the physical properties of hardened portland cement paste. *Bulletin*, 22.
- [Rasmussen and Williams, 2006] Rasmussen, C. and Williams, C. (2006). *Gaussian Processes for Machine Learning*. Adaptive computation and machine learning series. University Press Group Limited.
- [Riesz and Szőkefalvi-Nagy, 1955] Riesz, F. and Szőkefalvi-Nagy, B. (1955). *Functional analysis*. F. Ungar Pub. Co., New York.
- [Roberts and Garboczi, 1999] Roberts, A. and Garboczi, E. (1999). Elastic properties of a tungsten–silver composite by reconstruction and computation. *Journal of the Mechanics and Physics of Solids*, 47(10):2029–2055.
- [Sab and Lalaai, 1993] Sab, K. and Lalaai, I. (1993). A unified approach to size effect in quasi-brittle materials. *Compte rendus de l'académie des sciences*, 316:1187–1192.
- [Scher and Zallen, 1970] Scher, H. and Zallen, R. (1970). Critical density in percolation process. *J. Chem. Phys.*, 53:3759.

- [Schickert, 1973] Schickert, G. (1973). On the influence of different load application techniques on the lateral strain and fracture of concrete specimens. *Cement and Concrete Research*, 3(4):487 – 494.
- [Schlangen and Van Mier, 1992] Schlangen, E. and Van Mier, J. (1992). Simple lattice model for numerical simulation of fracture of concrete materials and structures. *Materials and Structures*, 25(9):534–542.
- [Schlather, 2012] Schlather, M. (2012). RandomFields: simulation and analysis of random fields. <http://CRAN.R-project.org/package=RandomFields>.
- [Serra, 1982] Serra, J. P. (1982). *Image analysis and mathematical morphology*. Academic Press, London ; New York.
- [Shanno, 1970] Shanno, D. F. (1970). Conditioning of quasi-newton methods for function minimization. *Mathematics of Computation*, 24:647–656.
- [Simo and Hughes, 2008] Simo, J. and Hughes, T. (2008). Computational inelasticity.
- [Simo and Oliver, 1994] Simo, J. C. and Oliver, J. (1994). A new approach to the analysis an simulation of strain softening in solids. In *Fracture and Damage in Quasibrittle Structures*, E & FN Spon, pages 25 — 39. London, z. p. bazant, z. bittar, m. jirasek and j. mazars edition.
- [Simo et al., 1993] Simo, J. C., Oliver, J., and Armero, F. (1993). An analysis of strong discontinuities induced by strain-softening in rate independent inelastic solids. *Computational Mechanics*, 12:277 – 296.
- [Simo and Rifai, 1990] Simo, J. C. and Rifai, M. (1990). A class of mixed assumed strain methods and the method of incompatible modes. *International Journal of Numerical Methods in Engineering*, 29:1595–1638.
- [Skal et al., 1973] Skal, A. S., Shklovskii, B. I., and Efros, A. L. (1973). Percolation level in a three-dimensional random potential. *JETP Lett.*, 17:377.
- [Sluys and Berends, 1998] Sluys, L. J. and Berends, A. H. (1998). Discontinuous failure analysis for mode-I and mode-II localization problems. *International Journal of Solids and Structures*, 35(31–32):4257 – 4274.
- [Stein, 1999] Stein, M. (1999). *Interpolation of Spatial Data: Some Theory for Kriging*. Springer Series in Statistics. Springer New York.
- [Stoyan, 2002] Stoyan, D. (2002). Random systems of hard particles: models and statistics. *Chinese Journal of Stereology and Image Analysis*, 7(1).
- [Stoyan and Stoyan, 1994] Stoyan, D. and Stoyan, H. (1994). *Fractals, random shapes, and point fields: methods of geometrical statistics*. Wiley series in probability and mathematical statistics: Applied probability and statistics. Wiley.

- [Strang and Fix, 1973] Strang, G. and Fix, G. J. (1973). *An analysis of the finite element method*, volume 212. Prentice-Hall Englewood Cliffs, NJ.
- [Sukumar et al., 2001] Sukumar, N., Chopp, D. L., Moës, N., and Belytshko, T. (2001). Modelling holes and inclusions by level sets in the extended finite element method. *Computer Methods in Applied Mechanics and Engineering*, 190:6183–6200.
- [Szczesniak et al., 2013] Szczesniak, M., Rougelot, T., Burlion, N., and Shao, J.-F. (2013). Compressive strength of cement-based composites: Roles of aggregate diameter and water saturation degree. *Cement and Concrete Composites*, 37:249–258.
- [Taylor et al., 2001] Taylor, H., Famy, C., and Scrivener, K. (2001). Delayed ettringite formation. *Cement and Concrete Research*, 31(5):683–693.
- [Taylor, 2001] Taylor, J. E. (2001). *Euler characteristics for Gaussian fields on manifolds*. PhD thesis, McGill.
- [Taylor, 2006] Taylor, J. E. (2006). A gaussian kinematic formula. *The Annals of Probability*, 34(1):122–158.
- [Taylor and Adler, 2003] Taylor, J. E. and Adler, R. J. (2003). Euler characteristics for gaussian fields on manifolds. *Annals of Probability*, 31(2):533–563.
- [Taylor, 2003] Taylor, R. (2003). FEAP: a finite element analysis program. <http://www.ce.berkeley.edu/projects/feap/>.
- [Team, 2012] Team, R. C. (2012). R: A language and environment for statistical computing. <http://www.R-project.org/>.
- [Tomita and Murakami, 1994] Tomita, H. and Murakami, C. (1994). Percolation pattern in continuous media and its topology. In *Research of Pattern Formation*, page 197 – 203. R. Takaki, KTK scientific publishers edition.
- [Torquato, 2002] Torquato, S. (2002). *Random Heterogeneous Materials: Microstructure and Macroscopic Properties*. Interdisciplinary Applied Mathematics. Springer.
- [Torrenti, 1987] Torrenti, J.-M. (1987). *Comportement multiaxial du béton: aspects expérimentaux et modélisation*. PhD thesis, Ecole Nationale des Ponts et Chaussées.
- [van Mier, 1984] van Mier, J. (1984). *Strain softening of concrete under multiaxial loading conditions*. PhD thesis, University of technology, Eindhoven.
- [Wang et al., 1999] Wang, Z., Kwan, A., and Chan, H. (1999). Mesoscopic study of concrete i: generation of random aggregate structure and finite element mesh. *Computers & structures*, 70(5):533–544.
- [Washizu, 1982] Washizu, K. (1982). *Variational methods in elasticity and plasticity*. Pergamon Press, New York, 3 edition.

- [Weibull, 1951] Weibull, W. (1951). A statistical distribution function of wide applicability. *J. Appl. Mech.*, 18(3):293 – 297.
- [Wells, 2001] Wells, G. N. (2001). *Discontinuous modelling of strain localisation and failure*. PhD thesis, University of Cambridge.
- [Wells and Sluys, 2001] Wells, G. N. and Sluys, L. J. (2001). Three-dimensional embedded discontinuity model for brittle fracture. *International Journal of Solids and Structures*, 38:897–913.
- [Wentworth, 1922] Wentworth, C. K. (1922). A scale of grade and class terms for clastic sediments. *The Journal of Geology*, 30(5):pp. 377–392.
- [Weyl, 1939] Weyl, H. (1939). On the volume of tubes. *American Journal of Mathematics*, 61(2):pp. 461–472.
- [Wilson, 1974] Wilson, E. L. (1974). The static condensation algorithm. *International Journal for Numerical Methods in Engineering*, 8(1):198–203.
- [Wilson and Ibrahimbegović, 1990] Wilson, E. L. and Ibrahimbegović, A. (1990). Use of incompatible displacement modes for the calculation of element stiffnesses or stresses. *Finite Elements in Analysis and Design*, 7(3):229 – 241.
- [Winitzki and Kosowsky, 1997] Winitzki, S. and Kosowsky, A. (1997). Minkowski functional description of microwave background gaussianity. *New Astronomy*, 3(2):75–99.
- [Wittmann et al., 1985] Wittmann, F., Roelfstra, P., and Sadouki, H. (1985). Simulation and analysis of composite structures. *Materials science and engineering*, 68(2):239–248.
- [Worsley, 1996] Worsley, K. J. (1996). The geometry of random images. *CHANCE*, 9(1):27–40.
- [Wriggers and Moftah, 2006] Wriggers, P. and Moftah, S. (2006). Mesoscale models for concrete: Homogenisation and damage behaviour. *Finite elements in analysis and design*, 42(7):623–636.
- [Yip et al., 2005] Yip, M., Mohle, J., and Bolander, J. E. (2005). Automated modeling of three-dimensional structural components using irregular lattices. *Computer-Aided Civil and Infrastructure Engineering*, 20(6):393–407.
- [Zaanen, 1953] Zaanen, A. C. (1953). *Linear analysis; measure and integral, Banach and Hilbert space, linear integral equations*. Interscience Publishers, New York.
- [Zaitsev, 1985] Zaitsev, Y. (1985). Inelastic properties of solids with random cracks in mechanics of geomaterials. *Mechanics of geomaterials*.

- [Zaitsev and Wittmann, 1981] Zaitsev, Y. and Wittmann, F. (1981). Simulation of crack propagation and failure of concrete. *Matériaux et Construction*, 14(5):357–365.
- [Zallen, 1979] Zallen, R. (1979). *The Physics of Amorphous Solids*. John-Wiley and Sons.
- [Zhang et al., 2011] Zhang, M., Ye, G., and van Breugel, K. (2011). Microstructure-based modeling of water diffusivity in cement paste. *Construction and Building Materials*, 25(42):2046–2052.
- [Zhu et al., 2008] Zhu, Q.-z., Shao, J.-f., and Kondo, D. (2008). A micromechanics-based non-local anisotropic model for unilateral damage in brittle materials. *Comptes Rendus Mecanique*, 336(3):320–328.
- [Zienkiewicz and Taylor, 2001] Zienkiewicz, O. C. and Taylor, R. L. (2001). *The Finite Element Method, The Basis*, volume 1. Butterworth Heinemann, Oxford, 5 edition.